University of Strathclyde

Department of Physics

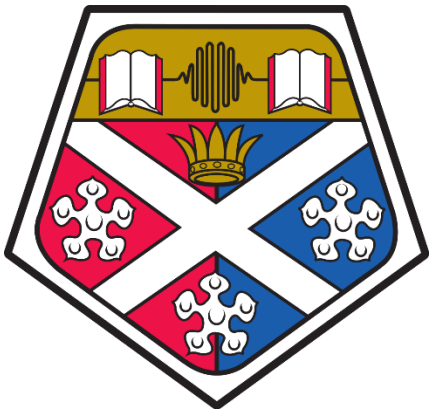

Millimetre and sub-millimetre wave input couplers for gyrotron travelling wave amplifiers

Jason R. Garner

(B.Sc (Hons) M.Sc University of Strathclyde)

A thesis presented in fulfilment of the requirements for

the degree of Doctor of Philosophy

2018

Copyright

Dedication

I would like to dedicate this thesis to my friends and family. My PhD research was made possible thanks to their unwavering support.

Table of Contents

Abstract

The input coupler is an important component for a microwave amplifier. A sidewall single-hole input coupler for a W-band gyrotron travelling-wave amplifier that operates at the frequency range of 90–100 GHz was designed and measured. Instead of using a cutoff waveguide, a broadband Bragg-type reflector with a small spread in phase was optimized for use as part of the input coupler. The minimum radius of the reflector was two times the size of a cutoff waveguide, which reduced the possibility for some of the beam electrons being collected in this section and lost to the amplifier interaction region. The design, simulation, construction and measurement of a W-band waveguide input coupler that used a backstop Bragg reflector that allowed for high electron beam transmission from a cusp electron beam source into a 3-fold helically corrugated interaction waveguide (HCIW) of a gyrotron travelling wave amplifier is presented. Experimental results are reported of a broadband, high power, gyrotron traveling wave amplifier (gyro-TWA) operating in the 75-110 GHz frequency band. The second harmonic cyclotron mode of a 55 keV, 1.5 A, axis-encircling electron beam was used to resonantly interact with a traveling TE_{21}-like eigenwave, achieving broadband amplification. The gyro-TWA demonstrated a 3 dB gain bandwidth of at least 5.5 GHz in the experimental measurement with 9 GHz predicted for a wideband drive source with a measured unsaturated output power of 3.4 kW and gain of 36-38 dB. The inclusion of the Bragg reflector in the W-band waveguide input coupler enabled efficient (4.4%) beam-wave interaction to be achieved within the gyro-TWA.

The design of 1) a T-junction fundamental mode rectangular to- circular waveguide input coupler, 2) a multiple-hole input coupler and 3) a higher order mode (HOM) input coupler for a low-terahertz gyrotron travelling wave amplifier were studied. The T-junction input coupler with a Bragg reflector and a multiple-hole directional coupler were optimized for operation between 360 and 384 GHz, the proposed bandwidth of a low THz gyro TWA. The T-junction coupler and the multiple-hole coupler achieved the respective bandwidths of 10% and 35%.

A higher order mode (HOM) two-branch waveguide coupler based on the even distribution of incident power was designed to couple the rectangular TE_{10} mode to the circular TE_{61} mode. The optimised tapered waveguide input coupler achieved an operating frequency range of 359–385 GHz, equating to a bandwidth of 7%. A prototype waveguide

coupler scaled to W-band (75–110 GHz) was manufactured. The vector network analyser measured return loss of the HOM coupler was shown to be <10 dB at 90–96 GHz. A transmission and phase measurement is presented to analyse TE_{61} mode conversion in the HOM coupler.

Acknowledgments

Primarily I would like to thank my supervisors Dr. Wenlong He and Prof. A.W. Cross. I would also like to thank Prof. A.D.R. Phelps who provided much needed help over the years. I would also like to thank them both for offering me the opportunity to conduct this research under their expert tutelage. I would like to thank the UK research Engineering Physical Science Research Council for providing the PhD studentship.

I gratefully acknowledge the contributions of Dr Liang Zhang and Dr Craig Donaldson who carried out many of the W-band Gyrotron Travelling Wave amplifier experiments and who were very helpful during the experimental phase and without whom this work would not have been possible. I would also like to thank David Barclay for manufacturing many of the experimental components. I would like to thank Dr. Peter Huggard and Mr. Mat Beardsley of the Millimetre Wave Technology Group at the STFC Rutherford Appleton Laboratory, UK for the construction of the W-band helically corrugated interaction waveguide.

I would like to thank the rest of the University of Strathclyde's Atoms, Beams and Plasmas group for their various contributions over the years.

Publications

[1] Liang Zhang, Wenlong He, Craig R. Donaldson, Jason R. Garner, Paul McElhinney, and Adrian W. Cross, “Design and Measurement of a Broadband Sidewall Coupler for a W-Band Gyro-TWA”, IEEE Transaction on Microwave theory and Techniques, 63, No. 6, pp. 3183 – 3190, Oct 2015.

[2] Jason R. Garner, Liang Zhang, Craig R. Donaldson, Adrian W. Cross, and Wenlong He, “Design Study of a Fundamental Mode Input Coupler for a 372-GHz Gyro-TWA I: Rectangular-to-Circular Coupling Methods”, IEEE Transactions on Electron Devices, **63**, No. 1, pp. 497 – 503, Jan 2016.

[3] Jason R. Garner, Liang Zhang, Craig R. Donaldson, Adrian W. Cross, and Wenlong He, “Design Study of a 372-GHz Higher Order Mode Input Coupler”, IEEE Transactions on Electron Devices, **63**, No. 8, pp. 3284 - 3290, Aug 2016.

Role of the author

Throughout this PhD study, the author gained experience in the theory, design, simulation and measurement of broadband input coplers for gryo-TWAs. The work presented in this thesis primarily involved the use of the CST microwave studio to design and simulate 4 different input couplers, but the author also measured the performance of those couplers that were constructed using a Vector Network Analyser.

Chapter 4: The author played a central role in the design, simulation, construction and measurement of a sidewall single-hole input coupler for a W-band gyrotron traveling-wave amplifier that operates at the frequency range of 90–100 GHz The minimum radius of the reflector in this coupler was two times the size of a cutoff waveguide, which reduced the possibility for some of the beam electrons being collected in this section and lost to the amplifier interaction region. This coupler was one of the key components used in a W-band gyro-TWA experiment, the results of which are presented in the thesis. I also designed, simulated and measured the transmission and reflection properties of a smooth profile output horn compatible for high vacuum operation that was used to generate a Gaussian mode with minimum reflections from the broadband 3-layer window. The gyro-TWA experiments were led by Dr C.R. Donaldson and Dr L. Zhiang (University of Strathclyde). The inclusion of the Bragg reflector in the sidewall W-band waveguide input coupler enabled efficient (4.4%) gyro-TWA beam wave interaction to be achieved with the excellent properties of the smooth profiled horn contributing to the zero drive stability of the amplifier.

Chapter 5: The author played the key role in the design and simulation of two fundamental mode rectangular to- circular waveguide input couplers for a low-terahertz gyro-TWA. A T-junction input coupler with a Bragg reflector and a multiplehole directional coupler were optimized for operation between 360 and 384 GHz, the proposed gyro-TWA bandwidth. The author fully analysed the data presented in this chapter writing up the results as first author in a refereed journal publication.

Chapter 6: the author played the key role in the design of a higher order mode (HOM) input coupler for a low-terahertz gyrotron travelling wave amplifier. A two-branch

waveguide coupler based on the even distribution of incident power was designed to couple the rectangular TE_{10} mode to the circular TE_{61} mode. The optimised tapered waveguide input coupler achieved an operating frequency range of 359–385 GHz, equating to a bandwidth of 7%. A prototype waveguide coupler scaled to W-band (75–110 GHz) was manufactured with its performance measured using a VNA. The author fully analysed the data presented in this chapter writing up the results as first author in a refereed journal publication.

Character Index

Latin alphabet:

A_0 – Cathode emission constant.

a – Rectangular waveguide width.

a_i – Coupling strength at i-th aperture.

$\boldsymbol{B}$ – Magnetic field.

B_K – Cathode magnetic field.

B_n – Susceptance at waveguide transition.

B_r – Radial magnetic field.

B_z – Axial magnetic field.

B_0 – Magnetic field at beam guiding centre.

B_ϑ – Azimuthal magnetic field.

b – Rectangular waveguide height.

C – Coupling.

c – Speed of light in a vacuum.

D – Directivity.

d – Helically corrugated waveguide axial period.

d_g – Spark gap switch electrode spacing.

$\boldsymbol{E}$ – Electric field.

E_K – Cathode electric field.

E_e – Electron energy.

E_r – Radial electric field magnitude.

E_0 – Electron at Fermi energy level.

e – Charge of an electron.

$F_C(x)$ – Fourier transform of total coupling distribution.

$F_D(x)$ – Fourier transform of total directivity distribution.

$F_i(\vartheta)$ – Fourier transform of coupling and/or directivity parameter at i-th aperture.

F_r – Electric beam repulsive force.

F_z – Magnetic beam attraction force.

f – Frequency.

f_{LOWER} – Lower bandwidth cut-off frequency.

f_{UPPER} – Upper bandwidth cut-off frequency.

f_c – Cut-off frequency.

f_q – Fractional bandwidth.

h – Planck's constant.

h_B – Bragg corrugation amplitude.

h_n – Axial wavenumber of mode n.

k – Boltzmann constant.

k_B – Bragg wavenumber.

k_z – Axial wavenumber.

I – Current.

I_b – Beam current.

$\boldsymbol{J}$ – Current density.

J_0 – Zero-field current density.

L_1 – Distance from near edge of waveguide reflector to rectangular input waveguide.

L_{CAB} – Blumlein Pulse Forming Line (PFL) cable length.

L_m –Coupling section length.

L_n – Step discontinuity length.

L_t – Waveguide taper length.

l_B – Electron beam length.

l_R – Rogowski coil total wire length.

l_S – Solenoid length.

m_B – Helically corrugated waveguide fold number.

m_e – Electron mass.

m_n – Azimuthal indices of mode *n*.

m_1 – Argument of elliptical integrals.

N – Integer number.

n_e – Electron number density.

P – Perveance.

P_b – Electron beam power.

P_{bCAV} – Beam power after beam-wave interaction.

P_{bDIS} – Beam power dissipated in the electron collector walls.

P_{bREC} – Fraction of beam power recovered by a depressed electron collector.

P_{out} – RF output power.

p – Bragg corrugation period.

R – Cylindrical waveguide radius.

R' – Aperture radius.

R_0 – Helically corrugated waveguide average radius.

R_1 – Helically corrugated waveguide corrugation depth.

R_A – Anode radius.

$R_{B(z)}$ – Solenoid bore radius.

R_C – Cut-off radius.

R_{IN} – E-plane bend inner radius.

R_K – Cathode radius.

R_R – Rogowski coil torus radius.

R_n – Resistance.

r_R – Rogowski coil turn radius.

r_b – Beam radius.

r_e – Electron distance from beam centre.

r_L – Larmor radius.

$r(\vartheta,z)$ – Helically corrugated waveguide profile.

s – Aperture spacing.

T – Temperature.

t – Time.

t_a – Aperture height.

t_W – Window thickness.

V – Electron beam charging voltage.

V_K – Cathode-anode gap potential.

V_R – Rogowski coil voltage.

V_b – Electron beam potential.

V_{in} – Input voltage.

$V_{oscilloscope}$ – Output voltage of test pulse at oscilloscope.

V_{out} – Output voltage.

v_c – Pulse propagation velocity.

v_e – Electron velocity.

v_g – Group velocity.

v_p – Phase velocity.

v_z – Axial electron velocity.

v_ϕ – Azimuthal electron velocity.

$v_\perp$ - Perpendicular electron velocity.

Y_n – Admittance at waveguide transistion.

Z – Impedance ratio.

Z_1, Z_2 – Transmission line impedance.

Z_L – Load impedance.

Z_n – Impedance mismatch at waveguide step n.

Greek alphabet:

α_p – Pierce gun geometric parameter.

β_n – Phase constant.

γ – Relativistic correction factor.

$\tan(\delta)$ – Loss tangent.

ε_0 – Permittivity of free space.

ε'_r – Real part of relative permittivity.

η_e – Electronic efficiency.

η_t – Total efficiency.

ϑ_B – Brewster angle.

ϑ_C – Coupling parameter.

ϑ_D – Directivity parameter.

ϑ_{EB} – Angle between electric and magnetic fields.

ϑ_{rot} – Prototype coupler rotation angle.

μ_0 –Permeability of free space.

ρ – Beam charge density.

ρ_{crit} – Cusp field critical radius.

τ – Pulse discharge duration.

λ_0 – Free-space wavelength.

λ_g^C – Circular waveguide guide wavelength.

λ_g^R – Rectangular waveguide guide wavelength.

ϕ – Electric potential ($e\phi$ is known as the work function).

$\phi(x)$ – Aperture coupling function.

$\phi_i(x)$ – Coupling function at *i*-th aperture.

$\Delta\phi$ – Work function reduction caused by Schottky effect.

ω – Angular frequency.

ω_c – Angular cut-off frequency.

ω_{ce} – Electron cyclotron frequency.

Figure List

Chapter 1:

Chapter 2:

Chapter 4:

Table List

1. Introduction

1.1. Introduction to Gyro-Travelling Wave Amplifiers

1.1.1. Principle of Operation

Gyro-travelling wave amplifiers (gyro-TWA) are sources of coherent electromagnetic radiation based on a beam wave energy share cycle which serves to deliver high power microwave signals at high frequencies. Electromagnetic (EM) radiation is amplified as a result of Bremsstrahlung emission, an emission mechanism caused by abrupt variation in charged particle velocity and direction, from velocity modulated electron bunches in an annular beam of gyrating electrons. The emission of microwave radiation from electrons following a rotating around an axial magnetic field is known as cyclotron resonance maser (CRM) emission. Early investigation into the CRM instability was carried out between 1958 and 1959. Twiss [1.1] and Schneider [1.2] postulated their understanding of the CRM emission process with quantum mechanics. Gaponov [1.3] used a classical approach to explain the emission process, stating that the dependence of the electron cyclotron frequency (ω_{ce}) on electron energy (eV) leads to orbital electron bunching. Axial bunching of electrons is described by Weibel [1.4], a process which also contributes to EM wave emission in a gyro-device. However, the contribution of axial bunching to wave growth is considerably less than the contribution from azimuthal bunching.

In CRM devices, electromagnetic energy is radiated from an electron beam gyrating in an externally applied magnetic field. The applied magnetic field (B) is induced longitudinally with respect to the direction of electron motion, with electrons travelling at velocity (v_e). The charged particles experience a v_e x B force and follow a helical path, either small or large orbit, around the lines of the magnetic field. For a net energy exchange from the electron beam to an electromagnetic wave, the electrons must become bunched in phase within their cyclotron orbital path [1.5]. Amplification of an incident wave is achieved if a resonance condition between the periodic motion of the electrons and the microwaves exist. The resonance condition is defined as

$$\omega - k_z v_z \cong s\omega_{ce} \tag{1.1}$$

where ω is the wave angular frequency, k_z is the axial wavenumber, v_z is the longitudinal electron velocity in the interaction region and s is an integer harmonic number. The electron cyclotron frequency (ω_{ce}) is defined as

$$\omega_{\mathrm{ce}} = \frac{eB_0}{m_{\mathrm{e}}\gamma} \tag{1.2}$$

where B_0 is the magnetic field at the centre of the hollow electron beam. The relativistic correction factor (γ) is dependent on the electron beam energy (eV), given by

$$\gamma = 1 + \frac{eV}{m_e c^2} \tag{1.3}$$

where V is the accelerating voltage. The relativistic correction factor plays a role for beam voltages of ~40 kV and greater. The electrons orbit the beam guiding centre at the Larmor radius (r_L) which is defined by

$$r_L = \frac{v_\perp}{\omega_{ce}} \tag{1.4}$$

where $v_\perp$ is the perpendicular velocity of the electron beam. For large orbit electron beams, typical of a cusp electron gun (Section 2.2.4), r_L is equal to the beam radius (r_b). If a Magnetron Injection (MIG) Gun (Section 2.2.3) is employed, the vacuum device operates with a small orbit electron beam ($r_L << r_b$).

The CRM instability, which causes the growth of the electromagnetic signal, will be analysed by considering a single beamlet of large orbit electrons in the presence of a variable electric field. To understand the azimuthal bunching of electrons within their orbital paths, two assumptions about the electron motion are made:

1. the electrons rotate anti-clockwise about the beam guiding centre and,
2. the electrons have zero longitudinal velocity (v_z).

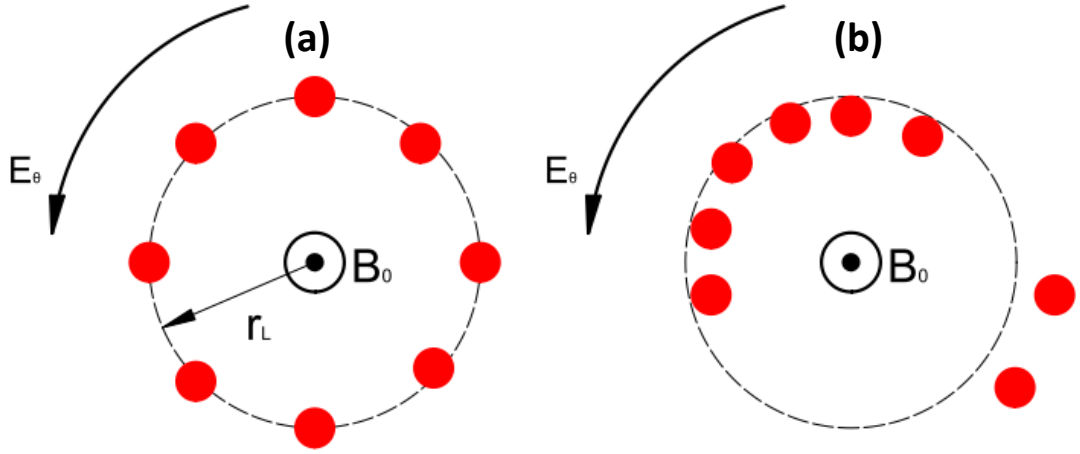

Fig. 1-1: Electron orbital distribution for (a) $\omega = \omega_{ce}$ and (b) $\omega > \omega_{ce}$, leading to electron bunching in the microwave decelerating phase and energy extraction.

A gyro-device typically operates with $v_\perp > v_z$. The large perpendicular velocity component allows for maximum beam-wave energy share due to the transverse components of the microwave field interacting solely with the orbital momentum of the electron beam [1.6]. A schematic of the initial electron orbital distribution is shown in Fig. 1-1(a). Fig. 1.1(a) shows the electrons being initially in random phase within their orbital paths, experiencing an RF electric field with equal oscillatory frequency ($\omega = \omega_{ce}$). The result of this is that there is no net energy transfer between the microwave field and the electron beam. Bunching of the electrons may be achieved in two discrete regimes. In the first regime, the wave frequency is less than the electron cyclotron frequency ($\omega < \omega_{ce}$) and, in the second regime, the wave frequency exceeds the electron cyclotron frequency ($\omega > \omega_{ce}$) [1.7]. Under the conditions of the first regime, the electron bunches are formed in the accelerating phase and, hence, no energy is transferred from the electrons to the wave. In the second regime,

initially decelerated electrons remain in the decelerating phase of the microwave field throughout the beam-wave interaction period. The decelerated electrons experience an increasing value of orbital frequency and move closer to exact resonance with the microwave field. As a result, the electrons lose an increasing amount of energy on each successive wave cycle and form bunches in the decelerating phase of the microwave field. The charged particles which are initially accelerated by the wave, experience a decrease in gyrofrequency and fall farther from resonance, gaining less energy on each successive cycle. The decrease in electron bunch velocity allows for the transfer of electron orbital kinetic energy to the wave. A convective instability develops which allows for the growth of the microwave signal over time as the electrons bunch in phase within their respective cyclotron orbits (Fig. 1-1(b)). Fig. 1-1(b) highlights a decrease in the Larmor radius of the decelerated electrons with electron bunches forming in the microwave deceleration phase. Accelerated electrons are shown to increase their orbital distance. The convective CRM instability is responsible for energy generation and amplification in gyro-devices.

A gyro-TWA is a broadband source because of beam-wave interaction at a position known as the 'grazing point' [1.8]. Fig. 1-2 shows the dispersion diagram of a gyro-TWA compared to a gyrotron and a gyro-backward wave oscillator (gyro-BWO) with smooth-bore interaction cavities. The electron beam dispersion is given by Eqn. 1.1 with the cavity mode defined by

$$\omega = \sqrt{(\omega_c^2 + c^2 k_z^2)} \tag{1.5}$$

where ω_c is the mode cut-off frequency in the waveguide. The gyrotron is shown to operate close to cut-off with a monochromatic output. The gyro-BWO has a single frequency output for a fixed *B*-field; however, a broad tuning bandwidth is achievable with variation of the magnetic field within the interaction cavity. A gyro-TWA is shown to interact with the cavity mode over a wide frequency range without the required adjustment of the beam

parameters and/or B-field amplitude. The instantaneous bandwidth of a gyro-TWA allows for high gain amplification of a feed signal without the added complexity of field tuning.

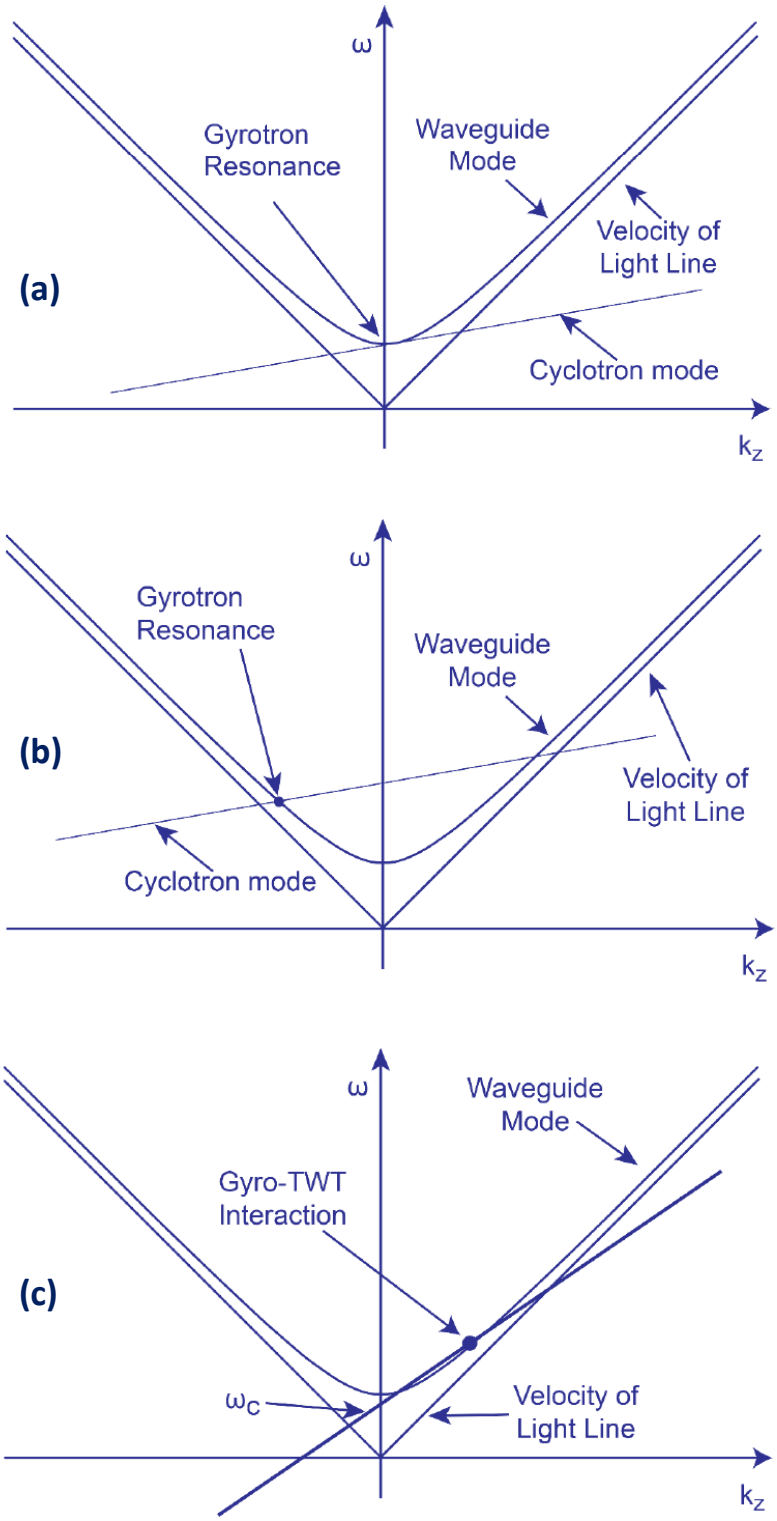

Fig. 1-2: Dispersion of (a) gyrotron, (b) gyro-BWO and (c) gyro-TWA for a smooth bore interaction waveguide.

1.1.2. Historical Review

The generation of high power microwave signals from vacuum electronic devices began with the construction of the magnetron [1.9 – 1.11] in 1921. A magnetron is a crossed-field device consisting of a central cylindrical cathode with a coaxial anode configuration. The static cathode – anode electric field causes initial electron trajectories propagating towards the anode structure. A magnetic field is induced parallel to the cathode resulting in the electrons experiencing a Lorentz force, resulting in the formation of rotating electron spokes. As the electrons traverse the anode cavities, a high frequency RF field is generated within the resonant structures. The magnetron is an efficient device (~ 85%) due to its ability to extract energy both from the ac and dc fields.

The Heil tube (1935) [1.12] is credited as being the primary linear beam tube to utilise the effect of electron velocity modulation and spatial electron bunching. The vacuum tube consists of an electron gun which produces a linear electron beam with a dominant axial velocity component. The beam is propagated through a drift region and into an electron collector. A variable voltage supply is applied at the entrance of the drift tube which results in the velocity modulation of the electron beam. The acceleration and deceleration of electrons leads to the formation of electron bunches. A resonant microwave circuit [1.13] is positioned at the drift tube exit with the oscillations of the charged particle bunches resulting in the generation of an RF signal.

The demonstration of velocity modulation of an electron beam in a linear beam device provided the basis upon which the klystron amplifier [1.14] was developed. A klystron amplifier [1.15 – 1.17] propagates a linear electron beam through a resonant circuit consisting of at least two resonant cavities. The first resonant cavity acts as the RF input within which a high frequency signal is excited. The cavity field extends over the interaction gap, which separates the resonant structure from the beam tube, with both axial and transverse field variations. The excited electric field in the gap varies sinusoidally allowing the propagating electrons to encounter either an accelerating or decelerating field. The electron bunches interact with the subsequent resonant cavities, exciting a cavity RF signal

as the electron beam traverses the interaction gap. A method of cavity coupling is employed in the final resonant structure to extract an amplified output signal.

The travelling wave tube (TWT) was developed during the Second World War in a bid to improve Allied Force communications and radar systems. Investigations into the manufacture of a TWT were being carried out simultaneously on each side of the Atlantic Ocean [1.18 – 1.19] with Rudolf Kompfner being the first to publish his research (1943). However, the use of dielectric support rods and solenoid focussing employed on J. R. Pierce's design is symptomatic of modern day TWT's. The active components of a TWT are similar in nature to a klystron amplifier. However, the microwave signal is propagated along a slow wave structure within the TWT cavity. A periodic slow wave structure, typically a helical [1.20], ring loop [1.21] or folded waveguide structure [1.22], is used to reduce the axial phase velocity of the wave. If the electron bunches are located in regions of the microwave decelerating field, the electron velocities are reduced and the electron energy is transferred to the wave. The microwave signal is amplified during synchronous operation as the wave traverses the TWT cavity; however, increased length can result in saturated gain.

Table I-I: Timeline of Historical Vacuum Tube Development.

Year	Milestone
1921	Hull introduces the magnetron
1935	Heil tube is developed
1937	Varian klystron amplifier
1943	Travelling wave tube development
1959	CRM instability is described
1964	"Bott's Bottle"
1967	Gyroton oscillator based on CRM instability

The formulation of the CRM instability (Section 1.1.1) led to the development of vacuum devices with gyrating electron beams. The first gyro-device published was 'Bott's Bottle' (1964) [1.23 – 1.24]. The vacuum device consists of a triode-like electron gun where the three electrodes are placed at 12° from the normal with both the control grid and anode meshed to allow for electron transport. A region of magnetic compression is employed to initiate the electron orbital motion. A name more familiar to the vacuum electronic community was associated with a gyro-device designed in 1967; the gyrotron [1.25 – 1.27]. The vacuum device comprised components which are employed on modern day gyro-devices; a MIG gun (Section 2.2.3) produced an annular electron beam, electron confinement was provided through solenoid focussing (Section 2.3.2) and a smooth-bore cylindrical waveguide (Section 2.4.1) was employed as the interaction cavity. The development of the gyrotron led to the design of various gyro-devices including the gyro-BWO, gyro-TWA and gyro-klystron which offer different operating characteristics based on CRM interaction [1.28]. An overview of the vacuum device historical timeline is shown in Table I-I.

1.1.3. Applications of the gyro-TWA

Vacuum devices have a broad range of applications in the defence, scientific and commercial industries. Radar system developers often employ vacuum electronic devices as final stage amplifiers [1.29 – 1.31] before transmission of the microwave signal into free space. The development of vacuum electronics was expedited by the requirement for improved security during the First and Second World Wars. The application of vacuum devices in modern day air surveillance and missile tracking surveillance highlights the continued strong links between vacuum electronics and military applications. However, radar systems have also been used for weather monitoring and cloud profiling. In the scientific community, as well as extensive research projects focussed on the development of vacuum electronics, high power amplifiers and oscillators are used as drivers for RF cavities [1.32 – 1.33]. The RF accelerator cavities provide the energy required to generate beam

energy levels of 6.5 TeV within the Large Hadron Collider. Also involved in large scale scientific experiments, high power, single frequency gyrotrons are used as the final stage heating in fusion plasma reactors [1.34 – 1.39]. High power vacuum electronic devices are employed in materials processing [1.40 – 1.42] which serve to alter the physical properties of the raw material or generate the energy required for plasma discharge cutting.

1.2. Strathclyde Gyro-Device Progression

Linear beam tubes and gyro-devices operate over a broad frequency range with varying levels of output power. Fig. 1-3 provides a comparison of output power from vacuum devices varying with the frequency of operation for microwave and mm-wave radiation. The progression of gyro-device research at the University of Strathclyde will be outlined. The red line (Fig. 1-3) indicates the achieved operating characteristics of gyro-devices operating at X-band and W-band with the dashed red line indicating the future progression into low-THz amplifier design. Research at Strathclyde has focussed on broadband amplifiers in recent years. Therefore, although the maximum output power of the devices is less than a gyrotron, the devices are capable of operation over a broad bandwidth. The centre frequency output power for broadband gyro-devices is plotted in Fig. 1-3.

Research interest into high power gyro-devices at the University of Strathclyde began with investigations into gyrotron oscillators [1.43 – 1.47]. The gyrotron system included an 11 T superconducting magnet allowing for a tuneable microwave output spectrum of 20 – 100 GHz operating at cavity modes from TE_{12} to $TE_{14,2}$. The peak output power from the gyrotron cavity ranged from 450 kW at 20 GHz to 300 kW at 100 GHz. The tuneable gyrotron, however, requires precise beam coupling to the operating mode to achieve a high power microwave output signal with the operation of the device dependant on the interaction cavity supporting higher order modes. Hence, the overmoded cavity is liable to parasitic oscillation and multi-mode coupling. Therefore, a high power source operating at the fundamental mode is desirable.

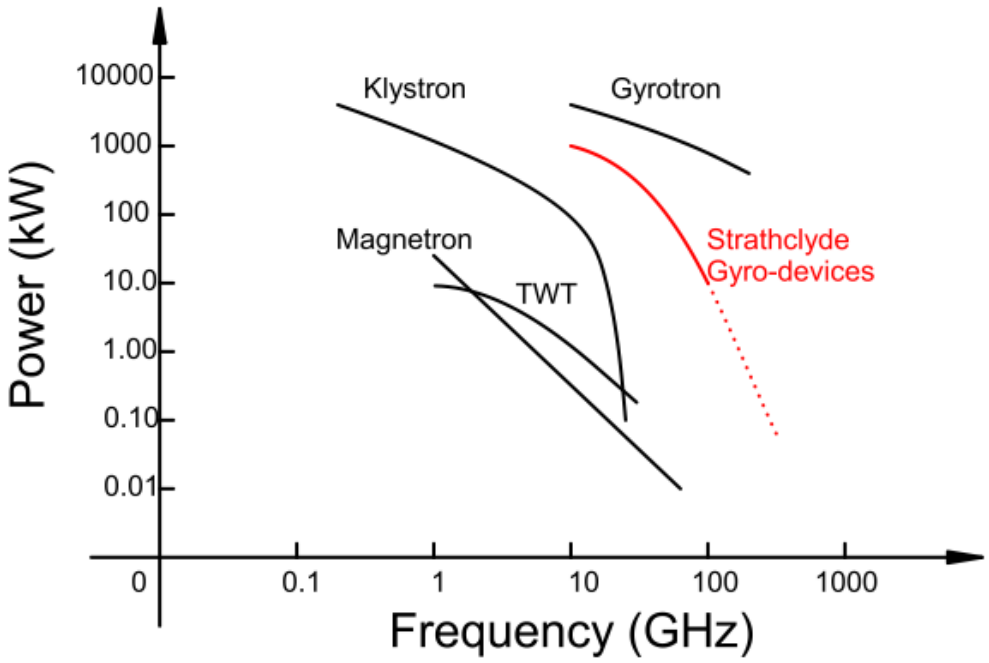

Fig. 1-3: Comparison of vacuum tube power at microwave and mm-wave frequencies.

Gyro-device research developments progressed to the investigation of fundamental mode X-band microwave sources. A 9.4 GHz gyro-TWA with a helically corrugated interaction waveguide (Section 2.4.2) [1.48 – 1.50] produced a 1.1 MW output power over a 20% instantaneous bandwidth (8.4 GHz – 10.4 GHz). The gyro-TWA exhibited a saturated gain of 37 dB with a 185 kV, 25 A electron beam. A competing X-band gyro-TWA from a research project conducted at UC Davis operated at a centre frequency of 9.3 GHz [1.51 – 1.52] with a bandwidth of 11%. The output power achieved from the UC Davies gyro-amplifier, operating at the fundamental harmonic, was 55 kW with a maximum output power of 207 kW exhibited at the second harmonic. The 9.4 GHz gyro-TWA based on 3-fold helical corrugated interactions is shown to have a larger maximum output power over a broader bandwidth compared to competing gyro-amplifiers.

The research into gyro-devices extended into the W-band due to potential application of the device in weather monitoring radar systems and as a millimetre wave source required for Electron Paramagnetic Resonance Spectroscopy. The design of W-band sources can be split into devices which maximise the power output at a single frequency or over a bandwidth on the order of ~ MHz, or broad 3dB bandwidth sources with limited

power output. A tuneable W-band gyrotron Backward Wave Oscillator (gyro-BWO) was developed at the University of Strathclyde with a unique broadband, high power output spectrum. The gyro-BWO design [1.53 – 1.57] with a cusp electron gun (Section 2.2.4) yielded a mm-wave signal of 5 kW maximum power over a 10% bandwidth (90 – 100 GHz) when driven with a 40 kV, 1.5 A electron beam.

In general, fast-wave W-band vacuum devices can be designated to one of the aforementioned categories. A comprehensive review of W-band sources can be found in [1.28]. Single frequency gyrotrons have been designed for 90 – 100 GHz operation with CPI operating a CW gyrotron with an output power of 120 kW at ~ 95 GHz [1.58]. Also at CPI, a 95 GHz gyro-TWA with a 6 kW pulsed output signal has been demonstrated [1.59]. The bandwidth of the device was ~ 3%. Other fast wave devices, which are defined as vacuum tubes which do not employ a resonant structure to reduce the wave velocity, based on the CRM instability are also capable of generating microwave radiation in the W-band. A gyro-klystron, which uses bunching cavities to modulate the axial velocity of a gyrating electron beam, has been developed by NRL. The W-band device operates around a centre frequency of 94 GHz with a bandwidth of 420 MHz (0.004% bandwidth) [1.60 – 1.61]. Although the device is narrowband, the peak output power is 92 kW whilst operating in the TE_{01} mode. A W-band TE_{02} gyro-klystron was demonstrated by IAP in Nizhny Novgorod which had a peak output power of 342 kW [1.62] driven by a 75 kV, 18.3 A electron beam. A gyrotwystron, which combines the operating characteristics of a gyro-klystron with an extended drift region for travelling wave interaction in a bid to improve the cavity bandwidth, was developed at NRL [1.63]. The device achieved a maximum output power of 50 kW at ~ 94 GHz with a bandwidth of ~ 1%. The results show the ability of the gyrotwystron to operate in a 'middle-ground' between the operating characteristics of the gyro-klystron and the gyro-TWA.

Table I-II: Target performance of 372 GHz gyro-TWA.

Frequency (GHz)	360 – 384
Output Power (W)	200 W
Gain (dB)	40
Run Time	> CW
Beam Voltage (kV)	40
Beam Current (A)	1.5

A low-THz gyro-TWA is under development at the University of Strathclyde with a view to application on a 600 MHz Dynamic Nuclear Polarisation Nuclear Magnetic Resonance (DNP-NMR) system. Current final-stage solid state amplifiers used in DNP-NMR systems output mW of average power resulting in high resolution images lasting for upwards of 12 hours. The amplifiers are much less powerful than the proposed low-THz gyro-TWA (Fig. 1-3). The DNP enhancement of proton-NMR can produce an improvement in spectral resolution by a factor of 600 [1.64] by transferring the high polarization electron spin reservoir to the much smaller nuclei spin reservoir. NMR relies on the Zeeman interaction between nuclear spins and external magnetic field. The measurable NMR signal is proportional to the nuclear magnetization, i.e., for spin 1/2 nuclei, the population difference between the two Zeeman levels. Since the energy separation between such levels is very small with respect to thermal energy, only a few spins contribute to the signal. For instance, under a magnetic field strength of 1 Tesla, at room temperature, hydrogen nuclei are polarized to only 3 x 10^{-6}%. Magnetic Resonance Imaging (MRI), one of the most relevant applications of NMR, is able to provide highly resolved images only because this sensitivity issue is circumvented by the huge number of hydrogen nuclei (more than 10^{19} per mm^3). However, such a poor polarization remains the main limitation for in-vivo detection of drugs administered to the patient at milli-molar concentrations (less than 10^8 per mm^3). DNP is nowadays the most promising strategy to overcome this sensitivity limitation. In a DNP

procedure, the compound, doped with free radicals (i.e. molecules with unpaired electrons [1.65] is subjected to a strong magnetic field (~1 T), at low temperature (~1 K) and is irradiated with microwaves. When the microwaves are off the unpaired electrons are strongly polarized because the electron Zeeman gap is thousands times larger than the nuclear one. When the microwaves are on, at a frequency close to the electron Zeeman gap, the interacting spin system of electron and nuclei re-organizes itself in a new out-of-equilibrium steady state characterized by an enhanced nuclear polarization, of up to 40%. Higher magnetic field DNP-NMR systems are being developed and hence the irradiance of an electron polarising agent with THz radiation, which causes the transfer of the electron spin polarisation to the nucleus, will result in much higher signal intensities removing the requirement for extensive signal averaging. A THz source used for DNP-NMR experiments should be able to produce power outputs of > 10 W over a run time of 1.5 days. Linear beam tubes and semiconductor amplifiers suffer from scalability problems which result in a limited output power. A gyrotron [1.66] has been designed for DNP-NMR at 600 MHz with an 8 T superconducting magnet. The device outputs a 30 W pulse operating in the TE_{06} mode. A 372 GHz gyro-TWA is under investigation with a view to producing a proof of principle vacuum tube which can be scaled to 394 GHz. The use of a gyro-TWA on DNP-NMR experiments has the potential to provide a further improvement in spectral resolution due to the tunability of the device [1.67 – 1.68]. The target operating characteristics of the 372 GHz gyro-TWA are shown in Table I-II.

1.3. Outline of the PhD Thesis

The aim of the PhD thesis is to design and manufacture passive waveguide input couplers for two gyro-TWA projects at W-band and 372 GHz respectively. The design of a 94 GHz fundamental mode rectangular-to-circular input coupler is presented and is subsequently implemented on a W-band gyro-TWA. Experimental analysis of the gyro-TWA is performed. The design of input couplers for a 372 GHz gyro-TWA, operating with a 3-fold and 8-fold helically corrugated interaction waveguide (HCIW) respectively, is presented. An analysis of two fundamental mode input couplers, operating within the 360 – 384 GHz bandwidth of the proposed gyro-amplifier, is made alongside a discussion based on the

effect of manufacturing tolerance discrepancies on the coupler performance. The design of a higher order mode (HOM) coupler for a low-THz gyro-TWA is presented. A tolerance study is also performed on the 372 GHz TE_{61} input coupler with a W-band prototype of the coupler made and experimentally examined.

An overview of the thesis chapter contents is presented.

Chapter 2: The theory chapter presents an overview of the passive and active gyro-TWA components and the physical processes which govern the beam-wave interaction within a gyro-amplifier. The generation of the electron beam is discussed with electron gun topologies which are applicable to a gyro-amplifier setup. The transport of the electron beam through the interaction waveguide is discussed, commenting on the internal beam forces and the electron beam guidance. The passive interaction waveguide and the output collector are also discussed.

Chapter 3: The design of a rectangular-to-circular side-wall input coupler for a W-band gyro-amplifier is presented. The numerical simulation and optimisation of the coupler is included. A comment on the manufacture of the input coupler is made and the input coupler is tested using a Vector Network Analyser (VNA). The transmission and reflection of the input coupler is measured and compared to numerical results.

Chapter 4: The input coupler is implemented alongside existing W-band gyro-device components and an experimental investigation of the device is performed. The passive components are measured using a Vector Network Analyser. A discussion of the power supply configuration and the solenoid focussing field is presented. The experimental investigation allows for the documentation of the time-dependant electron beam voltage and current and the magnitude of the microwave signal for a W-band gyro-BWO (backward wave oscillator).

Chapter 5: The design of two fundamental mode rectangular-to-circular input couplers for a 372 GHz gyro-TWA is presented. The design and numerical simulation of a T-junction input coupler with a waveguide reflector, similar to the W-band design of Chapter 3, and a multiple hole input coupler is presented. A comparison of the coupler topologies is made

and a selection of a coupler for a 372 GHz gyro-TWA with a 3-fold HCIW is presented. A numerical study of the effect of component parameter discrepancies on the waveguide coupler performance is included.

Chapter 6: A High Order Mode (HOM) input coupler for a 372 GHz gyro-amplifier is designed. The waveguide coupler design is based upon a waveguide power splitter with two potential topologies of the signal divider discussed. The passive components of the coupler design are numerically modelled individually. A coupler topology is chosen and a tolerance study is performed. The manufacture of a prototype HOM input coupler operating at 90 – 96 GHz is discussed and VNA testing of the component is presented.

Chapter 7: An overview of the main results gained from the W-band and low-THz projects is presented alongside the future work which will be undertaken on the respective project.

2. Theory

2.1. Introduction A gyro-TWA is a complex vacuum device constructed of a number of active and passive microwave components. The schematic of Fig. 2-1 shows the configuration of a gyro-TWA with an axial output. An electron beam, generated from a gun diode, interacts with an incident electromagnetic (EM) wave, coupled into the cavity through a passive input coupler. The electron beam and the propagating EM-wave interact and, as a result of the ECM instability (Section 1.1.1), electron energy is transferred to wave energy. If synchronous operation is achieved, the resultant EM-wave will be increased in magnitude compared to the incident wave. The spent electron beam is then deposited on the waveguide wall after the beam has transcended the magnetic field region. The amplified EM signal is extracted from the cavity through a microwave window.

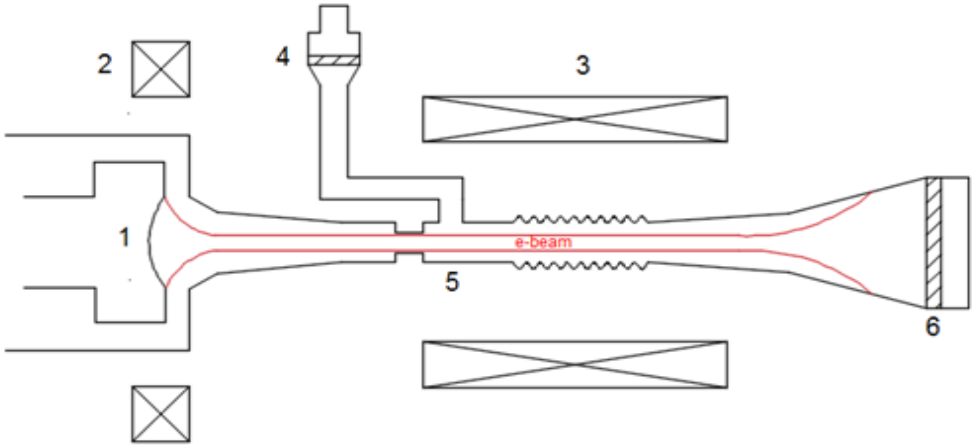

Fig. 2-1: Gyro-TWA schematic with 1- Electron gun, 2- Reverse coil for magnetic cusp, 3- Solenoid, 4- Pillbox window, 5- Input coupler feed to interaction cavity, 6- Vacuum window at output horn and electron collector.

This chapter will introduce the physical phenomena governing the operation of a gyro-TWA. The electron beam production from a cathode and the subsequent focussing forces will be discussed in Section 2.2, highlighting the Pierce, Magnetron Injection and Cusp electron gun topologies which can be used to generate the charged particles. A discussion of the electron beam focussing in the vacuum device and collection of the spent electron beam will also be introduced in Section 2.3 and Section 2.5 respectively. An overview of a smooth bore waveguide and a helically corrugated interaction region is presented in Section 2.4. The

output window, which allows high transmission of the amplified signal whilst sealing the vacuum alongside the pillbox window at the input coupler, will be discussed in Section 2.6.

2.2. Electron Gun

2.2.1. Cathode

J.R Pierce [2.1] stated four characteristics that an ideal cathode should possess;

1. able to emit electrons freely without any form of persuasion such as heating or bombardment,
2. supply an unlimited current density,
3. last forever without the electron emission being compromised and,
4. emission at every point on the cathode surface should be uniform, with the electrons travelling at zero velocity.

Although fanciful in a real vacuum electronic device, the four ideal characteristics highlight the important parameters for electron emission from a cathode. The mechanisms which result in the release of electrons from a cathode surface are discussed followed by the electron gun topologies within which the cathodes are employed.

2.2.1.1. Thermionic Emission

Fig. 2-2, adapted from [2.2], highlights the progression of electron current densities emitted from a thermionic cathode, the phenomenon of electron emission from a cathode surface as a result of a temperature (T) increase. The rate at which electrons are emitted from a cathode surface is strongly dependent on temperature as well as the properties of the material, mainly the material work function, from which the cathode is constructed. Figure 2-3 depicts an energy level diagram, representing the cathode-vacuum interface. Electrons with energies at the Fermi level ($E_e = E_0$) must acquire an energy equal to or greater than the work function ($e\varphi$) to enter the vacuum. At T = 0 K, no electron has energy greater than E_0 [2.3], hence the requirement for heating to effectively boil electrons from the cathode surface. The current density (J) of the electrons that are emitted from the cathode surface is given by

$$J = en_e v_z \tag{2-1}$$

where e is the electronic charge, n_e is the number density of electrons emitted from the cathode surface and v_z is the velocity of the electrons in the z-direction at the cathode surface. The axial velocity (v_z) can be found from

$$\frac{1}{2} m_e v_z^2 = E_0 + e\varphi \tag{2-2}$$

where m_e is the rest mass of the electron and φ is the applied voltage. The number density of the emitted electrons is not easily measured. A computation of the number density can be performed by analysing the density of energy states in the cathode and the probability that they are occupied [2.4]. This process equates a current density which is given by

$$J = A_0 T^2 exp\left(\frac{-e\varphi}{kT}\right) \tag{2-3}$$

where T is the cathode temperature, k is the Boltzmann constant and A_0 is the theoretical emission constant, equal to 1.20×10^6 $Am^{-2}K^{-2}$. Equation (2-3) is known as the Richardson-Dushman equation and this relationship governs the temperature limited regime of electron emission. It is shown in (2-3) that the current density released by the cathode is exponentially dependant on the cathode temperature and work function. Hence, for maximum electron emission it is desirable to maximise the temperature and minimise the work function. In practice, the measured emission constant varies from the theoretical value; however, the numerical value stated is an effective approximation for calculating cathode emission response with varying temperature. The derivation performed to define

the Richardson-Dushman equation assumes that the work function is independent of temperature. In reality, this is not generally the case.

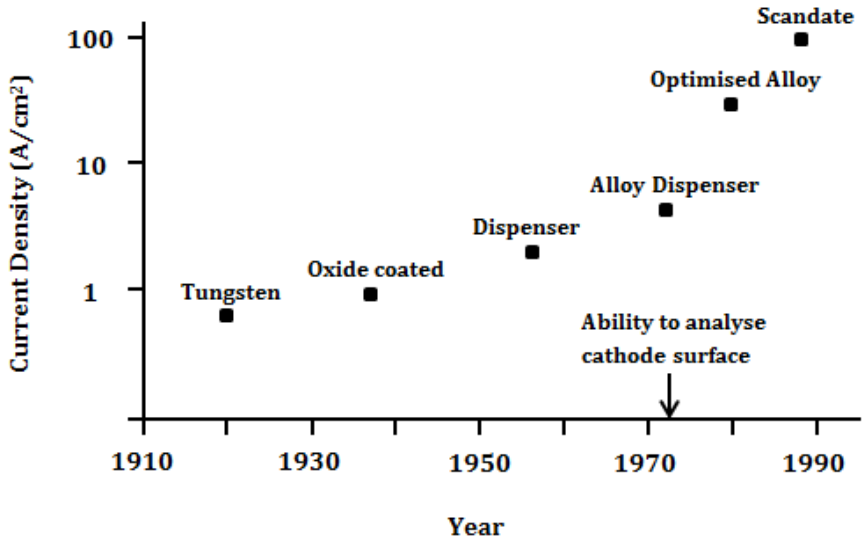

Fig. 2-2: Development of thermionic cathode technology over the past century [2.2].

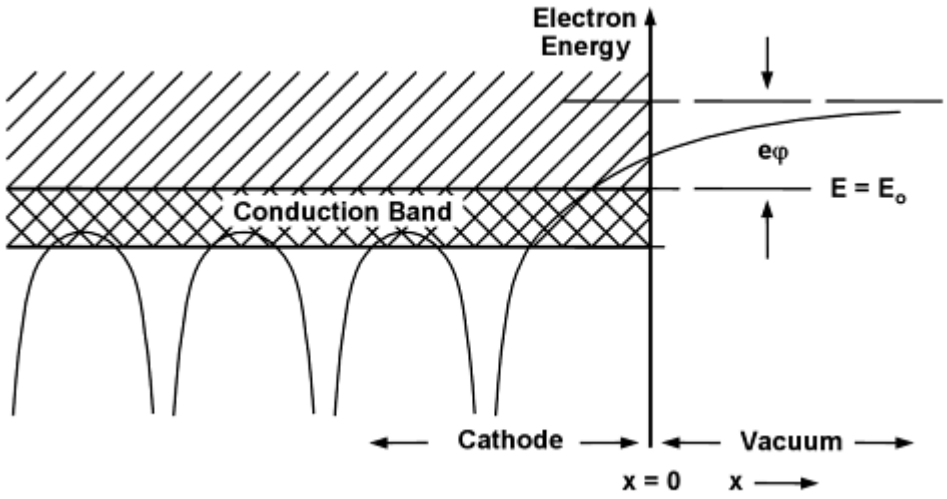

Fig. 2-3: Energy levels near the cathode-vacuum tube interface [2.4].

2.2.1.2. Schottky Effect

The derivation of (2-3) does not take into consideration the effect of an electric field at the cathode surface on the emission current density. When an electron leaves the

cathode surface, the particle experiences an accelerating force from a positive potential. The source of this positive potential is the anode. The anode potential results in the application of an electric field in the region between the cathode and the anode. The field close to the cathode reduces the potential barrier which the electrons have to cross to enter the vacuum level, as shown in Fig. 2-4, hence resulting in more electrons escaping the conduction band. Fig. 2-4(a) shows the potential barrier at the cathode-vacuum interface with no cathode-anode potential. Fig. 2-4(b) shows that the required electron energy to enter the vacuum level decreases upon the introduction of a potential at the cathode surface. The reduction in apparent cathode work function and hence increase in emission current caused by the onset of the electric potential in the cathode region is known as the Schottky effect [2.5].

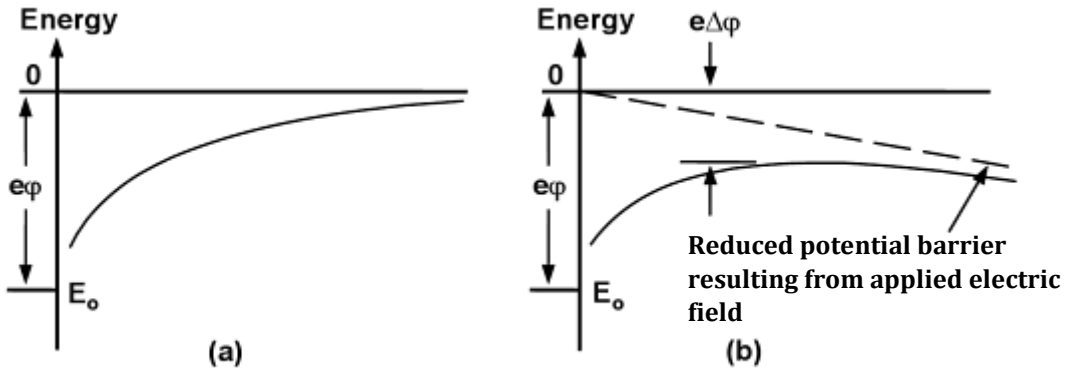

Fig. 2-4: Schottky effect shown to reduce the cathode-vacuum potential barrier.

The Schottky effect causes an effective reduction in the cathode material work function. The amount by which the work function is reduced, $\Delta\varphi$, is given by

$$\Delta\varphi = \left(\frac{eE_{\mathrm{K}}}{4\pi\varepsilon_0}\right)^{1/2} \qquad (2\text{-}4)$$

where E_K is the electric field in the cathode-anode region and ε_0 is the permittivity of free space. Using (2-4), the Richardson-Dushman equation (2-3) can be modified;

$$J = A_0 T^2 exp\left(\frac{-e}{kT}\left[\varphi - \left(\frac{eE_K}{4\pi\varepsilon_0}\right)^{1/2}\right]\right) \quad (2\text{-}5)$$

which can be re-written as

$$J = J_0 exp\left(\frac{e}{kT}\left[\frac{eE_K}{4\pi\varepsilon_0}\right]^{1/2}\right) \quad (2\text{-}6)$$

where J_0 is the zero-field current density [2.6].

2.2.1.3. Field Emission

Electron emission from a cathode surface can be split into three regimes; in a regime with high temperature and relatively low field strength, electrons with sufficient energy to overcome the potential barrier are emitted from the cathode surface. The temperature dependence of the distribution function (2-3) is largely responsible for the variation in emitted current. This is known as thermionic emission, discussed in section 2.2.1.1. An increase in electric field strength serves to effectively reduce the cathode work function and hence increase the emitted current, an effect described by Schottky (section 2.2.1.2). If the electric field were to be increased further, electron emission from a cathode would occur in a regime with relatively low temperature. This is known as field emission.

Field emission of electrons from a cathode surface occurs if the electric field at the interface of the cathode is increased to approximately 10^9 – 10^{10} Vm^{-1} [2.7]. For a surface electric field of this magnitude, electron emission is largely independent of temperature. The density of current emitted through field emission is governed by the Fowler-Nordheim equation [2.8], given by

$$J = \frac{e^3 E^2}{8\pi h\varphi} exp\left(-\frac{8\pi\sqrt{2m_e}}{3heE}\varphi^{3/2}\right) \quad (2\text{-}7)$$

where E is the electric field at the cathode, φ is the electric potential, h is Planck's constant and m_e is the electron rest mass. The electric field serves to reduce the potential barrier which the electrons must cross to leave the cathode surface and enter the system vacuum, an effect similar to that shown in Fig. 2-4. However, due to the applied field at the cathode surface being significantly larger than the field required for the effective reduction of the cathode work function, the potential barrier at the cathode is narrow in comparison. A schematic of potential barrier reduction is shown in Fig. 2-5. Due to the wave nature of the electron [2.9], it is possible for the electron to cross the potential barrier without possessing the kinetic energy required to enter the vacuum level. The electron may be assumed to leave the cathode surface, quantum tunnel through the potential barrier and enter the system vacuum. This phenomenon is known as the tunnelling effect.

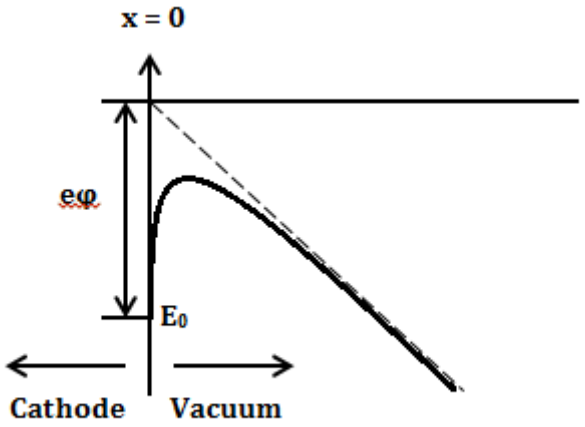

Fig. 2-5: Potential barrier reduction caused by increasing electric potential allowing for electron tunnelling.

2.2.1.4. Space Charge Limitation

The effect of the negatively charged electrons released from a cathode is to reduce the potential in the cathode-anode gap with respect to the potential in the absence of

electrons. As electron emission from the cathode increases, a space charge cloud begins to form in the cathode-anode gap. In the region close to the cathode surface, the electron density is greatest and, hence, the voltage depression is at maximum. Fig. 2-6 demonstrates the idea of voltage depression whilst traversing the cathode-anode gap. With no space charge effects, the voltage increases linearly between the cathode and the anode. When an electron cloud is present, the potential is reduced, with maximum reduction occurring in a region close to the cathode. As electron emission increases, the electron cloud potential becomes negative with respect to the cathode and, hence, electrons are repelled. Therefore, the temperature dependence on electron emission is saturated and the cathode is said to be operating in the space charge limited regime. In this regime the uniformity of electron emission from a cathode is not dependent on the uniformity of the temperature across the cathode area, meaning that cathode current and voltage do not have to be precisely controlled [2.10]. The space charge limited regime of a cathode is governed by the Child-Langmuir Law, which states that

$$I = PV_K{}^{3/2} \tag{2-8}$$

where I is the emission current, V_K is the gap potential and P is the perveance, which is a function of the cathode geometry.

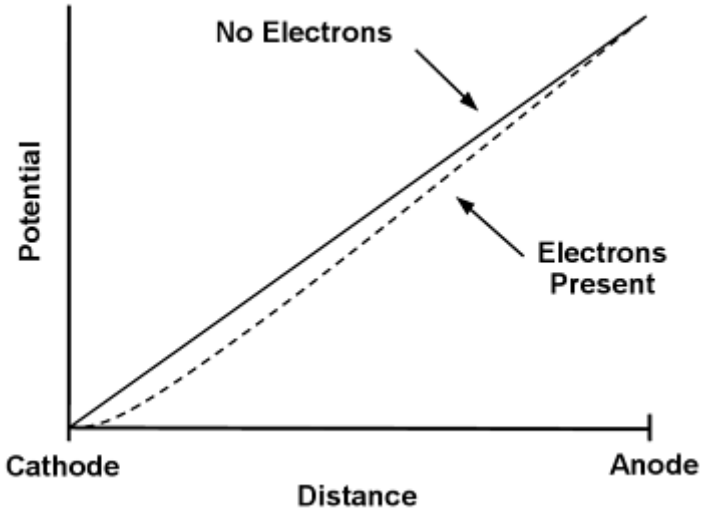

Fig. 2-6: Potential reduction caused by electron cloud in the cathode-anode gap [2.11].

An example of a thermionic cathode current emission varying with temperature at different anode potentials is shown in Fig. 2-7. When the cathode is operating in the temperature limited regime, the emission current density increases with temperature. As temperature increases, the emitted current density begins to saturate and becomes independent of temperature. The cathode is said to be operating in the space charge limited regime. An increase in voltage is shown to move the transition between temperature limited and space charge limited cathode operation to higher temperatures, corresponding to an increase in emission current. The steady state current emission for cathode operation in the space charge limited regime is apparent in Fig. 2-7. An optimum point of operation for a thermionic cathode would be at a temperature just above the space charge limited transition temperature to achieve a steady emission current whilst minimising energy loss due to excess heat in the cathode. However, the emitted electrons are susceptible to a large velocity spread under space-charge limited conditions.

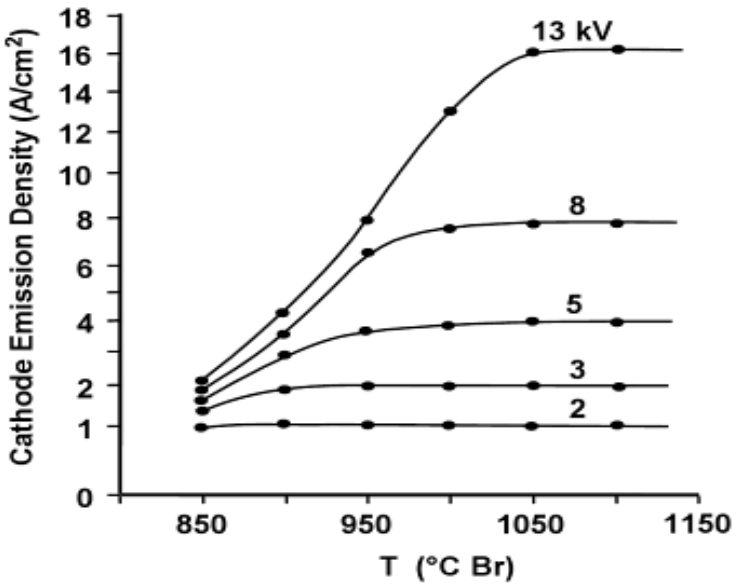

Fig. 2-7: Current emission from a thermionic cathode for varying temperature [2.12].

2.2.2. Pierce Gun

The cathode, discussed in section 2.2.1, plays a pivotal role in the operation of an electron gun. A common and highly effective design for an electron gun was set out in 1954 by J.R Pierce. The manufacture of a gun based on the design principles laid out by Pierce is known as a 'Pierce' gun. The derivation of a Pierce gun stems from the current flow from an outer spherical cathode to an inner spherical anode, shown in Fig. 2-8. Current will freely flow from the cathode to the anode in a laminar fashion. The anode surface area is less than the cathode surface area; therefore, the electron density at the anode is greater than the electron density at the cathode. The space charge limited current flowing from the cathode to the anode is given by (Child-Langmuir law) [2.13]

$$I = \frac{16\pi\varepsilon_0\sqrt{2\frac{e}{m_e}}}{9}\frac{{V_K}^{3/2}}{{\alpha_p}^2} \tag{2-9}$$

where V_K is the potential in the anode-cathode gap and α_p is a geometric parameter dependant on the relative sizes of the cathode, R_K, and the anode, R_A, defined by

$$\alpha_{\mathrm{p}} = ln\left(\frac{R_{\mathrm{A}}}{R_{\mathrm{K}}}\right) - 0.3\left(ln\left(\frac{R_{\mathrm{A}}}{R_{\mathrm{K}}}\right)\right)^2 + 0.065\left(ln\left(\frac{R_{\mathrm{A}}}{R_{\mathrm{K}}}\right)\right)^3 - \cdots \tag{2-10}$$

This is an idealised model from which no current can be released and is, therefore, impractical. However, the concept of this model is used in the design of a Pierce gun typically operating with a cathode in the full space charge limited regime.

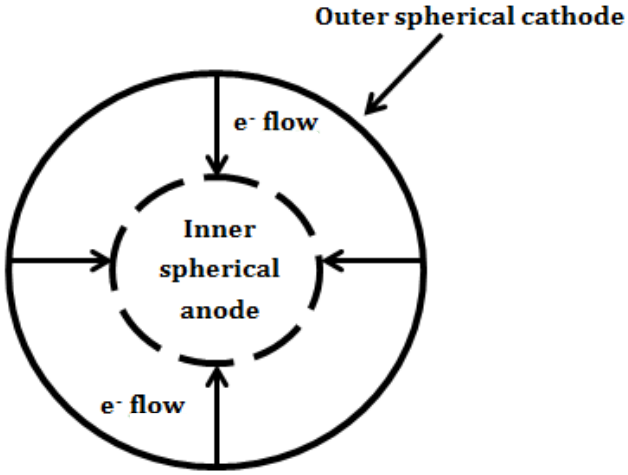

Fig. 2-8: Theoretical cathode-anode spheres used in the deduction of a Pierce gun.

A practical Pierce gun, such as that shown in Fig. 2-9 [2.14], has a part-spherical cathode surface from which electrons are emitted. The spherical anode from the model discussed previously has a drift tube insertion to allow for the electron beam to pass. The Pierce gun topology can be split into three distinct regions to highlight the physical processes governing the beam as the electrons traverse the cathode-anode gap. In Region 1, the focussing electrodes produce equipotential surface lines which act to form an electrostatic lens, similar in effect to an optical convex lens, which serves to focus the electrons into a beam of circular cross section. However, the equipotential surfaces are distorted by the gap

E-field. This results in a defocussing of the electron beam as it passes through the anode, shown in Region 2. In Region 3, the electron beam has left the accelerating electric field and the beam is free to propagate under its self-contained electrostatic forces, which will be discussed in section 2.3. Should the electron beam be allowed to propagate without any restoring force, the beam energy would be lost to the vacuum boundary wall due to beam spread caused by internal forces. Hence, a focussing force is required.

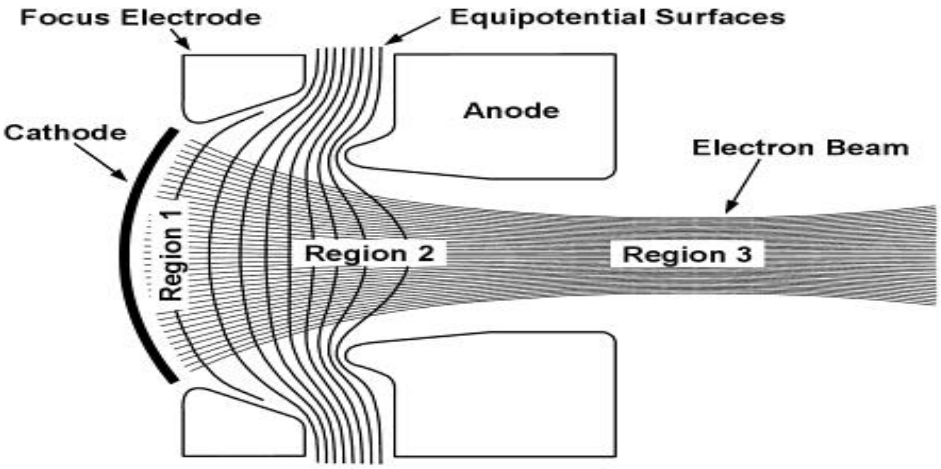

Fig. 2-9: Three-region schematic of a Pierce electron gun [2.14].

A Pierce electron gun generates a solid pencil-shaped beam with charged particles propagating at all points across a beam cross-section. Therefore, the linear electron beam is applicable to linear beam tubes such as the travelling wave tube or klystron. However, for a gyro-device, the Pierce gun would require an additional 'kicker' magnet in the design to generate a large orbit electron beam. The kicker magnet can operate with a pulsed power supply driving sets of Helmholtz coils to generate a transverse magnetic field or can be achieved by the use of adjacent periodic magnets of different polarity. With periodic magnets careful design of the Pierce gun is required to enable continuous wave (CW) operation. In addition, the large orbit pencil beam will result in localised power dissipation at the electron collector, adding complexities to the cavity and collector cooling. It was decided not to use a Pierce gun for gyro-amplifier operation.

2.2.3. Magnetron Injection Gun Unlike the part-spherical cathode shape typical of a Pierce gun, a magnetron injection gun (MIG), shown in Fig. 2-10, has a canonical emitting surface in the shape of a ring with a non-uniform radius. Therefore, a MIG gun can generate a hollow-centred annular electron beam. The MIG cathode typically emits electrons through thermionic emission allowing the beam current to be varied by adjusting the cathode temperature. A MIG used in a gyro-device operates in the temperature limited regime to minimise the electron velocity spread at the cathode surface. The gun topology is immersed in an axially symmetric magnetic field and, due to the azimuthal position of the anode with respect to the cathode surface, the initial electron motion occurs in crossed electric and magnetic fields. The cross product of the cathode electric, E_K, and magnetic, B_K, fields (E_K x B_K) determines the initial velocity of electrons at the emitting surface in the azimuthal direction. The initial velocity of the electrons in the azimuthal direction, v_φ, is given by [2.15]

$$v_\varphi = \frac{E_K cos\theta_{EB}}{cB_K} \tag{2-11}$$

where θ_{EB} is the angle between the electric and the magnetic field at the emitting surface. Depending on the θ_{EB} angle, a consequence of the gun design, the electron beam emitted from a MIG gun can be either quasi-laminar, where the electron trajectories will never intersect, or quasi-non-laminar, a regime in which the electron trajectories are likely to intersect.

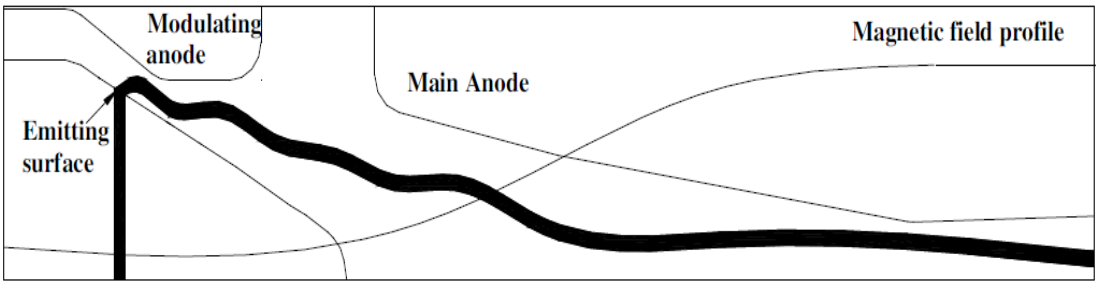

Fig. 2-10: MIG gun cathode-anode layout with overlaid magnetic field profile.

MIGs can be designed with two different cathode-anode configurations; the first configuration includes a single anode and is known as a diode MIG whereas the second design includes a second modulating anode with a variable potential, different to the main anode. This design is known as a triode MIG. The modulating anode allows for extra beam property control, including the tuning of the velocity ratio (α) and control over variations in the beam current density. The velocity ratio is defined by

$$\alpha = \frac{v_\perp}{v_z} \tag{2-12}$$

where $v_\perp$ is the perpendicular electron velocity and v_z is the axial electron velocity. The current intercepted by the modulation anode must be negligibly small to guarantee reliable operation [2.16]. However, the inclusion of a second anode, although allowing for enhanced beam control, requires a second power supply which incurs extra technical complexities. The main anode, included in both the diode and triode MIG topologies, serves to accelerate the electrons to the final beam energy.

Upon reaching the final accelerating energy, the electron beam enters a drift region within which the electrons experience a steady increase in magnetic field. The magnetic field profile of Fig. 2-10 demonstrates the increasing magnetic field magnitude after the electrons pass the anode. The increasing magnetic field results in an increase in the cyclotron frequency of the electrons and, hence, a decrease in the Larmor orbital radius. The reduction in the electron orbital radius results in a reduction in the radial beam thickness. The reduction in beam radius is described through Bush Theorem [2.17]. The increased magnetic flux experienced by the electron beam results in an increase in angular momentum and, therefore, a reduction in the beam diameter. The beam, in this region, is said to undergo magnetic compression. Magnetic compression serves to increase the gyration velocity of the electron beam [2.18], hence increasing the component of electron velocity perpendicular to the axial magnetic field. The effect of energy conservation means that the beam guiding centres axial drift velocity is subsequently reduced, resulting in an increase in velocity ratio,

α. A velocity ratio of ~ 1 is commonly used for millimetre and sub-millimetre gyro-devices [2.19 - 2.21].

MIG guns are commonly used in high power gyro-devices because of their ability to produce annular electron beams in which individual electron beamlets perform helical orbits around the applied magnetic field. The cyclotron orbits occur at a fundamental frequency, the electron cyclotron frequency, which can be tuned to allow for CRM interaction. The MIG electron gun can be employed in a high frequency gyro-device to excite the mode of a large diameter cavity operating just above cut-off, and can also operate at harmonics of the fundamental frequency. Therefore, a gyro-device with a MIG electron gun is able to operate at a harmonic of the fundamental frequency for the same value of magnetic field. The electron beam produced by a MIG bunches best at the fundamental cyclotron frequency and couples strongly to a cavity mode operating just above cut-off. It is advantageous for an electron gun to generate a mode selective beam, limiting parasitic oscillations through coupling to unwanted modes.

2.2.4. Cusp Electron Gun

The design of a magnetic cusp gun is founded on the dynamics of charged particles in non-adiabatic magnetic field transitions, known as magnetic cusp fields. A beam of electrons incident on a carefully modelled magnetic cusp field will create an axis-encircling electron beam with individual electron orbital trajectories [2.22]. Fig. 2-11 shows an idealised magnetic cusp transition [2.23] with the electron beam trajectory before and after the cusp magnetic field. The effect of the magnetic cusp, a transition from a negative to a positive *B*-field or vice-versa, is shown to convert the annular electron beam to an axis-encircling electron beam. Fig. 2-11 shows a cusp transition with an infinitely small magnitude which is a not achievable in practice.

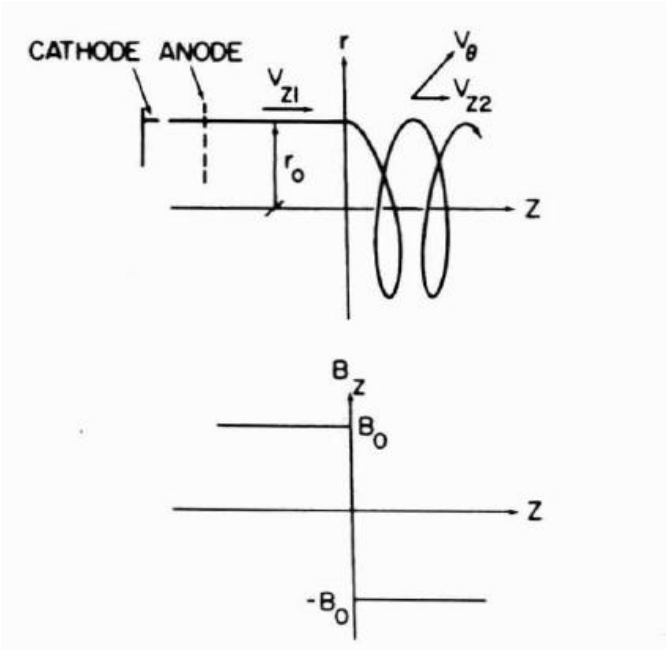

Fig. 2-11: Idealised magnetic cusp field with infinitely small transition region [2.22].

The topology of a cusp electron gun enables the magnetic cusp field to be varied to suit the system requirements. Variations in cusp gun operation are a result of the employment of a sharp cusp transition or a smooth cusp transition in the design. A sharp transition of the magnetic field, after the electron beam is accelerated to maximum energy, has been demonstrated. The configuration of a sharp cusp transition requires a magnetic pole piece to ensure that the magnetic field in the cathode-anode region is shorted at the anode, allowing for field reversal in the region post anode. A threshold beam radius, ρ_{crit}, is defined where an electron trajectory positioned at a radius from the beam guiding centre greater than the defined threshold would not transmit through the cusp field. This threshold radius is equated as [2.24]

$$\rho_{crit} = \frac{m_e v_z}{eB} \tag{2-13}$$

A smooth cusp transition has also been demonstrated. Unlike the sharp transition which occurs when the beam is at maximum energy, hence a necessity for large magnetic field

amplitude to create the axis-encircling beam, the smooth cusp transition occurs just after the electron emission from the cathode. The electrons are, therefore, at a relatively low energy meaning that a reduced magnetic field magnitude is required to form an annular beam. A gradual magnetic field transition phase from negative to positive for a gun configuration with the cusp transition before the anode is sufficient to create an axis-encircling electron beam [2.25]. The smooth cusp region also eliminates the requirement for a magnetic pole piece, reducing the technical complexity of the configuration. Either technique employed for electron cusp gun configuration can also include a magnetic compression region after electron acceleration to increase the velocity ratio, α.

Interactions in gyro-devices at high frequency often occur at harmonics of the electron cyclotron frequency to minimise the magnetic field required for electron cyclotron motion. Consequently, the interaction cavity operates with a higher order mode (HOM). The use of an axis-encircling electron beam produced by a magnetic cusp in high frequency gyro-devices is beneficial because, unlike MIGs, the generated electron beam will readily interact with HOM's. For high efficiency beam-wave interaction, the electron cyclotron harmonic number, *s*, must equal the azimuthal index of the waveguide mode, *m* [2.26], hence, limiting the coupling to unwanted cavity modes. Therefore, a cusp electron gun provides a novel method of generating an electron beam in a high efficiency gyro-device.

2.3. Electron Beam Transport

The mechanisms of electron beam production have been discussed in section 2.2. A travelling beam of charged particles is subject to internal forces which serve to spread the beam, resulting in the energy carried by the particles being lost to the cavity wall in the absence of a focussing force. Therefore, a method of beam confinement is required to prevent a low efficiency beam-wave coupling. The space charge forces experienced by a travelling charged particle beam will be introduced, alongside practical methods used to confine electron beams in the interaction region of a high power vacuum cavity.

2.3.1. Space Charge Effects in Cylindrical Electron Beams

The forces between two electrons of equal charge are considered. At rest, the particles experience a Coulomb force which results in a repulsive force serving to increase the gap between the two resting electrons. Should the particles be travelling at an initial velocity, v_z, they represent two parallel currents which experience a magnetic attractive force. However, for beam velocities below the speed of light, c, the repulsive forces are dominant meaning that the natural regime of the electron beam is to diverge. If the electron beam were travelling at the speed of light, the forces would balance and the electron beam would be self-confined. Figure 2-12 [2.27] depicts the forces acting between two travelling electrons and the overall repulsive force dominated by the Coulomb repulsion.

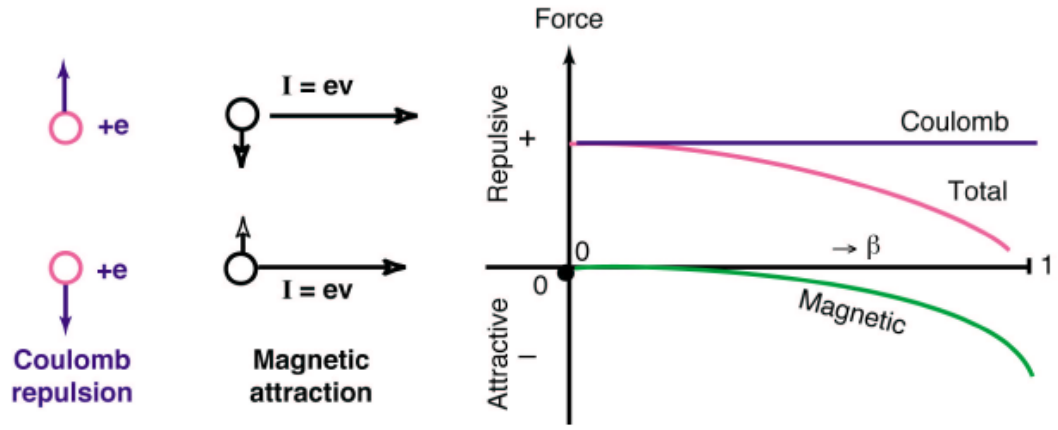

Fig. 2-12: Forces experienced by electrons at rest and at velocities < c.

The same forces exerted between two particles can be attributed to a bunch of charged particles; in this case a beam of electrons. For a cylindrical beam of electrons, the repulsive force will serve to drive electrons from the beam centre, with the force increasing with distance from the centre of the beam. The magnetic attractive force will attempt to confine the beam, with the corresponding force vector directed towards the beam centre. The self-electric field of the particle beam can be calculated by applying the divergence theorem to Gauss' law which states that

$$\nabla \cdot \boldsymbol{E} = \frac{\rho}{\varepsilon_0} = \frac{n_e e}{\varepsilon_0} \tag{2-14}$$

where ρ is the beam charge density. The application of the divergence theorem leads to

$$\int \boldsymbol{E} \cdot d\boldsymbol{S} = 2\pi r_e l_B E_r = \frac{\pi {r_e}^2 l_B n_e e}{\varepsilon_0} \tag{2-15}$$

where l_B is the length of the electron beam, r_e is the electron distance from the beam centre and E_r is the radial electric field magnitude. The number density of a cross section of the cylindrical electron beam is defined as

$$n_e = \frac{I_b}{e v_z \pi r_b^2} \tag{2-16}$$

where I_b is the beam current and r_b is the beam radius. By inserting the number density, n_e, into equation (2-15) and rearranging, a definition of the self-electric field of a beam of electrons is derived;

$$E_r(r) = \frac{I_b r}{2\pi\varepsilon_0 v_z r_b^2} \tag{2-17}$$

Therefore, the repulsive force experienced by an electron at a distance r from the centre of the cylindrical electron beam is given by

$$F_r(r) = eE_r(r) = \frac{eI_b r}{2\pi\varepsilon_0 v_z r_b^2} \tag{2-18}$$

The repulsive force, F_r, is a result of the Lorentz force acting on the charged particles and will cause a defocussing of the beam. From (2-18), it is shown that F_r increases with increasing current density and the force experienced by an electron increases linearly with distance from the beam centre. However, the repulsive force experienced within the beam envelope may be reduced by having a large beam radius r_b and a high beam energy.

The magnetic attraction force can be derived in a similar manner. By applying Stokes' theorem to Ampere's Law, defined as;

$$\nabla \times \boldsymbol{B} = \mu_0 \boldsymbol{J} \tag{2-19}$$

the self-magnetic field of the electron beam can be found. The azimuthal magnetic field, B_ϑ, is responsible for the radial electron attraction. The application of Stokes theorem to Ampere's law results in

$$\int \boldsymbol{B} \cdot d\boldsymbol{l} = 2\pi r B_\theta = \frac{\pi r^2 \mu_0 I_0}{\pi r_b^2} \tag{2-20}$$

The azimuthal magnetic field can therefore be written as

$$B_\theta(r) = \frac{\mu_0 I_0 r}{2\pi r_b^2} \tag{2-21}$$

The internal magnetic force, F_z, acting on the electron beam can then be found using the Lorentz equation ($\vec{F} = q\vec{E} \times \vec{B}$). Hence, the attraction force of an electron at a position r from the centre of the beam is given by

$$F_z(r) = ev_z B_\theta(r) = \frac{\mu_0 e v_z I_0 r}{2\pi r_b^2} \quad (2\text{-}22)$$

In contrast to F_r, F_z increases with beam velocity and, therefore, beam confinement is improved with high beam energy. However, the repulsive force (F_r) is significantly greater than the attractive force (F_z) for all beam velocities < c and, therefore, an external magnetic confinement field is used to prevent beam divergence.

2.3.2. Electron Beam Guidance

Electron beam confinement can be achieved through magnetostatic or electrostatic techniques. In vacuum devices, it is uncommon for an electrostatic technique, involving the focussing of an electron beam through an aperture lens with negative potential, to be used. Two magnetostatic techniques are employed on high power mm-wave devices; a periodic permanent magnet (PPM) stack or a solenoid magnet.

A PPM [2.28] acts as a series of magnetic lenses which cause the beam to converge. The rings are magnetised in the axial direction with alternating polarity to prevent beam spread. A PPM stack, once baked, has a fixed magnetic field strength with no tunability and achieving the desired field strength can be problematic due to the anisotropic nature of a magnetic material. Therefore, a PPM stack involves a design process which is both complex and delicate.

A solenoid magnet focussing array is based upon Ampere's law which states that a current carrying loop induces a magnetic field, B ($B = \mu_0 nI$), where μ_0 is the permeability of free space, n is the number of turns per unit length and I is the current. A strong axial magnetic field generated by a solenoid, coupled with the azimuthal electron beam rotational motion serves to balance the transverse defocussing forces resulting from space charge

effects. This technique is known as solenoid focussing. The cusp electron gun, discussed in section 2.2.4, imparts rotational motion to the electron beam; therefore, the combination of the solenoid magnet axial field strength and the cusp beam rotational motion is ideally suited for solenoid focussing in a gyro-device.

The magnetic field created by a current loop can be described by Legendre polynomials and complete elliptic integrals. However, the analysis resulting from Legendre polynomials provides poor beam convergence [2.29]; therefore, the magnetic field variation will be described by the elliptic integrals $K(m_1)$ and $E(m_1)$, where the magnetic field due to a current loop in the radial and axial direction respectively is given by [2.30];

$$B_r(r,z) = \frac{\mu_0 I}{2\pi}\left(\frac{z_0 - z}{r}\right)\left[\frac{r_0^2 + r^2 + (z_0 - z)^2}{(r_0 - r)^2 + (z_0 - z)^2} \cdot E(m_1) - K(m_1)\right] \cdot \{(r_0 + r)^2 + (z_0 - z)^2\}^{-1/2} \tag{2-23}$$

$$B_z(r,z) = \frac{\mu_0 I}{2\pi}\left[\frac{r_0^2 - r^2 - (z_0 - z)^2}{(r_0 - r)^2 + (z_0 - z)^2} \cdot E(m_1) + K(m_1)\right] \cdot \{(r_0 + r)^2 + (z_0 - z)^2\}^{-1/2} \tag{2-24}$$

where B_r and B_z are the radial and axial magnetic fields respectively at position (r,z) as a result of a current (I) carrying coil centred around (r_0, z_0). The argument of the complete elliptical integrals, m_1, is given by

$$m_1 = \frac{4rr_0}{[(r_0 + r)^2 + (z_0 - z)^2]} \tag{2-25}$$

Equations (2-23) and (2-24) show that both the radial and the azimuthal magnetic field increase with increasing current; however, the radial magnetic field highest magnitude is

located at the centre point of the coil with the field strength decreasing linearly approaching the boundary.

The electron beam used to drive the beam-wave interaction was produced by a thermionic cusp electron gun [2.31]. After being emitted from the annular cathode, the electrons accelerated by the electric field also experience a reversal of magnetic field direction with the cusp point just a few millimeters downstream from the cathode surface. As a result of conservation of the canonical angular momentum, an axis-encircling electron beam was formed when the electric and magnetic fields were properly matched. The electron beam was then compressed to achieve the desired velocity alpha ($\alpha = v_\perp / v_\parallel$) of ~1 for beam-wave interaction. α could be tuned by changing the amplitude of the magnetic field at the cathode surface. The use of an axis-encircling electron beam is advantageous in suppressing mode competition for a harmonic gyro-device, as such a beam only interacts with a waveguide mode $TE_{m,n}$ whose azimuthal index m equals the harmonic number s of the electron beam.

An experiment was designed and constructed using a magnetic field of ~1.82 T and a beam voltage of 55 kV. The operating beam voltage, α and the required magnetic field in the interaction region were chosen so that the beam line was matched with the dispersion curve of the operating eigenwave for broadband amplification

2.4. Waveguide Interaction Circuit

2.4.1. Smooth-bore Cylindrical Waveguide

A waveguide is a device used to propagate EM radiation from point-to-point without significant attenuation. The interaction circuit in a gyro-device can comprise solely of a hollow metallic tube, more commonly referred to as a smooth-bore cylindrical waveguide. Due to the fast-wave operation of a gyro-device, the interaction circuit does not need to scale linearly with increasing frequency. In slow-wave vacuum tubes, the interaction circuit must scale with the operating frequency to maintain synchronous operation. Therefore, the power handling capability of gyro-devices is significantly greater than power handling in a slow-wave device due to the over-sized interaction cavity. The cylindrical waveguide

structures often operate at higher order modes to maximise the power generation and aid in the effective cooling of the waveguide wall. Cylindrical interaction waveguide circuits are used in high power gyrotrons [2.32 – 2.34] which generate over 1 MW of power at frequencies 140 GHz, 170GHz. The radial periodicity of the interaction circuits can be linear for single frequency operation or comprise radial tapers to form interaction cavities with varying radii (R_N). The linear and tapered waveguide wall is shown in Fig. 2-13.

The dispersion of a hollow cylindrical waveguide in vacuum satisfies the wave equation in the presence of zero charge carriers, given by

$$\boldsymbol{\nabla}^2\boldsymbol{E} - \frac{1}{c^2}\frac{\partial^2\boldsymbol{E}}{\partial t^2} = 0 \tag{2-26}$$

$$\boldsymbol{\nabla}^2\boldsymbol{B} - \frac{1}{c^2}\frac{\partial^2\boldsymbol{B}}{\partial t^2} = 0 \tag{2-27}$$

for the electric (***E***) and magnetic (***B***) field components respectively.

Considering a TE mode propagating in a cylindrical waveguide, E_z = 0. Hence, by solving equation (2-26) and (2-27) with a time-varying wave of the form $\boldsymbol{E}(x,y,z,t) = E_0 expj(\omega t - k_z z)$ and $\boldsymbol{B}(x,y,z,t) = B_0 expj(\omega t - k_z z)$ propagating in the positive *z*-direction, the dispersion relation for a cylindrical waveguide can be deduced to be

$$\omega^2 = \omega_c^2 + k_z^2 c^2 \tag{2-28}$$

where ω is the operating frequency ($\omega = 2\pi f$), k_z is the axial wavenumber and ω_c is the waveguide cut-off frequency given by

$$\omega_c = \frac{\mu'_{mn} c}{R} \tag{2-29}$$

where μ'_{mn} is the Bessel root dependant on the mode of operation. The Brillouin diagram of the fundamental mode dispersion in a cylindrical waveguide is shown in Fig. 2-14.

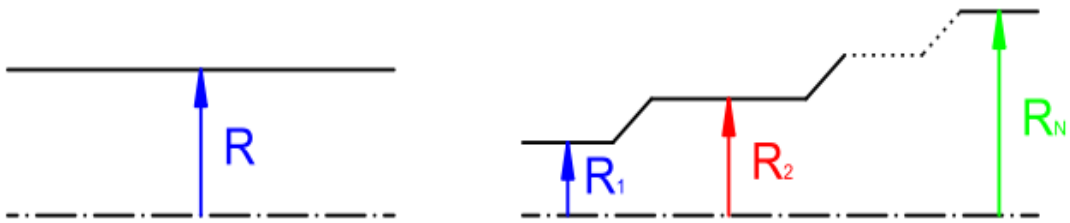

Fig. 2-13: Linear (L) and tapered (R) radii cylindrical waveguide profiles.

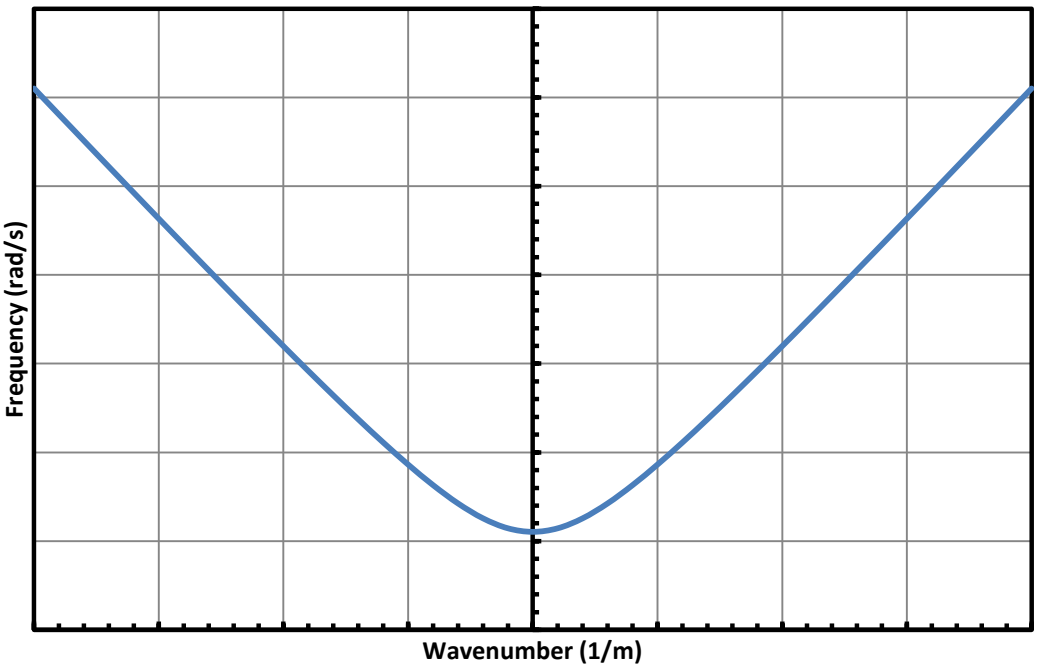

Fig. 2-14: Dispersion plot of a circular cross-section waveguide.

2.4.2. Helically Corrugated Interaction Waveguide

Smooth-bore cylindrical waveguide can only support propagating modes which have a phase velocity (v_p) > c; however, an interaction waveguide with a radial periodicity can support TE or TM modes with $v_p < c$. Therefore, the helically corrugated interaction waveguide (HCIW) [2.35], which has both axial and azimuthal periodicity, is highly suited to beam-wave interaction circuits as the waveguide can support synchronous operation between a gyrating electron beam and a propagating eigenmode generated in the cavity. The dispersion characteristics of the operating eigenmode are governed by the corrugation depth and period of the helical profile. The helical profile of the HCIW in cylindrical (r, ϑ, z) coordinates can be written as

$$r(\theta, z) = R_0 + R_1 cos\left(m_B\theta - \frac{2\pi}{d}z\right) \tag{2-30}$$

where R_0 is the mean radius of the cavity cross-section, R_1 is the corrugation depth, m_B is the fold number and d is the axial corrugation period. Coupling of two modes, when $R_1 \neq 0$, will occur when the axial and azimuthal wavenumbers satisfy the synchronous conditions given by

$$k_1 - k_2 = \frac{2\pi}{d} \tag{2-31}$$

$$m_1 - m_2 = m_B \tag{2-32}$$

where k_1 and k_2 are the axial wavenumbers of mode 1 and mode 2 respectively and m_1 and m_2 are the azimuthal indices of the coupling modes. The Bragg conditions of (2-31) and (2-32) allow for the circularly polarised nature of the cavity modes to be taken into consideration. In practice, mode 2 is always taken to be counter-polarised to mode 1 and, hence, k_2 and m_2 are negative. Therefore, (2-31) and (2-32) always yield positive integer numbers.

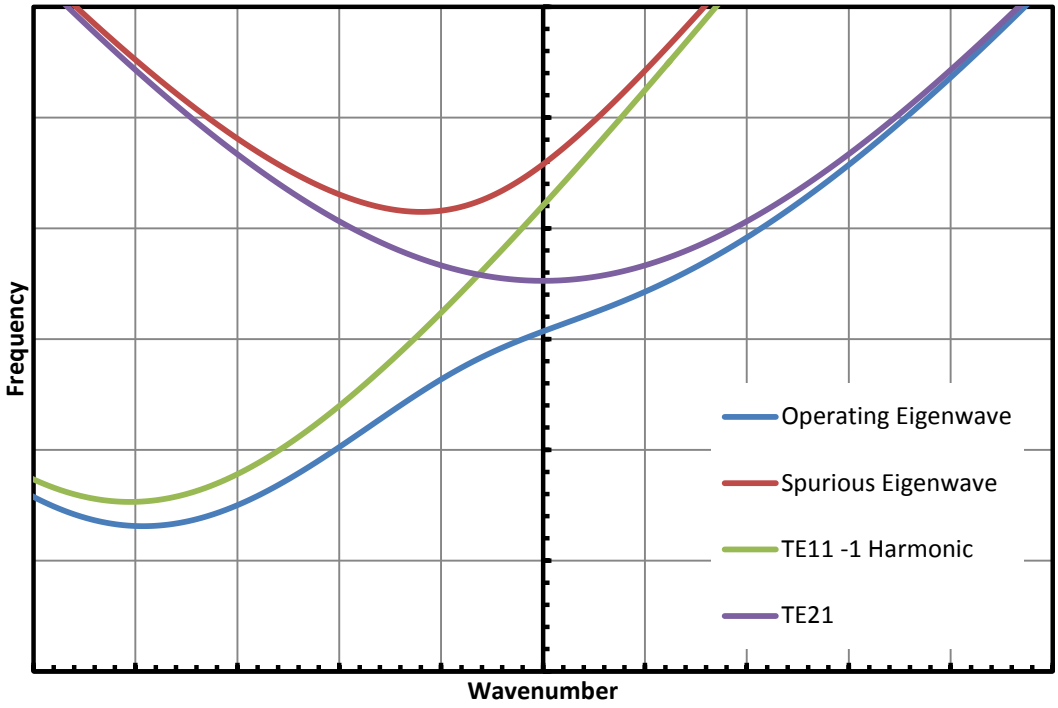

Fig. 2-15: Dispersion characteristics of a three-fold HCIW.

The azimuthal and axial periodicities allow the resonant coupling of two normal modes to generate new eigenwaves. For example, a threefold HCIW (m_B=3) allows the coupling of the TE_{21} mode and the first spatial harmonic of the TE_{11} mode. One of the resultant eigenwaves has nearly constant group velocity over a large frequency range at near zero axial wavenumber and can be matched to resonantly interact with a cyclotron mode of the electron beam for broadband, highly efficient interaction, such as gyrotron backward wave oscillators [2.36 - 2.37] and gyro-TWAs achieving an instantaneous gain bandwidth of over 20% [2.38]. A W-band (75-110 GHz) gyro-TWA using a 3-fold HCIW, with dimensions R_0 = 1.45 mm, R_1 = 0.23 mm, and d = 3.20 mm was designed and constructed.

The gyro-TWA beam-wave dispersion and the small signal gain can be calculated using the following normalized equation [2.39]:

$$[(k_{zn}^2 - 2\omega_n)(k_{zn} + \Delta_g - \omega_n/h_0) + 2\sigma^2/h_0][k_{zn} - (\omega_n - \Delta_H)/\beta_{z0}]^2 = C^3(k_{zn} + \Delta_g - \omega_n/h_0)\left\{1 + \frac{2s}{\alpha_0{}^2\beta_{z0}}[k_{zn} - (\omega_n - \Delta_H)/\beta_{z0}]\right\} \quad (2.33)$$

where ω_n and k_{zn} are the normalized frequency and axial wavenumber. The normalized equation is derived through analysis of the mode scattering in the perturbed waveguide. The dispersion of the eigenwave and the electron beam could be calculated by solving the uncoupled beam-wave equation, determined by setting the Pierce coupling factor (C) to zero. Equation (2.33) has four $\omega_n(k_{zn})$ roots with two real roots being the "hot" (electron beam present) eigenwaves, and a pair of conjugate complex roots, which are degenerates of the electron cyclotron mode due to the CRM interaction. The negative imaginary number of the solution gives rise to the small signal gain of the interaction. The dispersion diagram of the first spatial harmonic of the TE_{11}, the coupling TE_{21} mode, the operating eigenwave and small signal gain were calculated and are shown in Fig. 2-16.

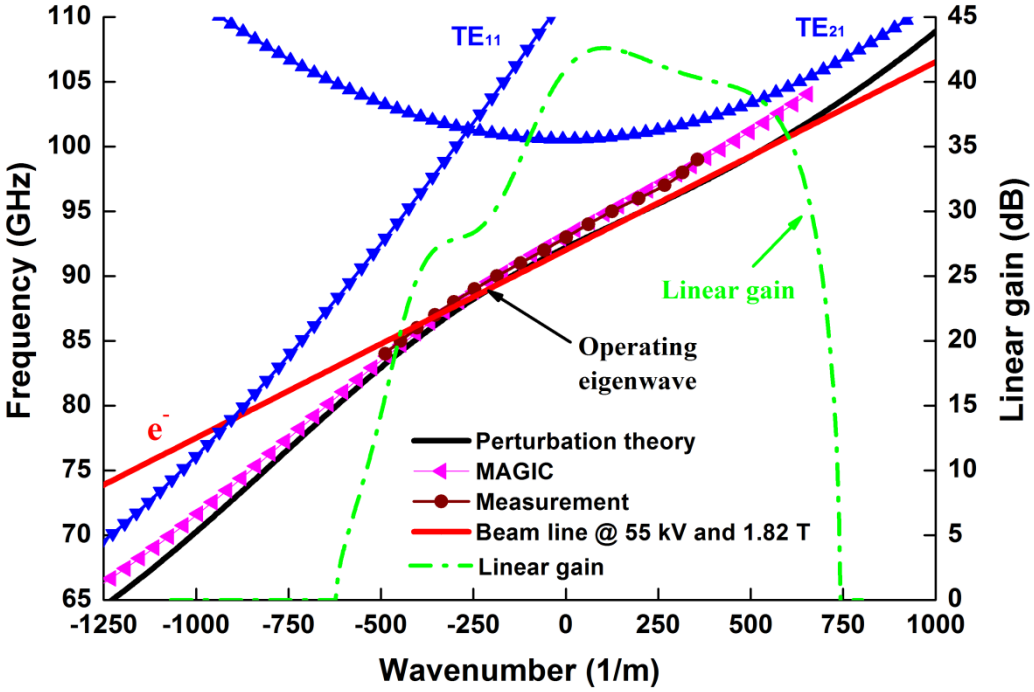

Fig. 2-16 The dispersion curve of the three-fold helically corrugated waveguide and the beam line [2.39].

The linear gain of the gyro-TWA, determined through analysis of (2-33), is shown to be at maximum for small positive axial wavenumbers. The highest potential gain is therefore determined to be at the area of strongest beam-wave coupling in the gyro-TWA, shown in Fig. 2-16. The design of the HCIW profile is focussed on achieving a constant v_g to enhance the beam-wave interaction efficiency. The dispersion of three-fold HCIW is shown in Fig. 2-

15. The group velocity of the operating eigenmode is shown to be linear over a broad frequency range in the interaction region compared with the two coupled modes (TE_{21} and a spatial harmonic of the TE_{11}) which have a constantly varying v_g for low positive axial wavenumbers. The measured dispersion properties of the operating eigenwave in comparison to the results from numerical simulation using the 3D finite-difference time-domain particle-in-cell code MAGIC [2.40] are also shown in Fig. 2-16.

2.5. Electron Collector and Energy Recovery

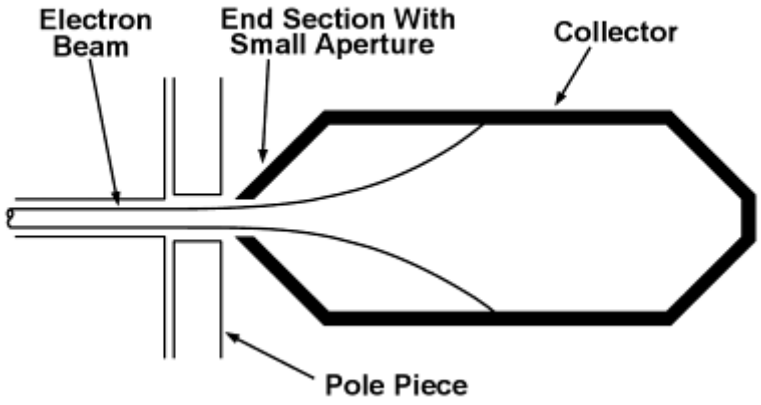

Fig. 2-17: Schematic of an electron collector for a vacuum device.

After beam-wave interaction in the vacuum cavity, the energy of the electron beam is dissipated on to the walls of a metallic collecting surface, known as an electron collector. A schematic of a typical electron collector is shown in Fig. 2-17. In a standard electron collector with no external power source, the collector cavity is designed to prevent a high impact rate of incoming electrons in a small surface area to ensure the dissipated power, and subsequent heat generation, can be controlled with an effective cooling system. However, the electron collector can be used to improve the electronic efficiency of a gyro-device. By applying a potential to the collector surface, the kinetic energy of the travelling electron beam is converted to potential energy which, in turn, can be utilised in a feedback mechanism to reduce the power consumption of the device.

The power dissipated from the incident electrons is partly removed through radiation but for the most part through conduction of heat. A large temperature increase at a specific

point in the collector can result in mechanical damage and collector distortion. To minimise heat build-up in the collector, the inner collector surface is designed to have as large an area as mechanically possible and constructed using a material with high thermal conductivity. The large surface area aids in cooling because the liquid coolant is exposed to a greater area of the collector surface.

A region of magnetic decompression beginning at the collector aperture will serve to defocus the electron beam, limiting the power density at the collector surface. The magnetic pole piece, shown in Fig. 2-17, serves to terminate the region of beam confinement. Hence, the internal beam defocussing forces serve to reduce the beam power per unit area and limit the power build up at the collector surface. A magnetic decompression region can also be used to defocus the electron beam [2.41], a technique which alleviates the requirement for a very large collecting system. A varying magnetic field can be generated by applying an AC current to magnetic coils surrounding the collector to sweep the spent electron beam across the collector to spread the spent electron beam across a larger area of the collector [2.42].

The electronic efficiency of a microwave tube with a conventional electron collector can be calculated using

$$\eta_e = \frac{P_{out}}{P_b} \tag{2-34}$$

where P_{out} is the RF output power and P_b is the power supplied to the charged particle beam, defined as

$$P_b = I_b V_b \tag{2-35}$$

where I_b is the beam current and V_b is the beam potential. The electronic efficiency of a microwave device can be increased by including a depressed collector in the design. The depressed collector [2.43 – 2.44] which uses one or more electrodes where the collector surface potential is depressed with respect to the anode potential to permit the recovery of beam energy. The collector surface must be of a potential which serves to slow the electrons down but does not repel electrons as this could cause particles to reverse into the interaction region, resulting in undesirable cavity noise and beam interference. However, by slowing the electrons down before they impact the collector surface, the energy they give up during deceleration can be used in a feedback system to increase the tube efficiency. The total efficiency of a vacuum device with a depressed collector energy recovery system is given by

$$\eta_t = \frac{P_{out}}{(P_b - P_{bREC})} \tag{2-36}$$

where P_{bREC} is the fraction of beam power recovered by the depressed collector, which is given by

$$P_{bREC} = P_{bCAV} - P_{bDIS} \tag{2-37}$$

where P_{bCAV} is the remaining beam power after interaction with the RF signal and P_{bDIS} is the power dissipated in the collector walls. The implementation of a depressed collector on a gyro-amplifier will improve the electronic efficiency of the device if the recovered power exceeds the amount of power required to supply the depressing potential. The additional power supplies required also increase the level of technical complexity on the amplifier electronic circuits.

2.6. Output Window

The microwave window is a critical component in the design of high power gyro-devices, separating the ultra-high vacuum (UHV) of the cavity with atmospheric pressure; hence, the window must be mechanically stable under high tensile strain and be leak tight. High power radiation is incident on the window material; therefore, the window material must have a high transmission ratio for mm-wave radiation and high thermal conductivity to prevent an accumulation of power in the vacuum barrier.

The transmission ratio of a microwave window is dependent on the loss tangent (tanδ) and the relative permittivity (ε'_r) of the window material. Therefore, the choice of window material is a very important aspect in the development of a mm-wave window. Materials such as CVD diamond, quartz and ceramic [2.45] are used in vacuum windows with the choice of material depending on the constraints of cost on the component design. However, the material chosen must have a high mechanical stability to ensure it withstands the axial pressure gradient from vacuum to air.

A microwave window has to be broadband to be applicable to a gyro-amplifier. To increase the operational bandwidth of a single disk microwave window, the reflections at the vacuum-material interface must be minimised. A method of reducing the reflections into the vacuum cavity is to ensure that the reflected signal from the vacuum-material discontinuity interacts destructively with reflections from within the window plate [2.46]. This phenomenon is achieved by making the window plate an integer (N) number of half-wavelengths in thickness (t_w);

$$t_w = \frac{c}{2f\sqrt{\varepsilon'_r}}N \tag{2-38}$$

The operation of a single disk window is narrowband relative to the operational frequency range of a gyro-oscillator or gyro-amplifier. Also, at higher frequency operation, t_w decreases resulting in an increasingly complex manufacturing process. Therefore, it is important to

increase the transmission bandwidth of the output window whilst ensuring the manufacturability of the component is achievable.

High frequency broadband windows can be achieved with a set of cascaded dielectric layers, known as a multi-layer window [2.47], or a window set an angle which serves to eliminate all reflections, known as a Brewster angle window [2.48]. A multi-layer window, shown in Fig. 2-18, has a series of impedance matching steps which serve to reduce the reflections at the vacuum-window discontinuity and reduce the power absorbed by the window material compared to the single disk window. The addition of dielectric or vacuum layers creates an upper- and lower-resonant pass band about the central transmission frequency of the inner dielectric plate and, hence, broadens the transmission range of the window. Due to the impedance matching of a multi-layer window, the incident wave can be polarised in any orientation and achieve a high transmission over a broad frequency range, eliminating the requirement of a waveguide polariser.

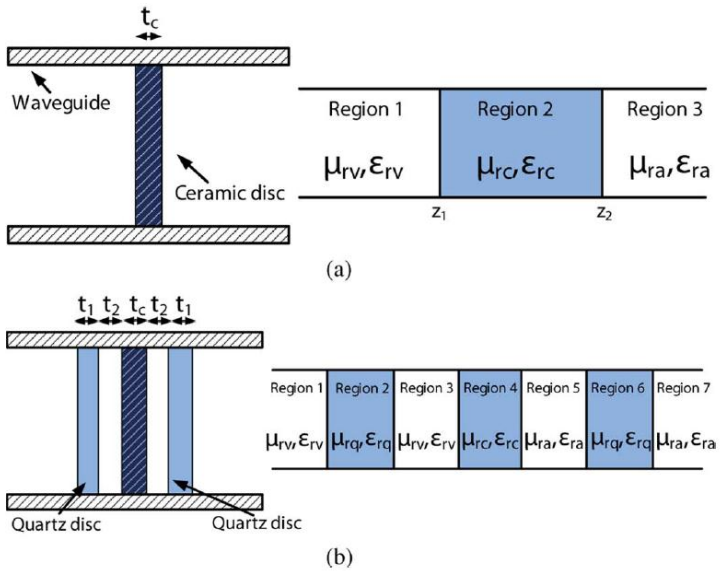

Fig. 2-18: Comparison of discontinuities in a single-layer and multi-layer microwave window [2.47].

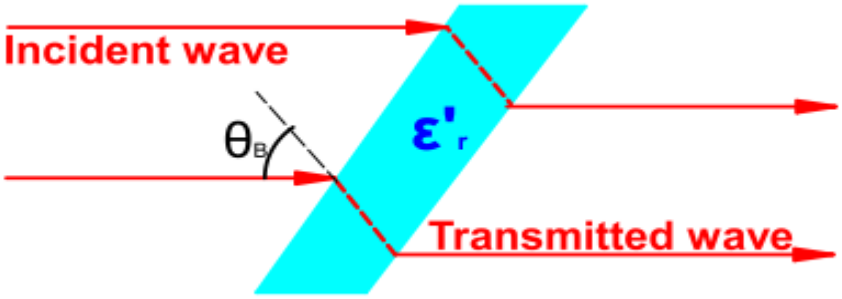

Fig. 2-19: Schematic of a Brewster angle window with incident plane wave.

A Brewster angle window (Fig. 2-19) is positioned so that the angle between the window plate normal and the propagation constant of the incident wave satisfies the Brewster angle condition;

$$\theta_B = tan^{-1}\left(\sqrt{\varepsilon'_r}\right) \tag{2-39}$$

If the window is placed at the Brewster angle, an incident plane wave will generate no reflections at the vacuum-window interface independent of the wave frequency. Therefore, the Brewster angle is defined solely by the window material. The requirement of a plane wave means that a corrugated section of waveguide is needed to achieve parallel polarisation and the window is sensitive to variations in angle; however, the Brewster window is shown to provide a lower absorption compared to multi-layer windows.

2.7. Summary

The physical processes which govern the operation of a gyro-TWA have been discussed. An overview of electron gun designs for vacuum devices has been provided. The selection of a cusp electron gun for a gyro-TWA was based on the generation of a mode selective, axis-encircling electron beam. A solenoid magnetic field was discussed to provide electron beam focussing which counteracts the internal defocussing forces. The passive components of a gyro-amplifier, excluding the input coupler, were discussed. A comparison

between the smooth-bore cylindrical interaction cavity and a HCIW was made. A HCIW has a near-constant group velocity near cut-off meaning that the helically corrugated cavity can support an instantaneous broadband beam-wave interaction. At the output region, the electron collector and the potential energy recovery of a depressed collector, capable of improving the electronic efficiency, was introduced alongside the single-layer, multi-layer and Brewster window used to seal the cavity vacuum and extract the mm-wave signal.

3. 94 GHz Input Coupler Design

3.1. Introduction

A mm-wave coupler plays a pivotal role in the performance of a high frequency gyro-TWA. A well designed coupler topology can be utilised as a method of coupling power into the interaction cavity and/or as a method of radially extracting the generated electromagnetic radiation. For a wide-band 94 GHz gyro-TWA, the design of the fundamental mode input coupler is central to the optimization of two parameters:

1. the coupling strength from the input mode to the desired cavity mode and,
2. bandwidth of the passive structure.

At frequencies approaching the THz region, the coupling process encounters enhanced difficulties due to the sub-mm waveguide dimensions and the subsequent increase in Ohmic losses caused by a reduction in the skin depth. Therefore, efficient coupling of an input signal is important to the achievable output power and the subsequent gain of a gyro-amplifier.

A side-wall input coupler for a W-band gyro-TWA is designed to couple the fundamental TE_{10} mode in a rectangular waveguide to the fundamental TE_{11} mode in a cylindrical waveguide. The configuration of a side-wall waveguide coupler can be adapted to suit the electric field profile of the desired cavity mode; however, all side-wall coupler topologies may be classified as either single-aperture [3.1] or multiple-aperture couplers [3.2]. The single aperture coupler has been designed to operate with a bandwidth of ~ 20% in the X-band; however, the design includes a small radius cut-off waveguide which will add complexity to cavity alignment and potentially degrade electronic performance in a high frequency gyro-amplifier. The multiple-aperture coupler has a target bandwidth of ~ 16%; however, the measured transmission of the coupler is ~ -2 dB resulting in a significant loss of input power to the interaction cavity.

The configuration of the coupler for the W-band gyro-TWA is selected based on physical constraints resulting from the narrow gap spacing between the cavity coil and the

vacuum jacket. Due to the area limitation, the compact nature of the single-aperture side-wall coupler is advantageous in comparison to the relatively long multiple-aperture coupler and, therefore, the topology will be implemented on the waveguide coupling structure.

The design of a single-aperture side-wall coupler for a centre-frequency 94 GHz gyro-TWA with ≥ 10% bandwidth is discussed. The W-band gyro-amplifier utilises a three-fold HCIW (Section 2.4.2) and, therefore, requires a TE_{11} feed signal to the interaction cavity. Hence, the coupler is optimised to convert the TE_{10}^{R} mode to the TE_{11}^{C} mode with high efficiency. The superscript 'R' and 'C' denote the rectangular and circular waveguides respectively. The design process for the rectangular-to-circular T-junction and waveguide reflector is outlined and the simulated performance of the coupler components and full coupler topology is presented in Sections 3.2 – 3.4. The manufacture of the input coupler is discussed in Section 3.4.2 and the simulated performance of the passive structure is verified with Vector Network Analyser (VNA) testing.

3.2. Rectangular-to-Circular T-junction

The mm-wave input coupler design is based upon a rectangular-to-circular T-junction, shown on the inset in Fig. 3-1. The microwave structure has practical applications including use as a filter [3.3], a polarizer [3.4] and in ortho-mode transducers [3.5]. Waveguide T-junctions in various forms can be designed analytically as well as with the use of modern computational techniques. Analytical methods have the advantage of reducing the computation time required to design the microwave structure. Several analytical techniques for understanding a rectangular-to-circular T-junction have been demonstrated using Fourier transform and/or mode matching techniques [3.6-3.10]. For simplicity and efficiency, the design of the rectangular-to-circular T-junction is optimised using mode matching software and verified using CST Microwave Studio [3.11].

The rectangular-to-circular T-junction has three variable parameters with modifications resulting in changes to the coupling strength. The variable parameters are the input waveguide width and height, a and b respectively, and the radius of the circular waveguide, R. For a gyro-TWA system, practical design limitations are often imposed on the

magnitude of R which, for manufacturing simplicity, will match the mean radius of the HCIW ($R = R_0$). For the design of the 94 GHz gyro-TWA, the beam tunnel radius is 1.30 mm. Fig. 3-1 shows the numerical scattering parameters of a rectangular-to-circular T-junction with R = 1.30 mm. Due to the symmetrical nature of the waveguide T-junction, the transmission from Port 1 to Port 2 (S_{21}) and Port 3 (S_{31}) will be identical with a maximum coupling coefficient of -3 dB. Fig. 3-1(b) shows that an S_{21} of -4 dB is achievable for R = 1.3 mm with optimal rectangular waveguide dimensions of a = 1.72 mm and b = 1.20 mm. The matching of the incident EM wave across the rectangular-circular boundary was undertaken through mode-matching i.e. reducing the impedance at the interface. A basic T-junction structure will transmit signals of equal magnitude towards the electron gun and the HCIW in a gyro-TWA system. Therefore, a method of terminating the signal at Port 3 and providing frequency selective feedback is required to enhance the coupling efficiency.

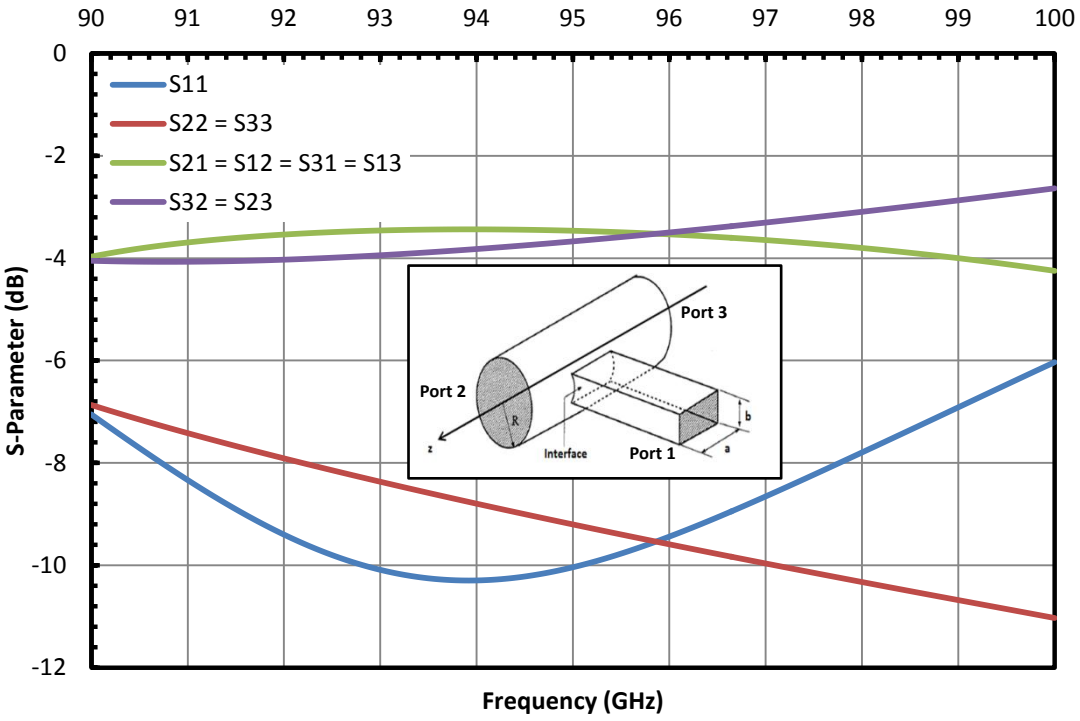

Fig. 3-1: T-junction geometry inset and numerical scattering of a waveguide T-junction.

An effective method of improving the transmission of radiation between Port 1 and Port 2 is by applying a cut-off waveguide at Port 3 [3.1]. The cut-off waveguide serves to prevent the propagation of microwave radiation to the electron gun region of the gyro-

device and, hence, prevent disruptions of the electric field profile in the gun diode which can have an adverse effect on the electron beam quality. For lower frequencies, the step down waveguide reflector is a simple, practical method which produces excellent results. A side view topology of the structure is shown in Fig. 3-2. However, at frequencies approaching the low-THz region, a cut-off waveguide can hinder the beam transportation through the cavity due to the reduction in waveguide diameter at high frequencies. At the input coupler region of a gyro-TWA, the Larmor radius of the electron beam is large due to the small magnetic field magnitude relative to the centre of the interaction region. Therefore, it is beneficial to increase the diameter of the waveguide structure within which the electron beam can propagate whilst ensuring a high reflectivity of incident radiation.

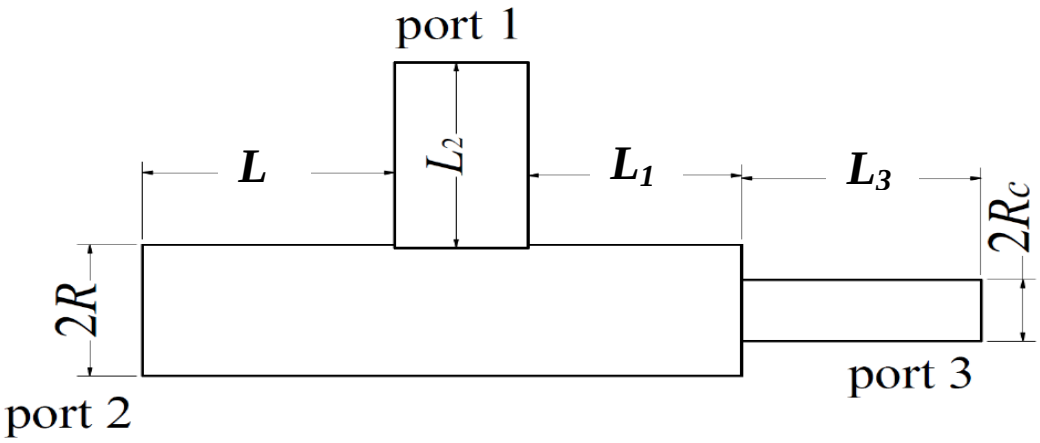

Fig. 3-2: Parametric side view of a waveguide T-junction with small-*R* waveguide reflector.

3.3. Bragg Reflector Design

A Bragg reflector [3.12] is a waveguide structure with radial periodicity which can be employed as a waveguide reflector, providing frequency selective feedback dependant on the axial period of the waveguide corrugations. The rippled corrugation of the waveguide wall, which is greater in diameter than a step down cut-off waveguide, scatters a forward propagating wave into a backward propagating wave if the Bragg condition is satisfied. The Bragg condition is defined as

$$2k_z = k_B \qquad (3\text{-}1)$$

where k_B is the Bragg wavenumber given by

$$k_B = \frac{2\pi}{p} \tag{3-2}$$

where p is the axial period of the corrugation. The generalised telegraphist's equations are used to represent the propagation of forward and backward waves in a waveguide with sinusoidal periodicity [3.13]. The radial profile of sinusoidally rippled waveguide is given by

$$h(z) = R + h_B cos(k_B z) \tag{3-3}$$

where h_B is the corrugation amplitude.

A sinusoidally rippled structure, although effective, is not readily practical due to manufacturing constraints. However, the analysis of the waveguide reflector in [3.13] highlights the reflectivity of the Bragg structure being dependant on the wave coupling coefficient and the total Bragg length. Hence, to maximise the reflectivity, the product of the two aforementioned variables must be maximised. At high frequency operation, it is beneficial to minimise the length of the Bragg reflector to prevent large energy loss to the waveguide wall. Hence, a high coupling coefficient is required. The wave coupling coefficient is dependent on the corrugation amplitude; therefore, high reflectivity can be achieved by employing a periodic waveguide with a large corrugation depth.

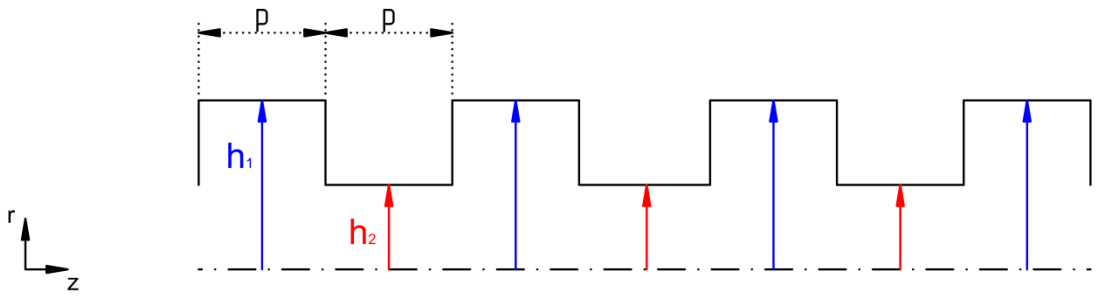

Fig. 3-3: Initial distribution of rectangular corrugations.

A periodic structure with rectangular corrugations can be employed as a waveguide reflector. The initial structure distribution, shown in Fig. 3-3, consists of two cylindrical waveguides of radii h_1 and h_2. A study of the rectangular corrugation [3.14] reflectivity and phase spread proves that high reflectivity can be achieved for a low section number; however, the resultant phase spread will reduce the bandwidth of the waveguide reflector. Therefore, the length of the Bragg reflector is increased to reduce the phase shift between the incident and reflected signals. The improved phase response with increasing section number is shown to saturate at 15-corrugations; therefore, an increase in length would primarily result in higher Ohmic losses without improving the reflector performance. A 15-section Bragg reflector will be used in the design of a W-band input coupler.

The Bragg reflector with 15-stage rectangular corrugations was simulated using finite element code CST Microwave Studio (CST-MS). Initial simulations highlighted that a uniform distribution of sections of radii R_1 and R_2 would not be sufficient to provide high reflectivity over a broad bandwidth. Therefore, an optimisation of the 15-stage reflector was carried out to achieve a high reflection coefficient with minimal phase spread for variable corrugation depths (h_B). The optimised section radii for the 15-corrugation steps are shown in Table III-I.

The 15-section Bragg reflector was manufactured using Computer Numerically Controlled (CNC) milling and electroforming techniques. The design process will be discussed in Section 3.4.2. An aluminium mandrel of the rectangular corrugations was made and the diameters of the corrugated sections were measured using Vernier callipers. The section diameters were found to differ from the simulated value on all 15 periods of the Bragg former with the discrepancy between the design value and the manufactured value shown

in Table III-I. By measuring the radii of the Bragg structure, the dimensions of the manufactured reflector former could be applied to the finite element simulation to compare the numerical reflectivity of the Bragg structure to the Vector Network Analyser (VNA) testing measurements. The VNA testing set-up and methodology is discussed in Section 3.4.3. The manufactured Bragg reflector reflectivity and phase response is compared with the numerical simulation of the reflector with the design radii and the actual radii in Fig. 3-4.

Table III-I: Diameters of designed and machined Bragg reflector.

Parameter	Design value (mm)	Manufactured value (mm)	Parameter	Design value (mm)	Manufactured value (mm)
Period	0.70	0.70	Radius 8	3.70	3.90 (+0.20)
Radius 1	4.20	4.30 (+0.10)	Radius 9	4.90	5.00 (+0.10)
Radius 2	3.50	3.60 (+0.10)	Radius 10	4.50	4.60 (+0.10)
Radius 3	4.60	4.70 (+0.10)	Radius 11	4.40	4.50 (+0.10)
Radius 4	4.70	4.80 (+0.10)	Radius 12	4.50	4.60 (+0.10)
Radius 5	3.40	3.50 (+0.10)	Radius 13	4.20	4.40 (+0.20)
Radius 6	3.90	4.00 (+0.10)	Radius 14	5.00	5.10 (+0.10)
Radius 7	4.40	4.50 (+0.10)	Radius 15	4.50	4.60 (+0.10)

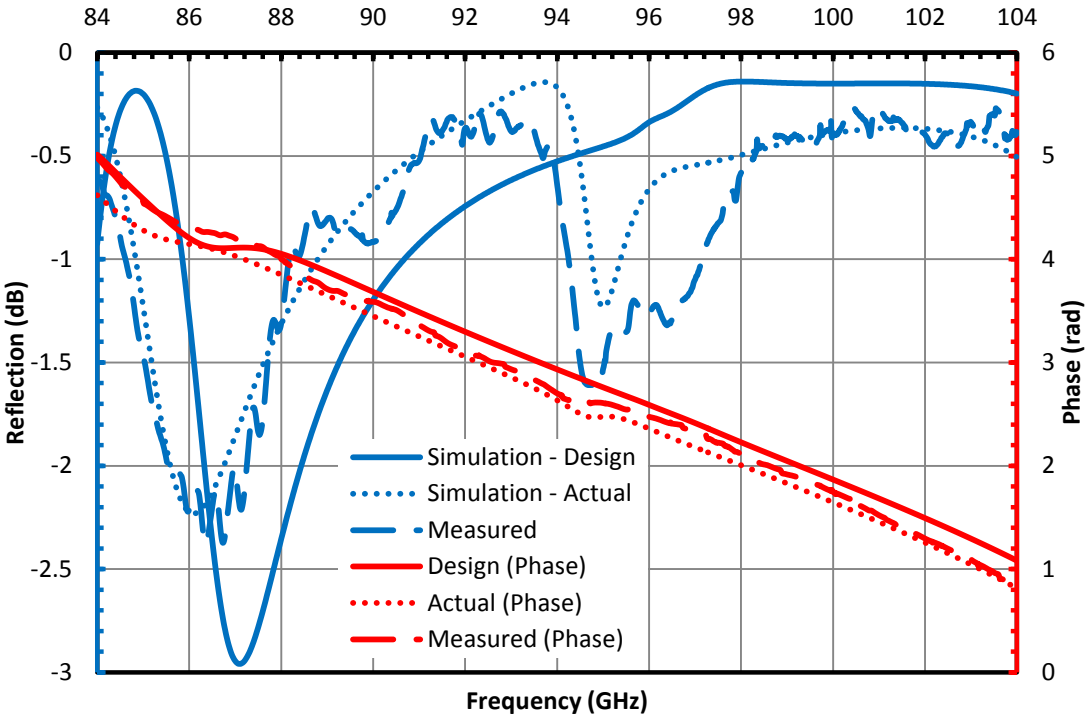

Fig. 3-4: Numerical and measured reflectivity of 15-section Bragg reflector.

Table III-I highlights the discrepancy between the designed and machined values of the Bragg reflector sections ranging from 30 µm to 170 µm with all the corrugation depths increasing from the designed parameter set. The result of the radii increase is a shift in the centre frequency of the waveguide reflector as shown in Fig. 3-4. The variations in the corrugation depth have also altered the resonant frequency of the Bragg reflector resulting in an acute frequency response around 95 GHz. The loss of signal energy around this frequency may be caused by energy storage in the waveguide cavity with no noticeable increase in transmission observed at ~ 95 GHz. Fig. 3-4 shows a good agreement between the numerically simulated reflection and phase response of the Bragg structure and the VNA test measurement.

3.4. 94 GHz T-Junction Input Coupler

3.4.1. CST-MS Simulation

The Bragg reflector (Section 3.3) is attached to the rectangular-to-circular T-junction (Section 3.2) to create the input coupler topology for the W-band gyro-TWA. Hence, the

parameter set of *a*, *b* and *R* are predefined alongside the waveguide reflector dimensions. Therefore, the only variable parameter within the topology is L_1 (Fig. 3-2) which is the distance from the front-edge of Section 1 of the Bragg reflector to the near-side of the rectangular input waveguide. A parametric sweep of the variable highlighted optimum S_{21} transmission is achieved when L_1 = 0.70 mm. The optimum L_1 value is determined by ensuring that the phase response of the Bragg reflector is ~ π at 94 GHz. Due to the non-uniform phase response of the reflector over the frequency band, variations in L_1 can be used to optimise the structure for the desired centre frequency. The numerical scattering plot of the optimised T-junction input coupler with Bragg reflector is shown in Fig. 3-5. The Bragg reflector dimensions were set at the designed values (see Table III-I). The input coupler is shown to have a bandwidth of 13.5%, including the 90 – 100 GHz operating frequency of the W-band gyro-TWA. The bandwidth is defined as the frequency range within which the transmission loss is > -1 dB i.e. 89 - 102 GHz from the numerical simulation of the W-band input coupler. An input coupler of similar topology has been shown to achieve a bandwidth of 20% [3.1] about a centre frequency in the X-band; however, this design would only be applicable to a relatively low frequency gyro-amplifier due to the small diameter waveguide required at the beam input port.

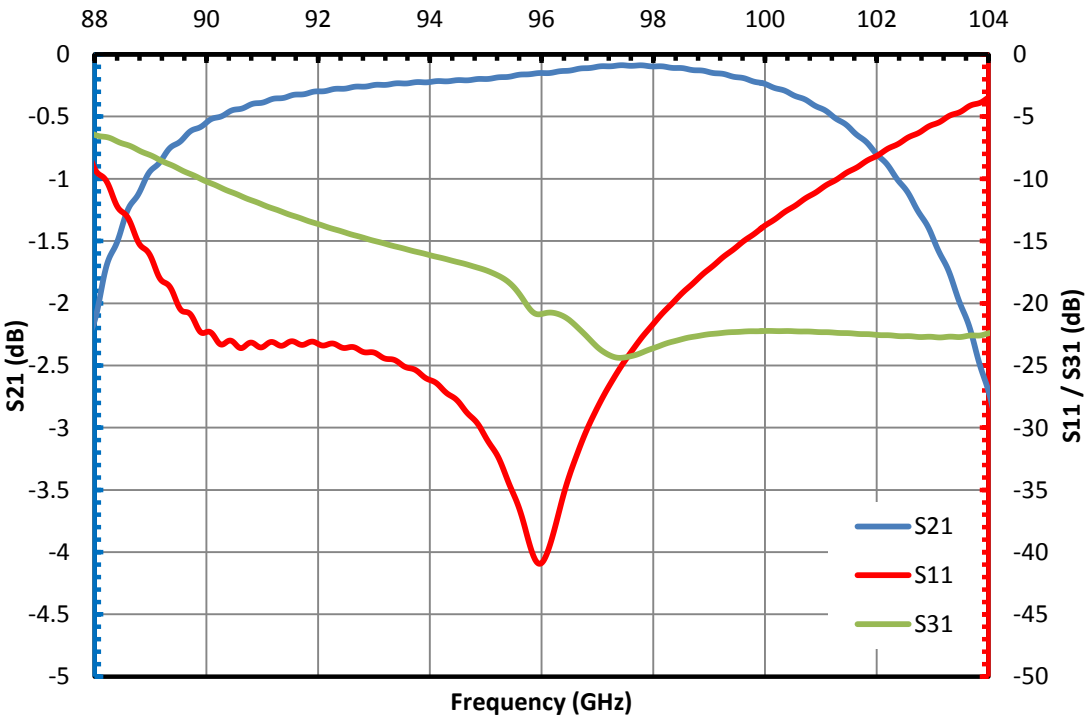

Fig. 3-5: Numerical scattering of a T-junction input coupler for a gyro-TWA.

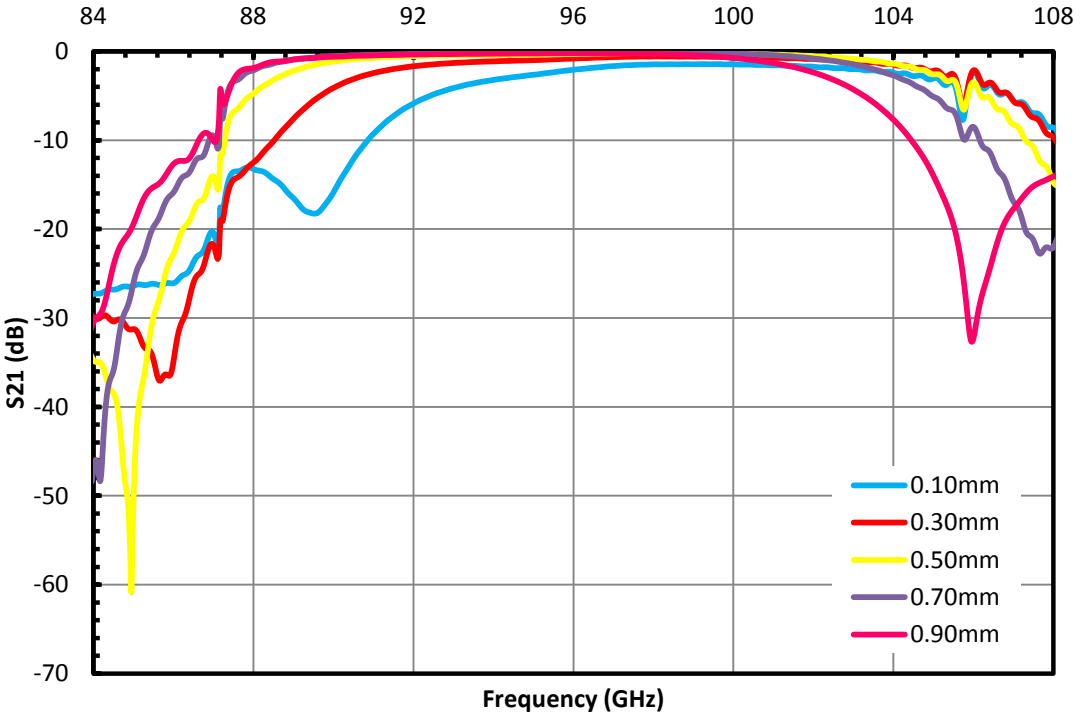

Fig. 3-6: Frequency shift of W-band input coupler with variation in L_1.

The T-junction input coupler topology was shown to be frequency tuneable with variations to L_1. Fig. 3-6 shows that a resultant frequency shift of ~ 2 GHz is evident with an increase in L_1 of 0.20 mm. The bandwidth of the input coupler is shown to reduce with the shortening of L_1, caused by a phase mismatch between the incident and reflected wave from the Bragg reflector. For a waveguide short there would be a constant phase shift of π-radians; however, due to the nature of the Bragg structure, the shift between the incident and reflected wave-fronts is more complex. Hence, it is important to design a coupler with a small phase difference to prevent destructive interference between the forward and backward wave propagation. For the designed coupler, an L_1-value of 0.70 mm magnitude produces the most coherent response between the incident and reflected waves.

3.4.2. Manufacture

The two components of the W-band input coupler, the Bragg reflector and the waveguide T-junction, were manufactured into two discrete metallic elements. The Bragg reflector was manufactured by creating an aluminium mandrel using a CNC milling machine

with the corrugation radii stated in Table III-I. The aluminium mandrel was then placed in an electrolytic bath containing a copper deposit. The copper is grown onto aluminium former to the desired thickness of ~ 2 mm and subsequently machined to form a uniform cylindrical block. The process of copper growing is known as electroforming. The aluminium mandrel is then dissolved from inside the copper block using an acidic solution, creating a hollow metallic waveguide with rectangular step corrugations. A 2D schematic of the Bragg reflector manufacture is shown in Fig. 3-7.

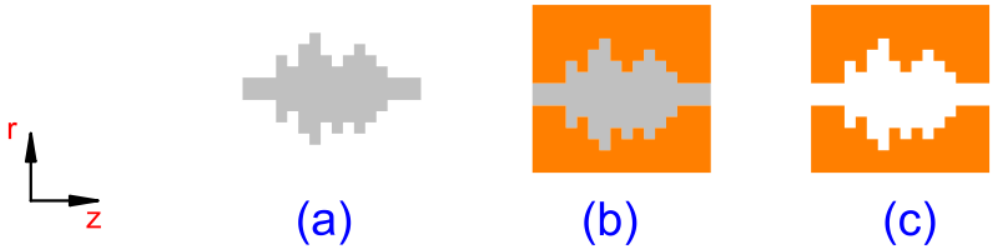

Fig. 3-7: Waveguide reflector with (a) aluminium mandrel, (b) mandrel with copper growth and (c) hollow Bragg reflector.

The rectangular-to-circular T-junction was formed through a process of wire erosion. A circular hole of radius *R* was cut into a copper block using the technique involving a high field discharge. The recurring current discharges remove the material which is placed between the tool-electrode, the wire, and the work-piece. A copper channel with dimensions *a* and *b* is then created with the spark discharge technique to form the rectangular input waveguide. The waveguide channels are then flushed to create a smooth inner wall with minimal surface roughness, important at high frequencies due to the reduction in skin depth.

Two waveguide transitions were also manufactured using the wire erosion technique. A rectangular-to-rectangular taper was manufactured to match WR-10 waveguide dimensions to the optimised *a* and *b* values of the input coupler. A circular-to-rectangular convertor was also machined to convert the TE_{11}^{C} mode from Port 2 to the TE_{10}^{R} mode required for measurement at the rectangular port of the VNA.

3.4.3. Vector Network Analyser (VNA) Testing

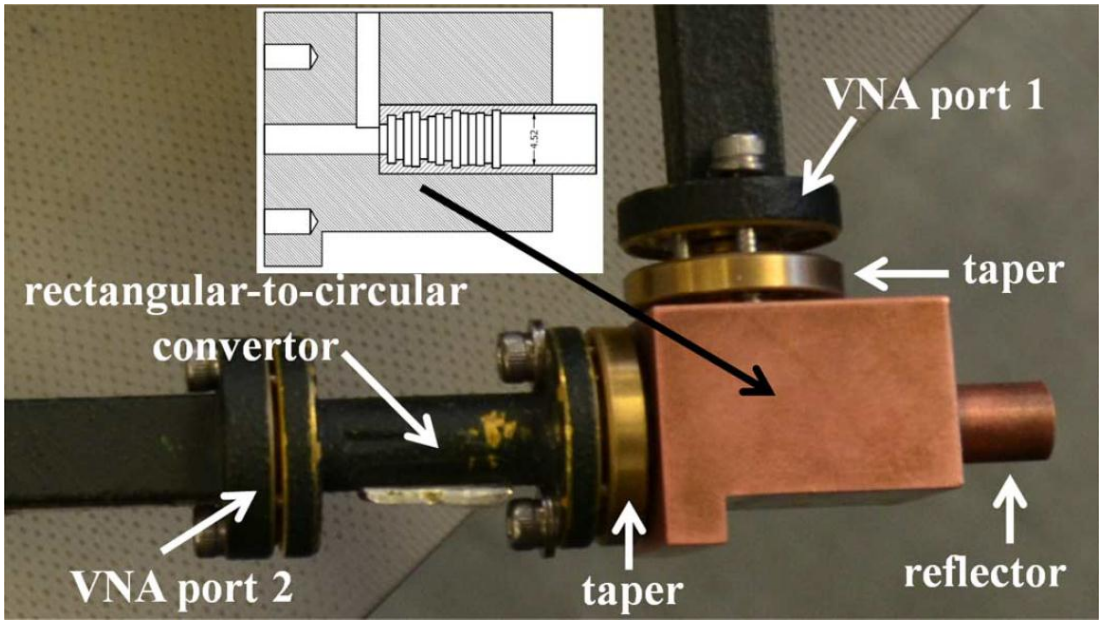

Fig. 3-8: VNA measurement set-up for W-band input coupler.

The experimental set-up for the VNA measurement is shown in Fig. 3-8. The configuration allows for measurement of the transmission coefficient (S_{21}) and reflection at the rectangular input port (Port 1) to be taken. The test set-up can also measure the S_{12} and S_{22} parameters; however, due to the directionality of the incident signal in the gyro-TWA, only the S_{11} and S_{21} parameters are of interest.

An Anritsu 37000D Lightning series VNA [3.15] with 75GHz to 100GHz OML transmit and receive extension heads were used in the experimental set-up. The VNA model requires an external Local Oscillator (LO) to generate a continuous source of frequency modulated radiation. The LO feeds a power splitter which delivers a signal of equal power to Branch 1 and Branch 2 of the VNA. The signal is further split on each Branch by a frequency mixer to provide a test signal, used by the VNA to monitor phase and amplitude of the incident signal, and a measurement signal delivered to the analyser Port. Measurements were performed throughout the W-band. The VNA has an incorporated switching mechanism allowing for the signal to be transmitted down Branch 1 to Port 1 and, in turn, transmitted down Branch 2 to Port 2. From Branch 1, the transmitted signal is propagated through the input coupler, or the Device Under Test (DUT), and received by Branch 2. This allows for measurement of S_{11} and

S_{21}. If the signal is propagated down Branch 2, the transmitter and receiver ports are switched and S_{12} and S_{22} are measured. The phase and amplitude of the transmitted and reflected signals are shown on the VNA digital display.

The experimental set-up was initially calibrated using the Short-Short-Load-Thru (SSLT) technique, also known as the Offset Short. The calibration technique monitors imperfections in the internal VNA match and the frequency response of external components ensuring that accurate measurement data for the DUT is achieved. The full 2-port SSLT calibration is performed over a frequency range of 84 – 104 GHz. Two rectangular waveguide shorts of different lengths are used to define the reflection behaviour at the VNA ports [3.16] with the two shorts connected to Port 1 and Port 2 in turn. The waveguide load is used to monitor the directivity of the internal directional coupler. The directional coupler within the VNA separates the signal incident on the DUT from the signal reflected from the DUT; therefore, consideration of the systematic errors within the directional coupler will ensure an accurate S-parameter profile is achieved for the DUT. A standard load with a broadband impedance match is connected at Port 1 and Port 2 independently. The thru, which is performed with a standard waveguide of known length connected at Port 1 and Port 2 simultaneously, monitors the transmission response over the frequency range and highlights any mismatch between the waveguide impedance and the port impedance.

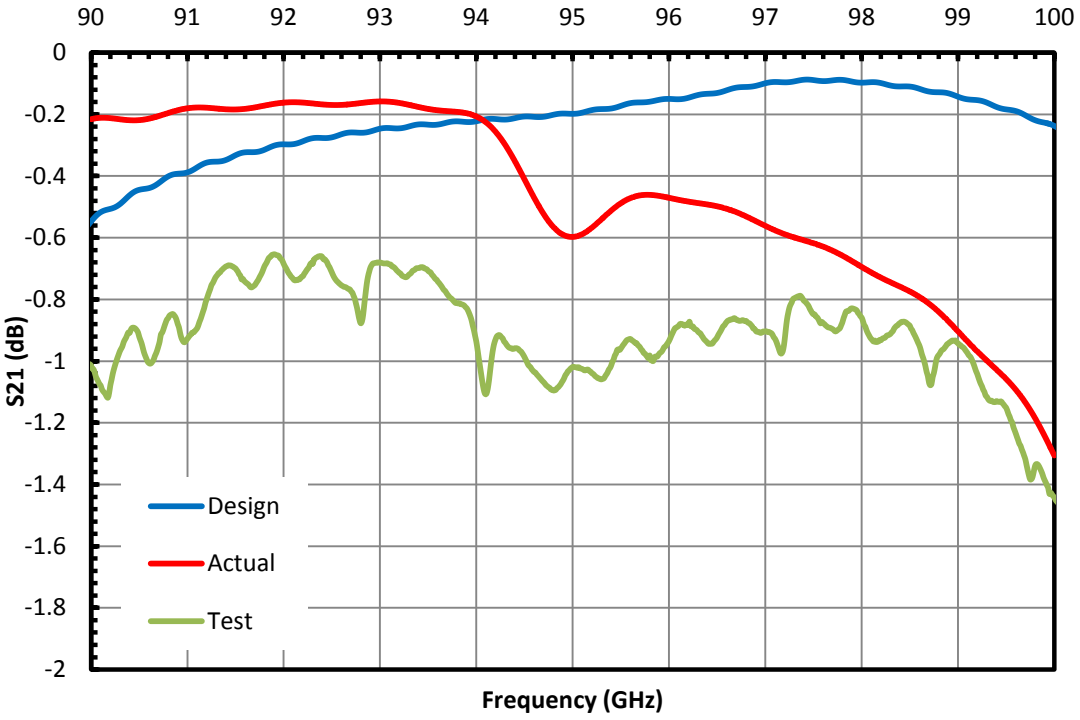

Fig. 3-9: Measured VNA transmission of W-band input coupler compared with numerical model transmission.

The measured transmission of the W-band input coupler is shown in Fig. 3-9, alongside the numerical transmission data for the designed parameter set and the machined parameter set (Table III-I). The 'Design' and 'Actual' data sets in Fig. 3-9, and subsequent figures, refer to the simulated coupler data for the optimised coupler design and the manufactured coupler design respectively. The 'Test' data is from VNA measurements. The average transmission for the input coupler is ~ -1 dB which is approximately 0.7 dB below the predicted value from the finite element simulation. However, considering the waveguide loss due to the skin depth of copper at high frequency and the large tolerances on the Bragg reflector, the performance of the input coupler is acceptable. The transmission coefficient suggests ~ 80% of the incident radiation would be transmitted to the gyro-TWA interaction circuit. Fig. 3-9 shows that a drop in transmission is witnessed ~ 95 GHz in the VNA test results. Hence, the frequency response predicted by the model with accurate Bragg dimensions (red plot-line) is validated supporting the suggestion from Fig. 3-4 that the discrepancy in Bragg reflector dimensions has affected the structures resonant frequency. Fig. 3-10 shows the reflection from the rectangular input port of the waveguide coupler. The

S_{11} plot highlights good agreement between the numerical model and the VNA measurement with < -15dB reflections witnessed over the majority of the frequency band.

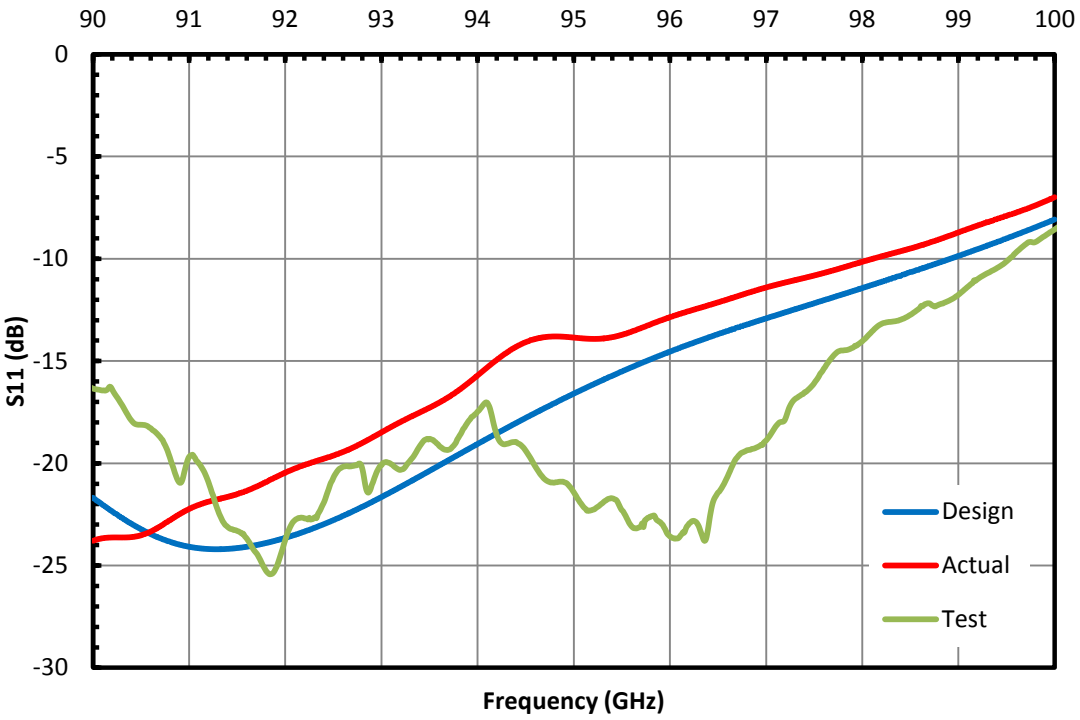

Fig. 3-10: Measured and simulated reflection at rectangular input port for T-junction input coupler.

3.5. Discussion of TE_{11} Input Coupler Design

The design and experimental testing of a single aperture input coupler for a W-band gyro-TWA is presented. The TE_{10}^{R} – TE_{11}^{C} waveguide coupler, based upon a rectangular-to-circular T-junction, achieved a 13.5% bandwidth covering the 90 – 100 GHz operating frequency range of the amplifier system. The use of a Bragg reflector on the fundamental mode coupler has been shown to be effective at preventing propagation of radiation towards the electron gun whilst enhancing the diameter of the beam tunnel compared to a step-down waveguide reflector.

A spark erosion technique was used to manufacture a prototype W-band coupler suitable for VNA testing. A measured transmission coefficient of -1.0 dB was achieved, equating to a ~ 0.7 dB decrease from the simulated coupling performance. The numerical and experimental return loss was shown to be in good agreement with a reflection

coefficient of ~ -15 dB witnessed across the operating bandwidth. Therefore, the side-wall coupler will not prevent significant drive power from propagating into the interaction cavity.

4. 94 GHz Gyro-Travelling Wave Amplifier Experiment

4.1. Experimental Setup

The experimental setup of the gyro-TWA, adapted from [4.1], is shown in Fig. 4-1. A schematic of the gyro-TWA configuration contained within the walled test bay is shown, consisting of a cusp electron gun, input coupler, Helically Corrugated Interaction Waveguide (HCIW) and an output window. A discussion of the gyro-TWA components was presented in Chapter 2 and Chapter 3. The electron beam guidance (Section 2.3.2) is provided using two solenoid magnets; the reverse coil provides the cusp magnetic field for electron beam gyration and the main solenoid is used to confine the electron beam and determine the interaction frequency. A diagram of the magnets enclosing the vacuum components is shown in Fig. 4-2.

The solenoid magnets and the power supply system for the 94 GHz gyro-TWA are discussed. The pulsed power system is discussed in Section 4.2 introducing the Blumlein Pulse Forming Line (PFL), the voltage dividers used to determine the beam voltage and the spark gap switch. The solenoid magnetic field configuration is introduced in Section 4.3 and the measurement of the main cavity field is presented. Results of the experimental investigation of the 94 GHz gyro-TWA are presented in Sections 4.4 – 4.7. An investigation into the passive components of the gyro-TWA is discussed in Section 4.4 and the corrugated horn presented and measured in Section 4.5. The characterisation of the electron beam is presented in Section 4.6 alongside the beam diagnostic techniques employed. The microwave output of the vacuum cavity is highlighted in Section 4.7.

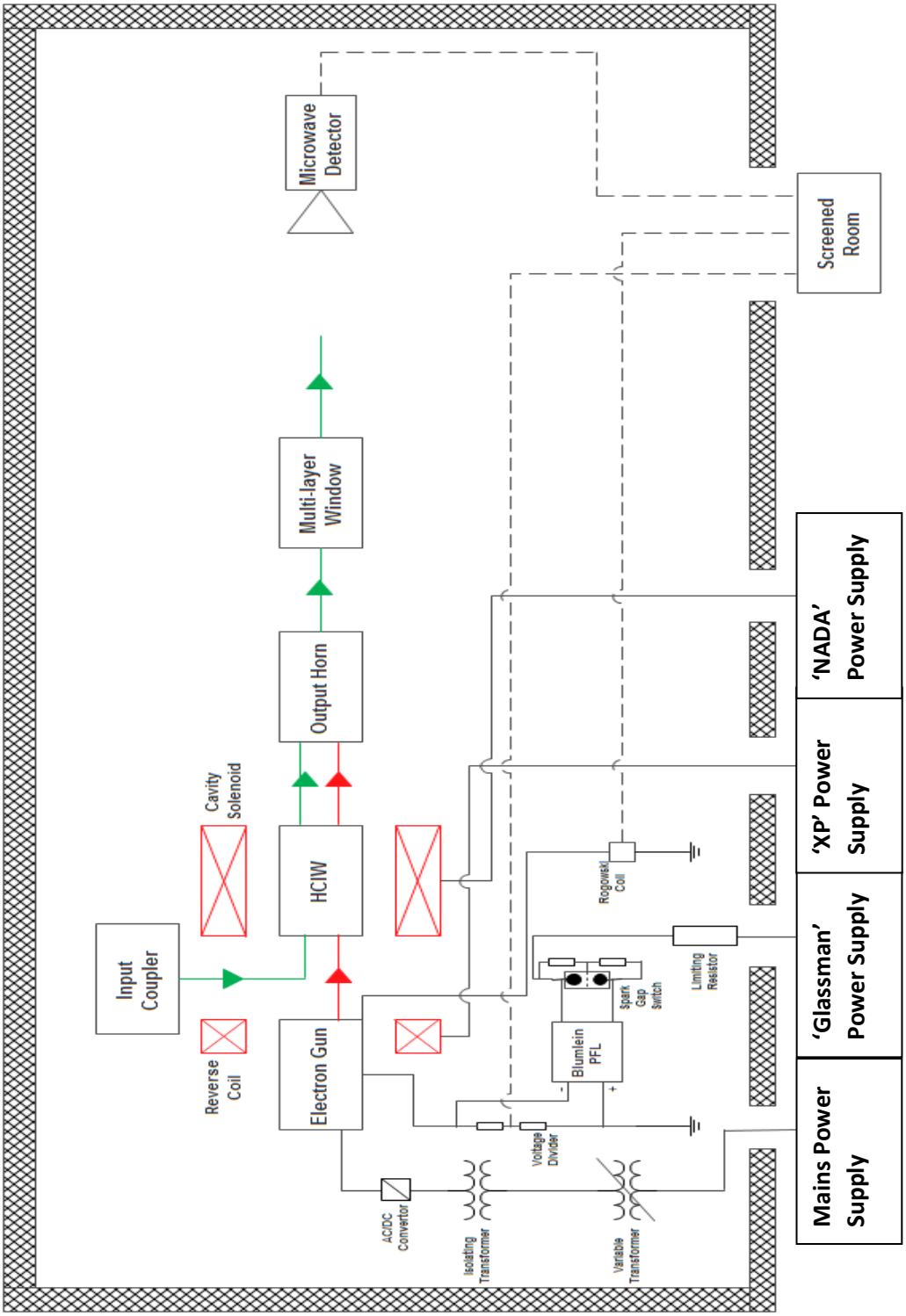

Fig. 4-1: Experimental setup of the 94 GHz gyro-TWA.

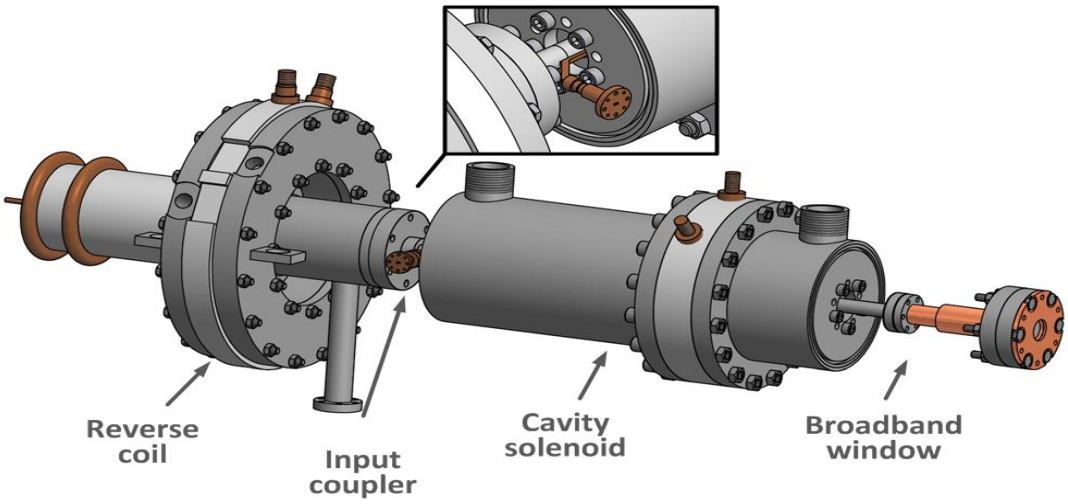

Fig. 4-2: A schematic of the reverse coil and cavity solenoid.

4.2. Pulsed Power System

The pulsed power system of the 94 GHz gyro-TWA experiment consists of 4 discrete power supplies (see Fig. 4-1). A 240 V mains supply heats the gun cathode to a temperature of 1050 °C which results in the thermionic emission of electrons from the M-type barium aluminate cathode (Section 2.2.1.1). The heater power supply is floated at the same potential as the cable Blumlein pulse generator and insulated from the mains using a high voltage (500kV) 1:1 isolating transformer. Two high current power supplies drive the magnetic field coils; an XP up to 300 A, 60V DC power supply delivers a tuneable current varying signal to the reverse coil allowing for variation of the cusp magnetic field within the diode region and; a 300 A, 70V NADA power supply provides the current to drive a maximum required magnetic field of 2.1 T in the interaction region. A 100 kV, 40 mA Glassman power supply is used to charge the double stacked cable Blumlein pulsed generator to allow for single shot or high Pulse Repetition Frequency (PRF) (up to 100Hz) operation of the gyro-TWA. A voltage divider (Section 4.2.2) on the cable Blumelin pusled generator is used to measure the pulsed (400ns) voltage applied to the cathode A spark gap switch (Section 4.2.3) is used to switch the output of the cable Blumlein pulsed generator which allows for a PRF rate of up to ~ 100 Hz with a short rise time (~ 40 ns). An overview of the high voltage pulsed power supply, the magnetic field systems and the electron beam diagnostics are presented.

4.2.1. Blumlein Pulse Forming Line

A Blumlein Pulse Forming Line (PFL) is designed based on the physical properties of electrical signals propagating along a transmission line. A single cable pulse generator can only achieve an output voltage (V_{out}) of less than, or equal to, the input voltage (V_{in}). A Blumlein PFL can generate an output voltage of double the input voltage, or greater. Therefore, the use of a Blumlein PFL reduces the required V_{in} magnitude and, hence, reduces the complexity of power supply integration.

The circuit diagram for a Blumlein PFL is shown in Fig. 4-3. Initially, with the circuit switch open, the transmission lines of length L_{CAB} are charged with a high voltage input of magnitude V_{in}. When the switch is closed, the electrical signals stored in the two transmission lines discharge with the superposition of the two discrete signals resulting in a rectangular pulse across the load (Z_L). The magnitude of the output voltage (V_{out}) is given by

$$V_{out} = \frac{2V_{in}Z_L}{Z_1 + Z_2 + Z_L} \tag{4-1}$$

where Z_1 and Z_2 are the impedances of the transmission lines. The duration of the pulse discharge (τ) is dependent on the length of the transmission lines (L_{CAB}) and the propagation velocity of the electrical signals within the lines (v_c). Hence, τ is defined by

$$\tau = 2\frac{L_{CAB}}{v_c} \tag{4-2}$$

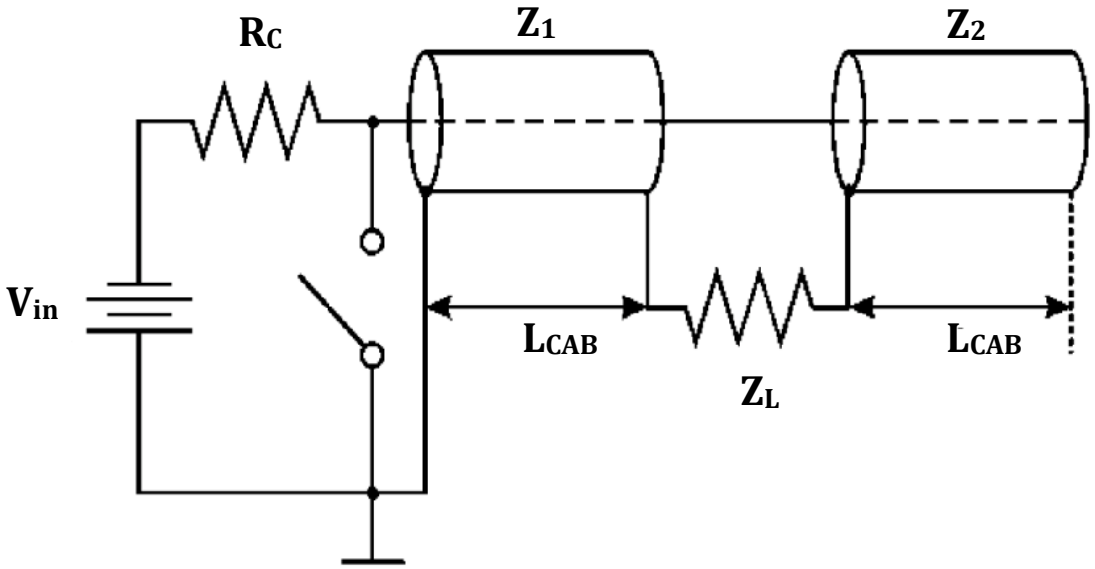

Fig. 4-3: Circuit diagram for Blumlein PFL.

An additional transmission line can be added to the Blumlein PFL to create a double cable Blumlein PFL. The circuit diagram of a double cable PFL is shown in Fig. 4-4. The addition of a further transmission line allows for series charging and parallel discharging of the PFL resulting in a V_{out} magnitude of up to four times the charging voltage (V_{in}). If points *b* and *c* and *e* and *d* ae joined together discretely, a voltage magnitude of ~ $2V_{in}$ is achieved; however, by connecting *c* and *e* an output voltage of ~ $4V_{in}$ can be generated at the load (Z_L). The V_{out} magnitude from a double cable Blumlein PFL may be written as

$$V_{out} = 4\frac{V_{in}Z_L}{Z_1 + Z_2 + Z_3 + Z_4 + Z_L} \tag{4-3}$$

where Z_1, Z_2, Z_3, and Z_4 is the impedance of the respective transmission line.

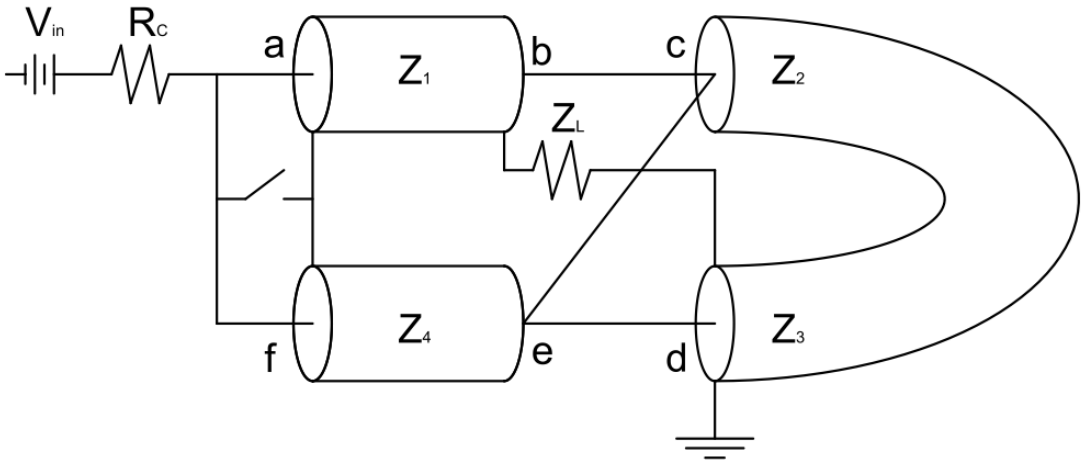

Fig. 4-4: Circuit diagram for a double cable Blumlein PFL.

In the 94 GHz gyro-TWA experimental setup, a double cable Blumlein PFL is used to produce a signal voltage of up to -4V_{in} at the gun diode. The notation of +/- indicates the use of a non-inverting or inverting Blumlein pulse generator respectively. An inverting Blumlein PFL was designed, as shown in Fig. 4-5, resulting in a required V_{in} magnitude of ~ 20 kV at the input to produce -60 kV at the cathode. The rise time of the output pulse delivered to the cathode is largely determined by the closing time of the switch. The closing time dictates the circuit transition period from an insulating to a conducting state. Upon circuit closure, a small portion of the discharge pulse is split from the main signal through a voltage divider to measure the pulse characteristics. The spark gap switch and the voltage divider used in the experimental setup are subsequently discussed.

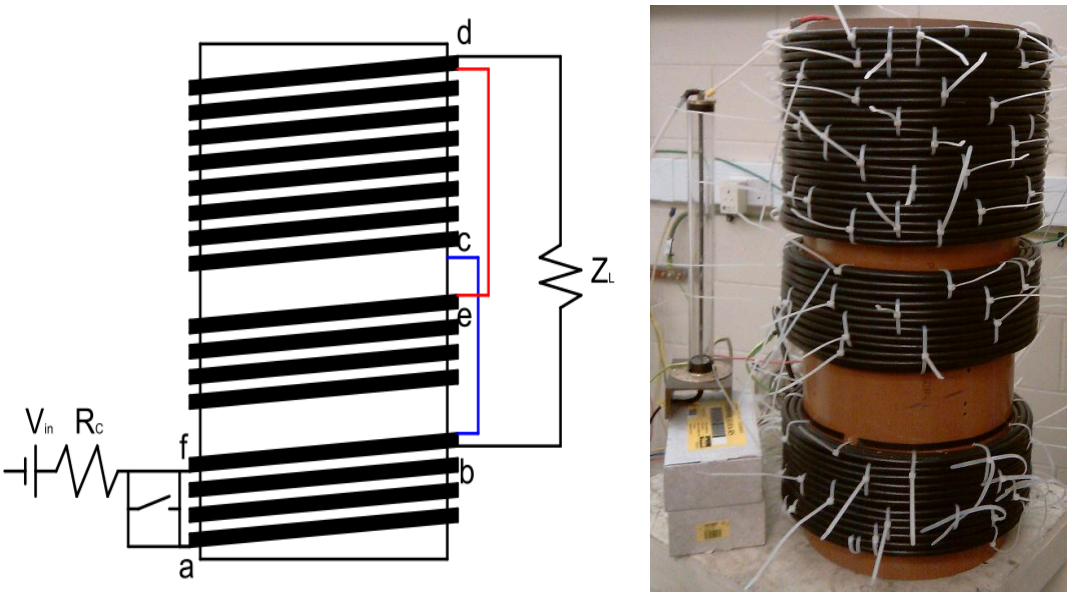

Fig. 4-5: (L) Schematic of double cable Blumlein PFL and (R) laboratory photograph of PFL.

4.2.2. Spark Gap Switch

A spark gap switch [4.2] can be employed as the insulating-to-conducting switching mechanism in a high voltage power supply. The switch component in all forms consists of two main electrodes separated by a gap distance (d_g) with the area between the electrodes filled with, typically, a gaseous substance; however, a liquid mercury or solid state switch may be used in certain applications. A two electrode spark gap switch operates solely in self-breakdown mode creating a closed circuit when the potential between the two electrodes exceeds the breakdown voltage of the substance within the gap spacing; hence, an arc discharge changes the circuit operation from insulating to conducting. The simplicity of a two electrode spark gap switch is advantageous; however, the switch output voltage is determined solely by the breakdown voltage. Therefore, if a larger or lesser voltage is required, the spark gap switch must be pressurised without damaging the switch or reconfigured with changes made to d_g and/or the spacing substance, a time consuming process.

A three electrode, triggered spark gap switch is a practical solution to the two electrode problem. The addition of a trigger electrode between the two main electrodes allows for switch operation in the self-breakdown mode and trigger mode. Therefore, the

output voltage of the spark gap may be tuned by varying the trigger potential without reconfiguring the switch components. The gap spacing between the two main electrodes in a triggered spark gap exceeds the distance required for an arc discharge to occur when the electrodes are charged with the desired output voltage. In trigger mode operation the application of a short trigger pulse of variable magnitude, superimposed with the potential between the main electrodes resulting from the charging voltage, results in an arc discharge within the spark gap. Hence, the circuit becomes conducting.

For a three electrode spark gap operating in self-breakdown mode, an external voltage divider is applied between the three electrodes. Voltage dividers will be discussed in Section 4.2.3. When the charging potential is applied to the main electrodes, a portion of the potential is distributed to the trigger electrode. The trigger electrode is subsequently charged to a potential which results in the breakdown of the spark gap and, hence, the circuit is closed. The output voltage of a three electrode spark gap switch operating in self breakdown mode is variable based on the ratio of the voltage divider (R_1 and R_2); therefore, the switch operates with similar characteristics compared to triggered mode operation without the requirement of an additional power supply.

A circuit diagram of the switch is shown in Fig. 4-6 alongside a photograph of the constructed switch. The voltage divider used had resistance values of R_1 = 250 MΩ and R_2 = 200 MΩ.

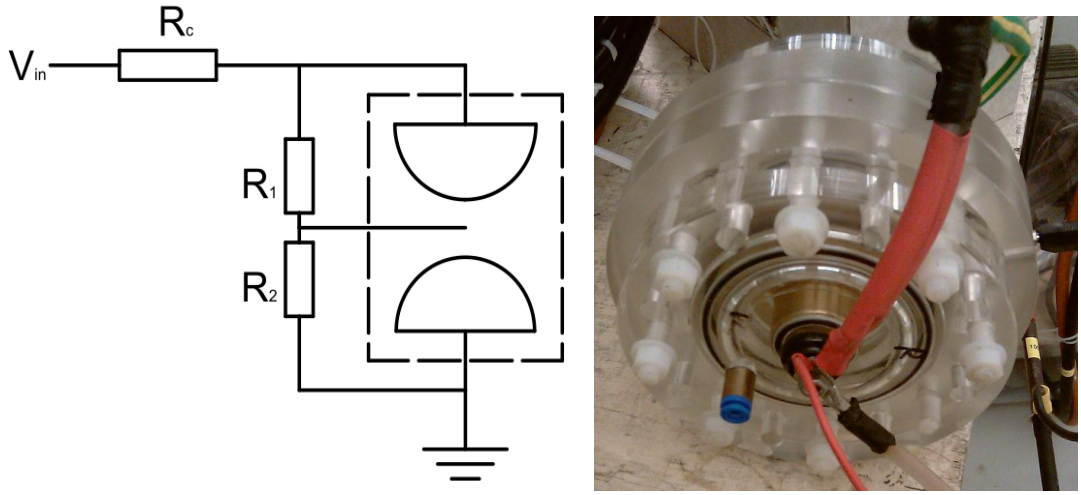

Fig. 4-6: (L) Circuit diagram of spark gap switch and (R) constructed spark gap switch.

4.2.3. Voltage Divider

A voltage divider is a component consisting of two impedances used to reduce the magnitude of a high voltage signal. A voltage divider may be constructed with resistive or capacitive elements [4.3] with the impedance values determined by the required magnitude of the output signal. Two voltage dividers are included in the pulsed power setup; the first determines the trigger voltage in the spark gap switch and the second determines the pulse magnitude at the load. For high voltage pulsed power applications, the implementation of a voltage divider within the circuit allows for characterisation of the input pulse magnitude, shape and pulse duration. A resistive voltage divider is employed within the experimental setup to provide a low voltage test pulse used to characterise output pulse from the Blumlein PFL.

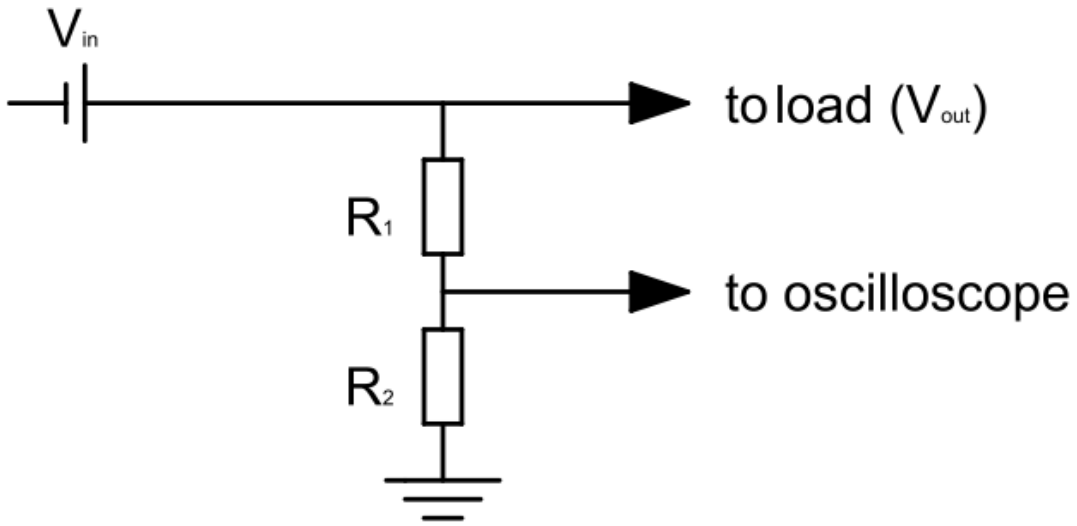

Fig. 4-7: Circuit diagram of a two-element resistive voltage divider.

A circuit diagram of a resistive voltage divider is shown in Fig. 4-7. The basic configuration of the voltage divider includes two resistors of resistances R_1 and R_2. The division of the input signal (V_{in}) results in the generation of two discrete output pulses; V_{out} is delivered to the load and $V_{oscilloscope}$ is delivered to a 4-channel oscilloscope used to test the pulse characteristics. In the 94 GHz gyro-TWA experimental setup, the voltage delivered to the electron gun should greatly exceed the test pulse voltage ($V_{out} >> V_{oscilloscope}$). Therefore,

R_1 >> R_2. The pulse magnitude delivered to the oscilloscope, dependant on the ratio of the resistances, may be written as

$$V_{oscilloscope} = \frac{R_2}{R_1 + R_2} V_{in} \tag{4-4}$$

The voltage delivered to the load (V_{out}) is subsequently reduced with V_{out} defined by

$$V_{out} = V_{in} - V_{oscilloscope} \tag{4-5}$$

In the experimental setup, the resistive voltage divider is designed with resistance values of R_1 = 2.73 kΩ and R_2 = 2.72 Ω equating to a resistance ratio (R_2/R_1) of ~ 0.1%. Therefore, an input voltage of 60 kV will result in 60 V pulse transmitted towards the oscilloscope for pulse characterisation. With the incorporation of an attenuator, a voltage pulse with corresponding magnitude may be detected safely by the oscilloscope.

4.3. Solenoid Magnetic Field

A solenoid magnetic field [4.4] is generated from a helically-wound current-carrying wire about a bore of radius, $R_{B(z)}$, which acts as a channel for magnetic flux lines. The pitch of the helical winding is small; therefore, the magnetic field generated from the solenoid may be treated as a set of discrete current-carrying wire rings. The generation of a solenoid magnetic field from a current carrying ring is described by Ampere's Law which, in the integral form, is written as

$$\int \boldsymbol{B} \cdot d\boldsymbol{l} = \mu_0 I \tag{4-6}$$

where *I* is the current carried in the wire. A solenoid magnetic field induced by a number of wire rings is a superposition of the individual *B*-field components, generating an axial magnetic field profile. For a solenoid magnet with *N* turns, the magnetic field at the bore centre, derived from (4-6), may be written as

$$B = \mu_0 \frac{N}{l_s} I \tag{4-7}$$

where l_s is the length of the solenoid. For a multiple layer solenoid, the *B*-field may be calculated discretely for each layer, with the subsequent superposition of the field components resulting in the total magnetic field.

The 94 GHz gyro-amplifier experimental setup includes two solenoid magnets; a reverse coil and a main cavity coil. The polarity of the magnetic field produced by the reverse coil is opposite to the polarity of the main coil *B*-field to generate a magnetic cusp. The magnetic cusp field causes the gyro-rotation of the electron beam (Section 2.2.4) required for efficient beam wave interaction. The cavity coil also counters the effects of internal beam forces (Section 2.3.1) to confine the beam propagation within the interaction cavity. The reverse coil of the experimental setup, situated towards the gun diode, is created with 10 wire turns per layer over 4 layers. The reverse coil magnetic field magnitude was simulated with MAGIC FDTD-PIC solver. The magnetic field profile is shown in Fig. 4-8.

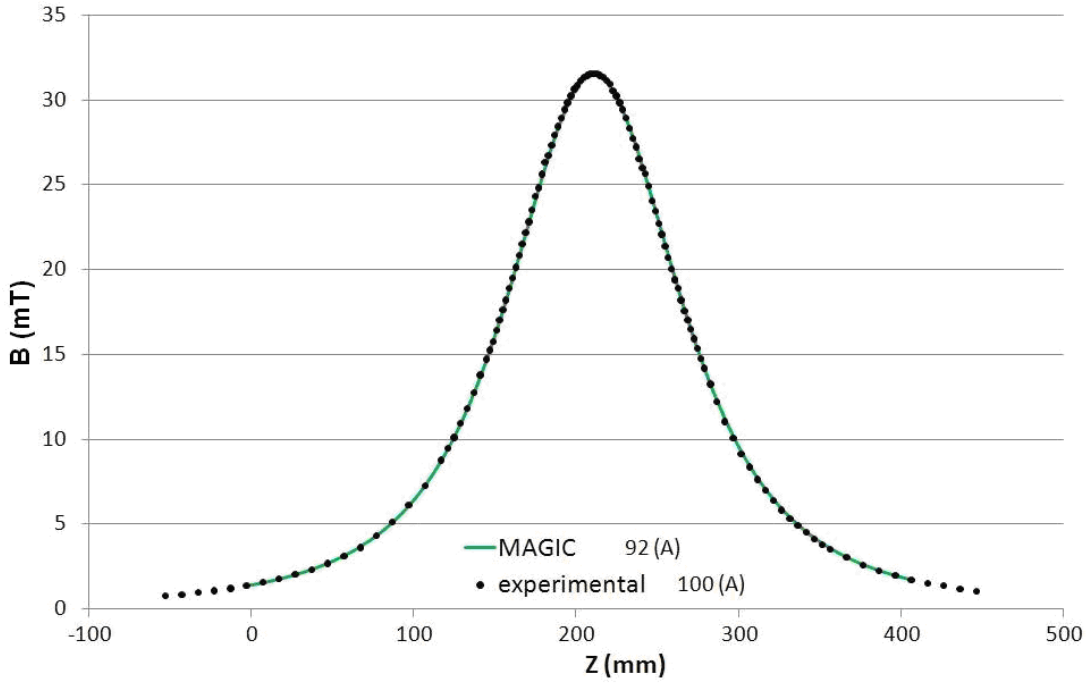

Fig. 4-8: Comparison of the simulated *B*-field of the reverse coil with the measured *B*-field.

The cavity coil is designed to have 14 layers with 103 turns of copper wire per layer. Two shim coils (2 layers of 15 wire turns) are wound at the left and right edges of the main coil to maintain the flat-top region over the boundary of the HCIW. The main cavity coil was tested using an axial Hall probe with the measured results compared with simulated data. A plot of the magnetic field varying with axial position is shown in Fig. 4-9 for a current magnitude of 92 A. The measured plot data is shown to agree well with the simulated data for a current of 100 A. The discrepancy in current values may result from inaccurate readings from the power supply. The gradient of the measured *B*-field profile away from the flat-top region is shown to be greater than the simulated prediction. This suggests that the extra coil layers wound at the left and right edges of the cavity solenoid are less effective at maintaining the axial magnetic field than numerically suggested.

An investigation of the magnetic field variation with changing current was also performed with the Hall probe position fixed in the flat-top region of the *B*-field profile. The result of current variation on the magnetic field magnitude is shown in Fig. 4-10. The magnetic field is shown to linearly increase with increasing current which is predicted from equation (4-7).

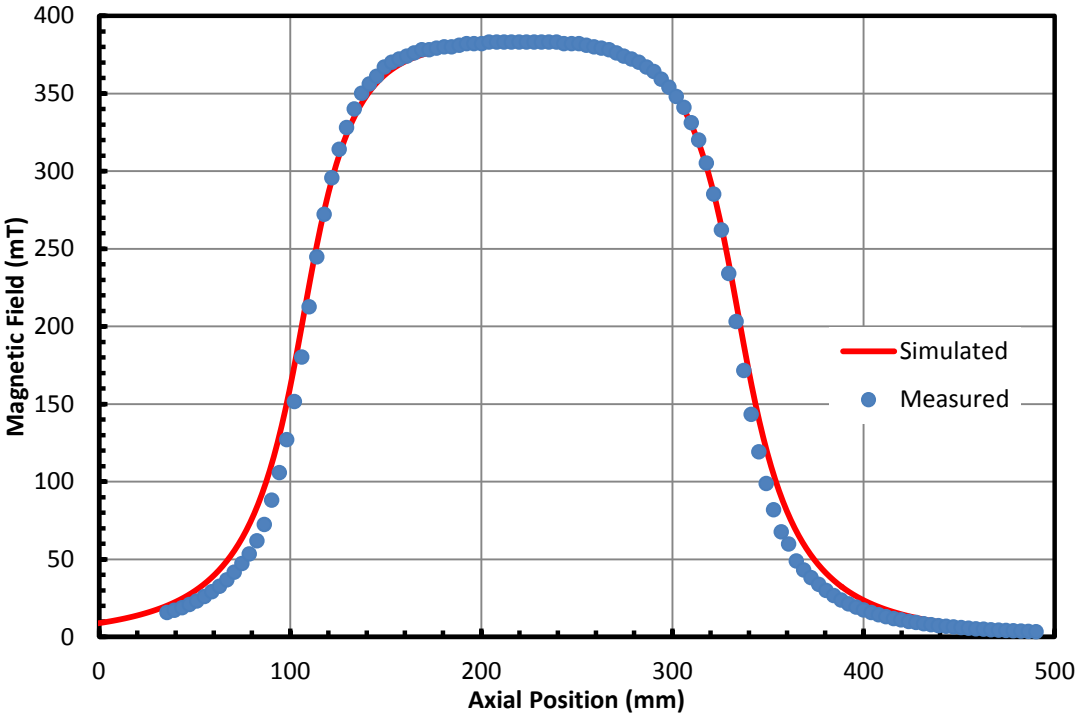

Fig. 4-9: Variation of magnetic field at the bore centre with changing z-position.

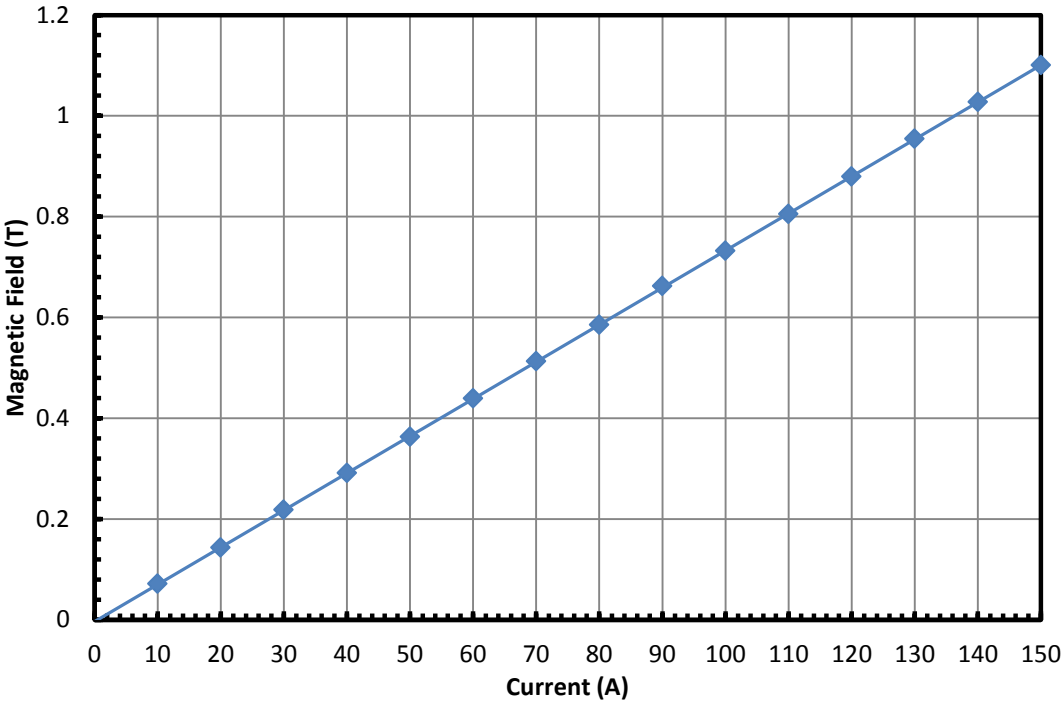

Fig. 4-10: Magnetic field variation with changing current in the *B*-field flat-top region.

4.4. Gyro-TWA Waveguide Component VNA Testing

The W-band rectangular-to-circular input coupler transmission and reflection characteristics were measured using a Vector Network Analyser (VNA) with the results presented in Section 3.4. The input coupler testing results showed that high transmission (~ -1 dB) was achieved for TE_{10}^{R} – TE_{11}^{C} mode coupling. However, the experimental setup of the gyro-TWA has additional passive waveguide components included throughout the cavity which determine the achievable coupled wave power from the incident wave at the input coupler to the interaction circuit and on to the output window interface. The incident wave is transmitted through a pillbox window, the input coupler (Section 3), a circular polariser, the helically corrugated interaction waveguide (HCIW) and a circular waveguide taper before the wave interacts with the output window of the amplifier. Therefore, the total scattering characteristics of the waveguide components should be investigated before the components are added to the gyro-TWA experimental setup.

The experimental setup of the gyro-TWA waveguide component VNA testing is shown in Fig. 4-11. Fig. 4-11(c) highlights the difference in propagation length for an incident wave travelling through an individual input coupler and an incident wave travelling through the passive input and interaction waveguide components of a gyro-TWA (Fig. 4-11(a) and (b)). Hence, an increase in waveguide loss through the gyro-TWA setup is expected. The VNA was calibrated with an Offset Short calibration technique (Section 3.4.3). The experimental components consist of a pillbox window, the rectangular-to-circular input coupler designed in Section 3.4, a circular polariser [4.5] at the input and output of the HCIW (contained within the stainless steel sheath in Fig. 4-11), a linear circular waveguide and a circular-to-rectangular waveguide taper to convert the circular TE_{11} mode to the fundamental rectangular mode. The transmission and reflection measurements of the passive waveguide components are shown in Fig. 4-12 and Fig. 4-13 respectively.

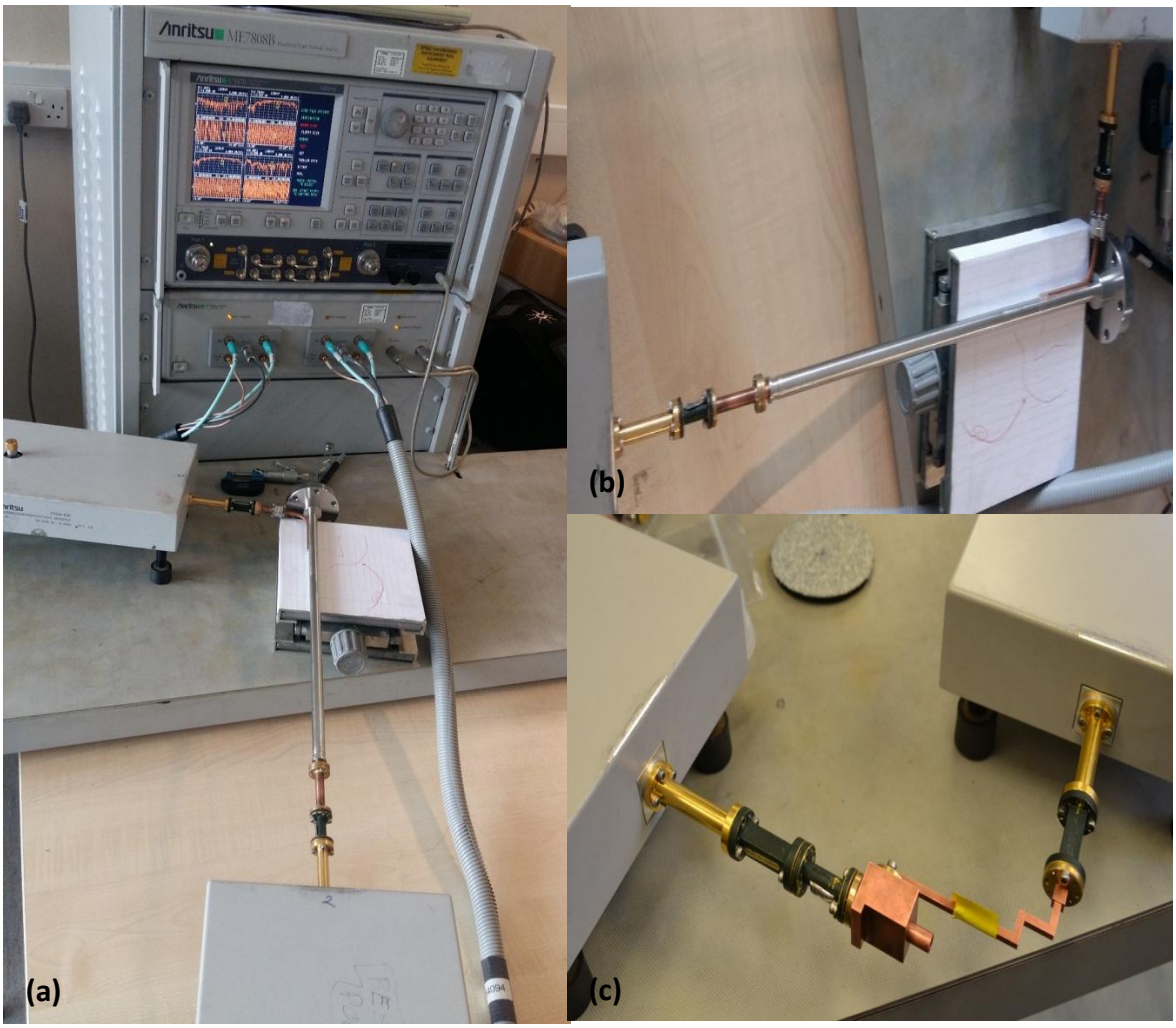

Fig. 4-11: VNA experimental setup for testing of gyro-TWA passive waveguide components shown in (a) and (b). The experimental setup of the rectangular-to-circular input coupler is shown in (c).

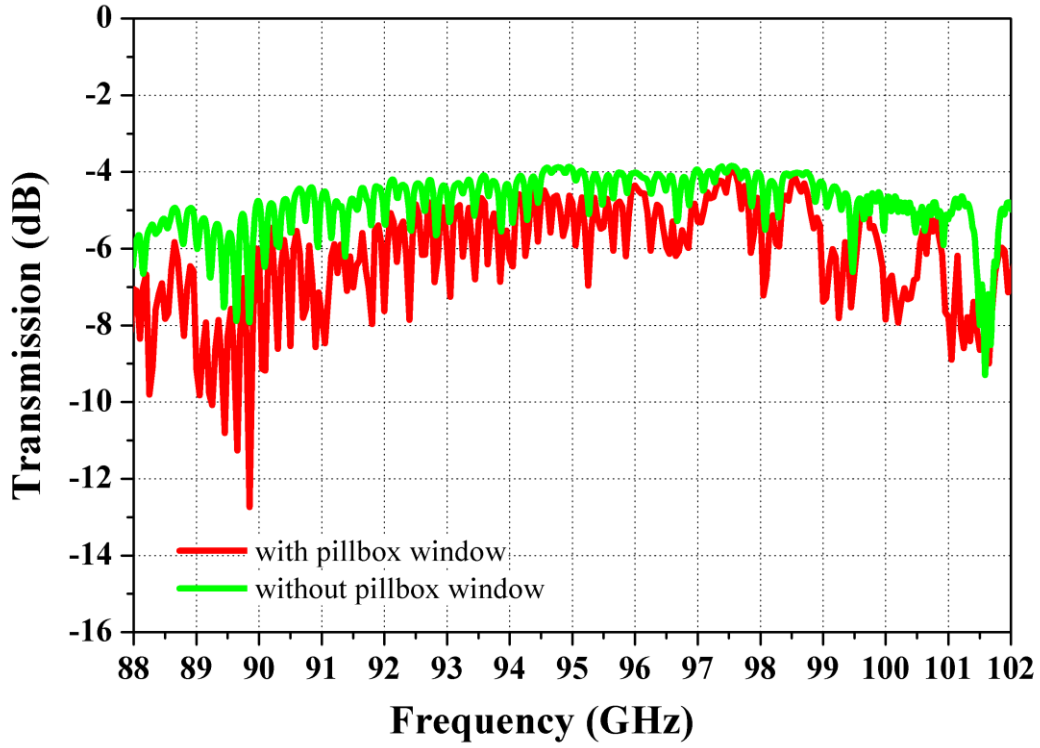

Fig. 4-12: Transmission measurement of passive waveguide gyro-TWA components using a VNA.

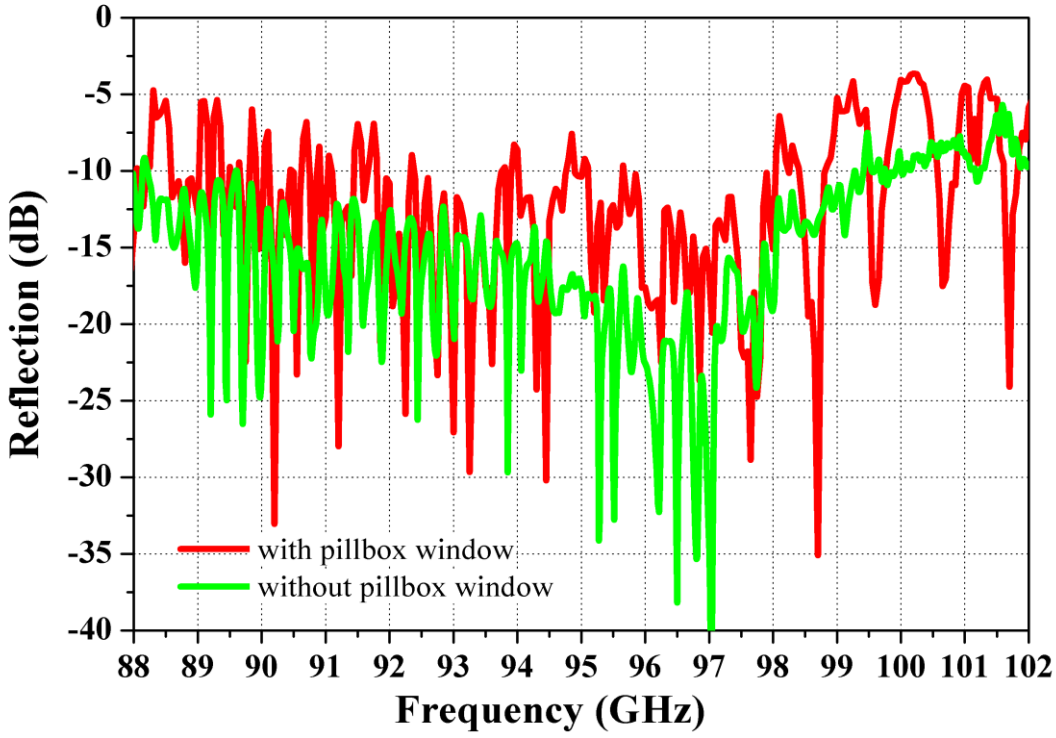

Fig. 4-13: Reflection measurement from passive waveguide gyro-TWA components using a VNA.

Fig. 4-12 shows that, with the pillbox window enclosing the input coupler, the average transmission is ~ -5.5 dB. The individual components included in the gyro-TWA setup were tested explicitly. The smooth rectangular waveguide which feeds the pillbox window has an insertion loss of -0.2 dB with the pillbox window exhibiting an insertion loss of -0.6 dB. The input coupler, as discussed in Section 3.4, has a transmission loss of -1.0 dB. The input polarizer and the output polarizer have transmission losses of -0.6 dB and -0.9 dB respectively. The helical waveguide has a -1 dB loss and the linear circular waveguide exhibited a -0.6 dB loss. The rectangular to circular convertor used in the VNA experimental setup has a measured insertion loss of -0.3 dB. Therefore, the VNA testing results suggest that minimal loss occurs at the adjoining waveguide interfaces and hence, the waveguide components are accurately aligned. For the gyro-TWA experiment conducted under vacuum, only the insertion losses exhibited from the pillbox window, input coupler, one polarizer, the HCIW and linear waveguide should be considered. Therefore, the measured transmission loss for the gyro-TWA components is ~ 3.8 dB.

The reflections at the pillbox window port of the gyro-TWA experimental setup are shown in Fig. 4-13. The average reflection is ~ -8 dB at 90 – 100 GHz. On the gyro-TWA experiment, the pillbox window port accepts incident radiation from the solid-state amplifier which, in turn, is transmitted into the cavity. High reflections at the pillbox window can result in power overloading of individual components in the amplifier; however, a return of -8 dB from the input port will not result in amplifier component damage when a broadband isolator is used. Therefore, the passive gyro-TWA component scattering characteristics allow for implementation on the 94 GHz gyro-TWA vacuum system.

4.5. Profiled Horn Measurement

The 94 GHz gyro-TWA utilizes an axially propagating output system to transmit the amplified radiation into free space. The propagation of the cavity radiation in the TE_{11}^{C} mode through a microwave window would result in high losses at the window-air boundary and a non-directional propagation of the wave-beam into free space. Therefore, a quasi-optical profiled horn [4.6] was designed to improve wave-beam directivity and reduce loss at the output window. The profiled horn couples the TE_{11} and TE_{1n} mode components from the

HCIW into a HE_{11} mode, which has a high power density at the centre of the field pattern, before propagating the wave-beam towards the output window. The high power density at the centre of the HE_{11} *E*-field pattern reduces the losses at the waveguide boundary. A schematic of the horn axial profile is shown in Fig. 4-14.

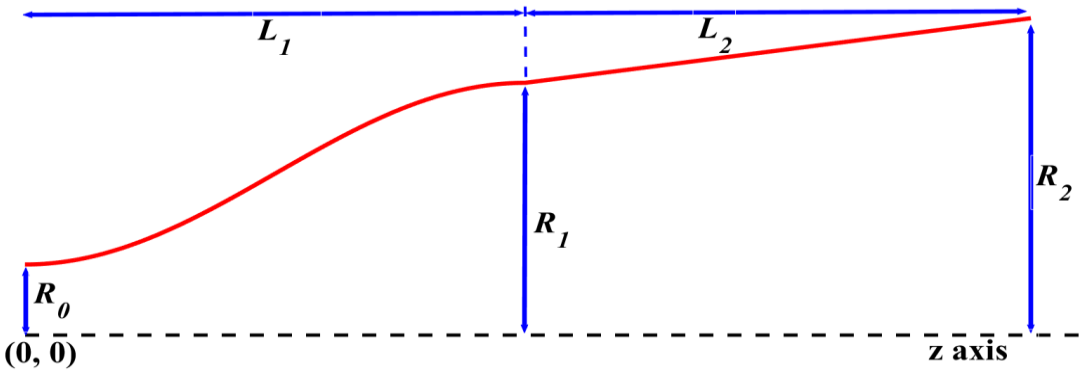

Fig. 4-14: Schematic of the profiled horn.

The manufacture of the profiled horn was undertaken in two separate waveguide components. The profiled section of the horn of length L_1 was machined using a precise Computer Numerical Control (CNC) machine to shape a copper rod into the desired shape. The tapered section of the profiled horn (L_2) was machined using a wire cutting method to create the linearly tapered profile. The two horn sections, alongside the vacuum flanges attached to allow for connection to the experimental setup, were brazed together to be a single solid piece. The final assembled horn together with a rectangular-to-circular converter and a waveguide taper used for microwave profiling of the horn using a VNA is shown in Fig. 4-15.

A measurement of the reflection of the profiled horn with an attached 3-layer microwave window (Section 2.6) was made using a VNA. An Offset Short calibration (Section 3.4.3) of the two VNA ports was undertaken; however, the reflection measurement requires the use of one VNA port only. The VNA port is connected to the profiled horn through a rectangular-to-circular taper followed by a circular waveguide up-taper which increases the aperture radius from 2.50 mm to the horn input radius of 5.6 mm. The transmitted radiation through the multi-layer window is propagated into a microwave absorbent material to

minimise background reflections. Fig. 4-16 shows the VNA reflection results from the profiled horn compared with simulated reflection data.

Fig. 4-16 shows that the reflection from the corrugated horn and microwave window is less than -35 dB over the 90 – 100 GHz operating region of the gyro-TWA. The measured reflectivity suffers from background noise interference which results in an increase in S_{11} measurement compared with simulated data. Low reflection levels from the output system are important because significant microwave feedback into the interaction region may result in the cavity oscillating as opposed to amplifying incident radiation. Hence, the corrugated horn and multilayer window are effective at maximising microwave transmission into free-space and minimising cavity reflections.

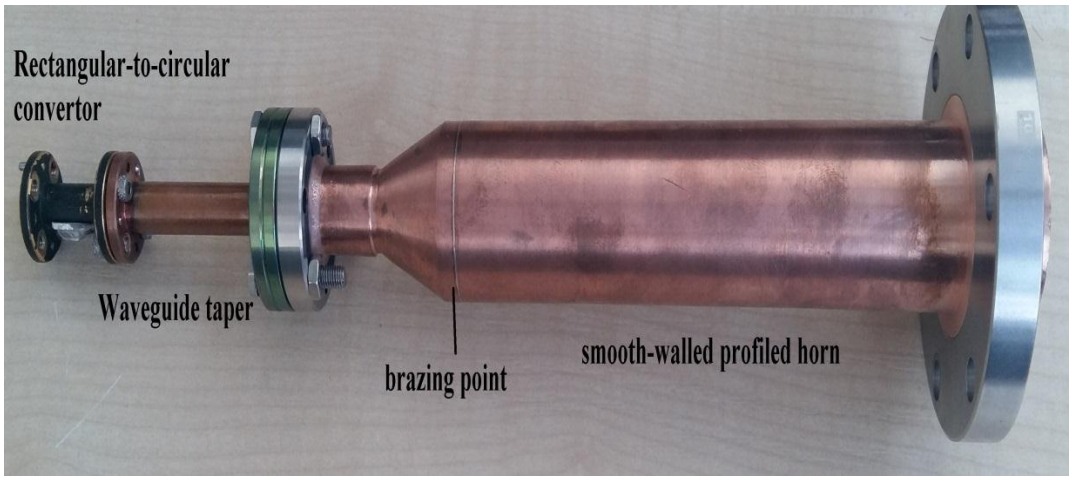

Fig. 4-15: Profiled horn and multilayer window attached to VNA for reflectivity measurement.

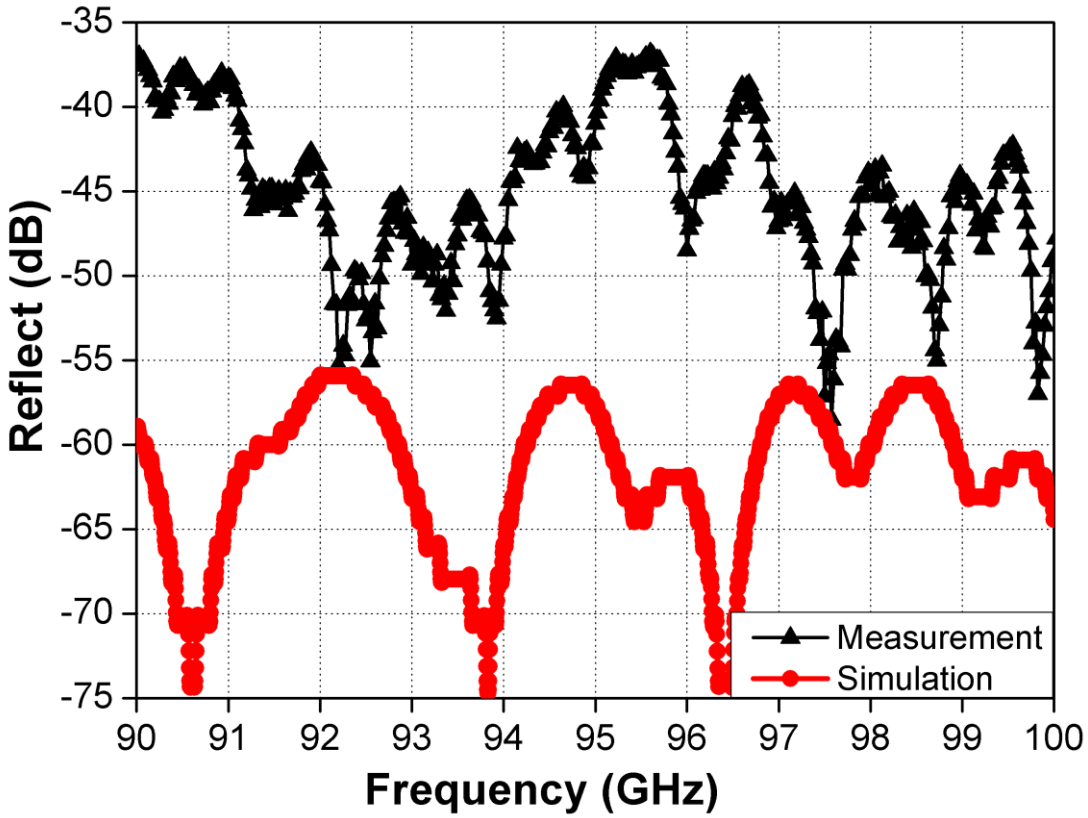

Fig. 4-16: Comparison of reflection data for a profiled horn with multilayer window.

4.6. Electron Beam Measurement

A measurement of the beam voltage and beam current with the input coupler and Bragg reflector included in the gyro-TWA setup was made to characterise the performance of the cusp electron gun and, hence, the power delivered to the interaction cavity. The electron beam voltage provided by the Blumlein PFL (Section 4.2.1) was measured using a digital storage oscilloscope. The magnitude of the voltage pulse was reduced using a voltage divider (Section 4.2.3) and an attenuator to ensure the safe detection of the pulse characteristics on the oscilloscope. The electron beam current was measured at the gun diode and at the cavity output using a Rogowski coil [4.7] and a Faraday cup, respectively. Current measurement at two positions within the vacuum cavity allows for any electron interception within the tube to be determined. A Rogowski coil is constructed with a toroidal coil of wire with N turns per unit length wound around a non-magnetic former with cross-section πR_R^2 where R_R is the torus radius. The turn density of a Rogowski coil is much less

than the solenoid magnets discussed in Section 4.3. The use of a non-magnetic former ensures that the coil measurements remain linear for high current operation allowing for low current calibration of the Rogowski coil. The input and output terminals of a Rogowski coil are located at the same point meaning the wire structure is flexible and prevents any disturbance of the conductor sample. If an alternating (AC) or pulsed current is propagated through the centre of the torus, a magnetic field is generated. An interaction between the magnetic field and the coil element local to the magnetic field results in the induction of a voltage pulse within the coil wire. The magnitude of the voltage pulse is directly proportional to the rate of change of the encircled current (I). The voltage produced by a Rogowski coil (V_R) is defined by

$$V_R = -\pi {r_R}^2 \frac{N}{l_R} \mu_0 \frac{\partial I}{\partial t} \tag{4-8}$$

where r_R is the radius of an individual wire loop, l_R is the total winding length ($2\pi R_R$) and $\partial I/\partial t$ is the rate of change of the conductor current. Therefore, from equation (4-8), the measured voltage pulse from a Rogowski coil can be used to determine the current from a pulsed electron beam if the design parameters (N, l_R and R_R) of the coil are known. The downstream current measurement was made using a Faraday cup, which is a metal basin with a diameter of 4.0 mm, inserted into the path of the electron beam. The electron beam diameter is estimated to be 0.8 mm; therefore, the Faraday cup is sufficiently large to collect all propagating electrons. The impacting electrical current is directly converted to a voltage signal which, in turn, is passed through a limiting resistor. The beam voltage and current is shown in Fig. 4-17.

The accelerating voltage of the electron beam was measured to be ~ 60 kV over a 400 ns pulse, as shown in Fig. 4-17. The accelerating voltage varies ~ ± 5% from the average value over the duration of the pulse. The rise time of the pulse is ~ 40 ns. The accelerating pulse duration is 400 ns; however, the gyro-TWA is designed to operate CW and therefore

the components are designed to handle high average power. The electron beam current is shown to average at ~ 1.5 A with a variation of ~ ± 3%. The comparison of the beam voltage and current pulses shown in Fig. 4-17 highlights the identical temporal characteristics of the measured pulses when a charging voltage from the PFL is applied to the cavity diode. The inclusion of a Bragg reflector in the input coupler, instead of the inclusion of a step-down waveguide reflector, has ensured that the beam transport is largely unhindered.

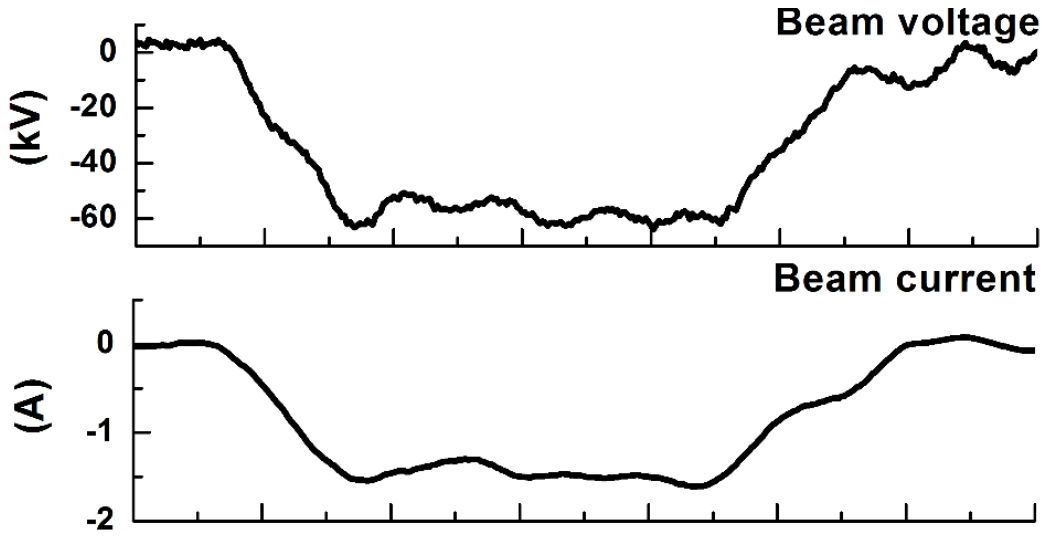

Fig. 4-17: Measurement of accelerating beam voltage and beam current.

4.7. Microwave Measurement

The experimental setup of the W-band gyro-TWA is shown in figure 4.18 (a) two solenoid coils were used to generate the CUSP magnetic field as well as the main cavity magnetic field of 1.82T that supported the cyclotron motion of the electrons, (b) the large shielded rectangular box containing the solid state source (fig 4.19) used to generates the W-band radiation to be amplified and (c) the microwave detector boxes.

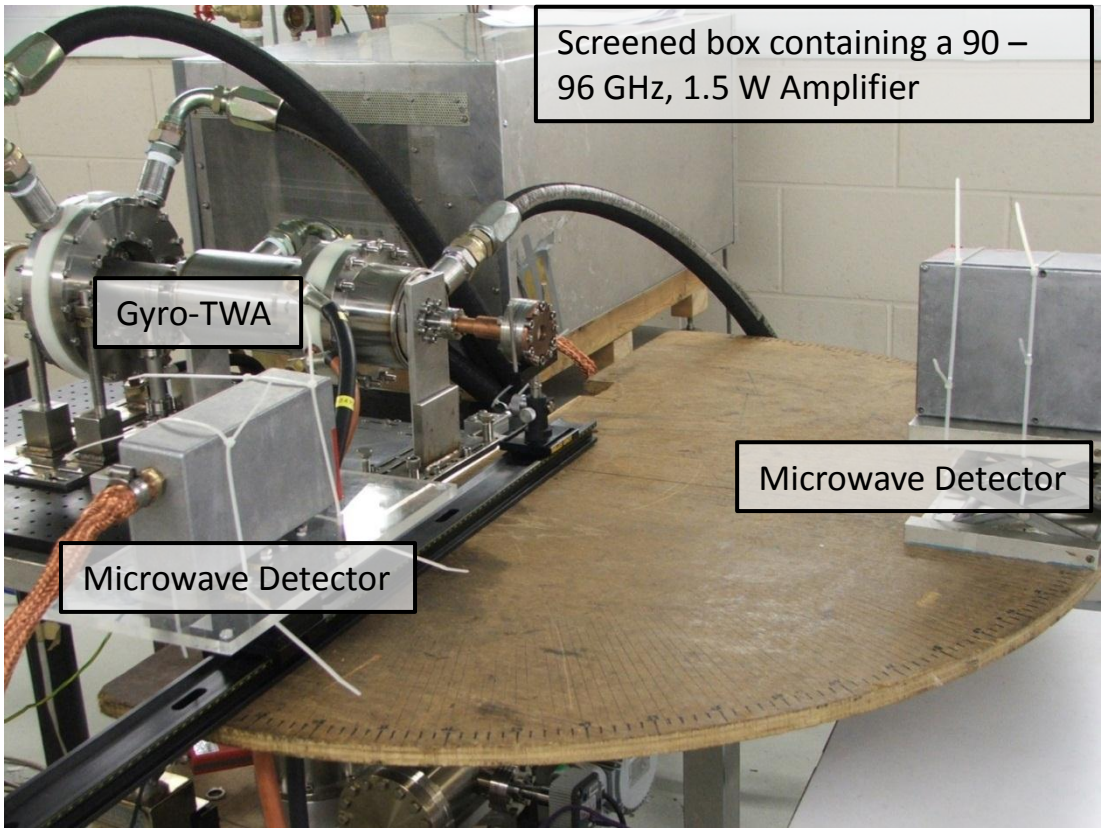

Fig. 4-18: Experimental setup of gyro-device for gyro-TWA microwave detection.

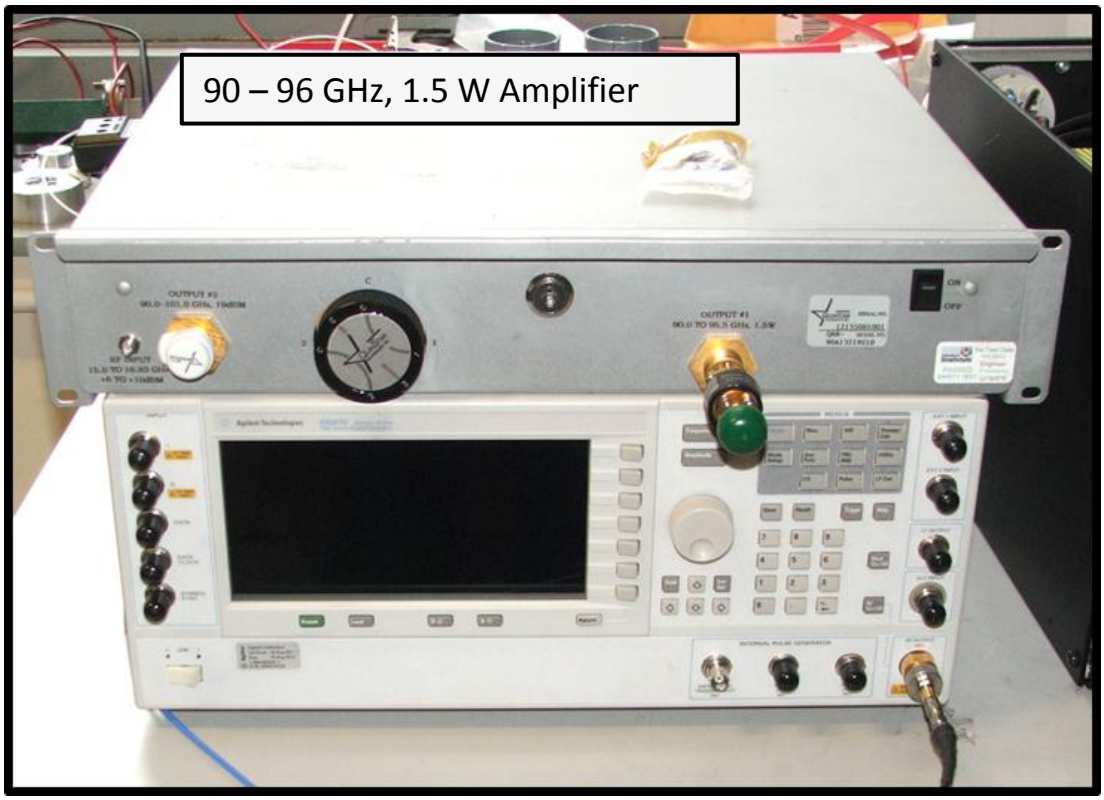

Fig. 4-19: 1.5W W-band Solid state source driven by a Vector Signal Generator.

The input millimeter-wave signal was from a tuneable solid-state source with a maximum output power of 1.5 W in the 90-96.5 GHz frequency range (Quinstar QAR-90A12319Z10) Fig. 4-19. The output power level of the source can be programmed from 0 to its maximum value of 1.5 W and was calibrated using a W-band power meter. The output frequency of the source was calibrated using an in-band fundamental mixer (Millitech MXP-10-R). Its local oscillator signal was produced by a Gunn diode (Millitech GDM-10-1013IR) at 94.9 GHz. The resultant intermediate frequency (IF) signal was directly measured by a 20 GHz, digitizing oscilloscope (Agilent DSX-X 92004A).

The amplified high power microwave pulse of the gyro-TWA radiated out through the multiple-layer window was measured by a crystal detector located in a shielded metal box and positioned 80 cm away from the millimeter-wave window. A standard gain W-band pyramidal horn and a calibrated variable 0 to 90 dB rotary vane attenuator were used before the detector so that the millimeter radiation before and after amplification could be measured. To find the amplification regime of the gyro-TWA, the magnitudes of the

magnetic fields at the cavity and cathode were systematically scanned. The amplifier was found to be 'zero-drive' stable when the electron beam had an α of ~1 and the cavity magnetic field was ~1.82 T. Typical time-correlated traces of the beam voltage, beam current and the amplified millimeter-wave signal were recorded and are shown in Fig.4.20.

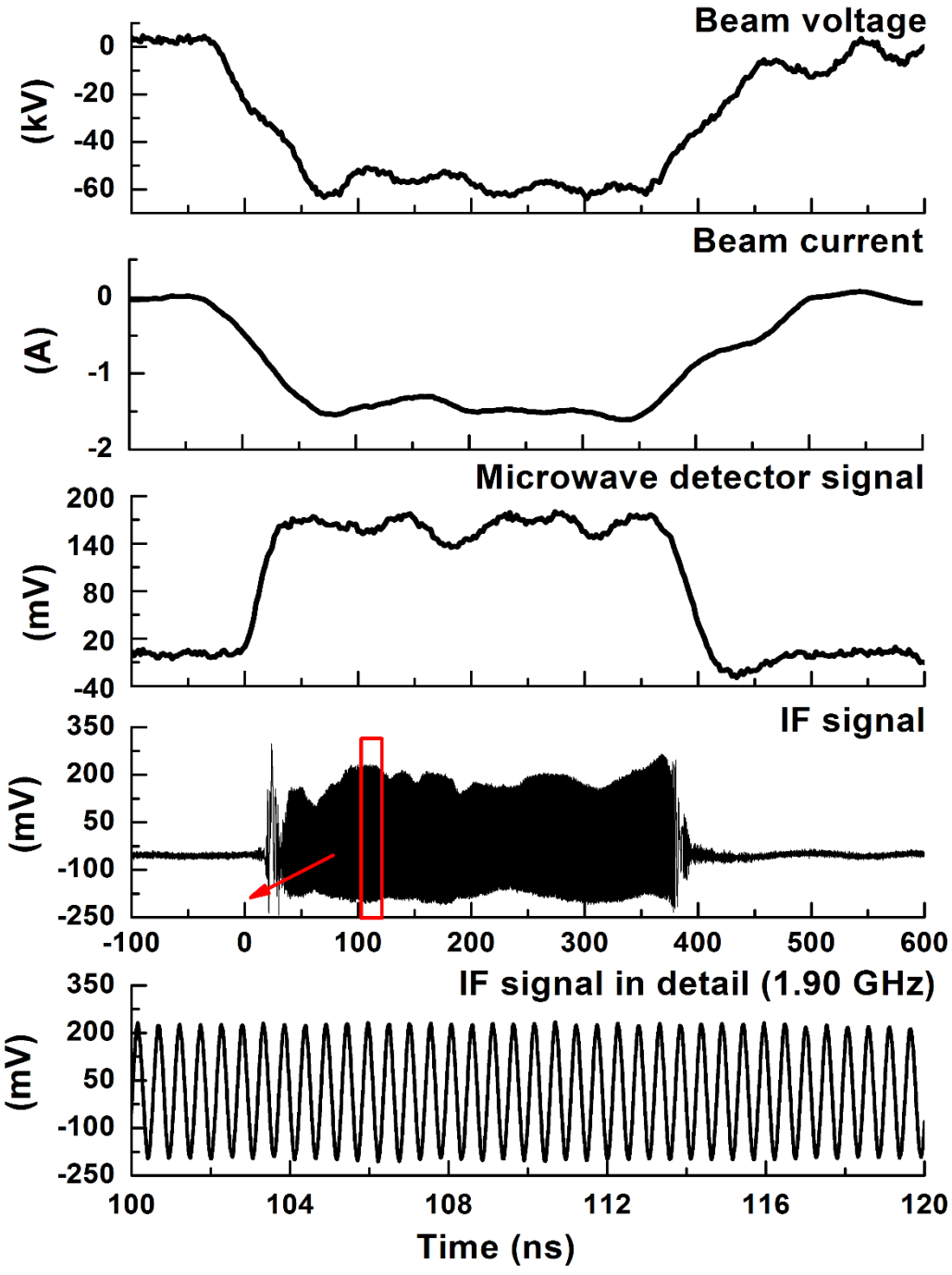

Fig. 4-20: Measured time-correlated beam voltage, current, millimeter-wave signal and the IF signal from mixer.

The output frequency of the gyro-TWA was also measured by the heterodyne mixing method. When the input frequency was set at 93 GHz, the mixer signal was recorded by the oscilloscope and is also shown in Fig. 4.20. The spectral analysis showed a clear peak IF amplitude at 1.9 GHz which proved the amplification of the input signal.

The responses of the crystal detector at different input power levels and different separation from the output window of the gyro-TWA were carefully calibrated. From the detector output in the “cold” and “hot” (without and with electron beam amplification) experimental conditions, the gain and the output power of the gyro-TWA at vaious input signal levels were measured. The transmission loss of the complete system was carefully measured by Dr Donaldson, Dr Zhang and Dr He using a VNA to be ~6 dB which meant the maximum "cold" power without amplification was ~0.52 W. Fig. 4.21 shows the measured gain and output power at 93 GHz as a function of input power. The gain was measured to be ~40 - 43 dB when the "cold" signal was in the range of 0.02 - 0.15 W. With the increase of the power of the seed signal, the gain reduced slightly. Fig. 4.21 shows that the amplifier had not reached saturation; however, the maximum output power is limited by the input power. The output power and amplification of the gyro-TWA as a function of input power at 93 GHz using beam parameters consistent with the experiment were simulated by Dr He using the PiC code MAGIC. A right-hand, annular, axis-encircling electron beam with a thickness of 0.1 mm and α of 1 was used to interact with a circularly polarized wave in the simulation. The simulated output power and gain were in excellent agreement with the measured results as the input power ranged from 0.01 -0.52 W. An α velocity spread of ~10% is assumed. The results of the simulation are also shown in Fig. 4.21. The saturated output power of 10 kW could be realized with a more powerful input source.

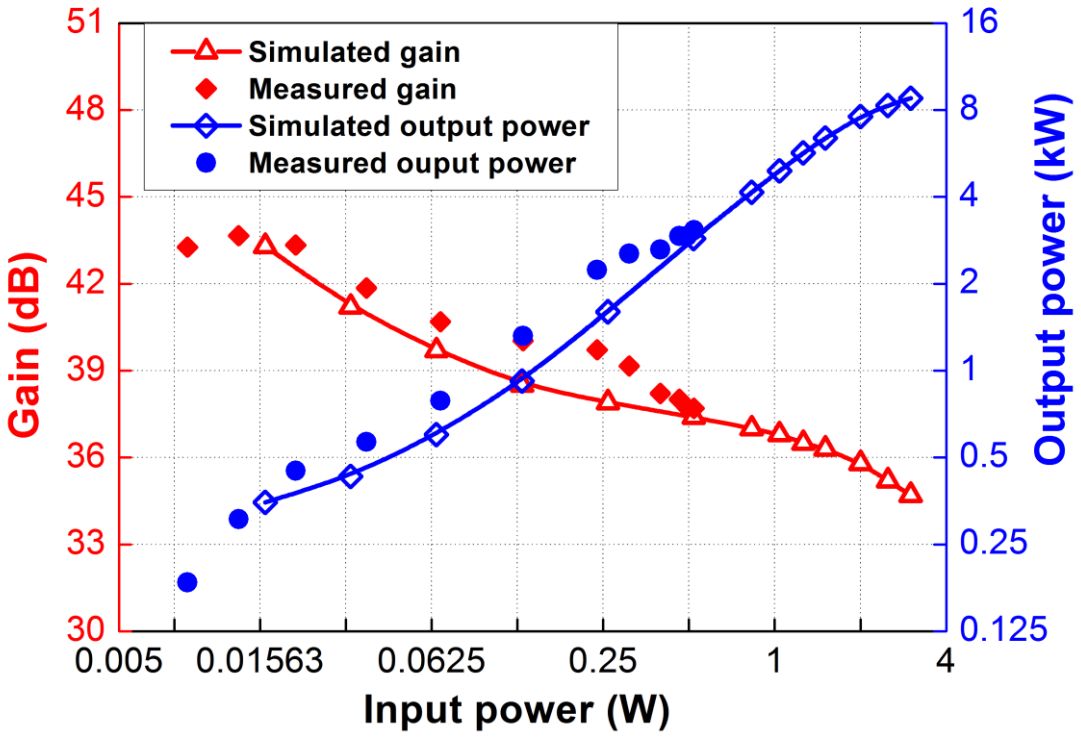

Fig. 4-21: The measured and simulated gain and output power at different input power levels at 93 GHz.

The "cold" power transmitted through the amplifier was measured as a function of the frequency and is shown in Fig. 4-22. The power of the “cold” signal was negligible when the frequency was above 96.5 GHz. The bandwidth of the gyro-TWA at the maximum available input power was also measured and the result is shown in Fig. 4-22. The peak output power of about 3.4 kW was measured at 94 GHz. However, it was not possible to determine the gain of the gyro-TWA above 96.5 GHz in the same conditions due to the input source being unable to generate significant millimeter-wave radiation at frequencies > 96.5 GHz. The simulated gain bandwidth (assuming an α spread of 10%) were found to be in good agreement with the measured results.

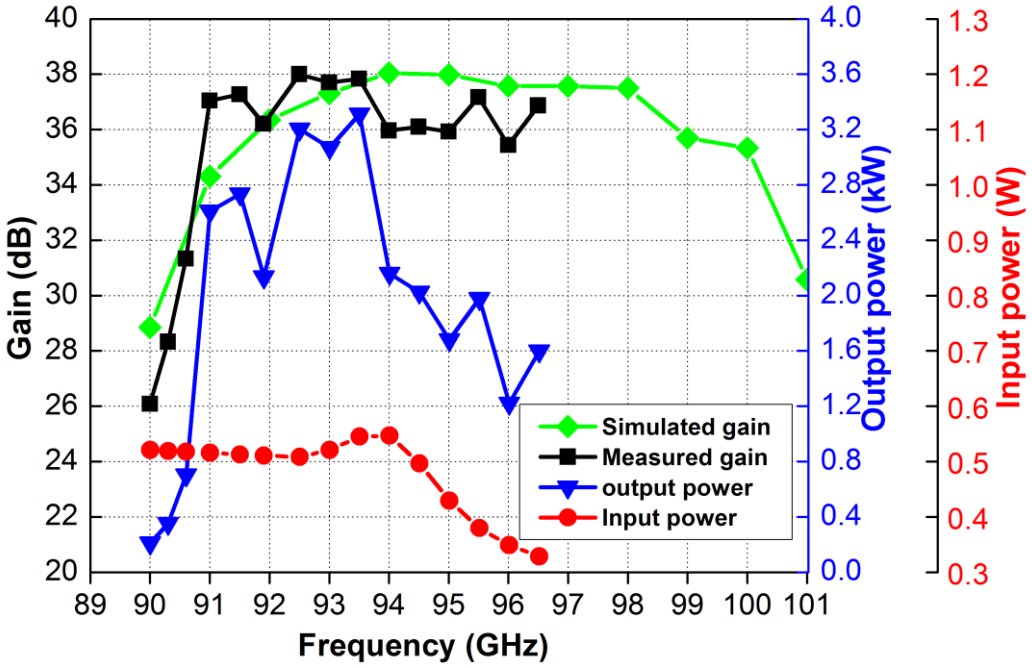

Fig. 4-22: The gain and output power at different frequencies**.**

The far-field radiation pattern of the output millimeter-waves generated by the gyro-TWA was measured to verify the Gaussian mode content. The simulated and measured results of the radial E-field component in the E-plane at 95 GHz are shown in Fig. 4-23. The simulation was carried out using CST Microwave Studio. Taking into account a 2° systematic error in the radial angle, the simulation and measurement results agreed well.

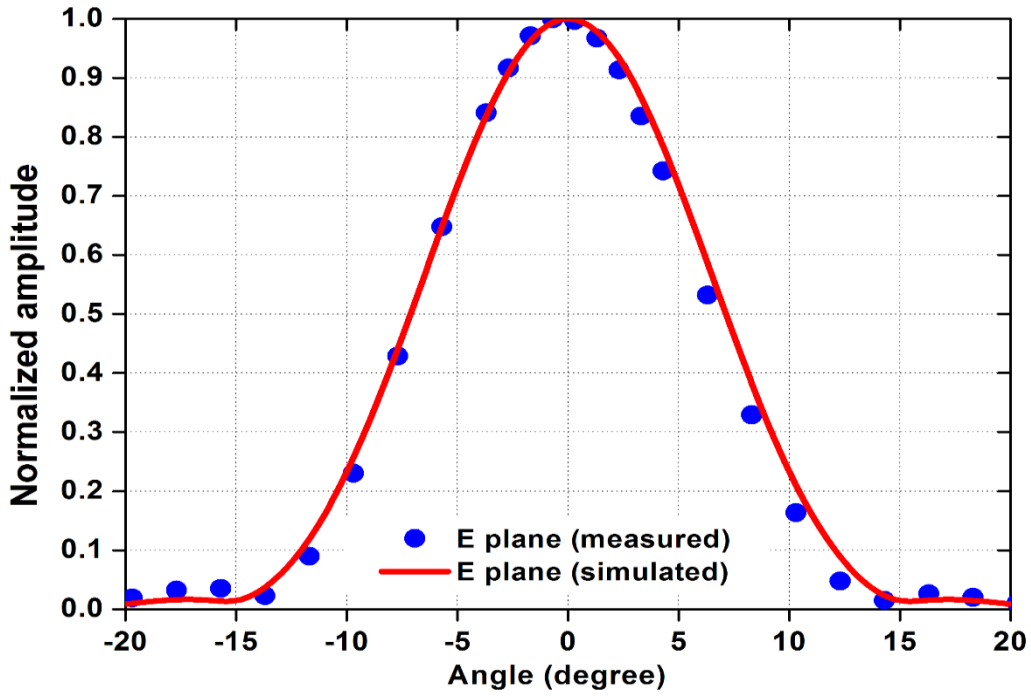

Fig 4.23 The far-field measurement of the gyro-TWA.

4.8. Discussion of Experimental Investigation

In the W-band gyro-TWA experiment, stable amplification over the frequency range of 91 – 96.5 GHz was achieved from an electron beam of 55 kV and 1.5 A. The maximum gain was measured to be 38 dB at 94 GHz with an input power of 0.52 W. Therefore, the maximum output power was determined to be 3.4 kW. The performance at higher input power levels and frequencies above 96.5 GHz were not measured due to limitations of the input drive source. The results were in good agreement with a simulated maximum output power of 10 kW and bandwidth of 91-100 GHz. Therefore the simulation code has shown that it could accurately predict the output power for gyro-devices based on HCIWs operating in W-band.

The inclusion of the Bragg reflector in the input coupler design has allowed for high electron beam transmission into the interaction cavity. A step-down waveguide reflector would have intercepted electrons as the particle beam traversed the input coupler region of the gyro-TWA. The beam current was measured to be 1.5 A at the exit from the HCIW for a 55 kV accelerating voltage. Therefore, the inclusion of the Bragg reflector in the input

coupler design has enabled efficient (4.4%) beam-wave interaction to be achieved within the gyro-TWA.

5. 372 GHz Fundamental Mode Input Coupler Design

5.1. Introduction

The progression of gyro-device research at the University of Strathclyde has led to the proposed design and manufacture of a high power, high frequency gyro-TWA operating with a centre frequency of 372 GHz. The broadband amplifier has potential applications in biological imaging with the implementation of the vacuum tube in a DNP-NMR spectroscopy system, discussed in Section 1.2. The variable frequency, high power signal can be used to obtain high resolution information from a thin substrate without damaging the structural integrity of the sample. The target parameters for the gyro-amplifier are shown in Table V-I.

Table V-I: Target gyro-TWA performance parameters.

Frequency (GHz)	360 - 384
Output Power (W)	200
Gain (dB)	~ 40
Beam Voltage (kV)	30
Beam Current (A)	0.5

The proposed design includes a broadband three-fold HCIW utilised as the interaction circuit, requiring an incident TE_{11} mode to be coupled into the HCIW. Efficient coupling of the required cavity mode into the gyro-TWA interaction circuit is important to the overall performance of the gyro-TWA. At frequencies approaching the THz region, the coupling process encounters tremendous difficulties due to the subsequent increase in Ohmic losses caused by a reduction in the skin depth.

The theoretical and numerical design of two mm-wave couplers, to be implemented on a gyro-TWA with a 3-fold HCIW, is presented. A TE_{10}^{R} – TE_{11}^{C} T-junction waveguide coupler, designed upon the principles outlined in Chapter 3, is modelled in Section 5.2 alongside a novel fundamental mode multiple-hole input coupler in Section 5.3. For high frequency operation, it is important that any discrepancy between the designed parameter

value and the machined parameter value is considered, ensuring that the coupler remains operable when manufacturing tolerances are included within the design. The effect of parameter discrepancies on Bragg reflector and waveguide coupler performance was shown in Chapter 3 for a W-band structure; hence, at higher frequencies the effect of the machining tolerances on coupler performance will be greater. Therefore, a detailed study on the effect of tolerances on the T-junction waveguide coupler and the multiple-hole coupler will be included in Sections 5.2.2 and 5.3.3 respectively. A discussion on the manufacturability and the potential advantages and limitations of each coupler topology is included in Section 5.4.

5.2. 372 GHz T-Junction Input Coupler with Bragg Reflector

The development of a T-junction coupler for a 372 GHz gyro-TWA is based upon the design process outlined in Sections 3.2 – 3.3. The optimised T-junction parameters and Bragg reflector dimensions are included in Table V-II and Table V-III respectively. The cavity radius (R) is determined by the mean radius (R_0) of the HCIW with a and b optimised to minimise reflections in a 3-port T-junction configuration. The Bragg reflector period (p) and radii are designed to achieve a unity reflectivity over the operating bandwidth. The waveguide reflector and the rectangular-to-circular T-junction are combined to form the TE_{10}^{R} – TE_{11}^{C} input coupler for the high frequency gyro-amplifier.

Table V-II: 372 GHz T-Junction Optimised Dimensions.

Parameter	Optimised value (mm)
R	0.35
A	0.55
B	0.50

5.2.1. Simulation

The numerical scattering parameters of an optimised TE_{10} – TE_{11} 372 GHz T-junction coupler with Bragg reflector for R = 0.35 mm was simulated and is shown in Fig. 5-1. A side view

topology of the coupler is included in the inset. The use of a Bragg reflector in the coupler geometry has proved to be an effective method of providing frequency selective feedback at low-THz frequencies whilst maximising the beam tunnel. The cusp electron gun for the high frequency gyro-TWA produces an electron beam of 0.20 mm in radius. Therefore, no unnecessary reduction in the electronic efficiency will occur as a result of electron power loss in the waveguide wall. The waveguide section length L_1 was optimised at 0.12 mm to achieve high coupling between 360 – 384 GHz with the attached waveguide reflector. Transmission loss of <1 dB was achieved over a ~10% bandwidth which includes the operational frequency range of the low-THz gyro-TWA. The Bragg reflector was effective in preventing the transmission of significant levels of radiation towards the electron gun with an S_{31} of less than -15 dB achieved over the desired bandwidth.

Table V-III: Optimised Parameter Set for 372 GHz Bragg reflector.

Parameter	Optimised value (mm)	Parameter	Optimised value (mm)
Period (*p*)	0.175	Radius 8	0.495
Radius 1	0.550	Radius 9	0.664
Radius 2	0.550	Radius 10	0.575
Radius 3	0.667	Radius 11	0.608
Radius 4	0.602	Radius 12	0.614
Radius 5	0.461	Radius 13	0.574
Radius 6	0.551	Radius 14	0.683
Radius 7	0.596	Radius 15	0.618

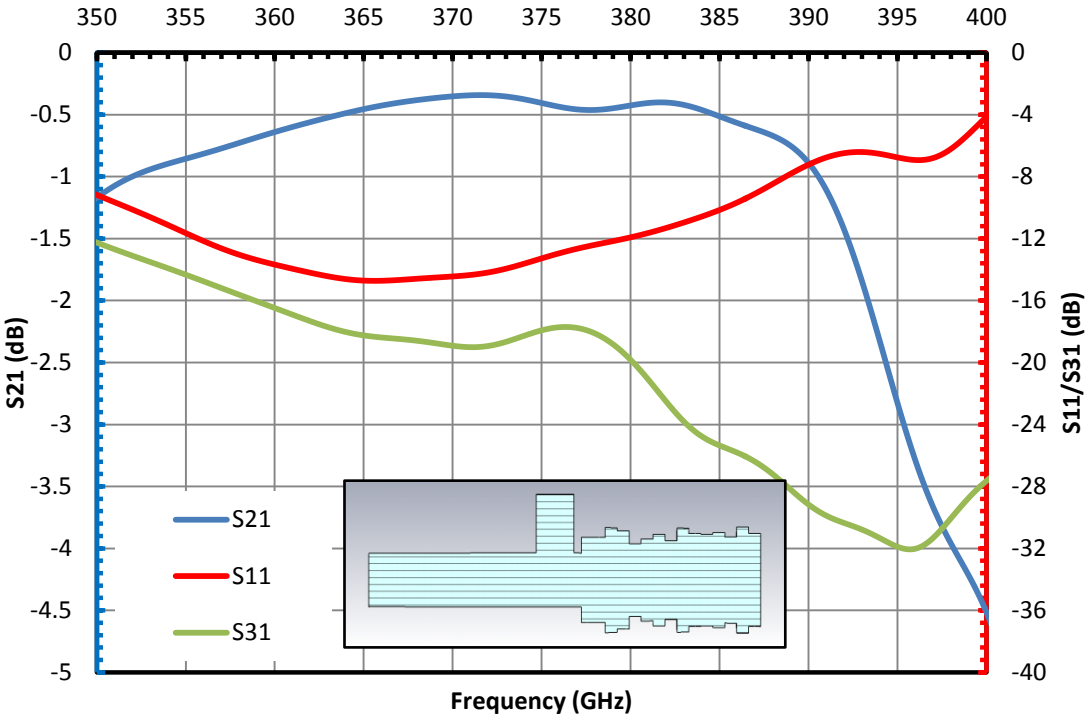

Fig. 5-1: Scattering parameters of a T-junction input coupler for a 372 GHz gyro-TWA.

The T-junction coupler topology displayed a degree of frequency tunability with variation of L_1 similar to the W-band coupler discussed in Section 3.4. The change in transmission frequencies is shown in Fig. 5-2 for variations in length L_1 for fixed values of a, b and R. The frequency shifts exhibited are a result of reflected wave phase changes from the Bragg structure caused by changes in waveguide length. An increase in L_1 is shown to lower the centre frequency of the T-junction coupler alongside reducing the coupling bandwidth. The L_1 parameter is optimised to achieve a phase shift of π at the centre of the frequency band in order to maximise the coupling coefficient over the operating bandwidth of the gyro-TWA.

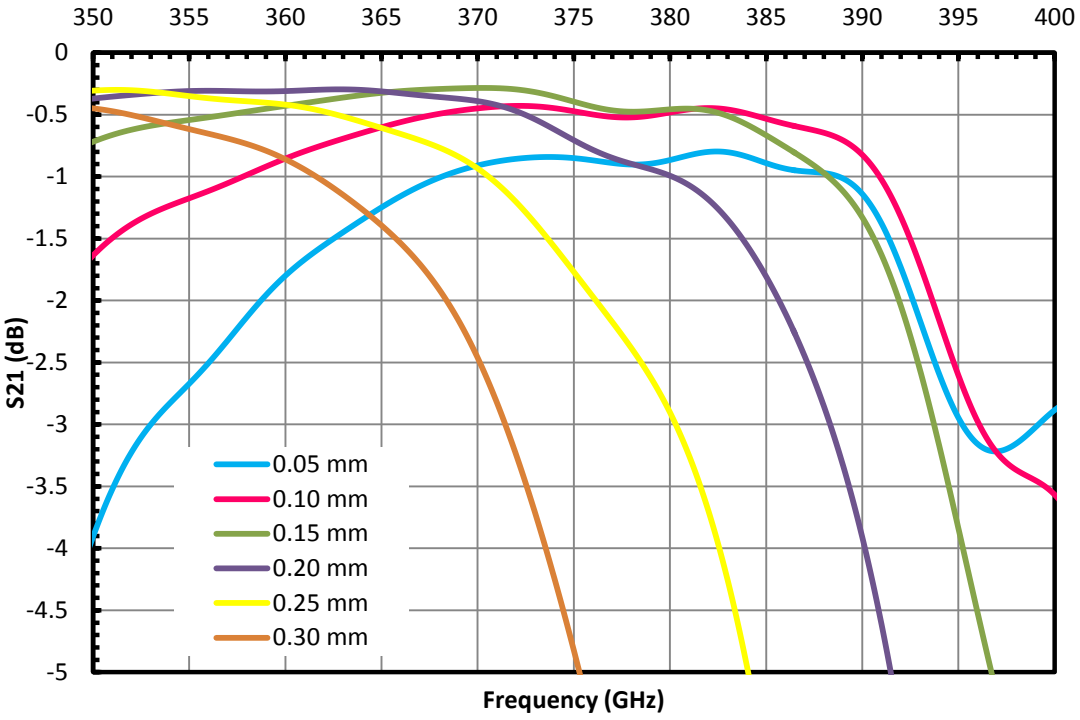

Fig. 5-2: Frequency response of T-junction input coupler with variations in *L*.

5.2.2. Tolerance Study

To test the feasibility of the input coupler, a tolerance study was undertaken. The critical parameters which dictate the frequency of operation and the coupling strength (*a*, *b* and *R*) were varied about the parameter optimum to monitor the effect of machining discrepancies on the waveguide coupler performance. A review of the effect from 10 - 20 µm changes to *R* on the input coupler transmission for fixed values of *a* and *b* is shown in Fig. 5-3. The resultant plot shows that small variations in the interaction waveguide radius will result in degradation of the total coupling achieved by the waveguide structure. The spark erosion technique, which can be used to manufacture circular waveguides of sub-mm radius, can achieve a tolerance of ± 10 µm about the optimum value. Fig. 5-3 suggests that a variation of 5 µm to *R* would ensure that high coupling to the TE_{11} mode is still achieved despite the radius discrepancy. A similar process involving waveguide width and height variations for fixed *R* was undertaken. The study highlighted that up to ± 25 µm variations of *a* about the optimum value of 0.55 mm will result in a centre frequency shift of ~ 2 GHz with minimal effect on coupling strength (Fig. 5-4). Alternatively, Fig. 5-5 shows that ± 25 µm

alterations to b will have no effect on the frequency response; however, the coupling strength is reduced by ~ 50% at the centre frequency. The CNC milling technique, used to manufacture waveguide channels, has a low limit positional accuracy of ± 1 µm. Therefore, if a modern milling machine is used in the coupler design the frequency shift caused by *a* and *b* variations will not result in the input coupler being unfit for operation at 360 – 384 GHz.

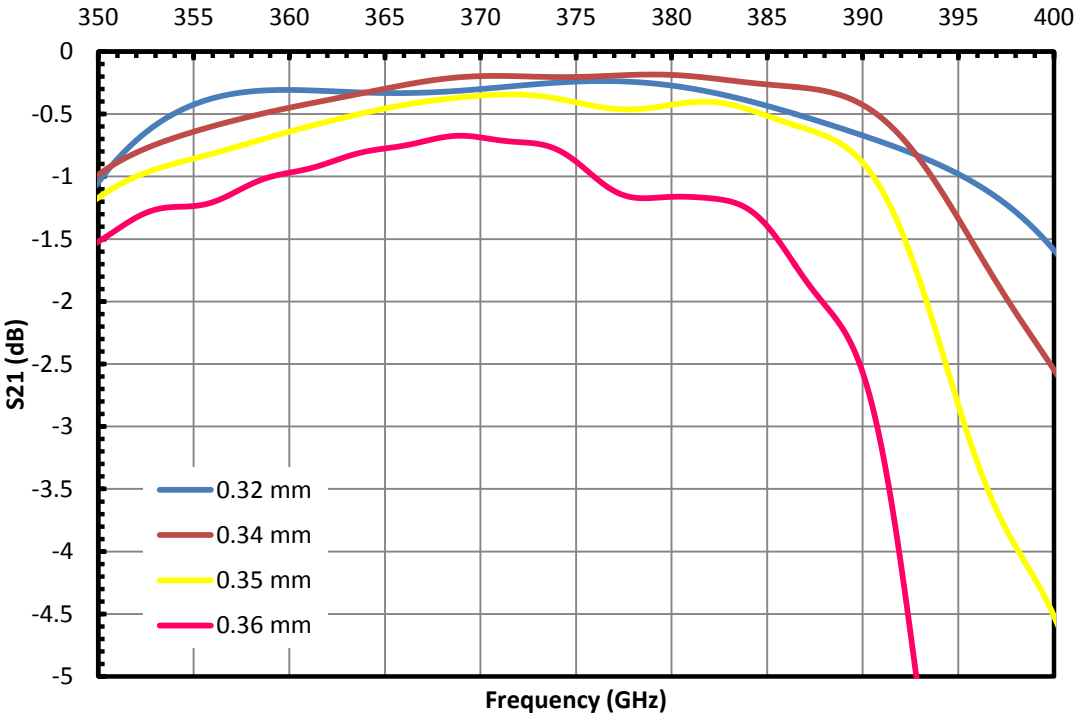

Fig. 5-3: Effect of small magnitude *R* variations on T-junction coupler transmission.

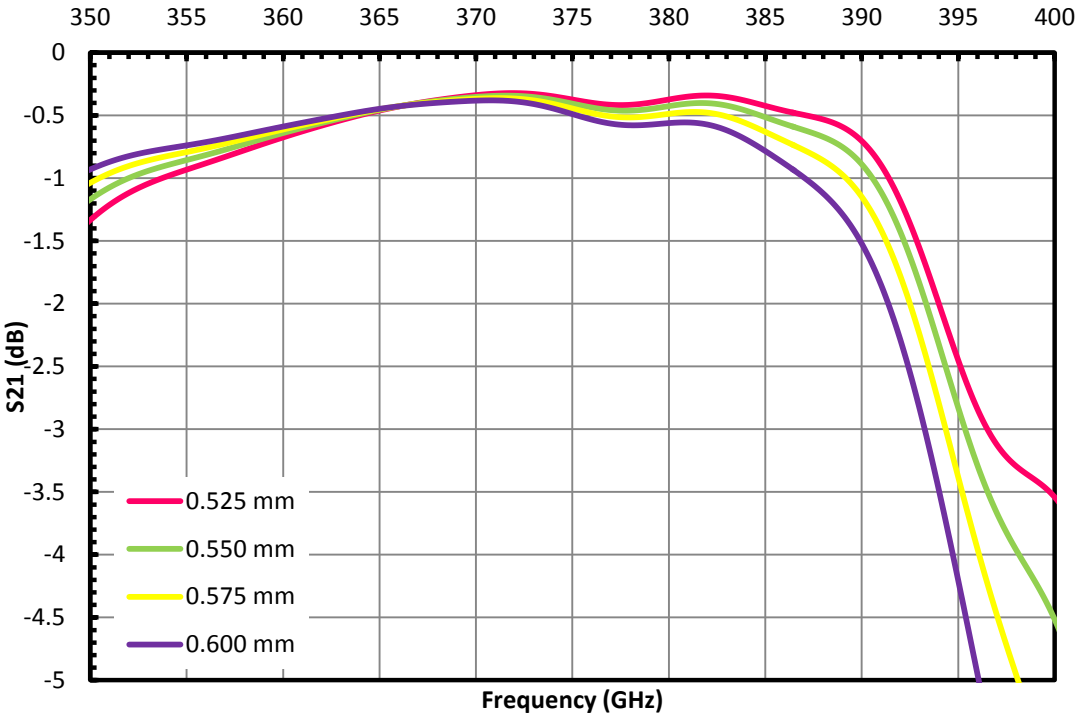

Fig. 5-4: Effect of *a* variation on T-junction coupler centre frequency.

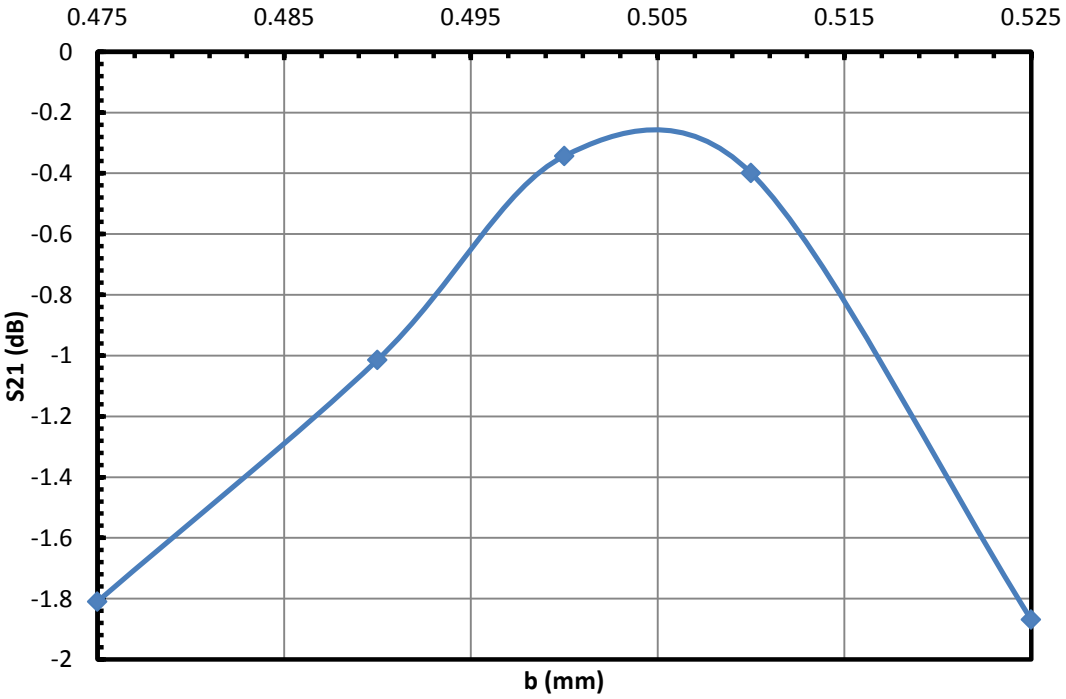

Fig. 5-5: Effect of *b* discrepancies on T-junction coupler transmission at 372 GHz.

5.3. 372 GHz Multiple-Hole Input Coupler

A multiple-hole coupler is, unlike the three port design described in Section 5.2, a four port device consisting of two transmission lines electromagnetically coupled through a series of common wall apertures. A commonly used power flow schematic of a four port network is shown in Fig. 5-6. Directional couplers can be designed for arbitrary power division with common coupling factors of (3, 6, 10, 20) dB often employed as a method of energy extraction from a mm-wave cavity. The theory of small aperture coupling between transmission lines [5.1] provides a description of the field profile through an individual coupling hole. A waveguide directional coupler often consists of two waveguides coupled through a series of individual coupling holes on a common broad wall [5.2 – 5.4]; however, narrow wall coupling has also been demonstrated [5.5]. Electromagnetic coupling between rectangular and circular waveguides is also feasible and a number of studies into couplers of this topology have been documented [5.6 - 5.8].

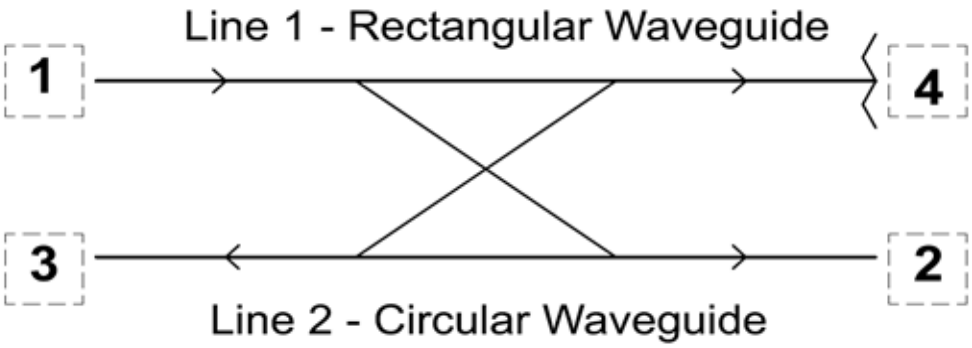

Fig. 5-6: Power flow of 4-port directional coupler with Port 1 – Input, Port 2 – Coupled, Port 3 – Isolated and Port 4 – Through.

5.3.1. Theory

The design of a rectangular-to-circular multiple-hole coupler, centred at 372 GHz, is based on achieving a high coupling factor for the desired mode and a high directivity. The coupling between the rectangular and circular transmission lines is defined as the ratio of the power at the input port to the power at the coupled port. The directivity is the ratio of

the power at the coupled port to the power at the isolated port. The coupling may be defined as

$$C = \frac{\int_{-L_m/2}^{L_m/2} \varphi(x) exp\left(-i\left(\frac{2\pi}{L_m}\right)\theta_C x\right) dx}{\int_{-L_m/2}^{L_m/2} \varphi(x) dx} \quad (5\text{-}1)$$

Similarly, the directivity may be defined as

$$D = \frac{\int_{-L_m/2}^{L_m/2} \varphi(x) exp\left(-i\left(\frac{2\pi}{L_m}\right)\theta_D x\right) dx}{\int_{-L_m/2}^{L_m/2} \varphi(x) dx} \quad (5\text{-}2)$$

where L_m is the length of the coupling section, $\varphi(x)$ is the coupling function and θ_C and θ_D are the coupling and directivity parameters respectively. The coupling and directivity parameters may be defined as

$$\theta_C = \frac{L_1}{2\pi}(\beta_1 - \beta_2) \quad (5\text{-}3)$$

$$\theta_D = \frac{L_1}{2\pi}(\beta_1 + \beta_2) \quad (5\text{-}4)$$

where β_1 and β_2 are the phase constants in Line 1 and Line 2 respectively, which may be written as

$$\beta_{1,2} = \frac{\omega}{c}\sqrt{1-\left(\frac{f_{c_{1,2}}}{f}\right)} \tag{5-5}$$

For the TE_{10} - TE_{11} mode coupler design, Line 1 is a rectangular waveguide excited by the TE_{10} mode which is electromagnetically coupled to Line 2, a waveguide of circular cross-section, through a set of discrete coupling points with equal size distribution. A tapered coupling distribution [5.9] can be employed to improve the coupling factor. However, for the low-THz work studied, it is decided to investigate a coupler with a linear size distribution to ease manufacturing constraints.

The coupling apertures are located on a common wall between the rectangular and circular waveguides. If it is assumed that $\varphi_i(x)$ is a known coupling function for the i-th aperture, then a finite Fourier transform (F_i) can be applied for a range of coupling and/or directivity parameters (θ);

$$F_i(\theta) = \int_{-L_m/2}^{L_m/2} \varphi_i(x) exp\left(-i\left(\frac{2\pi}{L_m}\right)\theta x\right) dx \tag{5-6}$$

By solving the Fourier transform at a discrete coupling point, the coupling function ($\varphi_i(x)$) can be expressed as

$$\varphi_i(x) = \begin{cases} a_i \text{ when } x = \pm\frac{s}{2}(2i\text{-}1),\ i = 1,2..N \\ 0 \qquad\qquad\qquad\qquad \text{otherwise} \end{cases} \tag{5-7}$$

where a_i is the coupling strength at a given aperture and s is the spacing between an even number ($2N$) of equally spaced apertures i.e. for 16 equally spaced apertures, N = 8. The coupling length (L_m) is the product of the number of coupling apertures and the spacing

between adjacent apertures (*2N * s*). The Fourier transform for the total coupling distribution can be written as

$$F_C(x) = 2\sum_{i=1}^{i=N} a_i cos\left(\frac{2i-1}{2N-1}\right)\pi\theta_C \tag{5-8}$$

and the Fourier transform for the total distribution with respect to the directivity may be written as

$$F_D(x) = 2\sum_{i=1}^{i=N} a_i cos\left(\frac{2i-1}{2N-1}\right)\pi\theta_D \tag{5-9}$$

Choung [5.8] states that the overall coupling (*C*) and directivity (*D*) between Line 1 and Line 2 can be defined as the ratio of the Fourier coupling parameter when $\theta \neq 0$ to the Fourier coupling parameter when $\theta = 0$;

$$C = \frac{\sum_{i=1}^{i=N} a_i cos\left(\frac{2i-1}{2N-1}\right)\pi\theta_C}{\sum_{i=1}^{i=N} a_i} \tag{5-10}$$

Similarly, the directivity (*D*) can be written as

$$D = \frac{\sum_{i=1}^{i=N} a_i cos\left(\frac{2i-1}{2N-1}\right)\pi\theta_D}{\sum_{i=1}^{i=N} a_i} \tag{5-11}$$

5.3.2. Design and Simulation

In order to achieve high coupling, the propagation of unwanted modes must also be considered. For the TE_{11} mode coupler, the three subsequent higher order modes (TM_{01}, TE_{21} and TE_{01}) are also evaluated. The cut-off frequencies of the four modes when R = 0.35 mm are shown in Table V-IV. For the frequency range of interest in the design of the multiple hole coupler (360 – 384 GHz), Table V-IV shows that the only unwanted mode that will propagate is the TM_{01}. Therefore, the coupler design should ensure that the TM_{01} mode has a lower coupling parameter and larger directivity parameter than the TE_{11} mode.

Table V-IV: Cut-off Frequencies of Wanted and Unwanted Modes in Coupled Line.

Mode	Cut-off Frequency (GHz)
TE_{11}	251
TM_{01}	328
TE_{21}	417
TE_{01}	523

The separation between neighbouring holes is determined by the radiation wavelength in the rectangular waveguide. Therefore, s can be defined by

$$s \cong \frac{\lambda_{10}^{R}}{2} \tag{5-12}$$

where $\lambda_{10}{}^{R}$ is the guide wavelength in the rectangular input waveguide, resulting in s = 0.50 mm. For a circular waveguide of R = 0.35 mm, the phase constants, $\beta_{10}{}^{R}$ and $\beta_{11}{}^{C}$, are matched when $a \approx 0.60$ mm. The coupling (5-3) and directivity (5-4) parameters for the $TE_{10}{}^{C}$ and $TM_{01}{}^{C}$ are plotted as a function of frequency in Fig. 5-7. For the analysis, β_1 is the phase constant in the rectangular waveguide and β_2 is the phase constant in the circular waveguide.

Fig. 5-7 shows that strong coupling to the TE_{11}^{C} mode is achieved whilst coupling to the TM_{01}^{C} mode is weak compared to the desired mode. The directivity parameter of the TE_{11} mode is less than ϑ_D for the TM_{01} mode over the entire frequency range; hence, the TM_{01} mode is isolated. Therefore, the TE_{11} mode would be dominant at the coupled port of the 4-port network. The coupling strength of the TE_{11} mode into Line 2 varies with the number of coupling apertures. Fig. 5-8 highlights the effect of the number of coupling apertures on the transmission to the coupled port. In the analysis of equation (5-10), the coupling parameter (ϑ_C) and the coupling strength (a_i) are constant.

Fig. 5-8 shows that the coupling improves as the number of apertures increases. However, with an increase in the number of apertures, the coupling length (L_m) also increases. For the high frequency mode coupler, an increase in L_m results in an increase in the Ohmic losses experienced by the propagating wave. Therefore, the range of interest for the total coupling aperture number (N) is chosen to be 12 - 30 apertures. For the chosen aperture number range, theory predicts that the coupling from the TE_{10}^{R} mode to the TE_{11}^{C} mode is > -1 dB at a single frequency. A numerical simulation is carried out in a bid to analyse the TE_{10}^{R} – TE_{11}^{C} transmission for 12, 18, 24 and 30 hole couplers (Fig. 5-9) for optimised hole radii.

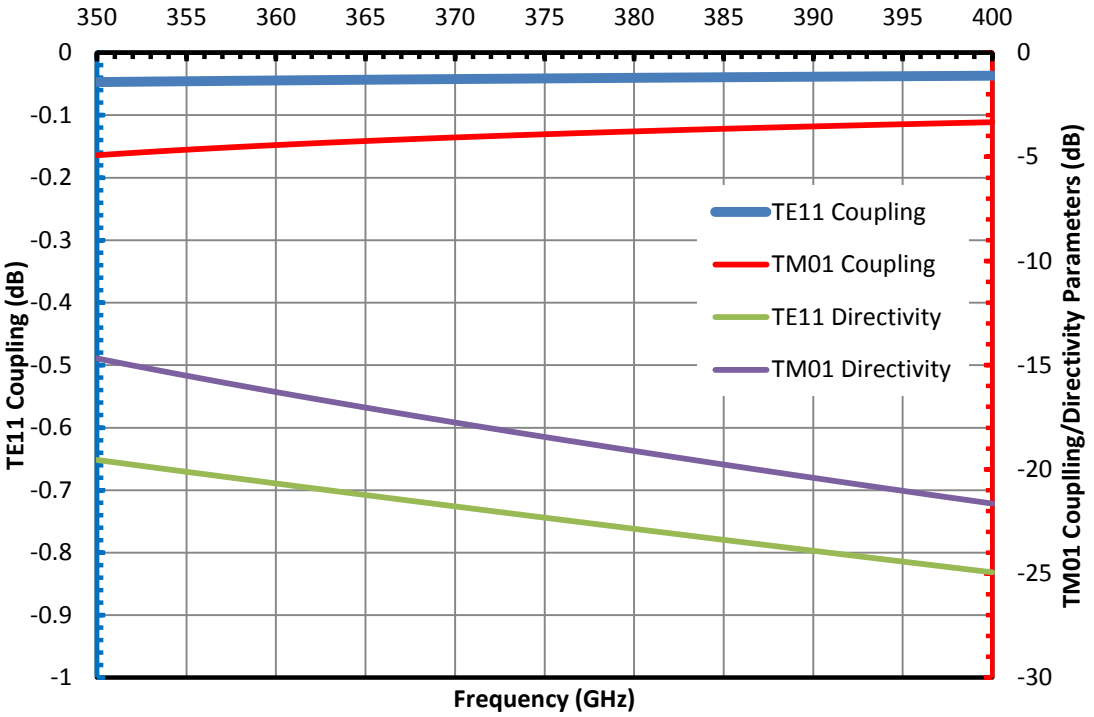

Fig. 5-7: Coupling and directivity parameters of wanted and unwanted modes.

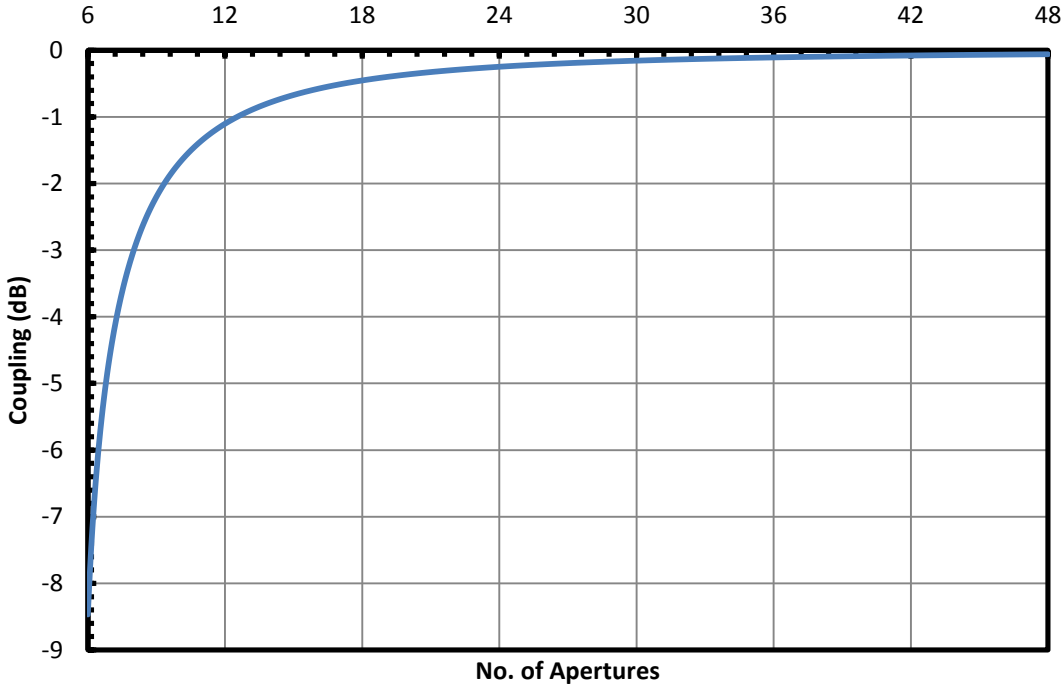

Fig. 5-8: Variation in coupling strength with number of common wall apertures.

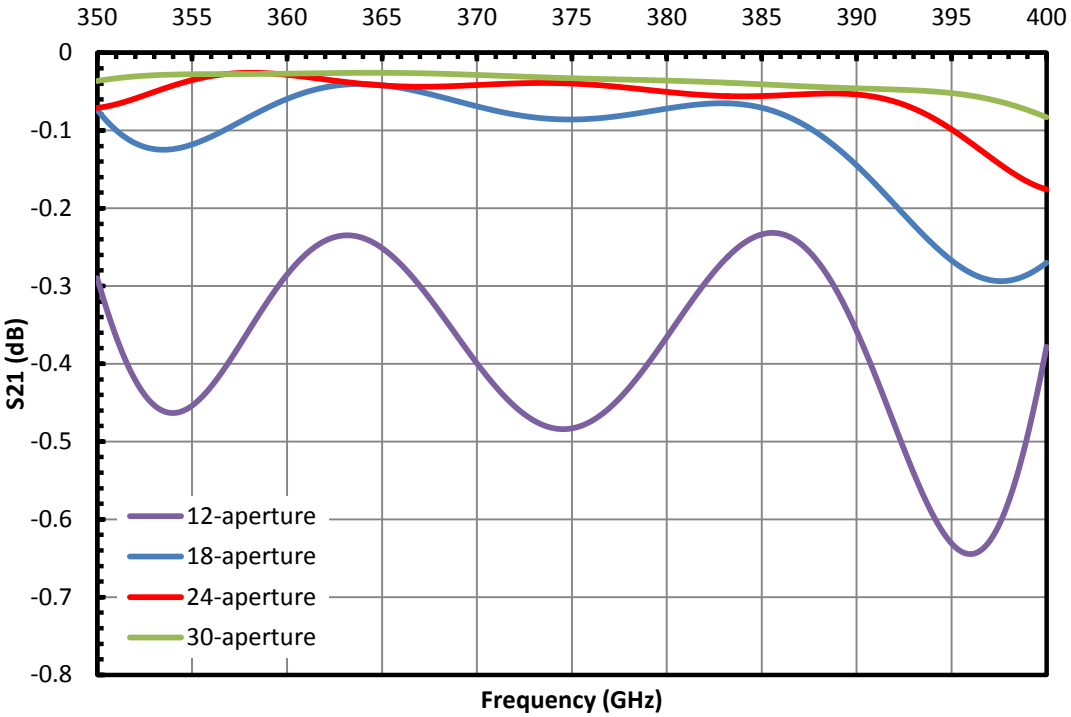

Fig. 5-9: Simulated transmission of 12-, 18-, 24- and 30- aperture couplers.

Fig. 5-9 has indicated that the transmission from Fig. 5-8 for the multiple aperture couplers is comparable to the theoretical prediction. A comparison of the coupling for a 12-hole coupler is shown to be ~1 dB in the theoretical model and ~0.4 dB in the CST simulation. However, a similar level of coupling can be achieved for 18-, 24- and 30-aperture couplers provided the hole radius (*R'*) is optimised. For 18-apertures, *R'* = 0.17 mm whereas 24- and 30-aperture couplers are optimised with *R'* = 0.16 mm and 0.15 mm respectively. The coupling strength achieved with 12 apertures is less than the 18-, 24- and 30-aperture couplers; however, the magnitude of the coupling strength is > -1 dB meaning it is within the target boundaries set for the input coupler design. For all four structures, the separation between Line 1 and Line 2 is 0.05 mm. The desired coupling response over the required bandwidth can be achieved with 12-apertures (*R'* = 0.18 mm). Therefore, subsequent designs will use 12 coupling holes. A numerical model of a 12-aperture coupler is shown in Fig. 5-10.

The dimensions of the theoretically calculated parameters are shown in Table V-V. The waveguide height (*b*) to waveguide width (*a*) ratio is initially set at 2:1. The parameters

are input into the numerical software and a simulated scattering parameter set is produced. Optimisation of the transmission and reflection within the coupling structure is carried out through parametric sweeps of the waveguide width and height, the radius of the coupling apertures (*R'*) and the spacing between Line 1 and Line 2 i.e. the aperture height. It is known that the spacing between the centre of adjacent coupling apertures (*s*) is ~ 0.5 mm; however, the *R'* value can be set for optimum performance within the upper limit of *s*/2. The CST- MS simulated scattering of the optimized 12-aperture coupler is shown in Fig. 5-11.

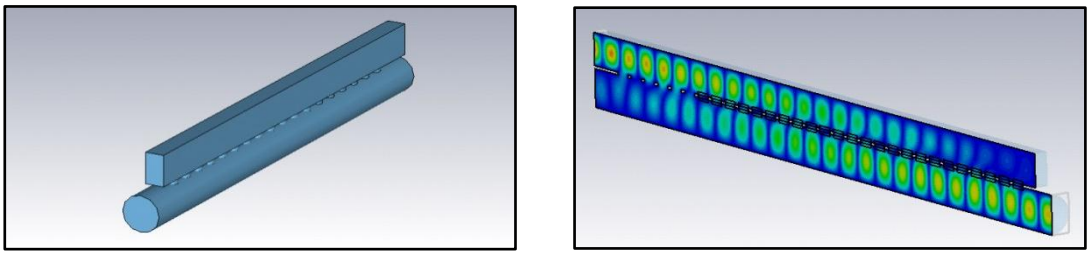

Fig. 5-10: (L) 3D multi-aperture coupler geometry and (R) microwave field progression.

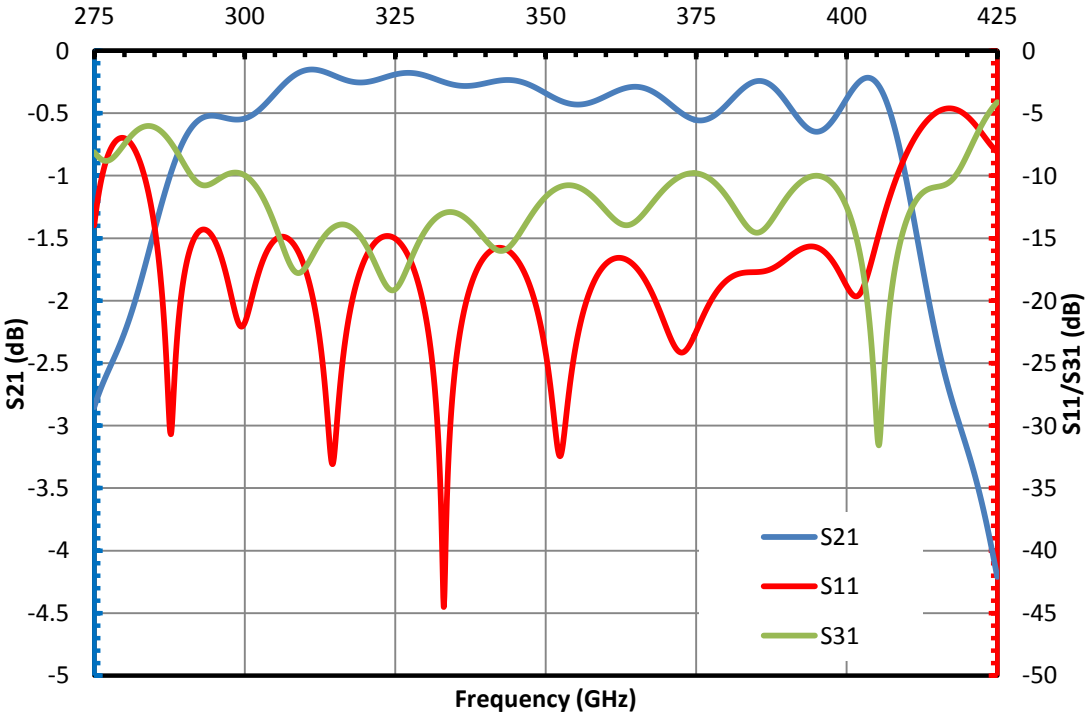

Fig. 5-11: Simulated scattering performance of a 372 GHz 12-aperture multi-hole coupler.

Fig. 5-11 shows that an operational frequency range of 121 GHz, equating to a bandwidth of over 35%, is achieved with the 12-aperture coupler. Fig. 5-8, however, shows that marginal

increases in coupling strength can be achieved by increasing the aperture number but additional length will lead to higher losses in the waveguide structure. The frequency range of the proposed fundamental mode gyro-TWA (360 – 384 GHz) is enclosed within the operational bandwidth of the 12-aperture input coupler and, therefore, is suitable for the proposed application. The optimised parameter set is documented in Table V-V, showing that the theoretically calculated set provided a good basis upon which to explore the coupler design. The optimised structure has a waveguide height (*b*) of 0.36 mm, minimising the reflections at the input port.

Table V-V: Theoretical and Optimised Parameter Set.

Parameter	Theoretical	Optimised
N	12	12
a	0.60 mm	0.57 mm
b	0.30 mm	0.36 mm
R	0.35 mm	0.35 mm
s	0.50 mm	0.40 mm

5.3.3. Tolerance Study

Due to the coupler operation at low-THz frequencies, the dimensional tolerances on certain structural parameters of the multiple-hole waveguide coupler are very sensitive. The input rectangular waveguide (Line 1) will be considered. The height of the input guide affects the coupling to the TE_{11}^{C} mode in Line 2; however, the effect of Δb variations between 0.30 mm and 0.50 mm inclusive is minimal to the overall coupling strength. Therefore, a larger tolerance can be applied to the *b* dimension in the manufacture of the waveguide coupler. Variations in the waveguide width (*a*) however can have serious implications on the coupling efficiency of the input coupler. The effect of ± 10 µm changes to the waveguide width on the amount of energy delivered to the coupled port is shown in Fig. 5-12. The feasibility study highlighted a ~ 20% reduction in the power coupled to Port 2 with a 40 µm deviation from

the optimum value of *a*. However, a ± 10 µm variation to the waveguide width, the typical tolerance of a state-of-the-art CNC mill, would ensure that the coupling coefficient is acceptable for the gyro-TWA. Therefore, it is permissible to construct the 12-aperture with modern numerically controlled manufacturing techniques.

Due to the broadband operating profile of the multiple aperture coupler, variations to the radius of Line 2 (ΔR) of ± 20 µm has minimal effect on the coupling strength.

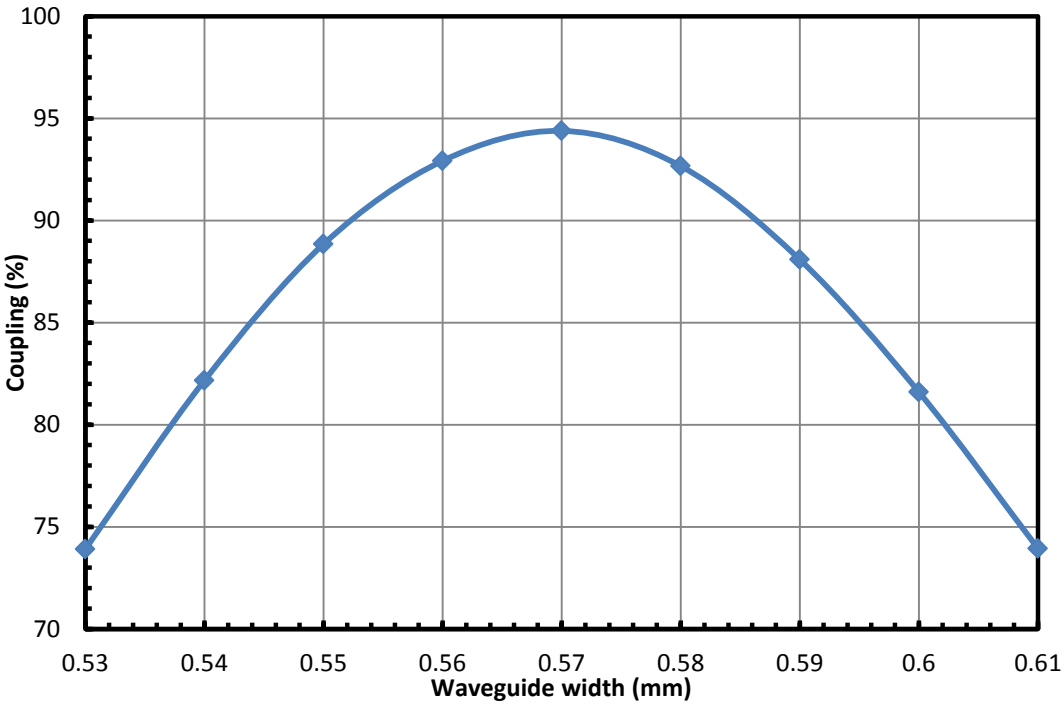

Fig. 5-12: Effect of *a* variations on TE_{11} coupling.

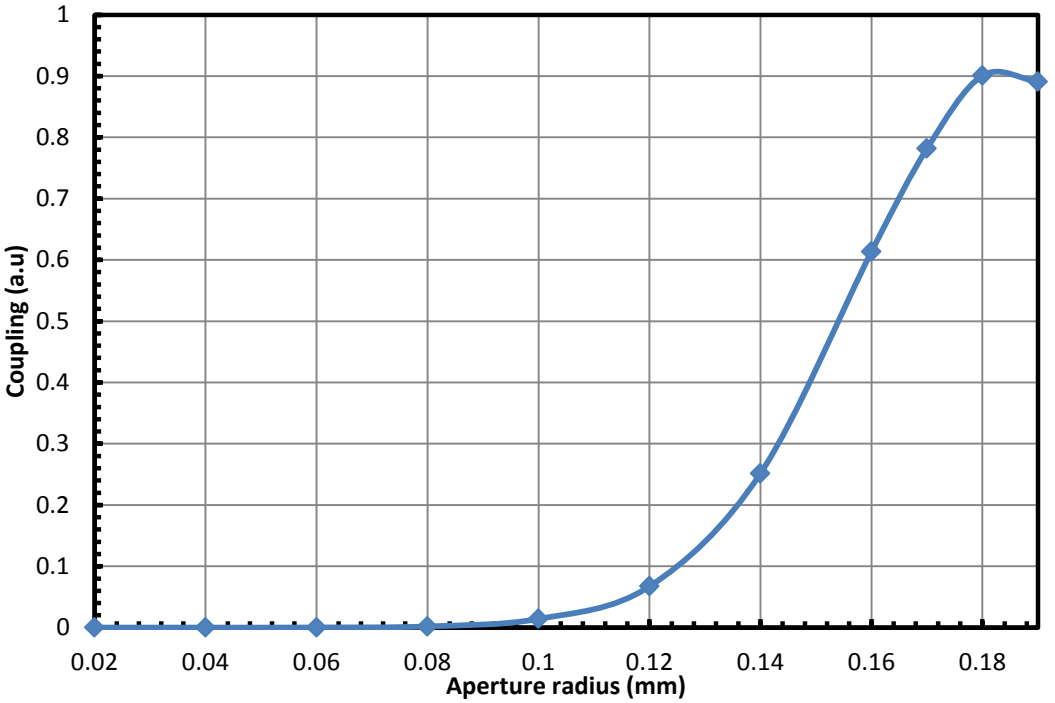

Fig. 5-13: Effect of *R'* variations on coupled power at 372 GHz.

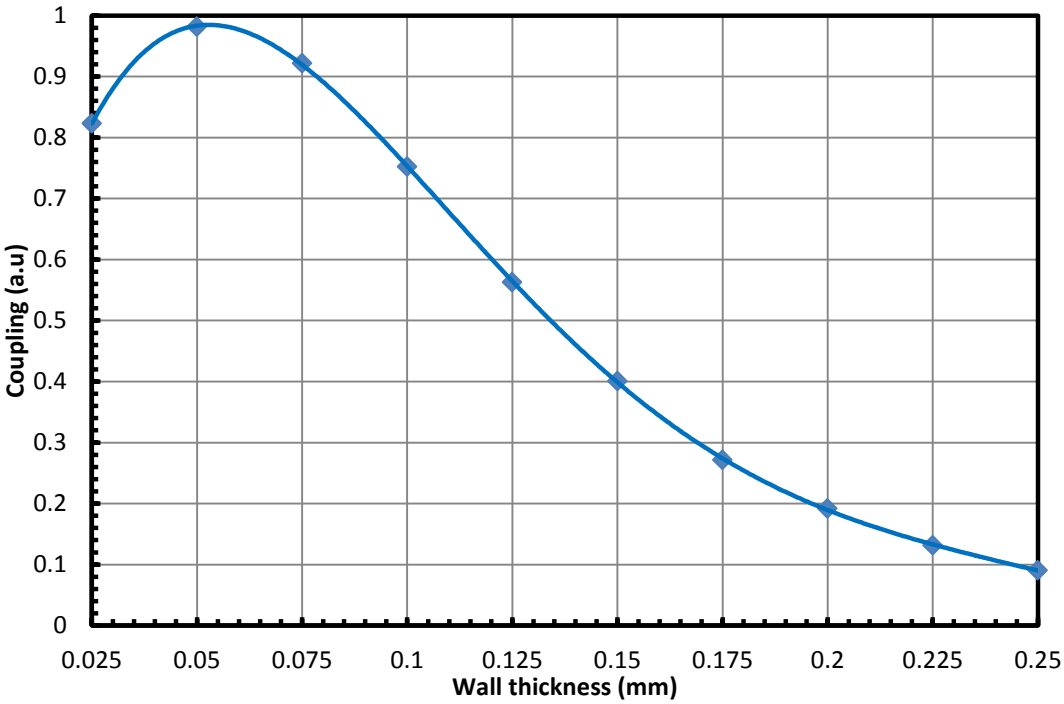

Fig. 5-14: Effect of Line 1 – Line 2 separation increase on coupling coefficient.

The machining tolerances for the coupling apertures are considered. The effect of *R'* variation on TE_{10}^{R} – TE_{11}^{C} coupling for a 12-aperture coupler is shown in Fig. 5-13. Fig. 5-13

shows that coupling to the desired mode is enhanced with increasing *R'* up to the optimum value of 0.18 mm. The upper limit of 0.19 mm is dictated by the optimal pitch between the centres of adjacent apertures (0.4 mm), allowing space for machining of adjacent holes. A marginal increase in *R'* has minimal effect on the coupling strength; however, a 20 µm reduction in the hole radius results in a ~ 30% decrease in coupled power at Port 2. Therefore, if a micro-hole drilling technique were to be used on the coupler manufacture, it is vitally important to ensure that the drill bit diameter is accurate.

The aperture height (t_a) is determined by considering the potential thickness of metal sheet used to separate the rectangular and circular waveguides in a practical coupler. The effect of sheet metal thickness on TE_{11} transmission to the coupled port for a 12-hole structure is shown in Fig. 5-14. Fig. 5-14 highlights a decrease in energy delivered to the coupled port with increased separation. A metal thickness of 0.05 mm would be chosen for a manufactured multiple aperture coupler. A sheet thickness of this magnitude would allow for a high transmission to the TE_{11}^{C} mode whilst ensuring that a high mechanical stability is achieved in the gap spacing. A 25 µm increase in aperture height leads to a decrease in coupler transmission of ~ 10 – 15%; therefore, it is important to ensure that the metallic separation sheet has a high tolerance on sheet thickness.

It is possible to manufacture the separation between Line 1 and Line 2 in the multiple aperture coupler design. The sheet of 0.05 mm thickness will allow the micro-hole drilling technique to be used in the manufacture [5-10]. The drilling process can micro-machine apertures of minimum 0.05 mm in diameter with an aspect ratio of 7:1 in reference to length of aperture required to the diameter of the drill bit. Therefore, a hole of length 0.05 mm and *R'* = 0.18 mm, values used in the multiple-hole coupler simulation, is achievable.

5.4. Discussion of Fundamental Mode Input Coupler Design

A review of the design of two fundamental mode rectangular-to-circular input couplers has been presented. The design of the T-junction coupler and the multiple-aperture coupler has focused on achieving a high coupling factor from the TE_{10}^{R} mode to the TE_{11}^{C} over a broad bandwidth, ensuring that the field purity in the coupled waveguide is of a high

quality. The use of a Bragg reflector has proven to be an effective method of providing frequency selective feedback of electromagnetic radiation at high frequency whilst maximising the region within which an electron beam can propagate unhindered. The use of a step-down waveguide reflector for a fundamental mode coupler, although effective at rejecting oncoming radiation, limits the radius of a gyrating electron beam and can affect the efficiency of the device. The reduced beam tunnel diameter will result in challenging alignment at W-band frequencies with enhanced complications at 372 GHz.

The operational frequency range of transmission for the T-junction input coupler is 352 – 390 GHz, equating to a bandwidth of ~ 10%. The bandwidth of the T-junction design is limited because the required beam input port diameter is relatively large compared to the beam tunnel. Therefore, an optimal achievable bandwidth of ~ 20% is not practical in the low-THz design. The bandwidth of the multi-hole coupler is 35%, meaning that of the two couplers, this has the widest operational frequency range. The coupler exceeds the bandwidth exhibited by the multiple-arm coupler of [5.6]. The use of a multiple aperture directional coupler means that the requirement for a frequency selective wave reflector is eliminated. Careful design of a waveguide coupler with high directivity will limit any reflections at the terminated port and, hence, propagation of a forward wave towards the isolated port will be limited. The 12-hole coupler design has < 10% of the incident radiation propagated to Port 3.

Ohmic losses are not included in the simulations with a perfect electrical conductor background employed. However, at 372 GHz the skin depth is ~ 0.1 μm which is comparable to, or smaller than, the surface roughness. This will result in increased ohmic loss. The effect of the surface roughness and skin depth can be analytically evaluated with a reduced electrical conductivity background material in CST-MS. While there is no comprehensive measured conductivity as a function of the surface roughness published at the operating frequency, an arbitrary reduction factor of 12 was used to monitor the potential losses within the designed couplers. The simulated waveguide losses for the T-junction coupler are 0.25 dB and 0.42 dB for the multi-aperture coupler at 372 GHz with a respective corresponding bandwidth of 8% (357 – 387 GHz) and 28% (301 – 399 GHz). Coupling

degradation of this magnitude would not pose a significant problem to either input coupler operation.

The T-junction and multiple aperture waveguide couplers discussed are effective at converting the fundamental TE_{10} mode from a rectangular input port to the TE_{11} mode in a circular through port. However, to achieve strong coupling strict manufacturing tolerances must be applied to the construction of the couplers to achieve optimum coupling strength. The sensitivity of the T-junction input coupler to variations in *R* mean that strict tolerances must be applied to this parameter. Similarly, the 12-aperture coupler is very sensitive to variations in the aperture radius (*R'*) and the input rectangular waveguide width (*a*). Therefore, manufacture of the low-THz passive components will present a significant challenge. However, due to the large coupling bandwidth which results in the coupler performance being less sensitive to manufacturing tolerances, it is proposed a 0 dB 12-aperture directional coupler would be used for a fundamental mode input coupler on a 372 GHz gyro-TWA with a 3-fold HCIW. The length requirements on the high frequency gyro-amplifier are less strict than on the W-band device where the solenoid spacing is defined; therefore, it is permissible to implement the relatively long waveguide coupler.

6. 372 GHz Higher Order Mode Input Coupler Design

6.1. Introduction

The design of a high frequency input coupler for a gyro-TWA is challenging due to the complexity of sub-mm waveguide manufacture. However, unlike a slow wave structure which should scale directly with frequency, a gyro-device can be operated at a higher order mode (HOM) to increase the dimensions and maximise power capability [6.1] – [6.3]. A proposal for a HOM gyro-TWA used for DNP-NMR spectroscopy is discussed. The target operating performance of the 372 GHz gyro-amplifier is shown in Table V-I.

The proposed 372 GHz gyro-TWA, unlike the design of Chapter 5, will incorporate an 8-fold HCIW as the interaction cavity. The 8-fold helix supports the interaction of the TE_{61} mode with spatial harmonics of the TE_{22} mode, generating an eigenwave with almost constant group velocity when k_z tends to 0. The HCIW average radius (R_0) is ~ 3x larger than the TE_{21} – TE_{11} coupling cavity, easing manufacturing constraints. Efficient coupling of the TE_{61} mode into the interaction cavity is required for a high efficiency device. The input coupler will be designed with focus on the following three parameters:

1. the bandwidth of the input coupler should incorporate 360 – 384 GHz,
2. the transmission from TE_{10}^{R} – TE_{61}^{C} should exceed -1 dB over the desired frequency range and,
3. mode purity of the TE_{61} mode should exceed 90%.

By adding the HOM coupling requirement, the design of the input coupler is more complex than designing a fundamental mode coupler, as a result of cavity lower order mode (LOM) competition. A TE_{11} field pattern is readily excited and is the dominant mode within a cylindrical waveguide. Therefore, to ensure high TE_{61} field purity, a complex waveguide coupling geometry is required.

A coaxial input coupler can be designed to convert the fundamental mode in a rectangular feed waveguide to the fundamental or higher order modes in a circular waveguide with a high degree of mode purity. A coaxial cavity structure is employed as a

TE_{01} input coupler on gyro-klystron amplifiers [6.4 - 6.6]. The TE_{01} coupler achieves an operating bandwidth of ~ 3% with a centre frequency of 35 GHz. The coaxial cavity coupler topology is also used on a 94 GHz gyro-TWA [6.7 – 6.8]. The gyro-amplifier achieves a saturated output power of 59 kW with a 3 dB bandwidth of 1.3%. The passive input coupler operates about a centre frequency of ~ 95 GHz with a bandwidth of ~ 3%. A proposal for a W-band gyro-TWA with a Photonic Band Gap (PGB) interaction circuit, utilising a coaxial coupler at the microwave input [6.9], has also been proposed. The input waveguide can also be designed to propagate all incident radiation along the same vector path around the coaxial cavity [6.10]; however, the wraparound coupler designs are fundamentally limited in bandwidth due to the mismatch between the electric field and coupling apertures with varying wavelength. Therefore, a coaxial coupler will not be designed for TE_{61} waveguide coupling.

The design of a power dividing input coupler for a 372 GHz HOM gyro-TWA is presented. The numerical modelling of a waveguide splitter input coupler is shown in Section 6.2. The waveguide power divider will be modelled with a stepped-transformer waveguide (Section 6.2.2.1) and a tapered waveguide (Section 6.2.2.2). An E-plane waveguide bend is designed in Section 6.2.3. The theory and CST-MS design of the two waveguide splitter couplers is presented in Section 6.2.4. A tolerance study of the selected coupler is presented in Section 6.2.5. A discussion of the input coupler manufacture at W-band is included in Section 6.3 with the Vector Network Analyser (VNA) experimental setup and test results presented in Section 6.4 and Section 6.5 respectively. A discussion of the TE_{61} coupler design and manufacture at 372 GHz is included in Section 6.6.

6.2. TE_{61} Waveguide Splitter Waveguide Coupler

6.2.1. Introduction

The design of a 372 GHz TE_{10}^{R} – TE_{61}^{C} waveguide coupler employs the principal of incident wave power distribution to couple to a HOM. The waveguide splitter divides an incident TE_{10} mode into equal signal intensities, propagating with matched phase towards the cylindrical coupled cavity. The possible modes which may be coupled into the interaction

cavity are dependent on the number of branches employed within the designed waveguide splitter. The coupling process between each individual waveguide branch and the cylindrical beam tunnel is discussed in Section 3.2. A table of branch numbers and the relevant potential coupled modes, when equal length waveguide branches are used, is shown in Table VI-I. By implementing the waveguide splitter, the generation of a HOM in the interaction cavity is simplified due to a reduction in mode competition. A single branch coupler (Chapter 3 and Section 5.2) can be used to generate HOM with careful cavity radius selection; however, the mode completion from lower order TE-modes results in coupling degradation of the desired HOM due to increased mode competition. Therefore, the use of a waveguide splitter reduces the number of modes propagating in the cavity and, as a result, will improve the coupling efficiency of the required cavity mode.

Table VI-I: Waveguide Splitter Branch Number and Potential Modes.

Waveguide Branch No.	**Converting Mode**	**Cavity TE_{mn} Modes**
2	TE_{21}	TE_{21}, TE_{41}, TE_{61}, TE_{81} …
3	TE_{31}	TE_{31}, TE_{61}, TE_{91}, $TE_{12,1}$ …
4	TE_{41}	TE_{41}, TE_{81}, $TE_{12,1}$ …
5	TE_{51}	TE_{51}, $TE_{10,1}$, $TE_{15,1}$ …

The design of a waveguide TE_{61}^{C} input coupler can include a waveguide splitter with 2- or 3-branches (Table VI-I). The 3-branch splitter would result in less mode competition inside the cylindrical cavity with a single lower order TE_{m1} mode propagating within the cavity (TE_{31}); however, the phase matching of the 3 waveguide channels results in added complexity to the coupler design and manufacture. Therefore, a TE_{10}^{R} – TE_{61}^{C} input coupler with a 2-branch waveguide splitter will be designed for a 360 – 384 GHz gyro-TWA. Two models of the waveguide transition, a stepped-transformer waveguide and a tapered waveguide, will be modelled and discussed. An E-plane waveguide bend is designed to propagate the divided signal within the respective branch and ensure the two signals reach the beam tunnel in-phase. A stepped transformer input coupler and a tapered waveguide

input coupler are designed and simulated with a tolerance study of the selected model presented.

6.2.2. E-Plane Waveguide Splitter

6.2.2.1. Stepped-Transition Waveguide

The design of a waveguide stepped-transformer is based on a periodic step discontinuity [6.11] employed to support an electrical transition between two waveguides. The field profiles of propagating TE modes for single step (E-plane) and double step (E- and H- plane) waveguide transitions has been discussed [6.12 – 6.13]. The design of a 372 GHz E-plane waveguide transformer with an impedance ratio (*Z*) of *Z* = 2.0 is outlined based on the procedure given in [6.14]. An impedance ratio of *Z* = 2.0 describes a waveguide transition from rectangular-to-square waveguide.

The rectangular-to-square waveguide transition is designed with an integer number (*N*) of step discontinuities. The required number of steps is dependent on the fractional bandwidth (f_q) within which the HOM input coupler should operate. The fractional bandwidth is defined as

$$f_q = 2\left(\frac{f_{UPPER} - f_{LOWER}}{f_{UPPER} + f_{LOWER}}\right) \tag{6-1}$$

where f_{UPPER} and f_{LOWER} are the upper and lower operational frequencies of the waveguide coupler respectively. For the 372 GHz gyro-TWA input coupler, f_{LOWER} = 360 GHz and f_{UPPER} = 384 GHz. The fractional bandwidth is considered alongside the Voltage Standing Wave Ratio (VSWR), which is a measure of the reflection from the waveguide transition, to select the step discontinuity number. From pp. 263 from reference [6.14], a minimum VSWR = 1.0 can be achieved with an *N* = 3 step waveguide transformer which is able to support the required frequency range with minimum reflections over the operational bandwidth. The 3-stage transformer, as defined, consists of 3 intermittent waveguide transitions between the rectangular and square waveguide; therefore, the transformer incorporates a total of 4 step discontinuities. A schematic of the waveguide transition is shown in Fig. 6-1.

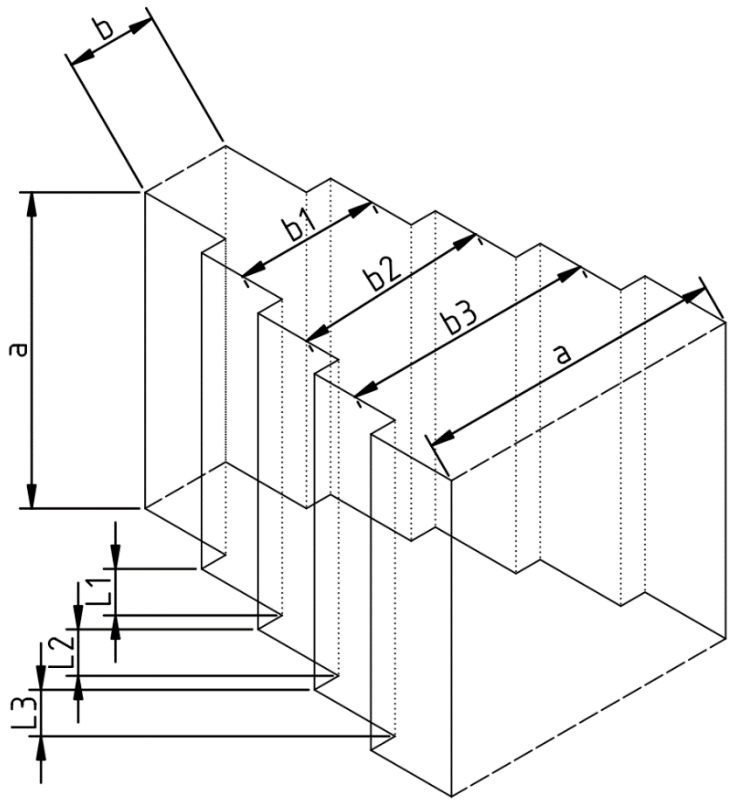

Fig. 6-1: A schematic of a rectangular-to-square waveguide transformer.

The waveguide transformer is designed with a constant waveguide width (a). However, the step height (b) will vary axially between the discontinuities. The impedance mismatch between each waveguide step is dependent on f_q and the required impedance ratio (Z = 2.0). From pp 272 [6.14], which depicts a table of initial impedance mismatches (Z_1) for a range of f_q and Z values, Z_1 = 1.09247 for a transformer with a fractional bandwidth $f_q \approx 0.2$ and Z = 2.0. The impedance mismatches at step two and step three (Z_2 and Z_3) are defined by

$$Z_2 = \sqrt{Z} \tag{6-2}$$

$$Z_3 = \frac{Z}{Z_1} \tag{6-3}$$

Therefore, the waveguide heights (b_n) for the step discontinuities (n = 1,2,3) are given by

$$b_n = b_0 \cdot Z_n \tag{6-4}$$

where b_0 is the input waveguide height and Z_n is the impedance mismatch at the respective step. The values for b_n are shown in Table VI-II.

The length of each step (L_n) is given nominally by

$$L_n = \frac{\lambda_0^{cf}}{4} \tag{6-5}$$

where λ_0^{cf} is the free space wavelength of the centre frequency. A process of length correction is outlined in [6.14], varying the length of the step discontinuities based on the admittance (Y_n) and susceptance (B_n) mismatches between the waveguide transitions which affects the electrical length. The consideration of Y_n and B_n means that the current flow between each step discontinuity and the waveguide wavelength is also considered in the analysis. The corrected lengths are shown in Table VI-II.

A numerical model of a stepped transformer waveguide was designed in CST-MS. The waveguide width (a) was initially set at 0.600 mm with a width-to-height (a : b) ratio of 2 : 1. The derived b_n and L_n parameters were defined in CST-MS to create a numerical model of the stepped transformer waveguide. A parametric optimisation of the waveguide width and discontinuity lengths (L_n) was undertaken to minimise the reflections at the input rectangular port. The b_n dimensions were set according to the impedance mismatch (Z_n) values derived with no alteration made. The derived b_n and optimised L_n parametric values are shown in Table VI-II. The reflection and transmission of the 3-stage waveguide transformer with a = 0.570 mm is shown in Fig. 6-2. A modelling depiction of the transformer is included in the inset. The sharp waveguide steps were rounded to accurately represent a machined waveguide channel. The stepped waveguide is shown to support TE_{10} transmission with a high coupling factor from rectangular to square waveguide between 360 – 384 GHz.

The transformer also demonstrates a reflection coefficient of < -35 dB over the desired frequency range ensuring minimal transmission loss at the incident port.

Table VI-II: Optimised Stepped Transformer Waveguide Parameters.

Transformer Step	Waveguide Height (b_n) (mm)	Length (L_n) (mm)
0	0.285	N/A
1	0.311	0.260
2	0.403	0.240
3	0.522	0.215
4	0.570	0.140

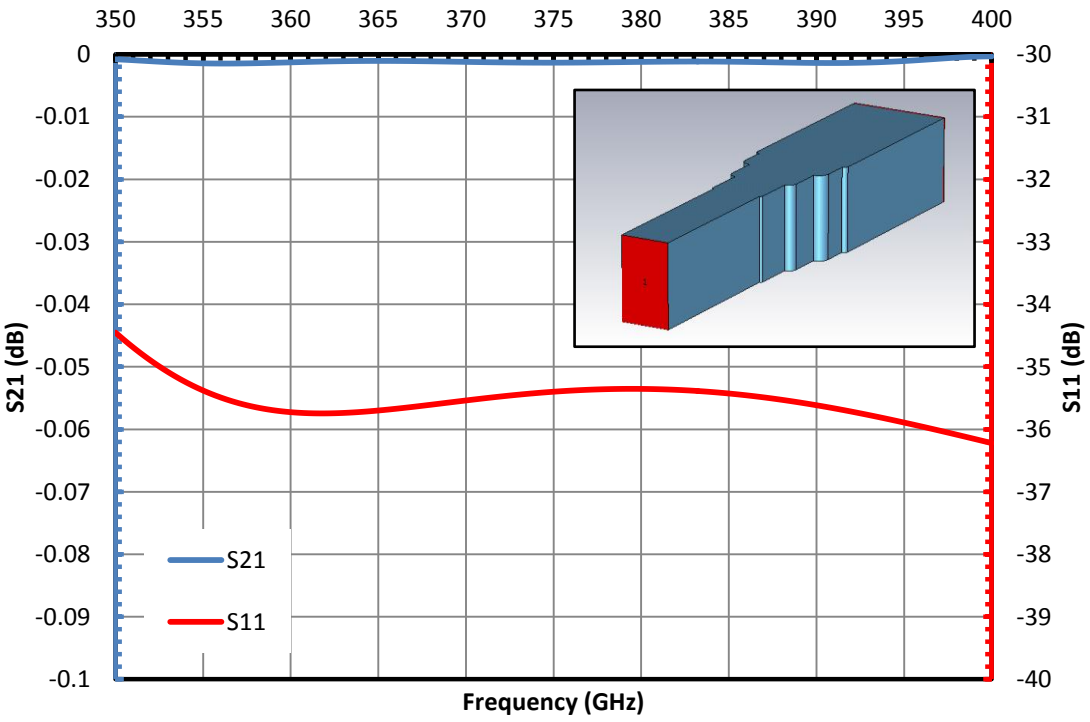

Fig. 6-2: Transmission and reflection of a 360 - 384 GHz stepped waveguide transformer.

6.2.2.2. Tapered Waveguide

A tapered waveguide can be employed to provide an impedance match between two waveguides of similar geometries without the complex manufacturing of step discontinuities. Tapered waveguides are designed with linear or part-sinusoidal axial tapers with single E-plane variations [6.15], or double tapers which vary in the E- and H- plane simultaneously [6.16]. A linearly or sinusoidally tapered waveguide can be analytically examined using infinite step discontinuities [6.17], the process used in the understanding of waveguide transformers (Section 6.2.2.1). A 372 GHz waveguide taper with a linear wall profile will be designed for a rectangular-to-square (Z = 2.0) waveguide transition.

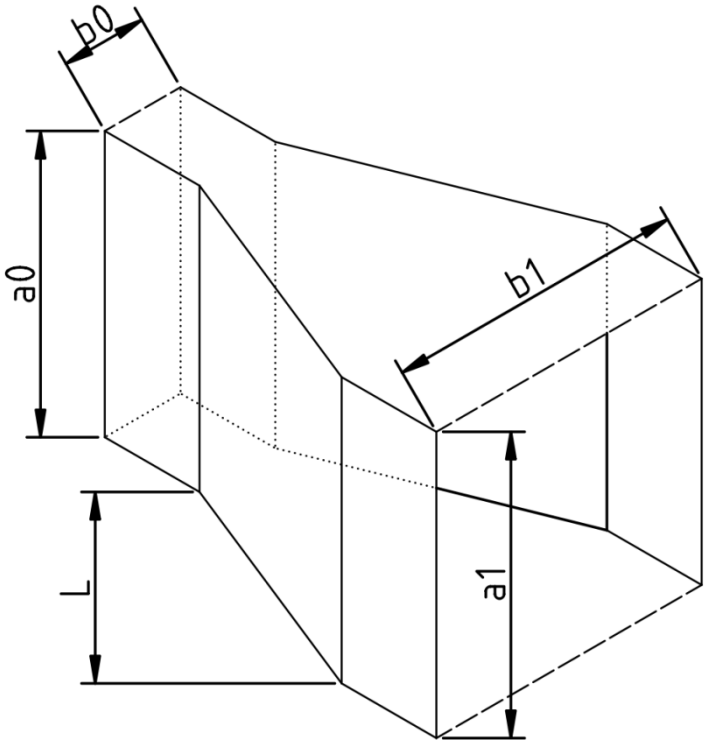

Fig. 6-3: Schematic of a rectangular-to-square linearly tapered waveguide.

A rectangular-to-square waveguide taper is shown in Fig. 6-3. The reflection coefficient (Γ) of a rectangular waveguide taper supporting TE_{10} mode propagation can be defined as [6.16];

$$\Gamma = \frac{\lambda_g}{L_t}\left[\frac{K_0^2 + K_1^2}{64\pi^2} - \frac{K_0 K_1}{32\pi^2}cos(4\pi l)\right]^{\frac{1}{2}} \qquad (6\text{-}6)$$

where λ_g is the guide wavelength and L_t is the tapering section length. K_0, K_1 and l are given by

$$K_0 = \frac{\frac{(b_1 - b_0)}{b_0} - \left(\left[\frac{(a_1 - a_0)}{a_0}\right] / \left[1 - \left(\frac{\lambda_g}{2a_0}\right)^2\right]\right)}{\sqrt{1 - \left(\frac{\lambda_g}{2a_0}\right)^2}} \tag{6-7}$$

$$K_1 = \frac{\frac{(b_1 - b_0)}{b_1} - \left(\left[\frac{(a_1 - a_0)}{a_1}\right] / \left[1 - \left(\frac{\lambda_g}{2a_1}\right)^2\right]\right)}{\sqrt{1 - \left(\frac{\lambda_g}{2a_1}\right)^2}} \tag{6-8}$$

$$l = \frac{1}{\lambda_g}\int_0^{L_t} \sqrt{1 - \left(\frac{\lambda_g}{2a}\right)^2}\, dx \tag{6-9}$$

respectively, where a_0 and b_0 are the initial waveguide width and height, a_1 and b_1 are final waveguide width and height and a (6-9) is the waveguide width at the respective position along the integral 0 to L_t. A variation of a is only witnessed for a taper with an H-plane projection. For an E-plane rectangular-to-square taper where $a_0 = a_1$ and $b_1 = 2b_0$, equation (6-6) simplifies to

$$\Gamma = \frac{\lambda_g}{16\pi L_t}\left[5 - 4cos\left(\frac{4\pi L_t}{\lambda_g}\right)\right]^{\frac{1}{2}} \tag{6-10}$$

Analysis of equation (6-10) highlights a minimum reflection coefficient when $L \approx N\lambda_g$, where N is an integer number. The guide wavelength at 372 GHz is ~ 1.10 mm;

therefore, the taper length is set at N * 1.10 mm. To minimise wall losses, the taper length should be minimised. Therefore, $N = 1$.

A 372 GHz impedance matching tapered waveguide was designed using CST-MS. The waveguide width (a) was initially set at 0.600 mm with a waveguide width-to-height (a : b) ratio of 1 : 2. The taper length (L_t) was set at 1.10 mm. A parametric optimisation of a was performed to minimise reflections at the rectangular input port (Port 1). The numerically simulated transmission and reflection of a $Z = 2.0$ rectangular-to-square E-plane waveguide taper is shown in Fig. 6-4. The topology of the simulated waveguide taper is included in the inset. The waveguide width (a) was optimised at 0.570 mm, equating to $b_0 = 0.285$ mm and $b_1 = 0.570$ mm, with the reflection at Port 1 less than -27 dB over the desired operating bandwidth. The taper reflections are ~ 8 dB greater than the reflections at the input port of the stepped waveguide transformer; however, the reflections (<< -10 dB) from both waveguide structures will not result in damaging oscillations being returned to the gyro-TWA power source.

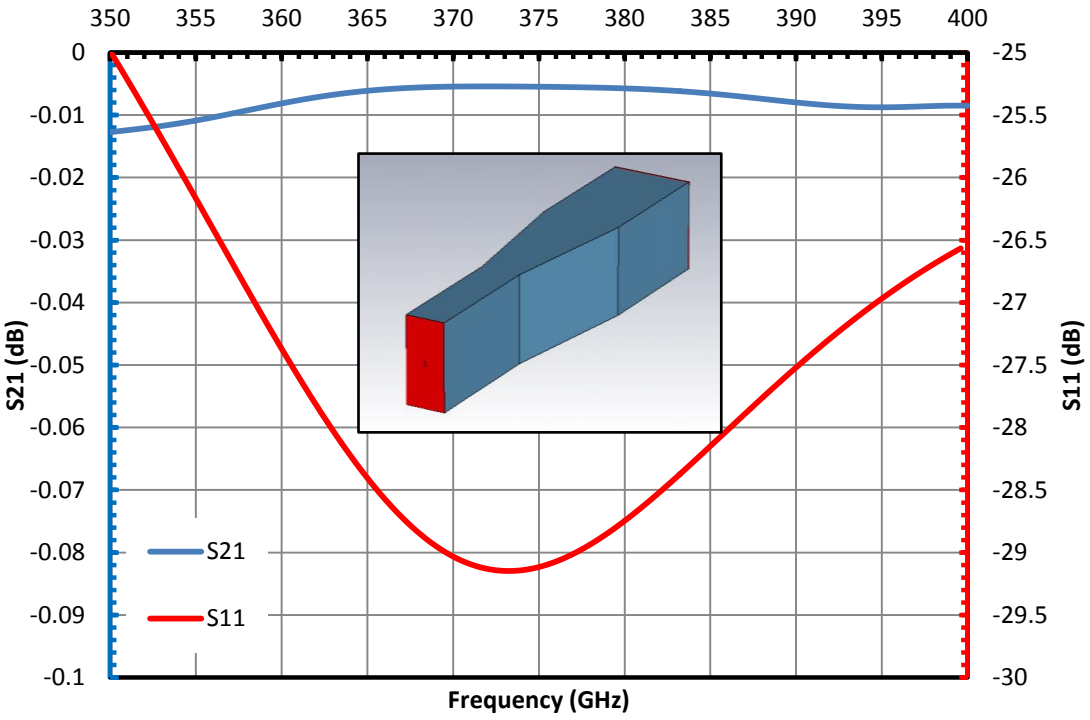

Fig. 6-4: Simulated scattering of a 372 GHz rectangular-to-square waveguide taper.

6.2.2.3. E-plane Waveguide Bend

An E-plane waveguide bend is a fundamental component of waveguide engineering. A rotation of a waveguide about an angle, commonly between 15° to 90°, creates a smooth-walled waveguide junction. The smooth E-plane transition can be designed to be compact (small R_{IN}) or broad (large R_{IN}) with small return losses; however, the design and fabrication can be complex and expensive [6.18]. Therefore, waveguide systems with the requirement for E-plane bends often employ mitred junctions to ease manufacturing constraints [6.19]. However, a mitred waveguide component will generate greater reflections at the incident interface than a smooth-walled bend. E-plane waveguide bends of smooth and mitred profiles can be analysed using Maxwell's equations [6.19], mode matching techniques [6.20] and equivalent circuit composition [6.21] to develop understanding of the wave propagation in the waveguide junction. For complex waveguide coupling to HOM's, the losses of individual components can have a critical impact on the transmission strength to the desired cavity mode. Therefore, a smooth-walled E-plane bend is chosen for application to a 372 GHz HOM input coupler.

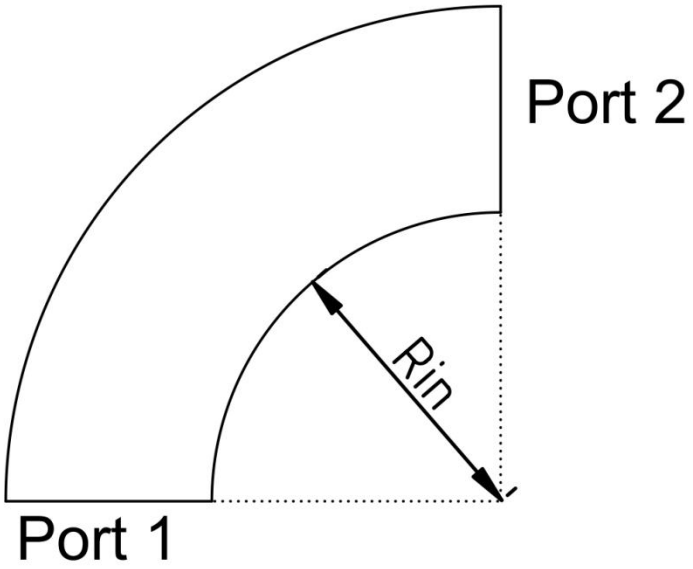

Fig. 6-5: A schematic view of an E-plane smooth-wall waveguide bend.

A smooth-walled 90° E-plane waveguide bend with a = 0.570 mm and b = 0.285 mm was designed using CST-MS. The waveguide parameters a and b are set to match the

waveguide transitions designed in Section 6.3.2.1 and Section 6.3.2.2. A schematic top-down view of the E-plane bend is shown in Fig. 6-5. The inner radius of the E-plane bend (R_{IN}) is optimised to minimise reflections at the incident waveguide port. All values of R_{IN} > 0.05 mm will result in S_{11} ≤ -20 dB; however, a radius increase up to 0.25 mm is shown to improve transmission. The radii selection is then dependant on minimising reflection at the centre of the operating bandwidth. The simulated transmission and reflection of a 372 GHz 90° E-plane waveguide bend with R_{IN} = 0.800 mm is shown in Fig. 6-6. The return loss from the E-plane bend is < 40 dB over the required 360 – 384 GHz operating bandwidth. The minimisation of any internal component losses will serve to enhance the coupling strength to the desired cavity mode.

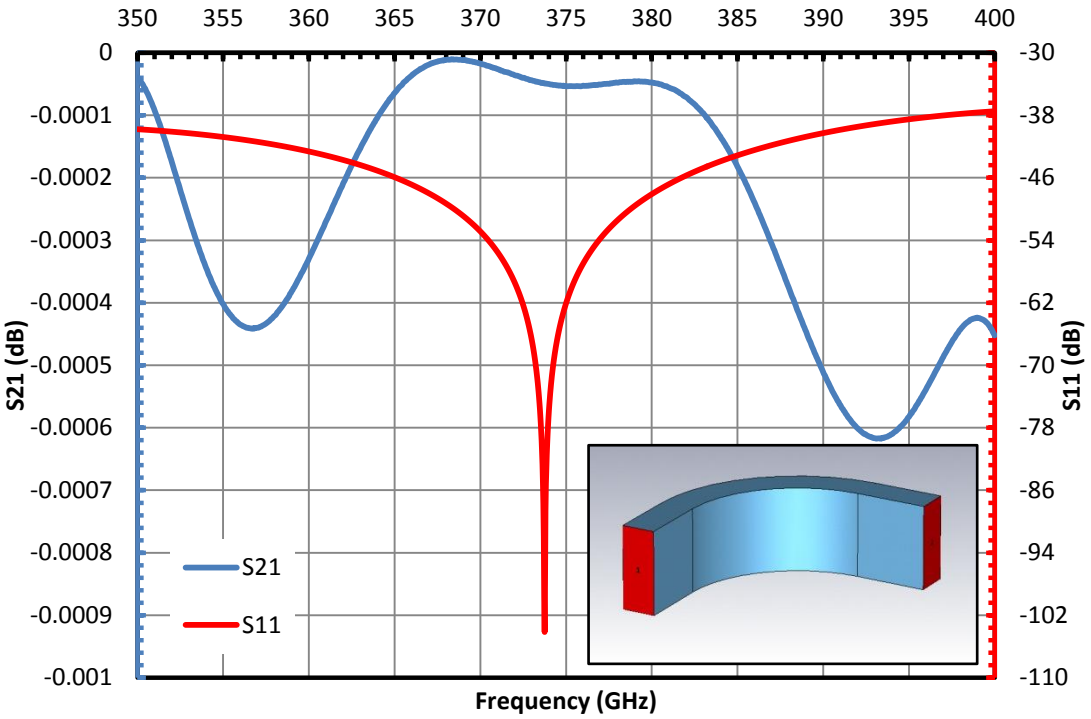

Fig. 6-6: Return loss and transmitted signal of 90° E-plane waveguide bend.

6.2.3. Design and Simulation

6.2.3.1. 372 GHz Stepped-Transition Input Coupler

The 372 GHz HOM stepped transition input coupler was designed using CST-MS to couple the TE_{10}^{R} mode to the TE_{61}^{C} mode using the waveguide transition and E-plane

waveguide bend, designed in Section 6.2.2.1 and Section 6.2.2.3 respectively, adjoined to a circular cavity of radius (R). The average radius (R_0) of the 8-fold HCIW for the 372 GHz gyro-TWA is 1.24 mm; however, due to the enhanced coupling complexity to the TE_{61} mode, a small taper may be employed between the input coupler and the HCIW to permit maximum coupling into the interaction cavity. Therefore, R can be varied within 1.00 mm (cut-off radius of TE_{61} at 360 GHz) to 1.24 mm to support the desired TE_{61} mode and meet the 8-fold HCIW requirements. Therefore, optimisation of R may be carried out on the TE_{61} input coupler. The beam tunnel is coupled to the rectangular input port from two discrete waveguide branches which consist of 3 E-plane bends adjoined to the stepped waveguide transition. The two waveguide branches evenly split the signal from the input port (Port 1), propagating the divided wave in the ± x-direction before propagating the two synchronous signals into the beam cavity. The progression of the mm-wave propagation in the x-z plane is shown in Fig. 6-7.

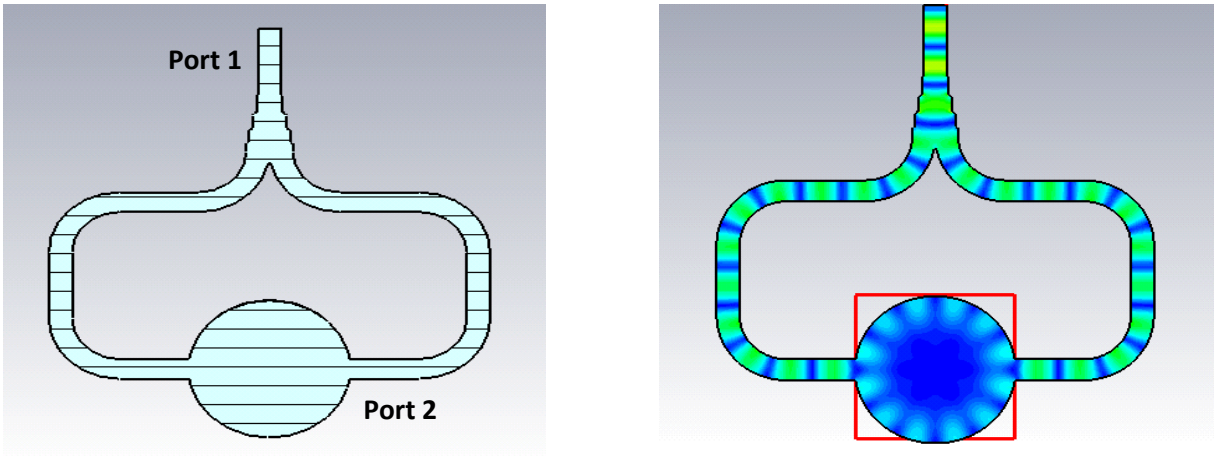

Fig. 6.7: View of stepped transition waveguide coupler x-z plane and field progression.

Fig. 6-7 highlights coupling to the TE_{61}^{C} mode for an optimised beam radius (R) of 1.03 mm. The generated HOM will be able to freely propagate towards the HCIW and the diode region of a gyro-TWA without the termination of Port 3, the port defined as being adjacent to the electron gun. In Chapter 3 and Chapter 5, a Bragg reflector was employed to reflect incident wave energy whilst maximising the beam tunnel diameter. However, for the 372 GHz gyro-amplifier, the average electron beam radius (r_b) from the cusp electron gun is 0.20 mm [6.22]; therefore, due to the oversized cavity a cut-off waveguide may be employed

to prevent the propagation of incident radiation into the cavity diode, without affecting the electronic efficiency. The cut-off radii (R_C) of the lower order coupled TE modes are shown in Table VI-III. A parametric optimisation of R_C is performed with a range of (0.70 – 0.85) mm to potentially cut-off all modes above the TE_{41} mode whilst ensuring a large beam tunnel diameter. The numerical scattering of a 372 GHz stepped transition waveguide splitter input coupler with R = 1.03 mm and optimised cut-off radius, R_C = 0.80 mm, is shown in Fig. 6-8. The distance between the near edge of the rectangular waveguide branches and the waveguide reflector (L_1) is 0.278 mm. The microwave field progression of the input coupler in the *x-y-z* plane is shown in the inset with port numbers defined.

Table VI-III: Cut-off Radii of Potential TE Coupling Modes at 360 GHz.

TE Mode Number	Cut-off radii (R_C) (mm)
TE_{11}	0.244
TE_{21}	0.405
TE_{41}	0.705
TE_{12}	0.707
TE_{22}	0.889
TE_{61}	0.995

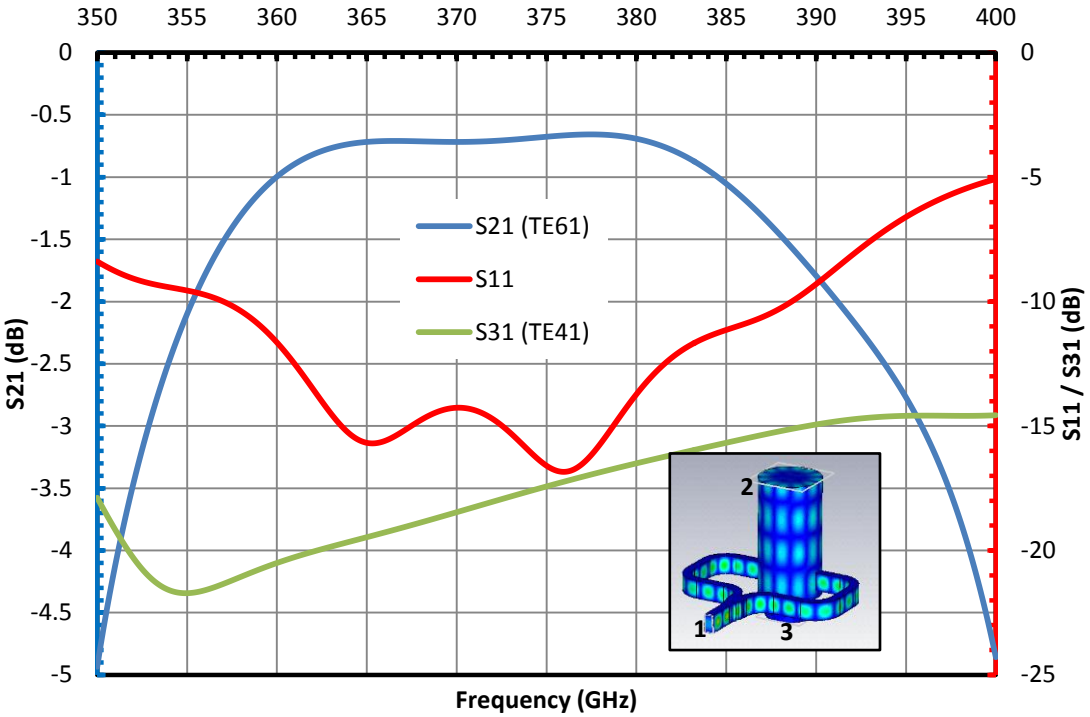

Fig. 6-8: Transmission and reflection of a 372 GHz TE_{61} stepped waveguide splitter input coupler.

Fig. 6-8 highlights the input coupler transmission loss from TE_{10} – TE_{61} mode is > -1 dB between 360 – 384.5 GHz, equating to a bandwidth of ~ 6.5%. Therefore, the coupler topology, constructed from the stepped transition waveguide (Section 6.3.2.1) and E-plane waveguide bends (6.3.2.3), is suitable for application to a 372 GHz gyro-TWA. The cut-off waveguide (R_C = 0.80 mm) has shown to be effective at preventing wave propagation towards the cavity diode with the signal magnitude of the dominant TE_{41} mode equal to < -15 dB; therefore, no field resultant field perturbation in the cavity diode will be witnessed. Coupling to the TE_{21} and TE_{41} modes is < -15 dB highlighting the accurate mode selectivity of the coupler topology. The higher order TE_{81} and $TE_{10,1}$ are below the cavity cut-off and will not propagate.

6.2.3.2. 372 GHz Tapered Waveguide Input Coupler

A 372 GHz TE_{10}^{R} – TE_{61}^{C} input coupler with a tapered waveguide signal splitter is designed based on the tapered waveguide transition and E-plane waveguide bend designed in Section 6.2.2.2 and Section 6.2.2.3. The construction of the input coupler from the rectangular waveguide components and beam tunnel optimisation was performed as

outlined in Section 6.2.3.1. However, unlike the stepped transformer waveguide optimisation, it was found that a b_0 reduction improved the coupling efficiency. Therefore, the waveguide height was reduced to 0.235 mm (b_1 = 0.470 mm). The beam tunnel and cut-off waveguide radii were optimised for R = 1.03 mm and R_C = 0.80 mm with L_1 = 0.272 mm. The R and R_C values are consistent between the stepped waveguide and tapered waveguide input couplers. The input signal progression for the tapered waveguide input coupler in the x-z plane is shown in Fig. 6-9 with the transmission and reflection of the 372 GHz input coupler shown in Fig. 6-10.

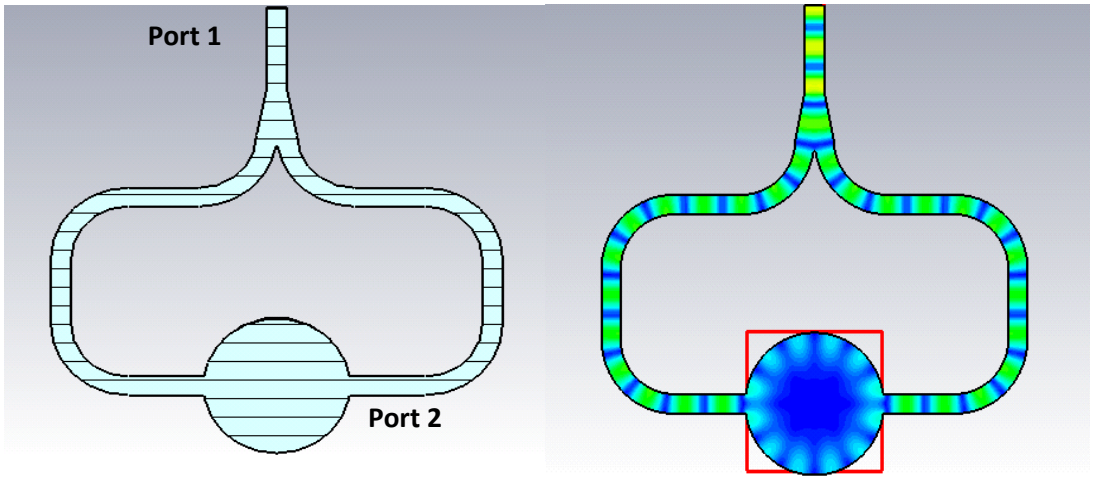

Fig. 6-9: Microwave field progression in x-z plane for tapered waveguide splitter input coupler.

Fig. 6-10 highlights the 372 GHz TE_{10}^{R} – TE_{61}^{C} tapered waveguide splitter input coupler operating between 359 – 385 GHz. The bandwidth of the input coupler equates to ~ 7% with an increased bandwidth of 1.5 GHz compared with the stepped waveguide splitter input coupler (Section 6.3.3.1). The cut-off waveguide reflector (R_C = 0.80 mm) is effective at preventing significant wave power from propagating towards the electron gun with a signal level of < -15 dB for the dominant TE_{41} mode. The coupler shows a high TE_{61} mode selectivity performance with low magnitude coupling to subsequent LOM's and HOM's. The electron beam will occupy ~ 25% of the cut-off reflector; hence, the potential of electron bombardment on the cavity boundaries is minimal. Reflected power at the input port (Port 1) is < -12 dB over the operating bandwidth of 360 – 384 GHz. The fabrication of a tapered waveguide splitter is less complex than the intricate stepped transformer waveguide where difference between step heights is as low as 14 µm; therefore, due to the small increase in

bandwidth and an ease in manufacturing complexity the 372 GHz tapered waveguide input coupler will be selected for use on a low-THz gyro-TWA.

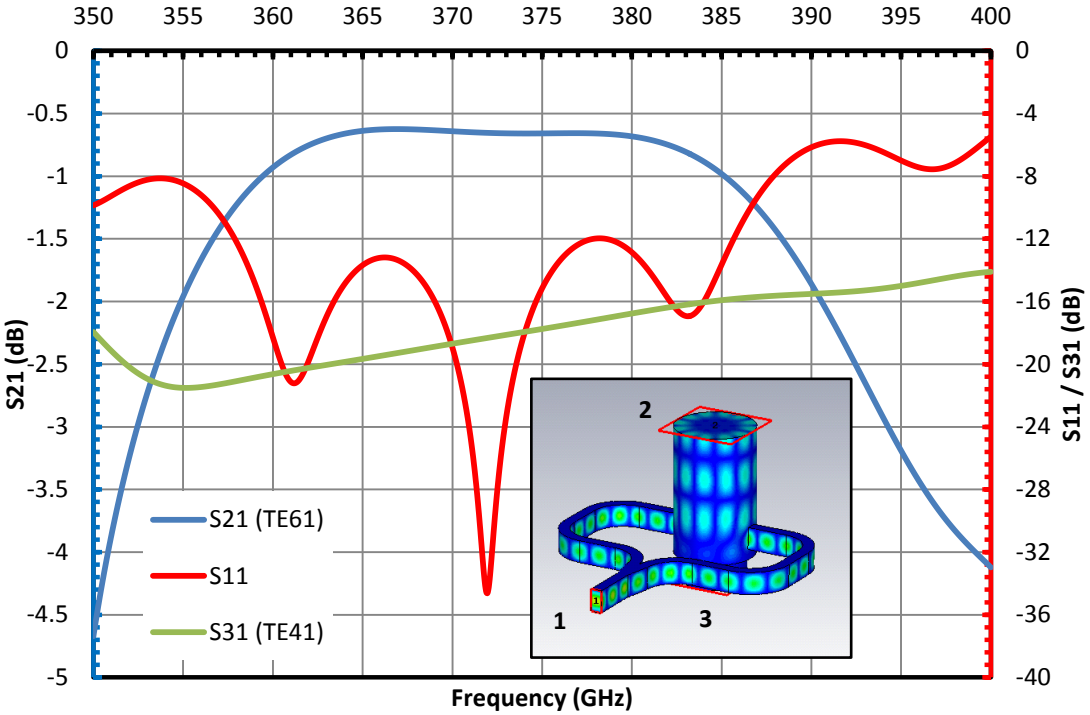

Fig. 6-10: Numerical scattering of a TE_{10} – TE_{61} tapered waveguide splitter input coupler.

6.2.4. Tolerance Study

A tolerance study was performed on the 372 GHz tapered waveguide input coupler (Section 6.2.3.2) to test the feasibility of the coupler performance with parametric discrepancies resulting from fabrication tolerances. Initially, the rectangular splitter waveguide is analysed. The parameters which govern the rectangular input waveguide dimensions (a, b, L_t and R_{IN}) were varied from the optimum value to test the tolerance range over which the coupler may operate with the desired bandwidth and coupling strength. A plot of waveguide width variation (a) for fixed values of b and L_t is shown in Fig. 6-11. The resultant change to the transmission coefficient for Δa = ± 20 µm, shown in Fig. 6-11, highlights an operational frequency shift of ~ 0.5 GHz for a 10 µm variation. A frequency shift of 0.5 GHz magnitude would not affect the coupler performance at 360 – 384 GHz; however, larger magnitude a discrepancies would result in a frequency shift out with the desired bandwidth. The waveguide height (b) was varied for fixed a and L_t. The investigation

highlighted minimal frequency or coupling strength response for Δb = ± 20 µm; therefore, the waveguide height has no strict tolerance requirement. The taper length (L_t) is subsequently varied with no detrimental effects on coupling performance for ± 25 µm. The waveguide bend radius (R_{IN}) is investigated with optimum values of a, b and L_t. For R_{IN} values of ± 100 µm, no effect on coupling strength or frequency response is observed. However, an R_{IN} increase will result in enhanced waveguide losses due to an increase in propagation length. The coupler performance as a result of rectangular waveguide discrepancies remains broadly unaffected.

An investigation into the coupled cavity is subsequently performed for R and L_1. The cavity radius (R) should be carefully manufactured to ensure a tight tolerance. Fig. 6-12 shows the effect of up to ΔR = ± 20 µm on the tapered input coupler performance. The effect of R variations is shown to have a significant effect on the coupler centre frequency with a 10 µm discrepancy in R resulting in a 3 GHz shift. Hence, the machining of R must be very precise.

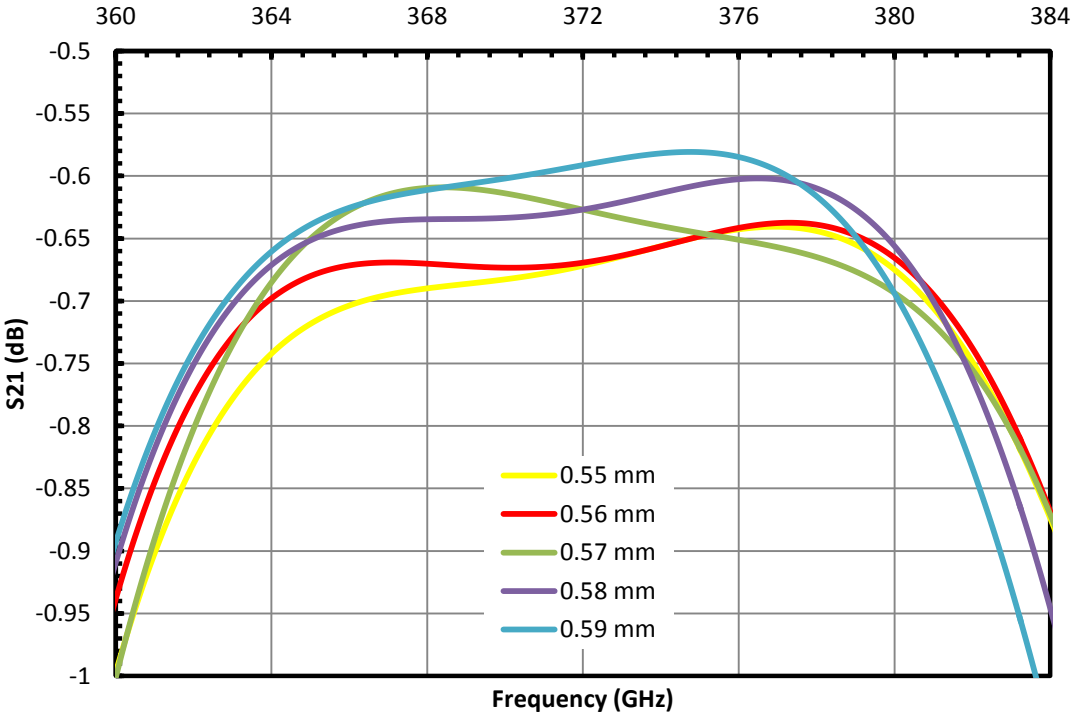

Fig. 6-11: Effect of a parametric variation on TE_{61} input coupler transmission response.

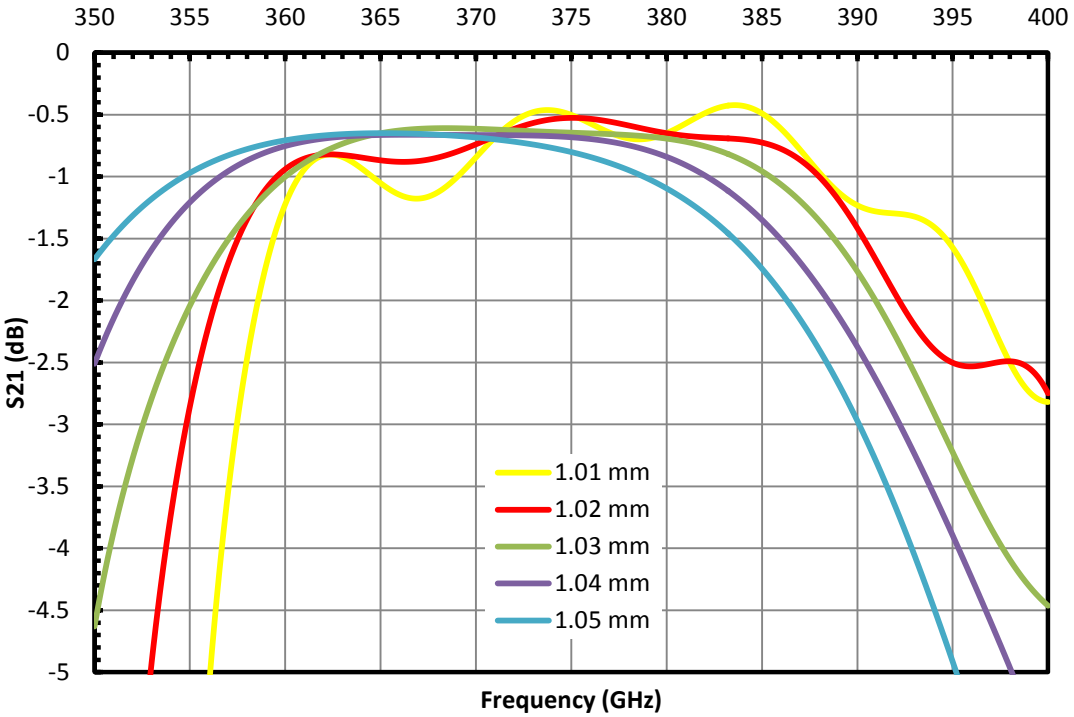

Fig. 6-12: TE_{61} Input coupler transmission with *R* variations.

A review of the L_1 parameter was performed. A plot of the effect of 25 µm variations on the input coupler operational frequency is shown in Fig. 6-13. Alterations resulting in 25 µm increases to L_1 are shown to decrease the centre frequency by ~ 2 GHz. The discrepancies to L_1, which result in a phase mismatch between the incident and reflected wave at Port 3, is shown to affect the coupler bandwidth and coupling strength with deviation from the optimum.

The tolerance study has investigated the effect of parametric discrepancies, resulting from manufacturing tolerances, on the input coupler transmission response. The input coupler is shown to exhibit stable performance characteristics for variations in the rectangular input waveguide and tapering section (a, b, L_t and R_{IN}), with the largest frequency shift of ~ 0.5 GHz caused as a result of ± 10 µm a variation. However, the coupler cylindrical cavity must be accurately fabricated to ensure the input coupler remains operational between 360 – 384 GHz.

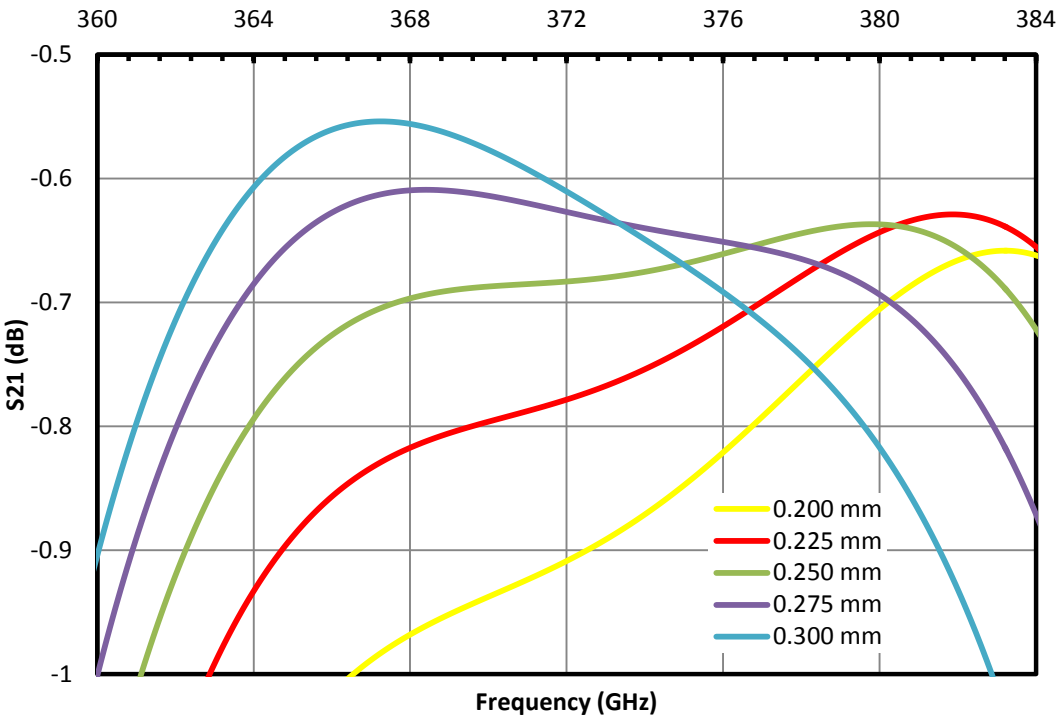

Fig. 6-13: Effect of L_1 variation on input coupler transmission response.

6.3. TE_{61} Input Coupler Manufacture

A W-band prototype TE_{61} tapered power splitter input coupler was manufactured within a (70.0 x 50.0 x 50.0) mm aluminium block. The waveguide coupler is employed as the input and output section of the passive component to permit direct connection to a VNA, eliminating the requirement for a circular-to-rectangular mode convertor. The coupler was scaled to operate at 90 – 96 GHz due to limitations on achievable tolerances using in-house manufacture. The circular coupled waveguide is scaled directly with a 4x dimension increase on the 372 GHz design. The rectangular input waveguide was designed to maintain the aspect ratio used in the 372 GHz design between standard WR2.2 (a' x b') waveguide and a x b_0. A tapered section from standard W-band waveguide ((2.54 x 1.27) mm) to the optimised coupler waveguide is included in the scaled design. A technical drawing of the input coupler block is shown in Fig. 6-14. A numerical model of the TE_{61} input coupler with additional waveguide taper, scaled to operate within the W-band, is shown in Fig. 6-15.

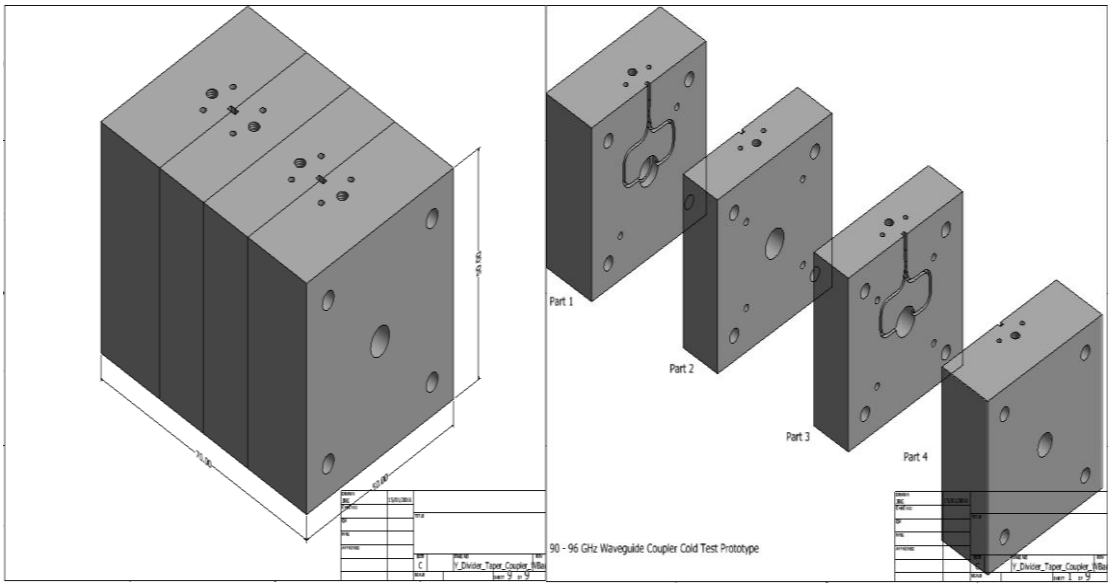

Fig. 6-14: Technical drawing of 4-part TE_{61} coupler with a power splitting waveguide taper.

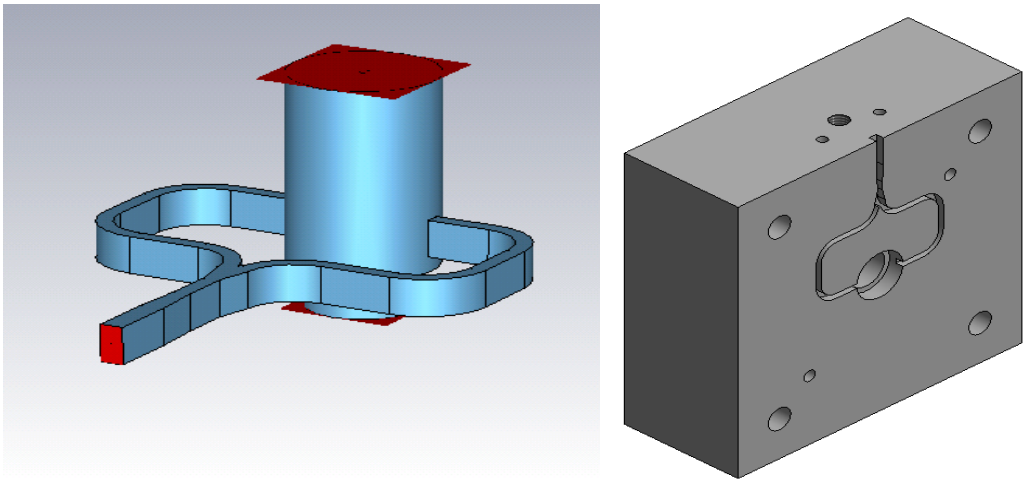

Fig. 6-15: (L) A numerical model of the waveguide coupler and (R) a CAD model of a machined block from the prototype coupler.

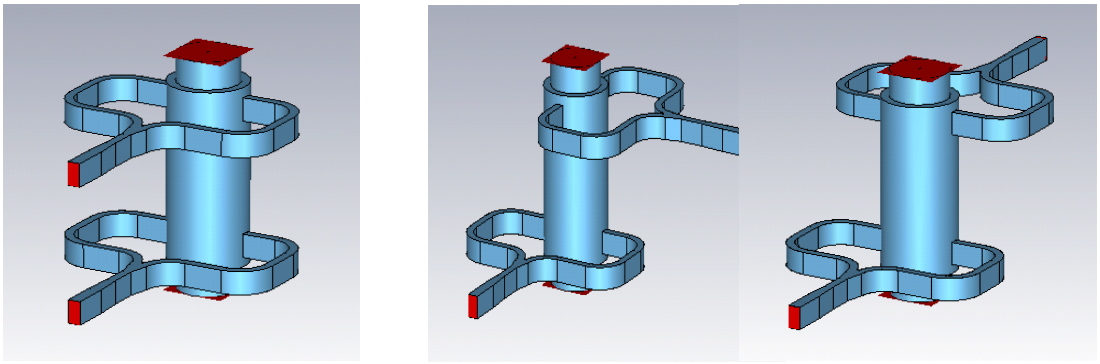

Fig. 6-16: Potential orientation of split-block coupler VNA setup with (L) ϑ_{rot} = 0° (C) ϑ_{rot} = 90° and (R) ϑ_{rot} = 180°.

The aluminium block was split into four discrete sections with two end sections and two centre sections. The end section length in Fig. 6-14 (Part 1 and 4), L_{end} = 20.0 mm and the centre section length (Part 2 and 3), L_{cent} = 15.0 mm. The waveguide channel was manufactured into each split-block using a 3-axis Computer Numerically Controlled (CNC) milling technique. A Computer Aided Design (CAD) model of the rectangular waveguide channel was programmed into a Haas Tool Room Mill using OneCNC software which defines the tool path. The tool path was machined into each split-block using a 0.60 mm end mill with half the waveguide channel width (1.27 mm depth) milled into each aluminium block (Fig. 6-15). A 3-section coupler geometry was initially proposed; however, the length of the end mill cutter would prohibit the machining of the full waveguide width into a single block. The circular waveguide and waveguide reflector radii (R = 4.10 mm and R_c = 3.20 mm) were subsequently drilled into Part 1 and Part 4 using the CNC machine with the waveguide through holes of radius R machined into Part 2 and Part 3. Alignment pin holes (Ø = 2.0 mm) were machined and alignment pins subsequently attached. The pin holes were placed to allow for experimental analysis with the input and output waveguide couplers at a rotation angle (ϑ_{rot}) of 0°, 90° and 180°. A diagram of the ϑ_{rot} orientation is shown in Fig. 6-16. The manufacture of the prototype TE_{61} waveguide coupler was completed with the machining of holes for split-block connection and experimental setup. Clearance holes (Ø = 1.59 mm) and tapped screw holes (Ø = 2.85 mm) were machined into the split-block coupler to allow for direct attachment to a W-band waveguide flange. A series of 4 through holes were machined into each block (Ø = 4.20 mm) to allow for the insertion of M4 threaded rod. The threaded

rods, in conjunction with threaded nuts, are used to clamp the split-block structure to prevent any loss of signal between the block faces. A series of images from the split-block input coupler are shown in Fig. 6-17.

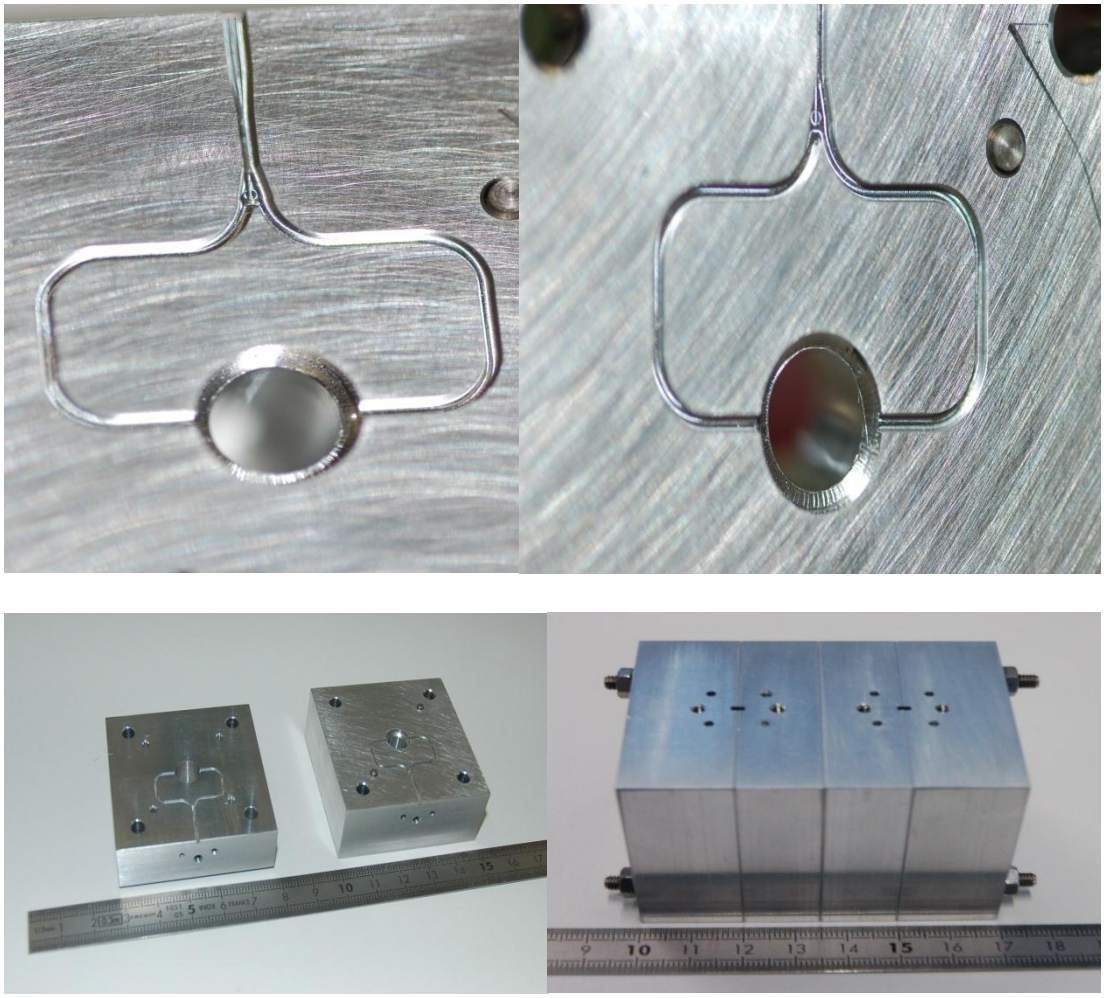

Fig. 6-17: Images of the TE_{61} split-block waveguide input coupler.

6.4. Input Coupler VNA Testing: Experimental Setup

A schematic of the experimental setup of the W-band TE_{61} prototype waveguide split-block coupler is shown in Fig. 6-18. The analysis of the input and output power splitting waveguide convertor was conducted with ϑ_{rot} = 180°. The experimental study was performed on an Anritsu 37000D Lightning series VNA with attached OML heads to improve the dynamic range to 75 – 110 GHz. An Offset Short Load Through calibration technique,

discussed in Section 3.4.3, was used to eliminate any internal losses from the VNA components and calibrate the phase mismatch between Port 1 and Port 2. The calibration technique was used to optimise the performance of the VNA at 84 – 104 GHz; incorporating the operating frequency range of the prototype HOM input coupler (90 – 96 GHz). Images of the attachment of the coupler split-block to the VNA are shown in Fig. 6-19.

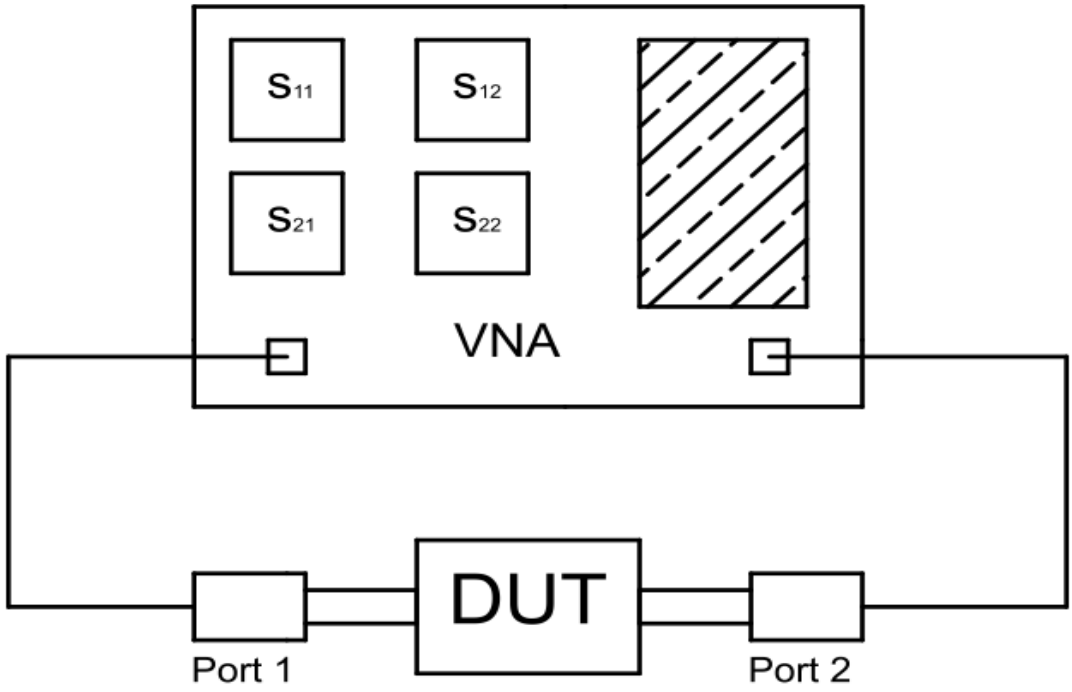

Fig. 6-18: Schematic of VNA testing of prototype TE_{61} split-block waveguide coupler.

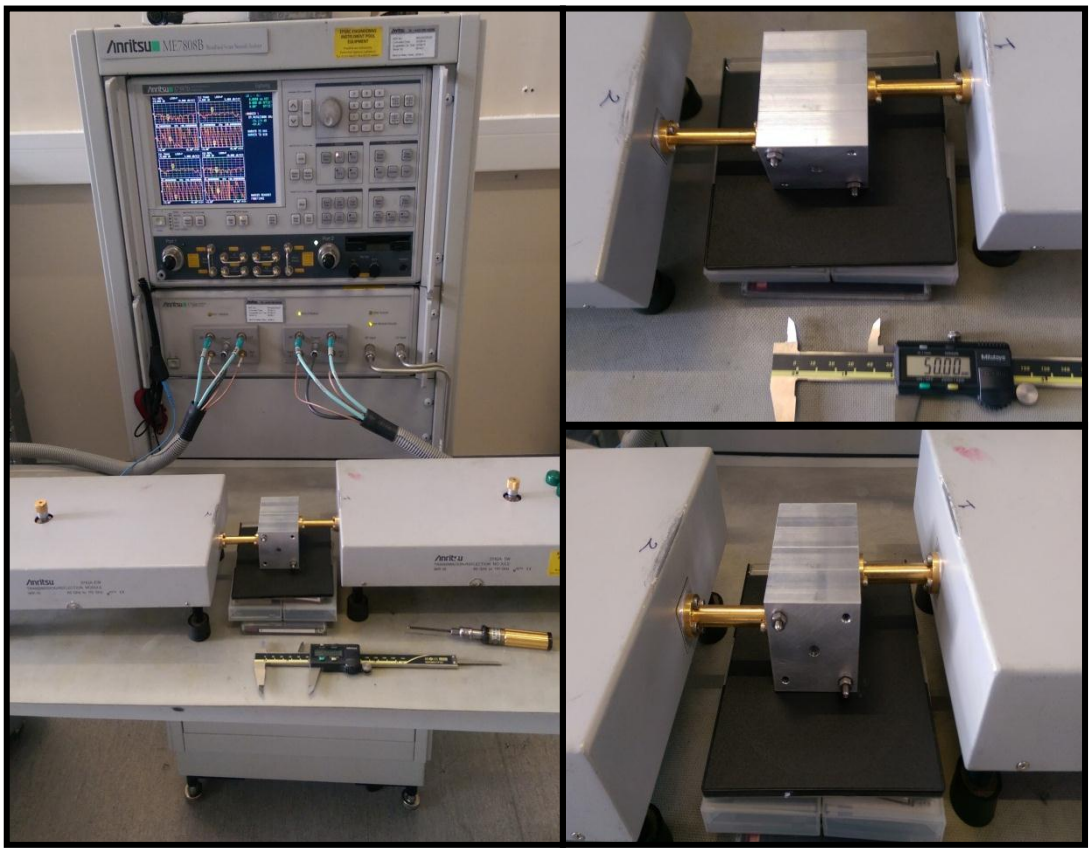

Fig. 6-19: Split-block coupler VNA experimental setup.

6.5. Input Coupler VNA Testing: Results

The W-band prototype tapered waveguide splitter input coupler is scaled from the design shown in Section 6.2.3.2 to operate at 90 – 96 GHz. A comparison of the 94 GHz and 372 GHz waveguide coupler dimensions is shown in Table VI-IV. A discrepancy between the designed and manufactured parameter sets was highlighted with precision measurement of the manufactured waveguide channel (Fig. 6-17) using a travelling microscope. Detailed measurement of the waveguide parameters will allow for comparison between the VNA coupling and reflection and simulation results with an accurate modelled parameter set. The manufactured parameter set is included in Table VI-IV. A comparison of the 90 – 96 GHz waveguide coupler numerical scattering with the designed and actual parameter set is shown in Fig. 6-20. The parameter discrepancies caused by manufacturing tolerances are

shown to down shift the operating frequency range of the W-band tapered waveguide coupler.

A comparison of the coupler numerical reflection for the designed and actual parameter set and VNA reflection results is shown in Fig. 6-21. The VNA setup included a single waveguide coupler consisting of two waveguide blocks (Fig. 6-14) with Port 2 and Port 3 propagating into air. The CST-MS model (Fig. 6-15) was modified to remove the circular waveguide ports (Port 2 and Port 3) and replaced with an open boundary at each circular structure face. The modifications improve correlation between the numerical and physical experimental setup.

Fig. 6-21 shows the measured VNA reflection from the rectangular input port (Port 1) is in good agreement with CST-MS simulation results when open boundaries replace waveguide ports at Port 2 and Port 3. The S_{11} insertion loss at the input port is < 10 dB between 90 – 96 GHz with a minimum reflection of ~ -25 dB; therefore, > 90% of incident radiation is propagated into the waveguide channel. The simulated and measured reflectivity magnitude exhibits close correlation at all considered frequencies (84 – 104 GHz).

Table VI-IV: Parameter Comparison between 372 GHz and 93 GHz Waveguide Coupler Design.

Parameter	372 GHz Design (mm)	93 GHz Design (mm)	93 GHz Actual (mm)
R	1.030	4.10	4.12
R_C	0.800	3.20	3.45
a	0.570	2.60	2.60
a'	0.560	2.54	2.60
b_0	0.235	0.95	0.90

b'	0.280	1.27	1.23
b_1	0.570	1.90	1.80
R_{IN}	0.800	2.72	2.75
R_{OUT}	1.085	3.67	3.65
L_1	0.272	1.10	1.17

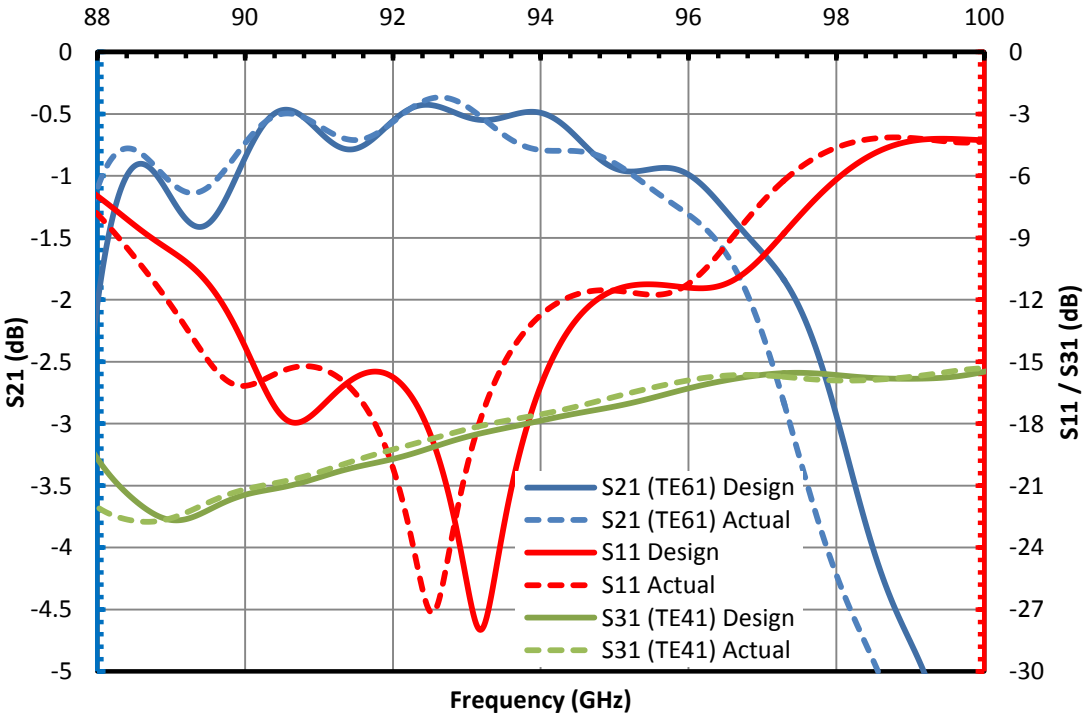

Fig. 6-20: Simulated transmission and reflection of W-band split block coupler for design and actual parameter sets.

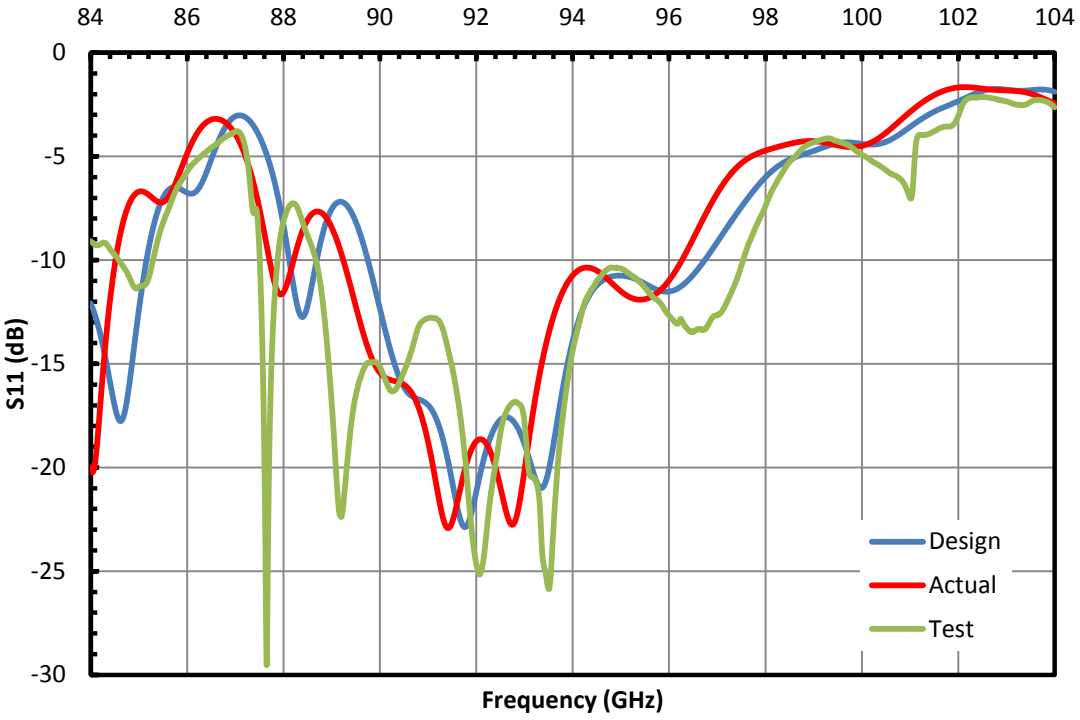

Fig. 6-21: Measured VNA reflection of single tapered waveguide input coupler compared to numerical reflection.

A measurement of the W-band coupler transmission was made with the VNA experimental setup shown in Fig. 6-19. The two discrete coupling sections were positioned at ϑ_{rot} = 180°. The waveguide coupler will convert $TE_{10}^{R} - TE_{61}^{C} - TE_{10}^{R}$ allowing for direct detection of the signal magnitude at VNA Port 1 and VNA Port 2. An aluminium background with reduced electrical conductivity (0.35×10^{7} Sm^{-1}) was employed to compare with the idealised PEC background. The waveguide reflector boundary, at either end of the circular cavity waveguide, was modelled with an open port to replicate the VNA setup. The E-field progression within the dual coupler is shown in Fig. 6-22 and the measured transmission compared to numerical data is shown in Fig. 6-23.

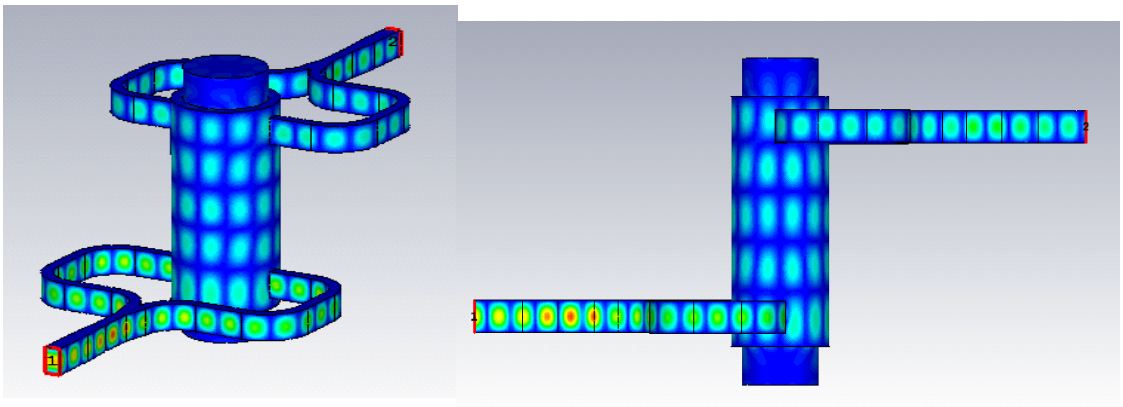

Fig. 6-22: E-field conversion and progression in W-band HOM prototype coupler experimental setup.

The transmission of the W-band HOM coupler (Fig. 6-23) is shown to be affected by resonances between the two coupling structures for the numerical and experimental setups. The inclusion of a waveguide reflector at opposing ends of the circular waveguide creates a resonant cavity; hence, energy is lost to cavity loading alongside attenuation in the waveguide walls. The internal reflections within the cavity result in a loss of coupling strength at resonant frequencies. Transmission loss in the back-to-back waveguide coupler averages at ~ 3dB equating to an individual coupler loss of -1.5 dB. The circuit loss in an individual aluminium coupler block is measured at -1 dB; therefore, high mode conversion is exhibited by the HOM waveguide coupler.

The cavity resonances are displayed in the S_{11} VNA measurement when the two coupling sections are analysed in the experimental setup. A comparison of the coupler reflectivity for a single coupling section and a dual coupler at ϑ_{rot} = 180° is shown in Fig. 6-24. A clearer indication of the coupler transmission would be provided if a TE_{61}^{C} – TE_{10}^{R} mode convertor [6.23 – 6.25] was designed with initial radius *R* and tapered to rectangular waveguide of cross-section *a* x *b*. However, the prototype coupler has allowed for accurate evaluation of the waveguide reflectivity and > 90% of incident radiation is propagated into the circular waveguide. Therefore, an improved experimental setup is likely to enhance the observed coupling coefficient from VNA testing of the HOM coupler prototype.

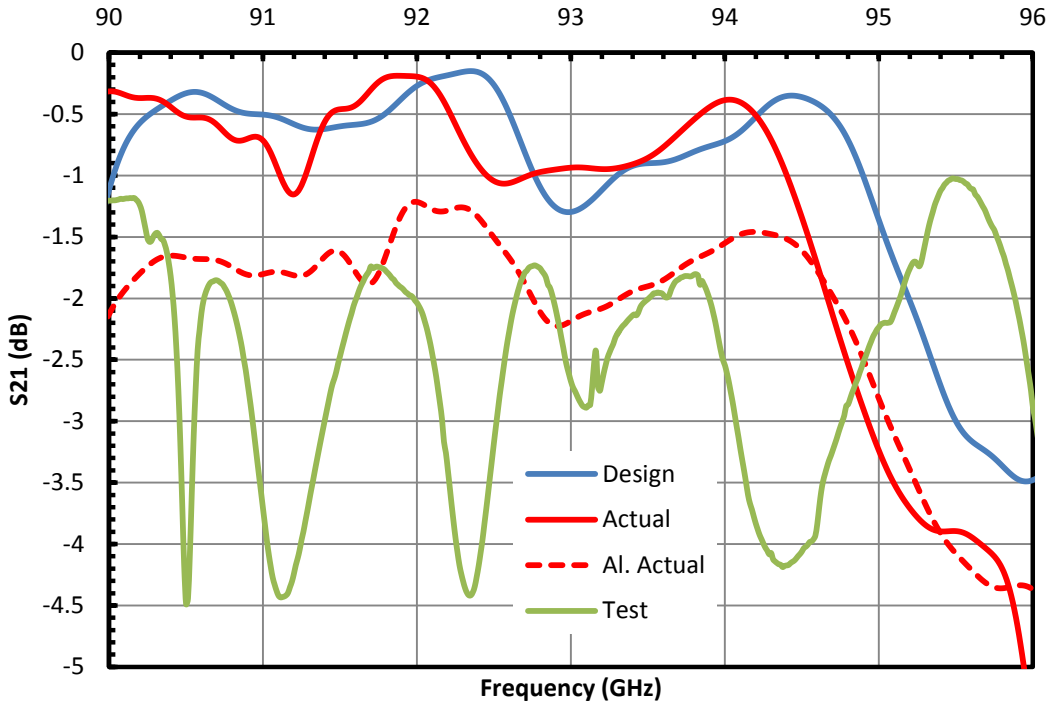

Fig. 6-23: Numerical and experimental transmission of W-band split-block HOM input coupler.

To confirm the mode of conversion, an additional waveguide section of length 3.00 mm was manufactured and inserted between the two couplers to measure the phase response. The measured phase is then compared with the theoretical phase response of the TE_{61} mode in a waveguide of radius R = 4.10 mm. The theoretical and measured phase is shown in Fig. 6-25. The phase measurement has close correlation to the theoretical TE_{61} phase at 88 – 98 GHz; therefore, the waveguide coupler is shown to have a high TE_{61} mode conversion efficiency. The insertion loss (< 10 dB) and phase measurements suggest > 90% transmission to the TE_{61} mode.

6.6. Discussion of HOM Input Coupler Design

The design of a 372 GHz TE_{10}^{R} – TE_{61}^{C} input coupler for a gyro-TWA, based upon a waveguide power divider, has been presented. The design of the HOM input coupler focussed upon achieving a broadband coupling with a high transmission coefficient whilst ensuring the TE_{61} mode was dominant within the coupled cavity. Two input couplers were presented for investigation; an input coupler with a stepped waveguide transition and an input coupler with a tapered waveguide transition were modelled to couple the TE_{61} mode

into a circular waveguide cavity with high mode purity. A coaxial cavity input coupler was discussed as possible solution to HOM waveguide coupling; however, the potential bandwidth achievable with the coupler topology (~ 3%) is not sufficient for application to a 360 – 384 GHz gyro-TWA.

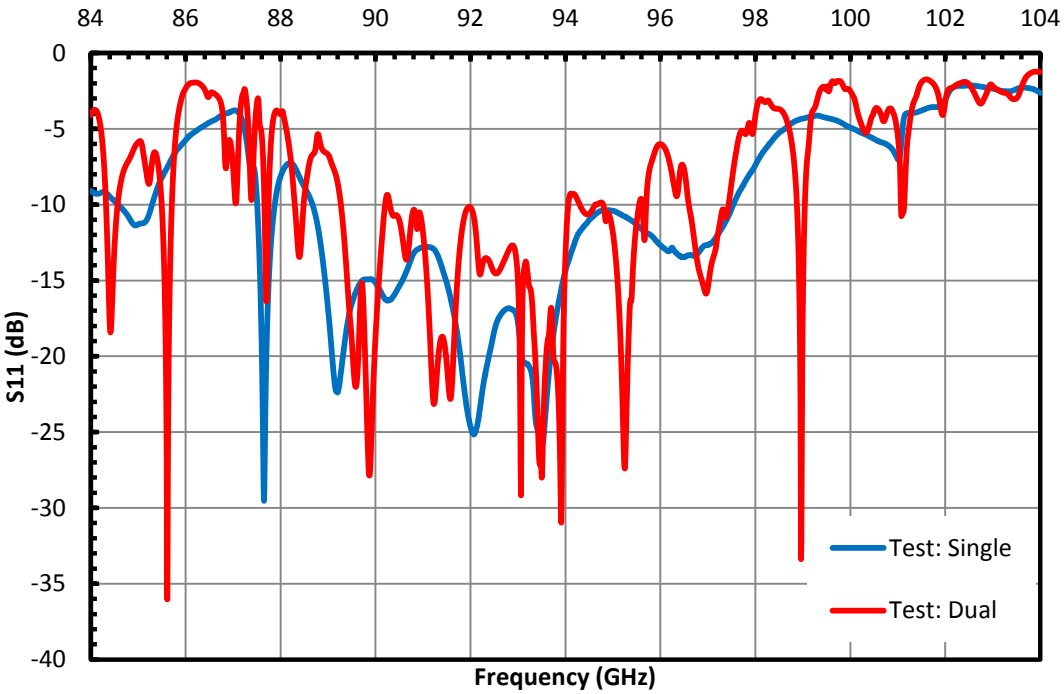

Fig. 6-24: Comparison of reflectivity for a single coupler and dual coupler VNA setup.

The two power divider input couplers were designed with low loss rectangular waveguide components. The stepped waveguide transition and the tapered waveguide were shown to have a return loss of < -35 dB and < -27 dB respectively. The incident split signal was coupled into a circular waveguide through smooth walled E-plane waveguide bends. The waveguide bends had a reflection coefficient of < -40 dB over the 360 – 384 GHz operating bandwidth. The stepped transition input coupler and the tapered waveguide input coupler achieved respective bandwidths of 6.5% (360 GHz – 384.5 GHz) and 7% (359 GHz – 385 GHz). The tapered waveguide input coupler was selected to be used on a gyro-TWA due to the reduced complexity in fabrication and broad bandwidth.

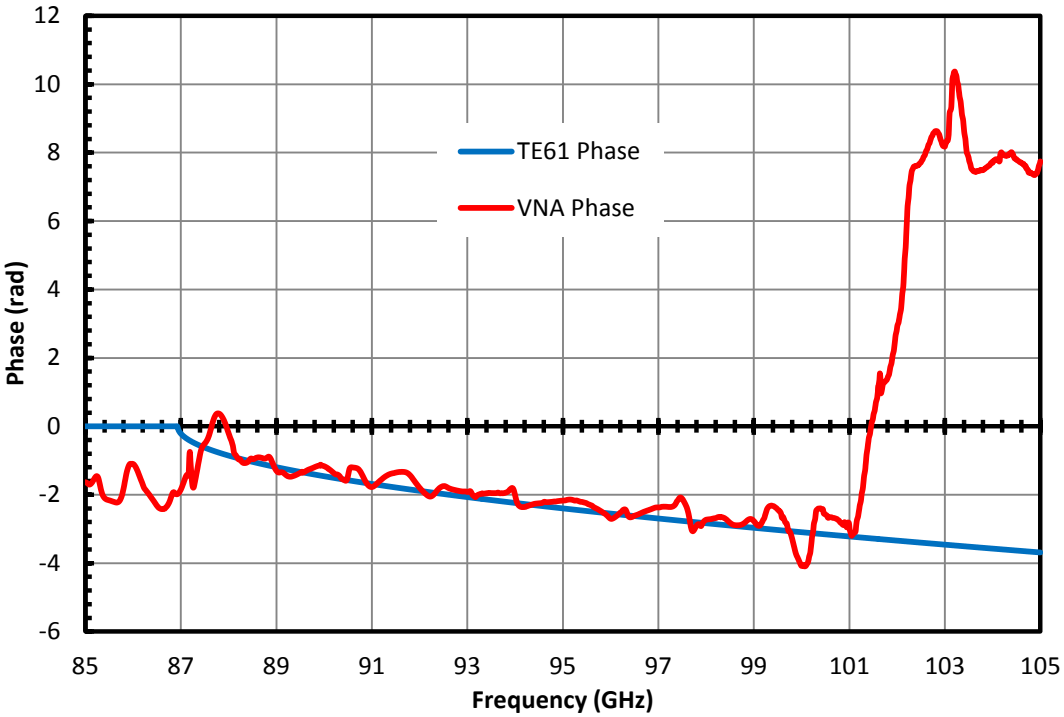

Fig. 6-25: Theoretical and numerical dispersion of TE_{61} mode in W-band coupler.

A tolerance study of the TE_{10}^{R} – TE_{61}^{C} tapered waveguide input coupler was performed to analyse the effect of manufacturing discrepancies on the coupler performance. The coupler was shown to be stable with manufacturing discrepancies associated to the rectangular splitter waveguide. A maximum coupling change of 0.1 dB was observed for 20 µm variations of a corresponding to a frequency shift of ~ 0.5 GHz. An investigation into the coupled cylindrical beam tunnel, however, highlighted a frequency and coupling strength sensitivity with R and L_1 variations. For ΔR = ± 10 µm, a 3 GHz centre frequency shift was observed and for ΔL_1 = ± 25 µm the centre frequency was shifted by ~ 2 GHz. A decrease in coupling strength was also associated with R and L_1 discrepancies (Fig. 6-12 and Fig. 6-13). Therefore, to ensure high coupling over the desired 360 – 384 GHz bandwidth the beam tunnel must be accurately manufactured with strict tolerances applied.

At 372 GHz, the skin depth of a mm-wave signal in a copper waveguide is ~ 0.1 µm. Hence, the depth at which the signal propagates within the waveguide wall is comparable to, or smaller than, the surface roughness. Therefore, Ohmic losses will increase with an uneven waveguide finish. The consequences of Ohmic losses on the tapered waveguide input

coupler need to be analysed to estimate the effect of the signal attenuation on the coupler performance. While there is no comprehensive measured metallic conductivity as a function of the surface roughness published at the operating frequency, an arbitrary reduction factor of 12 was applied to a copper background (0.5×10^7 Sm^{-1}) to monitor the potential losses within the tapered waveguide coupler. The coupling strength at 372 GHz, numerically simulated with CST-MS, was shown to decrease by 0.91 dB with a coupling strength of -0.77 dB for a perfect electrical conductor (PEC) background material and -1.68 dB for a reduced conductivity copper background. A smooth surface finish must (R_a = 2 – 3 μm) be achieved in manufacture to ensure a high TE_{61} coupling factor.

A W-band TE_{61} prototype coupler was manufactured to allow for VNA testing of the tapered waveguide input coupler. A CNC milling technique was used to machine a waveguide channel designed to operate at 90 – 96 GHz. The waveguide dimensions were scaled from the optimised 360 – 384 GHz TE_{10}^{R} – TE_{61}^{C} tapered waveguide input coupler. The 4-piece aluminium split block coupler design allowed for VNA testing of the coupler transmission and reflection. The measured S_{11} reflection from the input rectangular port (Port 1) of the coupler structure was shown to be < -10 dB between 90 – 96 GHz. The VNA measurement agreed well with simulated data, suggesting ~ 90% of incident radiation is transmitted into the circular coupled waveguide. A transmission and phase measurement with a reciprocal input coupler was presented. The phase difference analysis permitted the determination of the TE_{61} conversion into the coupled waveguide with the measurement shown to be in good agreement with theoretical TE_{61} phase over the operating bandwidth. However, the resultant transmission coefficient, from simulation and measurement results with the input and output ports rotated at ϑ_{rot} = 180°, are subjected to cavity resonances caused by the inclusion of waveguide reflectors at each end of the coupled waveguide. The average transmission over the operating bandwidth is ~ 3 dB. A proposed modification has been made which involves the inclusion of an axial TE_{61}^{C} – TE_{10}^{R} mode convertor into the experimental setup to improve the measured coupling performance. However, the coupler prototype allowed for the detailed analysis of manufacturing and measurement techniques applicable to the design of high frequency waveguide structures.

The manufacturing technique outlined for the W-band HOM input coupler may be used in the manufacture of a 372 GHz waveguide coupler; however, state-of-the-art micro-milling technology must be employed. High precision laboratories [6.26] have the capability to machine waveguide channels of 0.1 mm width with a positional accuracy of ± 0.3 µm using 5-axis micro-milling machines and an appropriate end-mill tool piece. A surface finish with R_a = ~ 2 µm would ensure that Ohmic losses would be minimised. Therefore, the design of a HOM power splitting waveguide coupler with waveguide *a* x *b* cross-section (0.57 x 0.24 mm) is realistic.

7. Conclusions and Future Work

7.1. 94 GHz Gyro-TWA Project

7.1.1. Input coupler

The design of a rectangular-to-circular side-wall input coupler was presented. The W-band T-junction coupler was designed to operate at 90 – 100 GHz with a TE_{10}^{R} – TE_{11}^{C} transmission loss of < 1 dB. A Bragg reflector was employed in the design to prevent wave propagation in the gun diode whilst maximising the beam tunnel diameter. A fundamental mode waveguide reflector was considered; however, the waveguide dimension may hinder beam transport and, hence, affect the gyro-TWA electronic efficiency. The design of a 15-section Bragg reflector was presented. A comparison between a numerical model and a VNA test of a manufactured Bragg reflector was included. The measured phase and reflectivity was shown to be in good agreement with the simulated data. The Bragg reflector achieved a reflection coefficient of > -1 dB between 90 – 100 GHz except for frequencies ~ 95 GHz where a cavity energy storage has occurred.

The Bragg reflector was attached to a rectangular-to-circular T-junction to form a 3-port TE_{10}^{R} – TE_{11}^{C} input coupler. The numerical model of the waveguide coupler with Bragg reflector was shown to have a bandwidth of 13.5% (89 – 102 GHz) where the transmission loss was < 1 dB. The Bragg reflector was effective at preventing wave propagation into the gun diode with a maximum signal magnitude of -10 dB delivered to Port 3. The waveguide coupler was shown to be frequency tuneable with variations in length *L* which serves to vary the reflection phase from the Bragg structure.

A spark erosion technique was used to manufacture a prototype W-band coupler suitable for VNA testing. The coupler transmission loss was shown to be ~ 1 dB between in the operating bandwidth which equates to a ~ 0.7 dB loss in transmission compared with the numerical model. The measured coupler reflection data was shown to be in good agreement with simulated data with a reflectivity of ~ -15 dB between 90 – 100 GHz.

The TE_{10}^{R} – TE_{11}^{C} waveguide coupler was incorporated in the design of a gyro-TWA with a 3-fold HCIW. The components required for the full amplifier system were outlined in Chapter 2 and Chapter 4.

7.1.2. 94GHz Gyrotron Travelling Wave Amplifier Experiments

In the W-band gyro-TWA experiment, stable amplification over the frequency range of 91 – 96.5 GHz was achieved from an electron beam of 55 kV and 1.5 A. The maximum gain was measured to be 38 dB at 94 GHz. The performance at higher input power levels and frequencies above 96.5 GHz were not measured due to limitations of the input drive source. The results were in good agreement with a simulated maximum output power of 10 kW and bandwidth of 91-100 GHz. The far field profile of the output horn from the gyro-TWA was shown to experimentally align with simulated power distribution after consideration of systematic angular uncertainties.

7.2. 372 GHz Gyro-TWA Project

7.2.1. Conclusions

The design of input coupler topologies for a fundamental mode 3-fold HCIW gyro-TWA and a HOM 8-fold HCIW gyro-TWA operating at 360 – 384 GHz has been presented. The design of a T-junction coupler and a multiple-aperture coupler focused on achieving a high coupling factor from the TE_{10}^{R} mode to the TE_{11}^{C} over a broad bandwidth (> 7%). The fundamental TE_{11} mode is coupled into a 3-fold HCIW which, in turn, generates an operating eigenwave through TE_{21} – TE_{11} mode coupling. The proposed gyro-amplifier design is similar to the operation of the W-band experiment. A comparison of the coupler topologies was presented. The operational frequency range of transmission for the T-junction input coupler with a Bragg waveguide reflector was shown to be 352 – 390 GHz. The bandwidth of the T-junction design (~ 10%) is limited because the required beam input port diameter is relatively large compared to the beam tunnel. The bandwidth of a 12-aperture multi-hole coupler is shown to be 35% (289 – 410 GHz) and the requirement of a frequency selective

waveguide reflector is eliminated. Therefore, a multiple-hole input coupler would be employed on a gyro-TWA with a 3-fold HCIW.

The design of a HOM input coupler for a gyro-TWA with an 8-fold HCIW was presented. The 8-fold waveguide generates an operating eigenwave from an incident TE_{61} mode to spatial harmonics of the cavity TE_{22} mode; hence, a TE_{10}^{R} – TE_{61}^{C} mode coupler was required. The use of an overmoded waveguide increases the coupled cavity cross section; however, the cavity is susceptible to parasitic oscillation. The input coupler design employed an incident TE_{10} wave splitter to reduce the LOM oscillation in the cylindrical coupled cavity. An input coupler topology with a stepped- and tapered-waveguide impedance matching section was designed. The couplers were designed to integrate low loss waveguide components to ensure maximum transmission into the coupled cavity. The stepped-waveguide input coupler and the tapered-waveguide input coupler exhibited respective bandwidths of 6.5% (360 GHz – 384.5 GHz) and 7% (359 GHz – 385 GHz). A broadband tapered-waveguide input coupler was chosen to be employed on an 8-fold gyro-TWA.

A review of machining tolerance effect on fundamental mode and HOM input coupler design was presented. Operation of the TE_{11} T-junction input coupler is dependent on accurate manufacture with variations in *a*, *b* and *R* shown to affect the coupling efficiency. Fig. 5-3 highlighted frequency shifting and coupling strength degradation with ± 20 µm *R* variations. The fundamental mode multiple hole coupler was shown to be maximally stable with *a*, *b* and *R* machining discrepancies; however, the coupler performance was shown to be sensitive to aperture variation (*R'* and *t*). A decrease in *R'* of 20 µm was shown to decrease coupling by 30% and a 25 µm increase in gap spacing (*t*) resulted in a 10 – 15% reduction in coupling efficiency. Therefore, the micro-hole drilling aperture manufacture must be precise to ensure a > 1 dB transmission loss. The HOM tapered-waveguide coupler operating bandwidth was shown to be stable with *a* and *b* variations associated with the power divider. However, an investigation into the coupled beam tunnel highlighted a frequency and coupling strength sensitivity with *R* and L_1 variations. For *R* = ± 10 µm, a 3 GHz centre frequency shift was observed and for L_1 = ± 25 µm the centre frequency was shifted by ~ 2 GHz. A decrease in coupling strength was also

associated with R and L_1 discrepancies. Therefore, the beam tunnel radius must be precision manufactured to ensure a high TE_{61} coupling coefficient.

The design objectives outlined for the TE_{11}- and TE_{61}-mode couplers were proposed to be realised under idealistic numerical conditions; however, to consider the performance of a manufactured mode coupler Ohmic losses were considered. The simulated waveguide losses for the fundamental mode T-junction coupler and multiple hole coupler with a reduced conductivity copper background were 0.25 dB and 0.42 dB respectively with corresponding bandwidths of 8% (357 – 387 GHz) and 28% (301 – 399 GHz). The coupling strength for the HOM input coupler at 372 GHz was shown to decrease by < 1 dB, a result of the increased waveguide length compared to the TE_{11} waveguide couplers. A smooth surface finish (R_a = 2 – 3 µm) must be achieved to limit signal loss to the waveguide wall for efficient high frequency mode couplers.

The manufacturing and VNA testing of a W-band prototype HOM input coupler was presented. A CNC micro-milling technique was employed to machine the scaled 372 GHz waveguide channel into a 4-block waveguide assembly. The prototype coupler design allowed for transmission and reflection measurement using a VNA. A 2-block setup was used to measure the coupler reflection at the rectangular input port. The measured return loss was shown to be < 10 dB between 90 – 96 GHz with a centre-band reflection of ~ -20 dB. The coupler numerical and VNA measured reflectivity results were shown to be in good agreement. A 4-block experimental setup was employed to measure the coupler transmission; however, the coupler transmission was shown to be affected by cavity resonances. The coupling coefficient between the simulated and VNA result is shown to be at similar levels (~ -1.5 to -2.0 dB at 92.5 – 94 GHz); however, the frequency response is unstable due to internal energy storage. A proposition to improve the transmission measurement, by incorporating an axial mode convertor into the experimental setup, was made.

7.2.2. Future Work

A prototype HOM input coupler operating at 360 – 384 GHz is to be manufactured by a high precision laboratory. The input coupler will be analysed using a travelling microscope to record a manufactured parameter set. The manufactured parameter set will be numerically modelled to compare the transmission and reflection of the tapered-waveguide input coupler with the designed and manufactured dimensions. VNA testing of the 372 GHz TE_{61} coupler will be undertaken. The transmission of the coupler will be studied by incorporating a low loss TE_{61}^{C} – TE_{10}^{R} mode convertor into the experimental setup. The improved coupler setup will ensure that the measured transmission is unaffected by cavity resonances.

A 372 GHz gyro-TWA with an 8-fold HCIW is to be designed and manufactured. The active and passive components required are consistent with those outlined in Chapter 2. A broadband TE_{61} input coupler, designed in Chapter 6, would be employed to couple the desired mode into the interaction cavity. HOM gyro-TWA operation would improve the power-handling capabilities and, hence, ensure maximum output power levels are achieved. The high power gyro-amplifier has the potential to increase the spectral resolution of a DNP-NMR spectroscope by a factor of 600.

References

[1.1] R. Q. Twiss, "Radiation transfer and the possibility of negative absorption in radio astronomy," *Aust. J. Phys.,* vol. 11, no. 4, pp. 564-579, Dec. 1958.

[1.2] J. Schneider, "Stimulated emission of radiation by relativistic electrons in a magnetic field," *Phys. Rev. Lett.*, vol. 2, no. 12, pp. 504-505, June 1959.

[1.3] A. V. Gaponov, "Addendum – Interaction between electron fluxes and electromagnetic waves in waveguides," *Izv. VUZ Radiofizika*, vol. 2, pp. 450, 1959.

[1.4] E. S. Weibel, "Spontaneously growing transverse waves in a plasma due to an anisotropic velocity distribution," Phys. Rev. Lett., vol. 2, no. 3, pp. 83-84, Feb. 1959.

[1.5] M. V. Kartikeyan, E. Borie and M. K. A. Thumm, *Gyrotrons: High-Power Microwave and Millimeter Wave Technology,* Berlin, Germany: Springer-Verlag, 2004, ch. 1, pp. 25.

[1.6] M. V. Kartikeyan, E. Borie and M. K. A. Thumm, *Ibid.,* 25.

[1.7] G. S. Nusinovich, "Introduction to Gyrodevices," *Introduction to the Physics of Gyrotrons,* Baltimore: The John Hopkins University Press, 2004, ch. 1, pp. 5.

[1.8] G. S. Nusinovich, T. M. Antonsen Jr., V. L. Bratman and N. S. Ginzburg, "Principles and Capabilites of High Power Microwave Generators," *Applications of High-Power Microwaves*, eds. A. V. Gaponov-Grekhov and V. L. Granatstein, Norwood: Artech House, 1994, ch. 2, pp. 77.

[1.9] A. W. Hull, "The magnetron," *J. Am. Inst. Elec. Eng.*, vol. 40, no. 9, pp. 715 – 723, Sept. 1921.

[1.10] A. W. Hull, "The Effect of A Uniform Magnetic Field on the Motion of Electrons between Coaxial Cylinders," *Phys. Rev. Lett.,* vol. 18, no. 31, pp. 31 – 57, Sept. 1921.

[1.11] F. R. Elder, "The Magnetron Amplifier and Power Oscillator," *Proc. Inst. Radio Eng.,* vol. 13, no. 2, pp. 159 -188, Apr. 1925.

[1.12] A. Arsenjewa-Heil and O. Heil, "A New Method for Producing Shirt Undamped Waves of Great Intensity," *Zeitschr fur Physik*, vol. 95, no. 11, pp. 752 – 762, 1935.

[1.13] A. S. Gilmour Jnr., "Basic Klystrons and their Operation," *Klystrons, Travelling Wave Tubes, Magnetrons, Crossed-Field Amplifiers, and Gyrotrons*, Norwood: Artech House, 2011, ch. 10, pp. 240.

[1.14] R. H. Varian and S. F. Varian, "A high frequency oscillator and amplifier," *J. Appl. Phys.,* vol. 10, pp. 321-327, May 1939.

[1.15] M. Chodorow, E. L. Ginzton, I. R. Neilsen and S. Sonkin, "Design and Performance of a High-Power Pulsed Klystron," *Proc. Inst. Radio Eng.,* vol. 41, no. 11, pp. 1584 – 1602, Nov. 1953.

[1.16] M. A. Allen, J. K. Boyd, R. S. Callin, H. Deruyter, K. R. Eppley, K. S. Fant, W. R. Fowkes, J. Haimson, H. A. Hoag, D. B. Hopkins, T. Houck, R. F. Koontz, T. L. Lavine, G. A. Loew, B. Mecklenburg, R. H. Miller, R. D. Ruth, R. D. Ryne, A. M. Sessler, A. E. Vlieks, J. W. Wang, G. A. Westenskow, and S. S. Yu, "High-Gradient Electron Accelerator Powered by a Relativistic Klystron," *Phys. Rev. Lett.,* vol. 64, no. 19, pp. 2337, May 1990.

[1.17] A. M. Sessler and S. S. Yu, "Relativistic klystron two-beam accelerator," *Phys. Rev. Lett.,* vol. 58, no. 23, pp. 2439 - 2442, June 1987.

[1.18] R. Kompfner, "The travelling wave valve. New amplifier for centimetric wavelengths," *Electron Wireless W.,* vol. 52, pp. 369 - 372, Nov. 1946.

[1.19] J. R. Pierce, "Theory of the beam-type travelling-wave tube," *Proc. Inst. Radio Eng.,* vol. 35, pp. 111 - 123, Feb. 1947.

[1.20] C. K. Chong and W. L. Menninger, "Latest Advancements in High-Power

Millimetre-Wave Helix TWTs," *IEEE Trans. Plasma Sci*., vol. 38, no. 6, pp. 1227 - 1238, June 2010.

[1.21] E. A. Ash, A. Pearson, A. W. Horsley and J. Froom, "Dispersion and impedance of dielectric-supported ring-and-bar slow-wave circuits," *Proc. Inst. Radio Eng.,* vol. 111, no. 4, pp. 329 – 641, Jan. 1964.

[1.22] S. Bhattacharjee, J. H. Booske, C. L. Kory, D. W. van der Weide, S. Limbach, S. Gallagher, J. D. Welter, M. R. Lopez, R. M. Gilgenbach, R. Lawrence Ives, M. E. Read, R. Divan and D. C. Mancini, "Folded Waveguide Traveling-Wave Tube Sources for Terahertz Radiation," *IEEE Trans. Plasma Sci*., vol. 32, no. 3, pp. 1002 - 1014, June 2004.

[1.23] I. B. Bott, "Tunable source of millimeter and submillimeter electromagnetic radiation," *Proc. IEEE,* vol. 52, no. 3, pp. 330 – 332, March 1964.

[1.24] I. B. Bott, "A powerful Source of millimetre wavelength electromagnetic radiation," *Phys. Lett.,* vol. 14, no. 4, pp 293, 1965.

[1.25] A. V. Gaponov, M. I. Petelin and V. K. Yulpatov, "The induced radiation of excited classical oscillators and its use in high-frequency electronics," *Radio Phys. Quantum Electr.,* vol. 10, no. 9, pp. 794 – 813, Sept. 1967.

[1.26] V. A. Flyagin, A. V. Gaponov, M. I. Petelin and V. K. Yulpatov, "The gyrotron," *IEEE Trans. Micorw. Theory Techn.,* vol. 25, no. 6, pp. 514 – 521, June 1977.

[1.27] A. A. Andronov, V. A. Flyagin, A. V. Gaponov, A. L. Goldenberg, M. I. Petelin, V. G. Usov and V. K. Yulpatov, "The gyrotron: High-power source of millimetre and submillimetre waves," *Infrared Phys.,* vol. 18, no. 5, pp. 385 – 393, Dec. 1978.

[1.28] M. K. A. Thumm, "Dispersion Diagrams of Fast Cyclotron Mode Interaction," *State-of-the-Art of High Power Gyro-Devices and Free Electron Masers,* Karlsruhe: KIT Scientific Publishing, 2014, ch. 3, pp. 3 – 11.

[1.29] M. E. MacDonald, J. P. Anderson, R. K. Lee, D. A. Gordon and G. N. McGrew, "The HUSIR W-Band Transmitter," *Linc. Lab. J.,* vol. 21, no. 1, pp. 106 - 114, Jan. 2014.

[1.30] M. Skolnik, "Role of Radar in Microwaves," *IEEE Trans. Microw. Theory Techn.,* vol. 50, no. 3, pp. 625 – 632, March 2002.

[1.31] G. L. Stephens, D. G. Vane, S. Tanelli, E. Im, S. Durden, M. Rokey, D. Reinke, P. Partain, G. G. Mace, R. Austin, T. L'Ecuyer, J. Haynes, M. Lebsock, K. Suzuki, D. Waliser, D. Wu, J.Kay,

A. Gettelman, Z. Wang and R. Marchand, “CloudSat mission: Performance and earlyscience after the first year of operation,” *J. Geophys. Res.,* vol. 113, pp. D00A18, Dec. 2008.

[1.32] G. Caryotakis, “High Power Klystrons: Theory and Practice at the Stanford Linear Accelerator Centre,” *SLAC-PUB 10620,* Jan. 2005.

[1.33] T. Mastorides, C. Rivetta, J. D. Fox, D. Van Winkle and P. Baudrenghien, “RF system models for the CERN Large Hadron Collider with application to longitudinal dynamics,” *Phys. Rev. Accel. Beam,* vol. 13, pp. 102801, Oct. 2010.

[1.34] S. Albertia, , A. Arnold, E. Borie, G. Dammertz, V. Erckmann, P. Garin, E. Giguet, S. Illy, G. Le Cloarec, Y. Le Goff, R. Magne, G. Michel, B. Piosczyk, C. Tran, M. Q. Tran, M. Thumm and D Wagner, “European high-power CW gyrotron development for ECRH systems,” *Fusion Eng. Des.,* vol. 53, no. 1, pp. 387 - 397, Jan. 2001.

[1.35] T. C. Luce, “Applications of high power millimeter waves in fusion energy research,” *IEEE Trans. Plasma Sci.,* vol. 30, no. 3, pp. 734-754, March 2002.

[1.36] M. Thumm, A. Arnold, E. Borie, O. Braz, G. Dammertz, O. Dumbrajs, K. Koppenburg, M. Kuntze, G. Michel and B. Piosczyk, “Frequency step-tunable (114–170 GHz) megawatt gyrotrons for plasma physics applications,” *Fusion Eng. Des.,* vol. 53, no. 1, pp. 407 - 421, Jan. 2001.

[1.37] R. K. Dhakad, G. S. Baghel, M. V. Kartikeyan and M. K. Thumm, “Output System for a 170-GHz/1.5-MW Continuous Wave Gyrotron Operating in the $TE_{28,12}$ Mode,” *IEEE Trans. Plasma Sci.,* vol. 43, no. 1, pp. 391 – 397, 2015.

[1.38] Z. C. Ioannidis, T. Rzesnicki, F. Albajar, S. Alberti, K. A. Avramidis, W. Bin, T. Bonicelli, A. Bruschi, I. Chelis, P. -E. Frigot, G. Gantenbein, V. Hermann, J. -P. Hogge, S. Illy, J. Jin, J. Jelonnek, W. Kasparek, G. Latsas, C. Lechte, F. Legrand, T. Kobarg, I. G. Pagonakis, Y. Rozier, C. Schlatter, M. Schmid, I. G. Tigelis, M. Thumm, M. Q. Tran, A. Zein and A. Zisis, “CW Experiments With the EU 1-MW, 170-GHz Industrial Prototype Gyrotron for ITER at KIT,” *IEEE Trans. Elec. Devices,* vol. 64, no. 9, pp. 3885 – 3892, 2017.

[1.39] B. Ell, I. G. Pagonakis, G. Gantenbein S. Illy, M. Thumm and John Jelonnek, "Study of the Influence of Stray Magnetic Fields on the Operation of the European Gyrotron for ITER," *IEEE Trans. Elec. Devices,* vol. 64, no. 8, pp. 3421 - 3428, 2017.

[1.40] M. A. Liebermann and A. J. Lichtenburg, "Wave Heated Discharges," *Principles of Plasma Discharges and Materials Processing,* New Jersey: John Wiley and Sons, 2005, ch. 13, pp. 491.

[1.41] D. Agrawal, "Latest global developments in microwave materials processing," *Mater. Res. Innov.,* vol. 14, no. 1, pp. 3 – 8, Feb. 2010.

[1.42] D. E. Clark, D. C. Folz and Jon K West, "Processing materials with microwave energy," *Mater. Sci. Eng.,* vol. 287, no. 2, pp. 153 – 158, Aug. 2000.

[1.43] A. D. R. Phelps and T. Garvey, "Electron cyclotron maser emissions from pulsed electron beams," *J. Phys. D: Appl. Phys.,* vol. 19, no. 11, pp. 2051 – 2063, 1986.

[1.44] A. D. R. Phelps, A. Z. Maatug and S. N. Spark, "Cold cathode 75-110 GHz gyrotron experiments," *Int. J. Electron.,* vol. 65, no. 3, pp. 369 – 376, Sept. 1988.

[1.45] S. N. Spark, A. W. Cross and A. D. R. Phelps, "Gyrotron based on a superconducting magnet," *Int. J. Infrared Milli.,* vol. 13, no. 5, pp. 625 – 646, May 1992.

[1.46] A. W. Cross, S. N. Spark and A. D. R. Phelps, "Gyrotron experiments using cavities of different ohmic Q," *Int. J. Electron.,* vol. 79, no. 4, pp. 481 – 493, Feb. 1995.

[1.47] M. Garven, S. N. Spark, A. W. Cross, S. J. Cooke, and A. D. R. Phelps, "Gyrotron Experiments Employing a Field Emission Array Cathode," *Phys. Rev. Lett.,* vol. 77, no. 11, pp. 2320 – 2323, Sept. 1996.

[1.48] G. G. Denisov, V. L. Bratman, A. W. Cross, W. He, A. D. R. Phelps, K. Ronald, S. V. Samsonov and C. G. Whyte, "Gyrotron Traveling Wave Amplifier with a Helical Interaction Waveguide," *Phys. Rev. Lett.,* vol. 81, no. 25, pp. 5680 – 5683, Dec. 1998.

[1.49] G. G. Denisov, V. L. Bratman, A. D. R. Phelps and S. V. Samsonov, "Gyro-TWT with a helical operating waveguide: new possibilities to enhance efficiency and frequency bandwidth," *IEEE Trans. Plasma Sci.,* vol. 26, no. 3, pp. 508 -518, June 1998.

[1.50] V. L. Bratman, A. W. Cross, G. G. Denisov, W. He, A. D. R. Phelps, K. Ronald, S. V. Samsonov, C. G. Whyte and A. R. Young, "High-gain wide-band gyrotron traveling wave amplifier with a helically corrugated waveguide," *Phys. Rev. Lett.,* vol. 84, no. 12, pp. 2746 – 2749, Mar. 2000.

[1.51] Q. S. Wang, D. B. McDermott and N. C. Luhmann Jr., "Demonstration of marginal stability theory by a 200kW second-harmonic gyro-TWT amplifier," *Phys. Rev. Lett.,* vol. 75, no. 23, pp. 4322 – 4325, Dec. 1995.

[1.52] Q. S. Wang, D. B. McDermott and N. C. Luhmann Jr., "Operation of a stable 200-kW second-harmonic gyro-TWT amplifier," *IEEE Trans. Plasma Sci.,* vol. 24, no. 3, pp. 700 – 706, June 1996.

[1.53] W. He, K. Ronald, A. R. Young, A. W. Cross, A. D. R. Phelps, C. G. Whyte, E. G. Rafferty, J. Thomson, C. W. Robertson, D. C. Speirs, S. V. Samsonov, V. L. Bratman and G. G. Denisov, "Gyro-BWO experiments using a helical interaction waveguide," *IEEE Trans. Electron Devices,* vol. 52, no. 5, pp. 839 - 844, Apr. 2005.

[1.54] W. He, C. G. Whyte, E. G. Rafferty, A. W. Cross, A. D. R. Phelps, K. Ronald, A. R. Young, C. W. Robertson, D. C. Speirs and D. H. Rowlands, "Axis-encircling electron beam generation using a smooth magnetic cusp for gyrodevices," *Appl. Phys. Lett.,* vol. 93, no. 12, pp. 121501, 2008.

[1.55] L. Zhang, W. He, A.W. Cross, A. D. R. Phelps, K. Ronald and C. G. Whyte, "Design of an Energy Recovery System for a Gyrotron Backward-Wave Oscillator," *IEEE Trans. Plasma Sci.,* vol. 37, no. 3, pp. 390 – 394, Mar. 2009.

[1.56] W. He, C. R. Donaldson, F. Li, L. Zhang, A. W. Cross, A. D. R. Phelps, K. Ronald, C. W. Robertson, C. G. Whyte and A. R. Young, "W-band gyro-devices using helically corrugated

waveguide and cusp gun: design, simulation and experiment," *THz Sci. Techn.,* vol. 4, no. 1, pp. 9 – 19, Mar. 2011.

[1.57] L. Zhang, W. He, C. R. Donaldson, A. W. Cross, A. D. R. Phelps, P. McElhinney and K. Ronald, "W-band gyro-BWO with a four-stage depressed collector," *THz Sci. Techn.,* vol. 4, no. 3, pp. 76 – 84, Sept. 2011.

[1.58] K. Felch, M. Blank, P. Borchard, P. Cahalan, S. Cauffman, T. S. Chu and H. Jory, "Demonstration of a 95 GHz, 100 kW, CW Gyrotron Oscillator," *IEEE IVEC 2004,* pp. 63 – 64, 2004.

[1.59] C. K. Chong, D. B. McDermott and N. C. Luhmann, Jr., "Large-Signal Operation of a Third-Harmonic Slotted Gyro-TWT Amplifier," *IEEE Trans. Plasma Sci.,* vol. 26, no. 3, June 1998.

[1.60] M. Blank, K. Felch, B. G. James, P. Borchard, P. Cahalan, T. S. Chu, H. Jory, B. G. Danly, B. Levush, J. P. Calame, K. T. Nguyen and D. E. Pershing, "Development and Demonstration of High-Average Power W-Band Gyro-Amplifiers for Radar Applications," *IEEE Trans. Plasma Sci.,* vol. 30, no. 3, June 2002.

[1.61] B. G. Danly, M. Blank, J. P. Calame, B. Levush, K. T. Nguyen, D. E. Pershing, R. K. Parker, K. L. Felch, B. G. James, P. Borchard, P. Cahalan, T. S. Chu, H. R. Jory, T. A. Hargreaves, R. B. True, W. G. Lawson and T. M. Antonsen, Jr., "Development and Testing of a High-Average Power, 94-GHz Gyroklystron," *IEEE Trans. Plasma Sci.,* vol. 28, no. 3, June 2000.

[1.62] E. V. Zasypkin, L. G. Gachev, I. I. Antakov and E. V. Sokolov, "W-band pulsed 300 kW gyroklystron amplifier," *26th International Conf. Infrared Milli. Waves,* pp. 5.86 – 5.88, Sept. 2001.

[1.63] M. Blank, B. G. Danly and B. Levush, "Experimental Demonstration of a W-Band (94 GHz) Gyrotwystron Amplifier," *IEEE Trans. Plasma Sci.,* vol. 27, no. 7, Apr. 1999.

[1.64] E. A. Nanni, A. B. Barnes, R. G. Griffin and R. J. Temkin, "THz Dynamic Nuclear Polarization NMR," *IEEE Trans. THz Sci. Technol.,* vol. 1, no. 1, pp. 145 – 163, Sept. 2011.

[1.65] H. Heise and S. Matthews, Modern NMR Methodology, Springer (2013).

[1.66] T. Idehara, I. Ogawa, L. Agusu, T. Kanemaki, S. Mitsudo, T. Saito, T. Fujiwara and H. Takahashi, "Development of 394.6 GHz CW Gyrotron (Gyrotron FU CW II) for DNP/Proton-NMR at 600 MHz," *Int. J. Infrared Mill.,* vol. 28, no. 6, pp. 433 – 442, June 2007.

[1.67] T. H. Chang, T. Idehara, I. Ogawa, L. Agusu and S. Kobayashi, "Frequency Tunable Gyrotron Using Backward-wave Components," *33rd International Conf. Infrared, Millimeter and Terahertz Waves,* pp. 1 – 2, Sept. 2008.

[1.68] S. Jawla, Q. Z. Ni, A. Barnes, W. Guss, E. Daviso, J. Herzfeld, R. Griffin and R. Temkin, "Continuously Tunable 250 GHz Gyrotron with a Double Disk Window for DNP-NMR Spectroscopy," *J. Infrared Milli. THz W.,* vol. 34, no. 1, pp. 42 – 52, Jan. 2013.

[2.1] Coupling JJ, a pseudonym of J.R Pierce, *Astounding Science Fiction,* Nov. 1946

[2.2] R.E. Thomas, J.W. Gibson, G.A. Haas and R.H. Abrams Jr., "Thermionic Sources for high-brightness electron beams," *IEEE Trans. Electron Devices*, vol. 37, no. 3, pp. 850-861, March 1990

[2.3] A.S. Gilmour Jnr., *Klystrons, Travelling Wave Tubes, Magnetrons, Crossed-Field Amplifiers, and Gyrotrons,* Norwood: Artech House, 2011, pp. 42

[2.4] *Ibid.* pp. 42

[2.5] S.O. Pillai, *Solid State Physics,* New Age International (P) Limited, 2005, pp. 280

[2.6] J.L. Cronin, "Modern dispenser cathodes," *IEE Proc*., vol. 128, no. 1, pp. 19-32, Feb. 1981

[2.7] A.S. Gilmour Jnr., *Microwave Tubes,* Norwood: Artech House, 1986, pp. 115

[2.8] Y. Okhawa, K. Matsumoto and S. Kitamura, "Field Emission Cathodes using Carbon Nanotubes," *21st MEWS*, Tsukuba, Japan, Oct. 2008

[2.9] A.S. Gilmour Jnr., *op. cit.,* 2011, pp. 47

[2.10] A.S. Gilmour Jnr., *op. cit.,* 2011, pp. 50

[2.11] A.S. Gilmour Jnr., *op. cit.,* 2011, pp. 49

[2.12] A.S. Gilmour Jnr., *op. cit.,* 2011, pp. 53

[2.13] J.R. Pierce, *Theory and Design of Electron Guns,* 2nd Edition, New York: Van Nostrand, 1954

[2.14] A.S. Gilmour Jnr., *op. cit.,* 2011, pp. 96

[2.15] M.V. Kartikeyan, E. Borie and M.K.A. Thumm, *Gyrotrons: High-Power Microwave and Millimeter Wave Technology,* Germany: Springer-Verlag Berlin Heidelberg, 2004, pp. 109

[2.16] B. Piosczyk, *Gyrotron Oscillators: Their Principles and Practice,* C.J. Edgcombe, London: Taylor and Francis Ltd., 1993, pp. 129

[2.17] S. I. Molokovsky and A. D. Shushkov, *Intense Electron and Ion Beams,* Springer, 2005, pp. 62

[2.18] B. Piosczyk, *Op. Cit. ,* pp. 126

[2.19] A. W. Cross, W. He, A. D. R. Phelps, K. Ronald, C. G. Whyte, A. R. Young, C. W. Robertson, E. G. Rafferty, and J. Thomson, "Helically corrugated waveguide gyrotron travelling wave amplifier using a thermionic cathode electron gun," *Appl. Phys. Lett.,* vol. 90, pp. 253501, 2007

[2.20] W. He, K. Ronald, A. R. Young, A. W. Cross, A. D. R. Phelps, C. G. Whyte, E. G. Rafferty, J. Thomson, C. W. Robertson, D. C. Speirs, S. V.Samsonov, V. L. Bratman, and G. G. Denisov, "Gyro-BWO experiments using a helical interaction waveguide," *IEEE Trans. Electron Devices,* no. 52, pp. 839, 2005

[2.21] W. He, C. R. Donaldson, F. Li, A. W. Cross, A.D.R. Phelps, K Ronald, C. W. Robertson, C. G. Whyte and L. Zhang, "Design, simulation and experiment of a cusp electron beam for millimetre wave gyro-devices," *IVEC,* Rome*,* 2009

[2.22] W.W. Destler, E. Chojnacki, R.F. Hoeberling, W. Lawson, A. Singh and C.D. Striffler, "High-power microwave generation from large-orbit devices," *IEEE Trans. Plasma Sci.* no. 16, vol. 2, pp. 71-89, April 1988

[2.23] M.J. Rhee and W.W. Destler, “Relativistic electron dynamics in a cusped magnetic field,” *Phys. Fluids*, no. 17, vol. 8, pp. 1574-1581, Aug. 1974

[2.24] J. Sinnis and G. Schmidt, “Experimental trajectory analysis of charged particles in a cusped geometry,” *Phys. Fluids*, no. 6, vol. 6, pp. 841-845, June 1963

[2.25] W. He, C.G. Whyte, E.G. Rafferty, A.W. Cross, K. Ronald, A.R. Young and C.W. Robertson, “Axis-encircling electron beam generation using a smooth magnetic cusp for gyrodevices,” *Appl. Phys. Lett*. vol. 93, no. 12, pp. 121501, Sept. 2008

[2.26] K.R. Chu, “Theory of electron cyclotron maser interaction in a cavity at the harmonic frequencies”*, Phys. Fluids*, vol. 21, no. 12, pp. 2354-2364, Dec. 1978

[2.27] K. Schindl, “Space Charge*,”* Singapore: World Scientific, 1999, pp. 127-151

[2.28] S.E. Tsimring, *Electron Beams and Microwave Vacuum Electronics*, New Jersey: John Wiley and Sons Inc., 2007, pp. 228

[2.29] M.V. Kartikeyan, E. Borie and M.K.A. Thumm, *op. cit.,* 114

[2.30] J.R.M. Vaughan, “Representation of axisymmetric magnetic fields in computer programs,” *IEEE Trans. Electron Devices*, vol. 19, no. 2, pp. 144-151, Feb. 1972

[2.31] C. R. Donaldson, et al., IEEE Trans. THz Sci. Techn. 6, 108 (2016).

[2.32] A.G. Litvak, G.G. Denisov, V.E. Myasnikov, E.M. Tai, E.A. Azizov and V.I. Illin, “Development in Russia of megawatt power gyrotrons for fusion,” *J. Infrared Millim. W.* vol. 32, no. 3, pp. 337-342, March 2011

[2.33] W. He et al., “Theory and simulations of a gyrotron backward wave oscillator using a helical interaction waveguide,” *Appl. Phys. Lett.,* vol. 89, 091504, 2006.

[2.34] W. He, et al., “High Power Wideband Gyrotron Backward Wave Oscillator Operating towards the Terahertz Region,” *Phys. Rev. Lett.,* vol. 110, 165101, 2013.

[2.35] L. Zhang, W. He, K. Ronald, A.D.R. Phelps, C.G. Whyte, C.W. Robertson, A.R. Young, C.R. Donaldson and A.W. Cross, "Multi-mode coupling wave theory for helically corrugated waveguide," *IEEE Trans. Microw. Theory Techn.* vol. 60, no. 1, pp. 1-7, Jan. 2012

[2.36] V. L. Bratman, et al., "High gain wideband gyro-travelling amplifier with a helically corrugated waveguide," *Phys. Rev. Lett.,* vol. 84, 2746, 2000.

[2.37] V. L. Bratman, et al., "Gyro-TWT with a helical operating waveguide: new possibilities to enhance efficiency and frequency bandwidth," *IEEE Trans. Plasma Sci.,* vol. 26, 508, 1998.

[2.38] G. G. Denisov, et al., "Gyrotron travelling wave amplifier with a helical interaction region," *Phys. Rev. Lett.,* vol. 81, pp. 5680 - 5683, 1998.

[2.39] W. He, C. R. Donaldson, L. Zhang, K. Ronald, A. D. R. Phelps, and A.W. Cross, "Broadband Amplification of Low-Terahertz Signals Using Axis-Encircling Electrons in a Helically Corrugated Interaction Region", *Phys. Rev. Lett.* vol. 119, Nov. 2017.

[2.40] T. Gray, D. N. Smithe, and L. D. Ludeking, Introduction to MAGIC, Mission Research Corporation, Newington, VA (2003).

[2.41] M.V. Kartikeyan, E. Borie and M.K.A. Thumm, *op. cit.,* 116

[2.42] O. Braz, G. Dammertz, M. Kuntze and M. Thumm, "D-band frequency step tuning of a 1 MW gyrotron using a Brewster output window," *J. Infrared Millim. W.* vol. 18, no. 8, pp. 1465-1477, Aug. 1997

[2.43] M.Y. Glyavin, A.N. Kuftin, N.P. Venediktov and V.E. Zapevalov, "Experimental investigation of a 110 GHz/1 MW gyrotron with the one-step depressed collector," *J. Infrared Millim. W.* vol. 18, no. 11, pp. 2129-2136, Nov. 1997

[2.44] L. Zhang, W. He, A.W. Cross, A.D.R. Phelps, K. Ronald and C.G. Whyte, "Numerical optimisation of a multistage depressed collector with secondary electron emission for an X-band gyro-BWO," *IEEE Trans. Plasma. Sci.* vol. 37, no. 12, pp. 2328-2334, Dec. 2009

[2.45] M. Thumm, "Development of output windows for high-power long pulse gyrotrons and EC wave applications," *J. Infrared Millim. W.* vol. 19, no. 1, pp. 3-14, Jan. 1998

[2.46] M.V. Kartikeyan, E. Borie and M.K.A. Thumm, *op. cit.,* 155

[2.47] C.R. Donaldson, W. He, L. Zhang and A.W. Cross, "A W-band multi-layer microwave window for pulsed operation of gyro-devices," *IEEE Microw. Compon. Lett.* vol. 23, no. 5, pp. 237-239, May 2013

[2.48] G. Gantenbein, A. Samartsev, G. Aiello, G. Dammertz, J. Jelonnek, M. Losert, A. Schlaich, T.A. Scherer, D. Strauss, M. Thumm and D. Wagner, "First operation of a step-frequency tunable 1 MW gyrotron with a diamond Brewster angle output window," *IEEE Trans. Electron Devices,* vol. 61, no. 6, pp. 1806-1811, June 2014

[3.1] C. G. Whyte, K. Ronald, A. R. Young, W. He, C. W. Robertson, D. H. Rowlands and A. W. Cross, "Wideband Gyro-Amplifiers", *IEEE Trans. Plasma. Sci.* vol. 40, no. 5, pp. 1303-1310, May 2012.

[3.2] D. E. Pershing, K. T. Nguyen, J. P. Calame, B. G. Danly, B. Levush, F. N. Wood and M. Garven, "A TE_{11} Ka-Band Gyro-TWT Amplifier With High-Average Power Distributed Loss," *IEEE Trans. Plasma. Sci.* vol. 32, no. 3, pp. 947-956, June 2004.

[3.3] K. L. Wu, M. Yu and A. Sivadas, "A novel modal analysis of a circular-to-rectangular waveguide T-junction and its application to design of circular waveguide dual-mode filters," *IEEE Trans. Microw. Theory Tech.* vol. 50, no. 2, pp. 465-473, Feb. 2002.

[3.4] N. Yoneda, M. Miyazaki, H. Matsumura and M. Yamato, "A design of novel grooved circular waveguide polarizers," *IEEE Trans. Microw. Theory Tech.* vol. 48, no. 12, pp. 2446-2452, Dec. 2000.

[3.5] G. Chattopadhyay, B. Philhour, J. E. Carlstrom, S. Church, A. Lange and J. Zmuidzinas, "A 96-GHz ortho-mode transducer for the polatron," *IEEE Microw. Guided Wave Lett.* vol. 8, no. 12, pp. 421-423, Dec. 1998.

[3.6] N. Yoneda, M. Miyasaki, T. Nishino, H. Asao, H. Nakaguro and S. Betsudan, "Analysis of circular-to-rectangular waveguide T-junction using mode-matching technique," *Electron. Comm. JPN, Part II: Electronics*, vol. 80, no. 7, pp. 37-46, July 1997.

[3.7] K. C. Hwang and H. J. Eom, "Scattering analysic for a circular to rectangular T-junction," *Microw. Opt. Techn. Lett.* vol. 41, no. 3, pp. 231-234, May 2004.

[3.8] P. Krauss and F. Arndt, "Rigorous mode-matching method for the modal analysis of the T-junction circular to sidecoupled rectangular waveguide," *IEEE MTT-S Microw. Symp. Dig.* Orlando FL, vol. 3, pp. 1355-1358, 1995.

[3.9] J. D. Wade and R. H. Macphie, "Scattering at circular-to-rectangular waveguide junctions*,"* IEEE Trans. Microw. Theory Tech. vol. 34, no. 11, pp. 1085-1091, Nov. 1986.

[3.10] J. Zheng and M. Yu, "Rigorous mode matching method for circular to off-centre rectangular side-coupled waveguide junctions for filter applications," *IEEE Microw. Theory Techn.* vol. 55, no. 11, pp. 2365-2373, Nov. 2007.

[3.11] www.cst.com 07/02/2015.

[3.12] C. K. Chong, D. B. McDermott, M. M. Razeghi, N. C. Luhmann Jr, J. Pretterebner and D. Wagner, "Bragg Reflectors," *IEEE Trans. Plasma Sci.* vol. 20, no. 3, pp. 393-402, March 1992.

[3.13] L. Solymar, "Spurious mode generation in nonuniform waveguide," *Instit. Radio Eng. Trans. Microw. Theory Techn.* vol. 7, no. 3, pp. 379-383, July 1959.

[3.14] L. Zhang, W. He, C. R. Donaldson, J. R. Garner, P. McElhinney and A. W. Cross, "Design and measurement of a broadband sidewall coupler for a gyro-TWA," *IEEE Trans. Microw. Theory Techn.* vol. 63, no. 6, pp. 3183-3190, Oct. 2015.

[3.15] www.anritsu.com/en-US/test-measurement 22/10/15.

[3.16] G. J. Scalzi, A. J. Slobodnik and G. A. Roberts, "Network analyser calibration using offset shorts," *IEEE Trans. Microw. Theory Techn.* vol. 36, no. 6, pp. 1097-1110, June 1988.

[4.1] C. R. Donaldson, *A W-band Gyrotron Backward Wave Oscillator with Helically Corrugated Waveguide,* Ph.D. Thesis, University of Strathclyde, pp. 190, Sept. 2009.

[4.2] H. Tang and V. Scuka, "The breakdown mechanism of a mid-plane triggered spark gap trigatron," *IEEE Trans. Dielectr. Electr. Insul.* vol. 3, no. 6, pp. 843 – 848, Aug. 2002.

[4.3] R. Sobot, "Electronic Devices," *Wireless Communication Electronics: Introduction to RF Circuits and Design,* New York: Springer-Verlag, 2012, ch. 4, pp. 99 – 104.

[4.4] L. S. Lerner, "Magnetism II: Magnetic Field of an Electric Current," *Physics for Scientists and Engineers: Volume 2,* London: Jones and Bartlett, 1997, ch. 29, pp. 806 – 808.

[4.5] L. Zhang, C. R. Donaldson and W. He, "Design and measurement of a polarization convertor based on a truncated circular waveguide," *J. Phys. D: Appl. Phys.* vol. 45, pp. 345103, 2012.

[4.6] L. Zhang, W. He, C. R. Donaldson and A. W. Cross, "Optimization and measurement of a smooth-walled profiled horn for a W-band gyro-TWA," To be published, 2017.

[4.7] S. Tumanski, "Magnetic Sensors," *Handbook of Magnetic Measurements,* Boca Raton: CRC Press, 2011, ch. 4, pp. 174 – 175.

[5.1] H. A. Bethe, "Theory of diffraction by small holes," *Phys. Rev. Lett.* vol. 66, no. 7 – 8, pp. 163, July 1944.

[5.2] W**.** Shelton, "Compact multi-hole waveguide directional couplers," *Microwave J.* vol. 4, pp. 89, 1961.

[5.3] C. H. Liang and D. K. Cheng, "On performance limitations of aperture coupling between rectangular waveguide," *IEEE Trans. Microw. Theory Techn.* vol. 30, no. 5, pp. 777-781, May 1982.

[5.4] A. J. Sangster, "Slot coupling between uniform rectangular waveguides," *IEEE Trans. Microw. Theory Techn.* vol. 27, no. 7, pp. 705-707, July 1979.

[5.5] H. Schmeidel and F. Arndt, "Field theory design of rectangular waveguide multiple-slot narrow-wall couplers," *IEEE Trans. Microw. Theory Techn.* vol. 34, no. 7, pp. 791-798, July 1986.

[5.6] W. X. Wang, W. Lawson and V. L. Granatstein, "The design of a mode selective directional coupler for a high power gyroklystron," *Int. J. Electron.* vol. 65, no. 3, pp. 705 – 716, Feb. 1988.

[5.7] W. X. Wang, “Improved design of a high power mode selective directional coupler,” *Int. J. Electron.* vol. 76, no. 1, pp. 131 – 142, July 1993.

[5.8] Y. H. Choung, K. R. Goudey and L. G. Bryans, “Theory and design of a Ku-band TE_{21} mode coupler,” *IEEE Trans. Microw. Theory Techn.* vol. 30, no. 11, pp. 1862 – 1866, Nov. 1982.

[5.9] S. E. Miller, “Coupled wave theory and waveguide applications,” *AT&T Tech. J.* vol. 33, no. 3, pp. 661 – 719, May 1954.

[5.10] www.microdrilling.co.uk 02/11/2015.

[6.1] K. Koppenburg, G. Dammertz, M. Kuntze, B. Piosczyk and M. Thumm, “Fast-frequency step-tuneable high-power gyrotron with hybrid magnet system,” *IEEE Trans. Electron Devices,* vol. 48, no. 1, pp. 101 – 107, Jan. 2001.

[6.2] M. Yu. Glyavin, A. N. Kuftin, N. P. Venediktov and V. E. Zapevalov, “Experimental investigation of a 110 GHz/1 MW gyrotron with the one-step depressed collector,” *Int. J. Infrared Milli.* vol. 18, no. 11, pp. 2129 – 2136, Nov. 1997.

[6.3] T. L. Grimm, K. E. Kreischer and R. J. Temkin, “Experimental study of a megawatt 200–300 GHz gyrotron oscillator,” *Phys. Fluids B,* vol. 5, no. 11, pp. 4135 – 4143, Nov. 1993.

[6.4] J. J. Choi, A. H. McCurdy, F. N. Wood, R. H. Kyser, J. P. Calame, K. T. Nguyen, B. G. Danly, T. M. Antonsen, Jr., B. Levush and R. K. Parker, “Experimental investigation of a high power, two cavity 35 GHz gyroklystron cavity,” *IEEE Trans. Plasma Sci.* vol. 26, no. 3, pp. 416 – 425, June 1998.

[6.5] A. H. McCurdy and J.J. Choi, “Design and analysis of a coaxial coupler for a 35 GHz gyroklystron amplifier,” *IEEE Trans. Microw. Theory Tech.* vol. 27, no. 2, pp. 164 – 175, Mar. 1999.

[6.6] M. Garven, W. M. Manheimer and M. Blank, “Simple theory of input couplers for gyroklystron amplifiers,” *IEEE Trans. Plasma Sci.* vol. 26, no. 3, pp. 433 - 443, June 1998.

[6.7] H. H. Song, D. B. McDermott, Y. Hirata, L. R. Barnett, W. Domier, H. L. Hsu, T. H. Chang, W. C. Tsai, K. R. Chu and N. C. Luhmann, Jr., "Theory and experiment of a 94 GHz gyrotron travelling wave amplifier," *Phys. Plasmas*, vol. 11, no. 5, pp. 2935 – 2941, May 2004.

[6.8] W. M. Manheimer, "Simple theory of the input coupler to the 94 GHz NRL gyroklystron," *NRL Memo 96-7891*, Oct. 1996.

[6.9] S. Yuvaraj, M. Thottappan and P. K. Jain, "Design and simulation of 94 GHz metal PGB waveguide," *2013 IEEE MTT-S International*, June 2013.

[6.10] D. S. Furuno, D. B. McDermott, C. S. Kou, N. C. Luhmann, Jr. and P. Vitello, "Operation of a large orbit high harmonic gyro-TWT amplifier," *IEEE Trans. Plasma Sci.* vol. 18, no. 3, pp. 313 – 320, June 1990.

[6.11] D. M. Pozar, *Microwave Engineering, 4th ed.* New Jersey: John Wiley and Sons, 2005, ch. 4, sec. 4.6, pp. 197 – 204.

[6.12] P. Arcioni, "Fast Evaluation of Modal Coupling Coefficients of Waveguide Step Discontinuities," *IEEE Microw. Guided W.* vol. 6, no. 6, pp. 232 – 234, June 1996.

[6.13] P. Jarry and J. Beneat, "Modal analysis of waveguide step discontinuities," *Advanced Design Techniques and Realizations of Microwave and RF Filters,* New Jersey: John Wiley and Sons, 2008, pp. 328 – 337.

[6.14] G. L. Matthaei, L. Young and E. M. T. Jones, "The Performance of Homogeneous Half Wave Filters," *Microwave Filters, Impedance-matching Networks and Coupling Structures,* New York: McGraw-Hill, ch. 6, pp. 172.

[6.15] K. Matsumaru, "Reflection coefficient of E-plane tapered waveguides," *IRE Trans. Microw. Theory Techn.* vol. 6, no. 2, pp. 143 – 149, Apr. 1958.

[6.16] R. C. Johnson, "Design of linear double tapers in rectangular waveguide," *IRE Trans. Microw. Theory Techn.* vol. 7, no. 3, pp. 374 – 378, July 1959.

[6.17] R. A. Waldron, "Theory of reflections in a tapered waveguide," *J. I. Electron. Rad. Eng.* vol. 32, no. 4, pp. 245 – 254, Oct. 1966.

[6.18] R. Meredith, *Engineers Handbook of Industrial Microwave Heating,* London, UK: The Institution of Electrical Engineers, 1998, pp. 127 – 129.

[6.19] P. Cornet, R. Dusseaux and J. Chandezon, “Wave propagation in curved waveguides of rectangular cross section,” *IEEE Microw. Theory Techn.* vol. 47, no. 7, pp. 965 – 972, July 1999.

[6.20] F. Alessandri, M. Mongiardo and R. Sorrentino, “Rigorous mode matching analysis of mitred E-plane bends in rectangular waveguide,” *IEEE Microw. Guided W.* vol. 4, no. 12, pp. 408 – 410, Dec. 1994.

[6.21] N. Marcuvitz, “Asymmetric Structures; Coupling of Two Guides,” *Microwave Handbook,* New York: Dover Publications, 1965, ch. 5, pp. 333 – 334.

[6.22] J. R. Garner, L. Zhang, C. R. Donaldson, A. W. Cross and W. He, “Design Study of a Fundamental Mode Input Coupler for a 372-GHz Gyro-TWA I: Rectangular-to-Circular Coupling Methods,” *IEEE Trans. Electron Devices,* vol. 63, no. 1, pp. 497 - 503, Jan. 2016.

[6.23] P. Fuerholz and A. Murk, "Design of a broadband transition using the constant impedance structure approach," *Prog. Electro. Research Lett.*, vol. 7, pp. 69-78, 2009.

[6.24] W. Lawson, M. R. Arjona, B. P. Hogan and R. L. Ives, “The Design of Serpentine-Mode Converters for High-Power Microwave Applications,” *IEEE Trans. Microw. Theory Techn.,* vol. 48, no. 5, pp. 809 – 814, May 2000.

[6.25] E. Luneville, J. M. Krieg and E. Giguet, “An original approach to mode converter optimum design,” *IEEE Trans. Microwave Theory Tech.*, vol. 46, pp. 1–9, Jan. 1998.

[6.26] Science and Technology Facilities Council, “CNC Nano-machining,” *www.ralspace.stfc.ac.uk*, 29 March 2016.

Design and Measurement of a Broadband Sidewall Coupler for a W-Band Gyro-TWA

Liang Zhang, Wenlong He, Craig R. Donaldson, Jason R. Garner, Paul McElhinney, and Adrian W. Cross

***Abstract*—The input coupler is an important component for a microwave amplifier. In this paper, a sidewall single-hole input coupler for a W-band gyrotron traveling-wave amplifier that operates at the frequency range of 90–100 GHz was designed and measured. Instead of using a cutoff waveguide, a broadband Bragg-type reflector with a small spread in phase was optimized for use as part of the input coupler. The minimum radius of the reflector was two times the size of a cutoff waveguide, which reduced the possibility for some of the beam electrons being collected in this section and lost to the amplifier interaction region.**

***Index Terms*—Bragg reflector, gyrotron traveling-wave amplifier (gyro-TWA), input coupler.**

I. Introduction

GYRO-DEVICES are high-power coherent radiation sources based on the electron cyclotron instability. The traveling-wave amplifiers (gyro-TWAs) are one kind of gyro-devices that can be used in various applications including electron paramagnetic resonance spectroscopy, high-resolution radar, deep space communication, and plasma diagnostics. A high-power wide-frequency-tunable source has significant advantages in these applications. However, to achieve broadband amplification is challenging for the gyro-devices. For a conventional gyro-TWA using a smooth waveguide as the beam-wave interaction region, broadband amplification only occurs far away from the cutoff frequency, which requires high beam voltage, as well as suffering from a high sensitivity to the electron beam quality.

The wide frequency tunability can be achieved by using a helically corrugated waveguide (HCW) that has a periodic corrugation on a smooth circular waveguide, as shown in Fig. 1(a). From the Floquet theory, the periodic structure has an infinite number of spatial harmonics [1]. From the coupled-mode theory [2], [3], the axial and azimuthal periodicities in the HCW allow the coupling of two different modes [modes 1 and 2 in Fig. 1(b)] in circular waveguide to generate new eigenmodes (W_1 and W_2). The synchronism conditions for both of the axial and azimuthal directions are

$$k_1 - k_2 = \frac{2\pi}{d} \qquad m_1 - m_2 = m \tag{1}$$

where d and m are the axial and azimuthal periodicities of the waveguide, k_1, k_2 are the axial wavenumbers, and m_1, m_2 are the azimuthal indices of the two coupling modes. If the dimensions of the HCW are properly designed, the eigenmode W_1 is able to achieve a constant large group velocity over a large range of axial wavenumbers around zero, as shown in Fig. 1(b). This ensures the gyro-TWA has broadband amplification (ω_1 to ω_2) as well as less sensitivity to the velocity spread of the electron beam.

Gyrotron backward-wave oscillators (gyro-BWOs) and gyro-TWAs based on HCWs have demonstrated excellent results in achieving high-power and wide frequency tuneability [4][5][6]. A W-band gyro-BWO with an HCW achieved a maximum output power of 12 kW. The frequency tuning band in the measurement was 88.0–102.5 GHz by adjusting the cavity magnetic field [7]. A W-band gyro-TWA that shares the same cusp electron gun, the solenoid system, and microwave output window with the gyro-BWO is currently being experimentally studied. It is predicted to achieve a saturated gain of 35 dB,

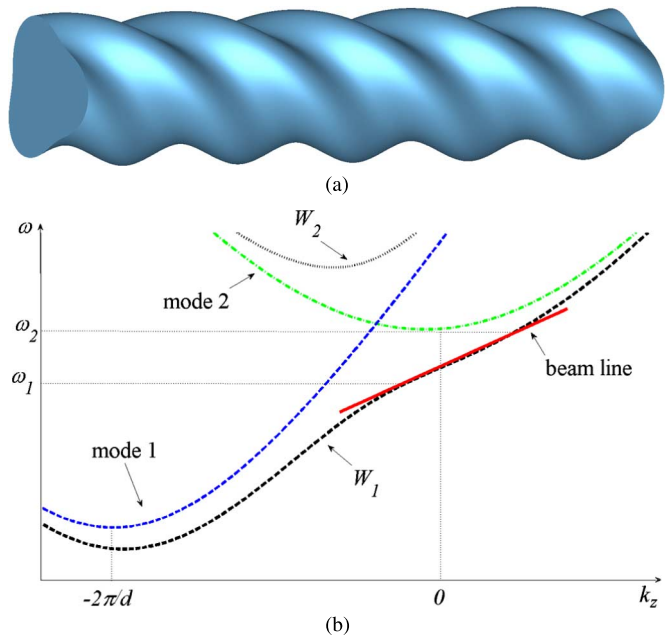

Fig. 1. (a) 3-D model of a HCW. (b) Mode coupling in the HCW. The operating mode W_1 has a constant large group velocity over a large range of axial wavenumbers around zero. d is the axial period of the HCW.

Manuscript received April 15, 2015; revised June 12, 2015; accepted July 27, 2015. Date of publication August 14, 2015; date of current version October 02, 2015. This work was supported by the Engineering and Physical Sciences Research Council (EPSRC), U.K., under Research Grant EP/K029746/1.

The authors are with the Department of Physics, Scottish Universities Physics Alliance (SUPA), University of Strathclyde, Glasgow G4 0NG, U.K. (e-mail: liang.zhang@strath.ac.uk; w.he@strath.ac.uk; craig.donaldson@strath.ac.uk; j.garner@strath.ac.uk; paul.mcelhinney@strath.ac.uk; a.w.cross@strath.ac.uk).

Color versions of one or more of the figures in this paper are available online at http://ieeexplore.ieee.org.

Digital Object Identifier 10.1109/TMTT.2015.2464302

and an output power of 5 kW in the frequency band of 90–100 GHz when driven by a 40-kV 1.5-A annular-shaped large-orbit electron beam [8].

In contrast to the gyro-BWO, the gyro-TWA requires an input microwave signal for amplification. The input signal is coupled into the system between the electron gun and the interaction region from the radial direction. The configuration of the sidewall input couplers may be different depending upon the required operating modes for the interaction, but can be categorized as a single-hole or a multiple-small-aperture type coupler. Both types have been used in the gyro-TWA experiments. The multiple small-aperture coupler is able to achieve good coupling over a narrow bandwidth (about 2%) and the performance degrades as the bandwidth increases. A multiple small-aperture input coupler designed for a Ka-band gyro-TWA achieved about a -2-dB transmission coefficient with 17% bandwidth from 33 to 39 GHz [9]. At W-band, higher loss is expected due to the smaller coupling holes (about 0.3 mm). A single-hole coupler with a cutoff waveguide achieved 20% bandwidth at X-band [10]. However, it is limited by the usage of the small-radius cutoff waveguide at high operating frequency.

Thus far, there are no input couplers reported that operate at W-band that achieve high transmission as well as broad bandwidth. In this paper, the single-hole coupler is discussed as it has the advantage of compact structure with a small area required to be brazed together to seal the vacuum, which is more suitable for the W-band gyro-TWA under development due to the space limitation between the cavity coil and the vacuum jacket. The input coupler with a Bragg reflector was optimized to achieve a maximum transmission from the input TE_{10} mode in the rectangular waveguide to the TE_{11} mode in the circular waveguide. The preliminary idea of the proposed coupler was introduced in [11] and [12]. In this paper, a detailed study of the principle, simulation, and optimization of the coupler is reported. The simulation results have been verified by measurement using a vector network analyzer (VNA) and good agreement achieved.

This paper is organized as follows. Section II describes the T-junction sidewall coupler with cutoff waveguide. Section III presents the design of the sidewall coupler with a broadband Bragg reflector. In Section IV, the construction and measurement results of the Bragg reflector, as well as the input coupler are reported and discussed. Section V contains the conclusion.

II. Single-Hole Sidewall Coupler With Cutoff Section

The general geometry of the single-hole sidewall coupler is a rectangular-to-circular T-junction. It is a basic microwave structure that can be used in applications such as an ortho-mode transducer (OMT) [13], polarizer, and microwave filter [14]. The scattering parameters of the rectangular-to-circular T-junction can be efficiently calculated by several methods, such as finite-difference time-domain (FDTD), finite-element method (FEM), or mode-matching method [15], [16]. If only the transmission coefficient from the TE_{10} mode of the rectangular waveguide to the TE_{11} mode of the circular waveguide needs to be calculated, a simple equation as described in [14] can be used to quickly predict the performance.

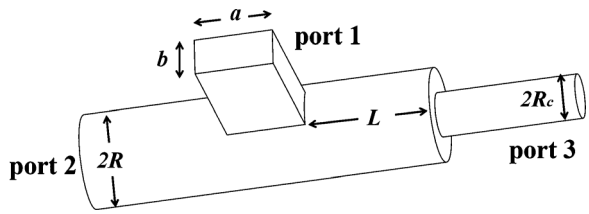

Fig. 2. Geometry of the T-junction with a cutoff waveguide with parameters' definition.

However, the T-junction is a symmetrical structure between ports 2 and 3, which means the transmission coefficient between ports 1 and 2 (S_{12}) will only have a maximum value of -3 dB (half of the input power). To improve the transmission coefficient between ports 1 and 2 in the T-junction, a cutoff waveguide is usually used at port 3. The cutoff waveguide can also stop the microwave radiation from propagating towards the electron gun region preventing it from interfering with the electron beam. The general geometry of the T-junction with a cutoff waveguide with the definition of the geometry is shown in Fig. 2. The transmission coefficients S_{21} with different radii R_c and lengths L of the cutoff waveguide are shown as Fig. 3. In the simulation, the radius R is 1.30 mm, which is same size as the mean radius of the HCW. The dimensions a and b are 1.20 and 1.72 mm, respectively, which provide the optimal S_{12} of the T-junction over the frequency band of 90–100 GHz.

Fig. 3(a) shows that the S_{21} is improved as the R_c value reduces when $L = 0$. A simple explanation is less microwave power will propagate to port 3 due to the geometry discontinuity of the circular waveguide step. By the principle of the conservation of energy, this power will either be reflected back to port 1 or travel to port 2 to enhance the transmission power. A smaller R_c means a higher reflection from the waveguide step, and a higher transmission coefficient can be achieved. The waveguide short with $R_c = 0$ has an unity reflectivity in all the frequencies and has the best transmission coefficient. If the operating bandwidth of the coupler is defined by the frequency range of -1-dB transmission, the radius of the cutoff waveguide needs to be smaller than 0.68 mm to achieve a full bandwidth of 90–100 GHz.

Fig. 3(b) shows that the bandwidth increases as the length of the cutoff waveguide reduces when a waveguide short ($R_c = 0$) is used. In this case, the phase response of the circular waveguide is the only parameter that affects the bandwidth. The phase of the TE_{11} mode in a circular waveguide with radius R and length L is $-k_z \cdot L$, where k_z is the axial wavenumber of the TE_{11} mode. The waveguide short has a constant phase response of π. The overall phase response by the circular waveguide with length L and the waveguide short is

$$P(L,\omega) = -2k_z \cdot L + \pi = -2\left(\left(\frac{\omega}{c}\right)^2 - \left(\frac{1.841}{R}\right)^2\right)^{\frac{1}{2}} \cdot L + \pi. \tag{2}$$

The phase spread in the operating frequency range can be defined as

$$Ps(L) = 2\pi - (|P(L,\omega_1)| + |P(L,\omega_2)|) \tag{3}$$

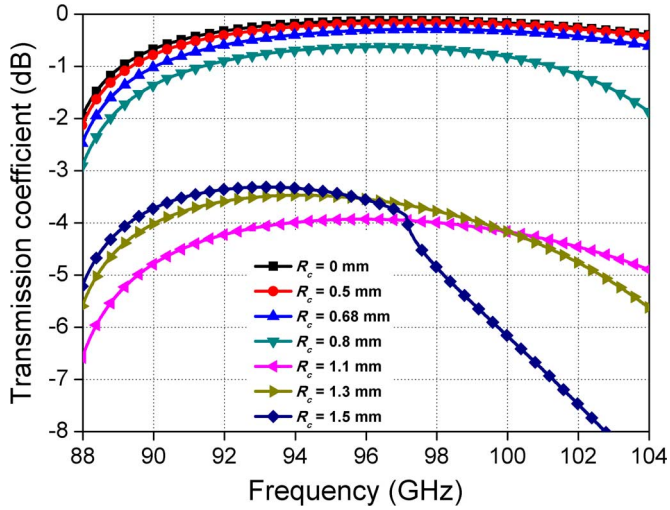

(a)

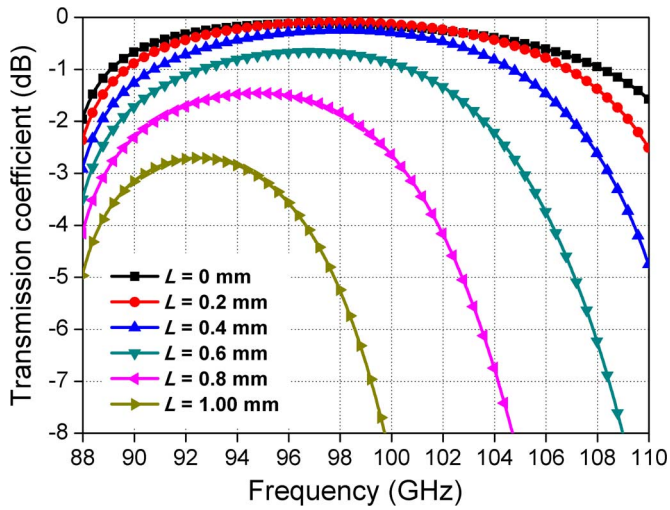

(b)

Fig. 3. Transmission coefficient as a function of: (a) R_c when $L = 0$ mm and (b) of L when $R_c = 0$ mm.

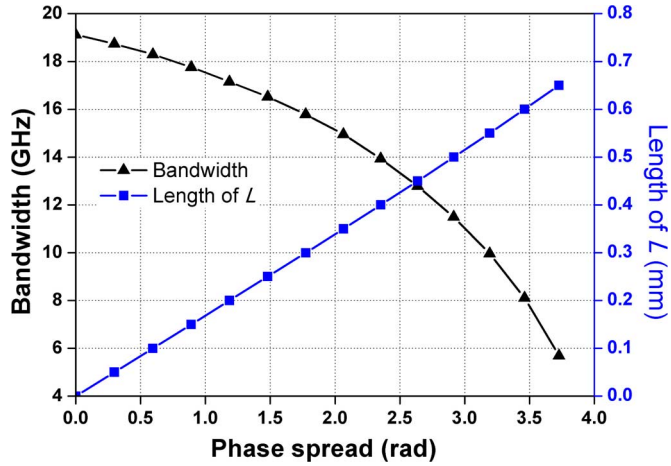

Fig. 4. Correlations between the phase spread, bandwidth, and length L.

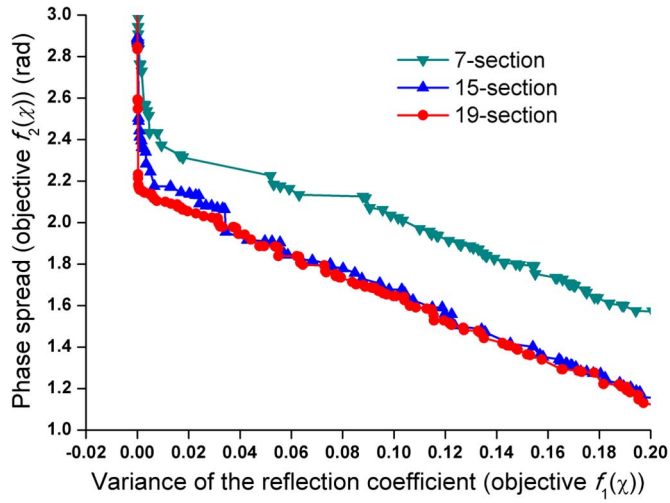

Fig. 5. Pareto fronts of the multiple-objective optimization with different corrugation sections.

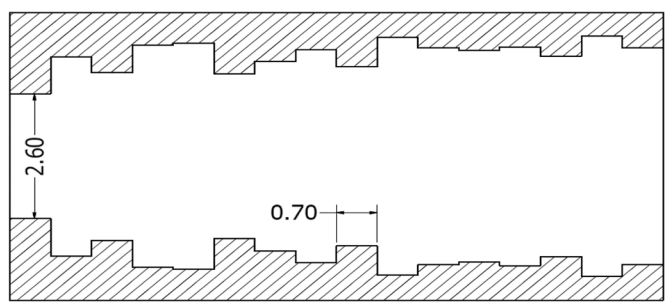

Fig. 6. Geometry of the optimized 16-section Bragg reflector (unit in millimeters).

where ω_1 and ω_2 are the start and end frequencies in (3). Fig. 4 shows the relation between the phase spread and the bandwidth for different waveguide lengths L. The phase spread becomes larger as L increases, and the larger the phase spread is, the narrower the bandwidth will be. The maximum bandwidth of about 19% can be achieved when $L = 0$, where $P(0, \omega)$ is a constant and no phase spread exists. Another useful result from Fig. 3(b) is the center frequency in the bandwidth shifts as the length L of the waveguide changes, which allows the coupler to have some tuning capability.

III. Sidewall Coupler With Bragg Reflector

The cutoff waveguide is a general solution to improve the transmission coefficient for the input coupler. The only requirement is the radius of the cutoff waveguide needs to be sufficiently small. For a low-frequency microwave vacuum electronic device, such as the X-band gyro-BWO/TWA, the requirement is easier to satisfy while keeping a high electron-beam transportation rate. For the W-band gyro-TWA, the average radius of the annular electron beam is about 0.37 mm at a beam alpha of 1.56 [17]. The beam radius is even larger in the input coupler region as the magnetic field is smaller. From the simulation results presented above, if a cutoff waveguide was used in the input coupler region, then the electron beam would be separated by a distance of less than 0.3 mm from the inner surface of the cutoff waveguide. It will be useful to have space for the electron beam to pass, as this alleviates the alignment problem of the beam in the diode region. Ideally a waveguide structure with a large inner radius, but having similar characteristics to

TABLE I
DIMENSIONS OF THE DESIGNED AND MACHINED BRAGG REFLECTOR. UNITS ARE ALL IN MILLIMETERS

Section number	1	2	3	4	5	6	7	8
Designed diameter	2.60	4.16	3.50	4.64	4.72	3.44	3.96	4.44
Tolerance point A	2.600	4.162	3.540	4.677	4.760	3.480	4.000	4.402
Tolerance point B	2.600	4.123	3.538	4.674	4.760	3.480	3.950	4.402
Measured diameter	2.60	4.26	3.61	4.73	4.80	3.47	4.03	4.50
Section number	9	10	11	12	13	14	15	16
Designed diameter	3.74	4.96	4.52	4.42	4.56	4.18	5.02	4.52
Tolerance point A	3.707	5.000	4.497	4.455	4.536	4.214	5.013	4.483
Tolerance point B	3.739	4.997	4.514	4.427	4.532	4.216	5.006	4.500
Measured diameter	3.86	5.01	4.58	4.49	4.62	4.35	5.06	4.58

a waveguide short, is required. From the analysis and discussion in Section II, this requirement can be specified by a high reflection coefficient and small phase spread over the operating frequency band. The phase spread has a greater effect than the reflection coefficient.

A. Design of the Bragg Reflector

Based on the general mode-coupling structure mentioned in Section I, a waveguide with only axial periodicity also allows one mode to couple with its spatial harmonic. In this case, the azimuthal resonance condition will be automatically satisfied. The axial resonance condition becomes $2k_1 = 2\pi/d$, which is also called "the Bragg resonance condition." A strong mode-selective reflection that scatters the incident wave coherently into a backward wave can be achieved. This axial periodic structure can also be overmoded, and therefore, a large radius is possible. It will be very useful in the high-frequency applications as the dimensions can be relatively large to release the tolerance requirement. Therefore, it has great potential to replace the waveguide short used in the coupler if a small phase spread can be achieved as well.

Among the various axial periodic structures, the simplest structure is the periodic rectangular-corrugation waveguide, which includes two circular waveguide sections with different radii in one period. The mode-selective Bragg reflector [18] based on the rectangular corrugation waveguide can achieve a high reflection, however, the bandwidth is small and not able to cover the frequency band of the gyro-TWA. It has been shown that the bandwidth of the Bragg reflector can be improved by varying the corrugation profile. A 13-section reflector has been designed to operate in the frequency range of 8.0–9.5 GHz for an X-band gyro-BWO to enable electron beam propagation and to reflect the microwave radiation in the forward direction [19]. Further simulations show that more corrugation sections will achieve larger bandwidth and higher reflection while the drawback is a larger ohmic loss.

However, these simulations only considered the reflectivity of the Bragg reflector. The phase spread is too large to provide adequate bandwidth to be used in the coupler and further simulations are required. As there is no analytical method to predict the performance of the Bragg reflector with arbitrary corrugation profile, the numerical mode-matching method [20] was employed to simulate such a waveguide structure. A multiple-objective optimization using a genetic algorithm was used to search for a broadband reflector with variable corrugation depths. Two goal functions were used in the optimization. One was to maximize the reflection, and the other was to minimize the phase spread. The equations are

$$\begin{aligned} f_1(x) &= \left(\frac{\sum_{F}^{N} \left[A_{11}(x,F) - 1 \right]^2}{N} \right)^{\frac{1}{2}} \\ f_2(x) &= \mathrm{MAX}(\mathrm{UNWRAP}\,(P_{11}(x)) \\ &\quad - \mathrm{MIN}(\mathrm{UNWRAP}\,(P_{11}(x)) \end{aligned} \tag{4}$$

where x are the parameters to be optimized. In this case, they are the dimensions of the reflector. F is the frequency index in the calculated frequency range, N is the number of the frequency samples, A_{11} is the reflection coefficient of S_{11}, and P_{11} is the phase of S_{11}. The value range of the period can be simply calculated from the Bragg resonance condition and the minimum radius of the corrugation section was set the same as the mean radius of the interaction region.

Fig. 5 shows the Pareto fronts of the goal functions in different numbers of corrugation sections. A high reflection can be achieved ($f_1(x)$ close to 0) if the phase spread does not need to be considered. However, a very high reflection as well as a small phase spread cannot be achieved at the same time. The practical design needs to tradeoff between the goal functions. Increasing

the number of corrugation sections will help to get a better performance, but not significantly better after this number exceeds 15.

The optimum geometry of the Bragg reflector was chosen to have a balanced performance of the reflectivity and phase spread, as shown in Fig. 6. The dimensions of the corrugation radii are listed in Table I. The phase spread is about 1.82. From Fig. 4, such a phase spread will give rise to a bandwidth larger than 10 GHz and is sufficient to cover the required frequency band. The tolerance sensitivity of the Bragg reflector was also studied by an optimization routine. In the optimization, all the dimensions were allowed to have random tolerances within ± 20 μm and the target was to maximize the goal functions in (4). The Pareto front is shown as Fig. 7(a). The reflectivity becomes worse with the tolerance applied. The tolerance will generally result in a larger phase spread while it also is possible to get an even smaller value. However, the difference is relatively small, with a maximum change of 0.03. Fig. 7(b) shows the comparison of the simulation results for the designed geometry and the ones at points A and B in Fig. 7(a). At point A, the radii of the third to sixth sections are nearly with maximum tolerance of 20 μm. It results in larger phase spread; however, it only has a small effect on the reflectivity. The dimensions at point B shows the last few sections have a bigger effect on the reflectivity. With the appearance of a spike at 97 GHz, the phase spread can be even smaller. Further simulations show that the spike is mainly caused by tolerance from the second corrugation section. As shown in Fig. 7(c), the spike appears when using the designed geometry, but with tolerance at the second corrugation section, and it disappears when using the geometry with tolerance at point B, except the designed radius at the second corrugation section. The tolerance from the other corrugation sections has less effect on the amplitude and the phase response of the Bragg reflector.

B. Sidewall Coupler With Bragg Reflector

The input coupler composed of the reflector and the T-junction was simulated using CST Microwave Studio. A good transmission of about -0.4 dB can be achieved over the frequency band of 90–100 GHz using the designed dimensions of the broadband reflector, as shown in Fig. 8(a). The simulation of the coupler with the designed Bragg reflector showed an average transmission coefficient of -0.4 dB over the frequency band. When considering the tolerance, the average transmission is still better than -0.6 dB, which meets the design criteria of the coupler for the gyro-TWA. It also confirms that the reflectivity of the Bragg reflector does not have a significant impact on the coupler.

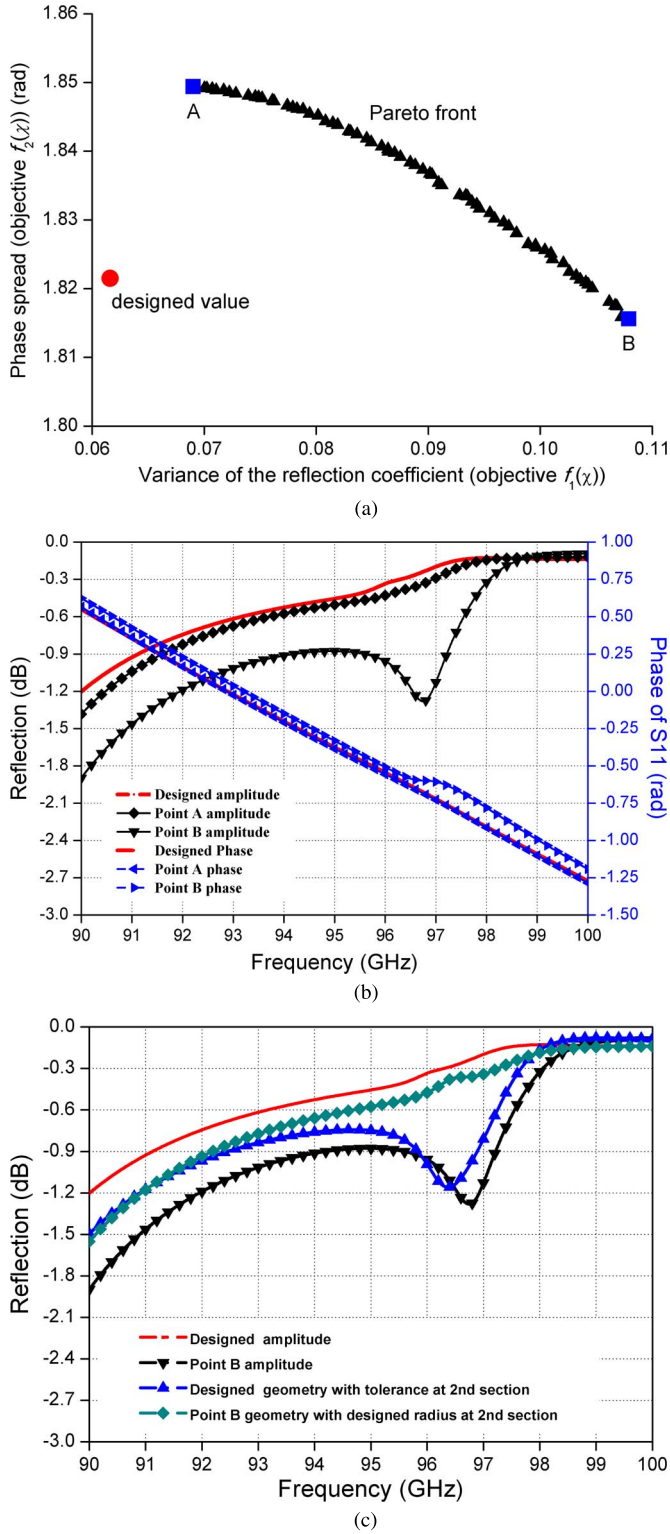

Fig. 7. (a) Pareto fronts of the tolerance sensitivity. (b) Comparison of the performance with designed parameters and the values at points A and B. (c) Detail tolerance study on Section II.

IV. Construction and Measurement

The reflector was manufactured using an electroforming method. An aluminum former with the inner cross section of the waveguide was firstly constructed by a computer numerical control (CNC) machine and then copper was grown on it. The aluminum mandrel was later dissolved away to form the copper waveguide. Before electroforming, the dimensions of the reflector were measured and then simulated. The comparisons of the designed and measured dimension of the broadband reflector are shown in Table I. Almost all the radii of the corrugation sections in the measurement are larger than the designed values, and the averaged machining error was about 0.1 mm. Generally a well-calibrated CNC machine should be

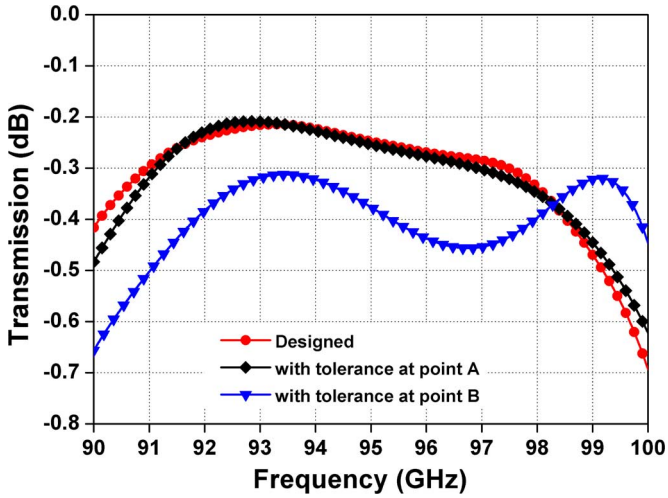

Fig. 8. Performance of the designed coupler and with tolerance at points A and B.

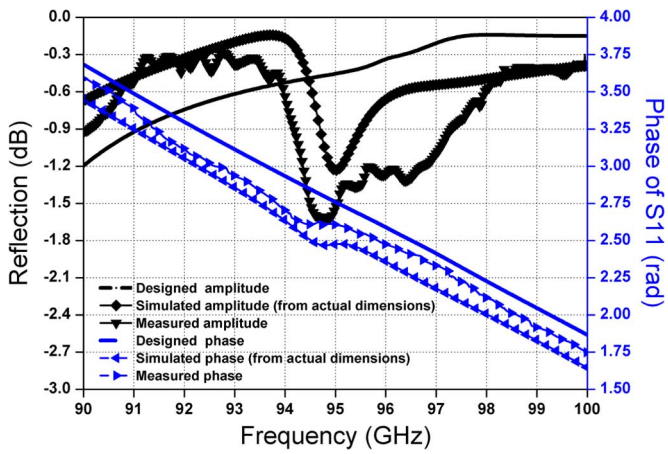

Fig. 9. S-parameters of the optimized 16-section Bragg reflector.

able to achieve a machining accuracy of ± 20 μm if operated by an experienced technician.

From the simulation, although the magnitude of the reflection has a different trend with the one designed, the phase spread of the two structures are similar with a phase shift of about 17°. This resulted in a shift of the central frequency. The measured results shown in Fig. 9 agree well with the simulation results using the actual dimensions. The spike at 95 GHz is mainly caused by the tolerance at the second section.

With the actual dimensions, the center frequency of the bandwidth is down shifted, which means the lower frequency side has an even better transmission while the higher frequency side becomes worse. From the analysis in Section II, it is possible to shift the center frequency by reducing slightly the length of the first section.

To measure the performance of the input coupler, a copper block that contains a T-junction was machined. The connection of the components and the measurement setup are shown in Fig. 10(a). A rectangular-to-circular convertor was used to convert the TE_{10} mode of the rectangular waveguide (VNA port) into the TE_{11} mode of the circular waveguide (port 2 of the T-junction). Two waveguide tapers were machined by

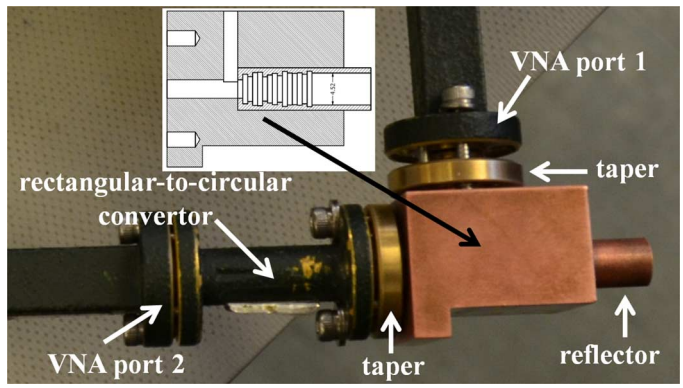

(a)

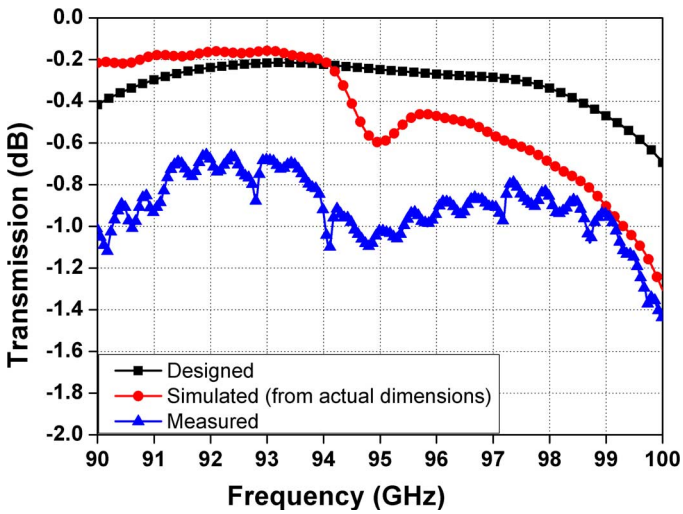

(b)

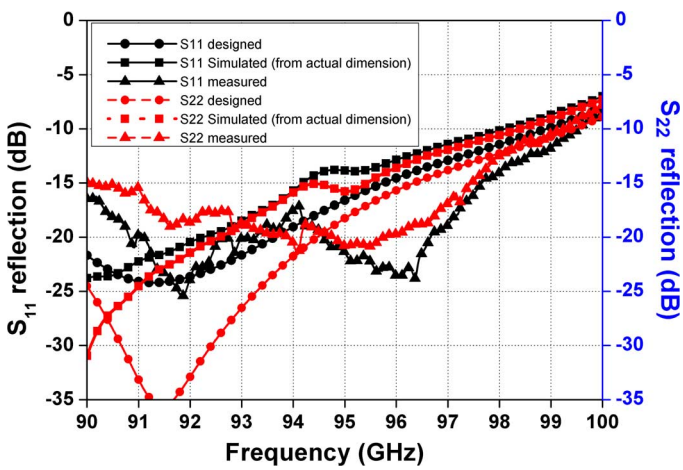

(c)

Fig. 10. (a) Measurement setup, (b) transmission coefficient, and (c) reflection coefficient of the input coupler.

wire erosion to match the dimensions of the waveguide components. The measured transmission and the reflection are shown as Fig. 10(b) and (c), respectively. The input coupler has an average -1.0-dB transmission over the desired frequency band. It is about 0.7 dB less than the designed performance. However, if considering the loss of the input coupler and the relatively big machining tolerance, such performance is quite acceptable for use in the W-band gyro-TWA. It also proves that

the reflector with periodic corrugations is not a tolerance-sensitive waveguide structure. Therefore, with a smaller machining tolerance this design could be used for higher frequency applications.

V. Conclusion

In this paper, a sidewall single-hole coupler based on a rectangular-to-circular T-junction and a broadband Bragg-type reflector was designed and measured. The relations between the bandwidth and the phase spread were analyzed numerically. It was used as one of the goal functions to optimize the dimensions of the broadband reflector. The measurement of the input coupler showed an average -1.0-dB transmission over the desired frequency band (90–100 GHz), which is acceptable to be used in the W-band gyro-TWA experiment. The proposed input coupler has much larger radius compared with the one using a cutoff waveguide, therefore greatly relaxing the strict alignment requirement of the gyro-TWA. The proposed coupler has potential for further improvements, such as using a more precise CNC machine to reduce the machining tolerance. Also, as the Bragg reflector has a relatively large tolerance allowance, it is possible to simplify the geometry by combining similar radii to reduce the machining difficulty, such as combining corrugation sections 4 and 5, and corrugation sections 11–13.

Acknowledgment

The EPSRC Engineering Instrument Pool is gratefully acknowledged for providing the vector network analyzer (VNA) used in the experiments. The authors would like to thank A. Ruddell for his assistance in setting up and installing the VNA in the laboratory.

References

[1] R. E. Collin, *Field Theory of Guided Waves, in Series of Electromagnetic Waves*, 2nd edition ed. New York, NY, USA: IEEE Press, 1991.
[2] G. G. Denisov and M. G. Reznikov, "Corrugated cylindrical resonators for short-wavelength relativistic microwave oscillators," *Radiophys. Quantum Electron.*, vol. 25, no. 5, pp. 407–413, 1982.
[3] L. Zhang *et al.*, "Multi-mode coupling wave theory for helically corrugated waveguide," *IEEE Trans. Microw. Theory Techn.*, vol. 60, no. 1, pp. 1–7, Jan. 2012.
[4] W. He *et al.*, "Theory and simulations of a gyrotron backward wave oscillator using a helical interaction waveguide," *Appl. Phys. Lett.*, vol. 89, 2006, Art. ID 091504.
[5] V. L. Bratman *et al.*, "High-gain wide-band gyrotron traveling wave amplifier with a helically corrugated waveguide," *Phys. Rev. Lett.*, vol. 84, no. 12, pp. 2746–2749, Mar. 2000.
[6] S. V. Samsonov *et al.*, "CW Ka-band kilowatt-level helical-waveguide gyro-TWT," *IEEE Trans. Electron Devices*, vol. 59, no. 8, pp. 2250–2255, Aug. 2012.
[7] W. He, C. R. Donaldson, L. Zhang, K. Ronald, P. McElhinney, and A. W. Cross, "High power wideband gyrotron backward wave oscillator operating towards the terahertz region," *Phys. Rev. Lett.*, vol. 110, Apr. 2013, Art. ID 165101.
[8] W. He *et al.*, "Latest experiments of W-band gyro-BWO using helically corrugated waveguides," in *38th Int. Infrared, Millimeter, Terahertz Waves Conf.*, Mainz, Germany, Sep. 1–6, 2013, pp. 1–2.
[9] D. E. Pershing *et al.*, "A TE11 Ka-band gyro-TWT amplifier with high-average power compatible distributed loss," *IEEE Trans. Plasma Sci.*, vol. 32, no. 3, pp. 947–956, Mar. 2004.
[10] C. G. Whyte *et al.*, "Wideband gyro-amplifers," *IEEE Trans. Plasma Sci.*, vol. 40, no. 5, pp. 1303–1310, May 2012.
[11] L. Zhang, W. He, C. R. Donaldson, K. Ronald, P. McElhinney, and A. W. Cross, "An input coupler for a W-band gyro-TWA," in *6th U.K., Europe, China Millimeter Waves and THz Technol. Workshop*, Rome, Italy, Sep. 9–11, 2013, pp. 1–2.
[12] J. R. Garner, L. Zhang, C. R. Donaldson, and P. McElhinney, "An input coupler for a W-band gyro-TWA," in *1st Annu. Active Passive RF Devices Seminar*, Glasgow, U.K., Oct. 29, 2013, pp. 47–50.
[13] J. Zheng and M. Yu, "Rigorous mode-matching method of circular to off-center rectangular side-coupled waveguide junctions for filter applications," *IEEE Trans. Microw. Theory Techn.*, vol. 55, no. 11, pp. 2365–2373, Nov. 2007.
[14] K. Hwang and H. Eom, "Scattering analysis for a circular to rectangular T-junction," *Microw. Opt. Technol. Lett.*, vol. 41, no. 3, pp. 231–234, Mar. 2004.
[15] P. Krauss and F. Arndt, "Rigorous mode-matching method for the modal analysis of the T-junction circular to side coupled rectangular waveguide," in *IEEE MTT-S Int. Microw. Symp. Dig.*, Orlando, FL, USA, May 1995, vol. 3, pp. 1355–1358.
[16] N. Yoneda, M. Miyasaki, T. Nishino, H. Asao, H. Nakaguro, and S. Betsudan, "Analysis of circular-to-rectangular waveguide T-junction using mode-matching technique," *Electron. Commun. Jpn., Part II: Electron.*, vol. 80, no. 7, pp. 37–46, Jul. 1998.
[17] C. R. Donaldson *et al.*, "A cusp electron gun for millimeter wave gyrodevices," *Appl. Phys. Lett.*, vol. 96, 2010, Art. ID 141501.
[18] C. K. Chong *et al.*, "Bragg reflectors," *IEEE Trans. Plasma Sci.*, vol. 20, no. 3, pp. 393–402, Mar. 1992.
[19] L. Zhang, W. He, A. W. Cross, A. D. R. Phelps, K. Ronald, and C. G. Whyte, "Design of an energy recovery system for a gyrotron backward-wave oscillator," *IEEE Trans. Plasma Sci.*, vol. 37, no. 3, pp. 390–394, Mar. 2009.
[20] G. L. James, "Analysis and design of TE11-to-HE11 corrugated cylindrical waveguide mode converters," *IEEE Trans. Microw. Theory Techn.*, vol. MTT-29, no. 10, pp. 1059–1066, Oct. 1981.

Liang Zhang received the B.Sc. degree in applied physics from the University of Science and Technology of China, Hefei, China, in 2004, the M.Sc. degree in application of nuclear techniques from the China Academy of Engineering Physics, Chengdu, China, in 2007, and the Ph.D. degree in physics from the University of Strathclyde, Glasgow, U.K., in 2012.

He is currently a Research Associate with the Scottish Universities Physics Alliance, Department of Physics, University of Strathclyde. His main research interests include pulse-power technology and gyrotron traveling-wave amplifier (gyro-TWA)/backward-wave oscillators.

Wenlong He received the B.Sc. degree in physics from Soochow University, Jiangsu, China, in 1983, the M.Sc. degree in accelerator physics from the China Academy of Engineering Physics, Chengdu, China, in 1988, and the Ph.D. degree in relativistic electron beams and masers from the University of Strathclyde, Glasgow, U.K., in 1995.

He is currently a Senior Research Fellow with the Scottish Universities Physics Alliance, Department of Physics, University of Strathclyde. His main research interests include relativistic electron beams, gyrotron traveling-wave amplifier (gyro-TWA)/backward-wave oscillators, cyclotron autoresonance masers (CARMs), free-electron lasers (FELs), and other high-power microwave and terahertz devices.

Craig R. Donaldson received the B.Sc. (Hons.) degree in physics and M.Sc. degree in high-power RF and Ph.D. degrees from the University of Strathclyde, Glasgow, U.K., in 2005, 2006, and 2009, respectively.

He has since continued as a Research Fellow with the Department of Physics, University of Strathclyde. His main research interests are high-frequency gyrotron traveling-wave amplifiers (gyro-TWAs)/backward-wave oscillators (BWOs) and electron beam generation.

Jason R. Garner received the B.Sc. (Hons) degree in physics and M.Sc. degree in high-power radio frequency science and engineering from the University of Strathclyde, Glasgow, U.K., in 2010 and 2012, respectively, and is currently working toward the Ph.D. degree at the University of Strathclyde.

He is currently with the Scottish Universities Physics Alliance, Department of Physics, University of Strathclyde. His main research interests include the design of passive components for millimeter-wave gyro-devices and traveling-wave amplifiers (gyro-TWAs).

Paul McElhinney received the B.Sc. degree in applied physics, M.Sc. degree in high-power RF science and engineering, and Ph.D. degree in physics from the University of Strathclyde, Glasgow, U.K., in 2005, 2009, and 2013, respectively.

He is currently a Research Associate with the Scottish Universities Physics Alliance, Department of Physics, University of Strathclyde. His main research interests include broadband quasi-optical components for high-power gyro-amplifiers and oscillators.

Adrian W. Cross was born in Hanover, Germany, in 1966. He received the B.Sc. degree (with honors) in physics and Ph.D. degree from the University of Strathclyde, Glasgow, U.K., in 1989 and 1993, respectively.

In 1993, he joined the Atoms, Beams, and Plasmas Group, University of Strathclyde, initially as a Research Fellow. He then became a Lecturer in 2000, a Senior Lecturer in 2003, a Reader in 2006 and was a Professor in 2014 with the Department of Physics, University of Strathclyde. From 2002 to 2007, he was an Engineering and Physical Science (EPSRC) Advanced Fellow and has been Group Leader since 2014. He has been involved in various aspects of research on gyrotrons, cyclotron autoresonance masers, free-electron lasers, superradiant sources, gyrotron traveling-wave amplifiers (gyro-TWAs) and plasma applications. More recently, he has primarily been concerned with research on microwave pulse compression, terahertz radiation sources, and pseudospark physics.

Design Study of a Fundamental Mode Input Coupler for a 372-GHz Gyro-TWA I: Rectangular-to-Circular Coupling Methods

Jason R. Garner, Liang Zhang, Craig R. Donaldson, Adrian W. Cross, and Wenlong He

***Abstract*— The design of two fundamental mode rectangular-to-circular waveguide input couplers for a low-terahertz gyrotron-traveling wave amplifier (gyro-TWA) is presented. A T-junction input coupler with a Bragg reflector and a multiple-hole directional coupler were optimized for operation between 360 and 384 GHz, the proposed gyro-TWA bandwidth. The T-junction coupler and the multiple-hole coupler achieved the respective bandwidths of 10% and 35%. The benefits and potential limitations of the low-terahertz wave coupler topologies are discussed alongside the challenging manufacturing methods of the submillimeter-wave components.**

***Index Terms*— Gyrotron-traveling wave amplifier (gyro-TWA), mode coupling, terahertz input coupler, waveguide coupler.**

I. Introduction

GYRODEVICES are the sources of coherent electromagnetic (EM) radiation based on the cyclotron resonance maser instability [1] capable of delivering high-power microwave signals at high frequencies. Applications of the gyrodevices include plasma heating [2], Radio Detection and Ranging (RADAR) systems [3], and spectroscopes [4].

A W-band gyrotron-traveling wave amplifier (gyro-TWA) has been developed at the University of Strathclyde for use on a weather monitoring RADAR system. The W-band device uses a threefold helically corrugated interaction region (HCIR) [5] as opposed to a standard smooth bore cavity. The HCIR couples the TE_{21} mode to the first spatial harmonics of the TE_{11} mode to generate an operating eigenwave, improving the bandwidth range for the gyro-TWA operation [6]. Research on gyrodevices at the University of Strathclyde has demonstrated excellent results in achieving high-power and wide-frequency tunability. A W-band gyrotron backward wave oscillator (gyro-BWO) achieved a maximum output power of 12 kW when driven by a 40-kV, 1.5-A, annular-shaped large-orbit electron beam [7]. The frequency tuning band of 88–102.5 GHz was achieved through the adjustments of the cavity magnetic field. The gyro-TWA incorporates the components designed for the gyro-BWO. A schematic of the gyro-TWA is shown in Fig. 1.

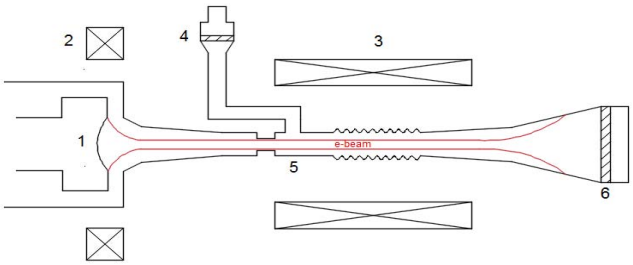

Fig. 1. Gyro-TWA schematic with 1—electron gun, 2—reverse coil for magnetic cusp, 3—solenoid, 4—pillbox window, 5—input coupler feed to HCIR, and 6—vacuum window at output horn.

TABLE I
Target Goals for Gyro-TWA Performance

Frequency (GHz)	360 - 384
Output Power (W)	200
Gain (dB)	~ 40
Beam Voltage (kV)	30
Beam Current (A)	0.5

A gyro-TWA operated at a center frequency of 372 GHz is being developed for the applications of electron paramagnetic resonance (EPR) and dynamic nuclear polarization (DNP) in a nuclear magnetic resonance (NMR) system. High-power (hundreds of watts) wide bandwidth (10%) gyroamplifiers are ideal for pulsed EPR and DNP-NMR applications. A list of targeted performance characteristics of the 372-GHz gyro-TWA is presented in Table I.

Efficient coupling of EM radiation into the gyro-TWA interaction cavity is important to the overall performance of the gyro-TWA. At frequencies approaching the terahertz region, the coupling process encounters tremendous difficulties due to the submillimeter dimensions and the subsequent increase in waveguide losses caused by a reduction in the skin depth. In this paper, the theoretical and numerical designs of two millimeter-wave couplers are presented. Discussion on the manufacturability of the designs is given alongside the selection of a coupler topology, deemed to be best suited for high-frequency operation, to be taken forward and implemented on a low-terahertz gyro-TWA.

Manuscript received October 9, 2015; revised November 11, 2015; accepted November 13, 2015. Date of publication November 26, 2015; date of current version December 24, 2015. This work was supported by the Engineering and Physical Sciences Research Council, U.K., under Grant EP/K029746/1. The review of this paper was arranged by Editor M. Thumm.

The authors are with the Department of Physics, Scottish Universities Physics Alliance, University of Strathclyde, Glasgow G4 0NG, U.K. (e-mail: j.garner@strath.ac.uk; liang.zhang@strath.ac.uk; craig.donaldson@strath.ac.uk; a.w.cross@strath.ac.uk; w.he@strath.ac.uk).

Color versions of one or more of the figures in this paper are available online at http://ieeexplore.ieee.org.

Digital Object Identifier 10.1109/TED.2015.2501028

A well-designed coupler topology can be utilized as a method of coupling power into the interaction cavity and/or as a method of radially extracting the generated EM radiation [8]. However, higher than expected reflections from the component can result in stimulated oscillations in the cavity and loss of the amplification characteristics. The design of the input coupler is centered on the optimization of two parameters:

1) the transmission ratio from the input mode to the desired cavity mode;
2) bandwidth of the passive structure.

The potential application of the input coupler designs will be based on achieving a transmission of larger than -1 dB in the frequency range of 360–384 GHz. The frequencies at which the transmission falls below -1 dB will determine the bandwidth of the passive component, with the percentage bandwidth determined by the deviation about the center operating frequency. A waveguide reflector is also presented, aiming to prevent the propagation of incident radiation to the electron gun, while maximizing the beam tunnel diameter.

II. T-Junction Input Coupler With Bragg Reflector

The proposed millimeter-wave coupler design is based upon a rectangular-to-circular T-junction. The waveguide T-junction transition has many practical applications, including the structures use as a filter [9], a polarizer [10], and in orthomode transducers [11]. Analytical methods can be used in the optimization of a simple microwave structure, also providing higher order mode information. Several analytical techniques for understanding a rectangular-to-circular T-junction have been demonstrated using Fourier transform and/or mode matching techniques [12].

The rectangular-to-circular T-junction has three parameters available for optimization, which will affect the coupling of the structure. The parameters in question are the rectangular waveguide width and height, a and b respectively, and the radius of the circular waveguide, R. Efficient coupling of the TE_{10}^{R} mode to TE_{11}^{C} is achieved when the wavelength of the incident wave is approximately unchanged when transmitted into the beam tunnel, i.e., when $\lambda_g^R \approx \lambda_g^C$, where the R and C superscripts denote the guide wavelength in the rectangular and circular waveguides, respectively.

For a gyro-TWA system, practical design limitations are often imposed on the magnitude of R, the radius of the beam tunnel. For the gyro-TWA operated at the center frequency of 372 GHz, the beam tunnel radius is 0.35 mm. In practice, the beam tunnel radius is chosen to allow for transmission of the desired mode to the interaction cavity and is made large enough to allow for unhindered electron beam propagation. The cusp electron gun for the high-frequency gyro-TWA produces an electron beam of 0.2 mm in radius. The parameters a and b were numerically optimized using Computer Simulation Technology (CST) Microwave Studio (CST-MS) to minimize reflections at the input port with the optimized values of 0.55 and 0.50 mm, respectively.

The input coupler design requires the majority of the input radiation to be transmitted to the interaction region. To prevent wave propagation into the diode region of the gyro-TWA, the use of a cutoff waveguide attached to a rectangular-to-circular T-junction is a general solution to improve the transmission coefficient over the operational bandwidth. For lower frequencies, the step-down waveguide reflector is a simple, practical method, which produces excellent results. However, at frequencies approaching the low-terahertz region, a cutoff waveguide can hinder the beam transportation through the cavity due to the reduced waveguide diameter at high frequencies. At the input coupler region of a gyro-TWA, the Larmor radius of the electron beam is large due to the small magnetic field magnitude relative to the center of the interaction region. Therefore, it is beneficial to increase the diameter of the waveguide structure within which the electron beam can propagate, while ensuring a high reflectivity of incident radiation.

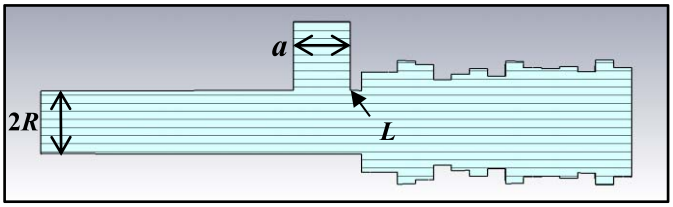

Fig. 2. Side view of T-junction coupler with Bragg reflector.

TABLE II
Parameter Set for 372-GHz Bragg Reflector

Parameter	Optimised value (mm)	Parameter	Optimised value (mm)
Period	0.175	Radius 8	0.495
Radius 1	0.550	Radius 9	0.664
Radius 2	0.550	Radius 10	0.575
Radius 3	0.667	Radius 11	0.608
Radius 4	0.602	Radius 12	0.614
Radius 5	0.461	Radius 13	0.574
Radius 6	0.551	Radius 14	0.683
Radius 7	0.596	Radius 15	0.618

A Bragg reflector [13] is a waveguide structure with radial periodicity, which can be used as a method of providing frequency selective feedback. A review of a Bragg reflector design in the W-band is presented in [14]. The design process was applied and an optimized reflection of $\sim$100% in the desired frequency band was achieved for the condition that the radii of the reflector sections are larger than R (Fig. 2). The radii of the individual sections of the Bragg reflector, listed sequentially from the section closest to the input coupler, are shown in Table II.

The numerical scattering parameters of an optimized TE_{10}–TE_{11} T-junction low-terahertz coupler with a Bragg reflector for $R = 0.35$ mm were simulated and are shown in Fig. 3. The use of a Bragg reflector in the coupler geometry has proved to be an effective method of achieving high transmission over the desired bandwidth, while maximizing the region through which an electron beam may propagate unhindered. Therefore, no unnecessary reduction in the electronic efficiency of the gyro-TWA will occur as a result of electron power loss in the waveguide wall. The waveguide section length L was optimized at 0.12 mm to achieve high coupling between 360 and 384 GHz with the attached waveguide reflector.

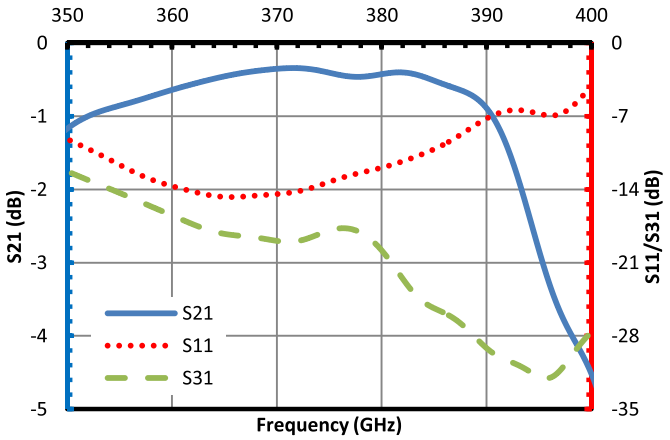

Fig. 3. Scattering parameters of a TE_{10}–TE_{11} T-junction coupler with Bragg reflector.

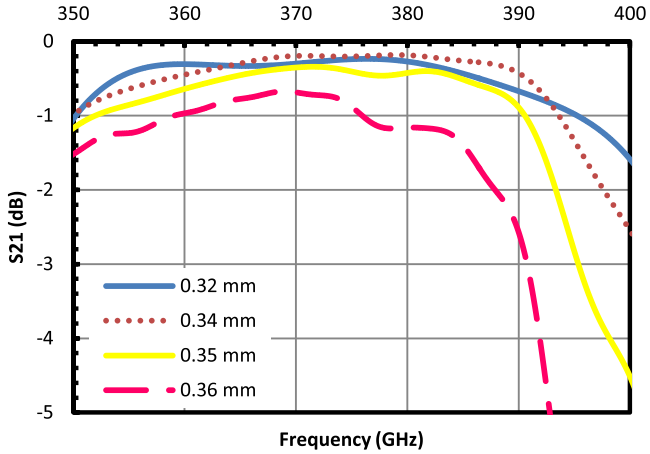

Fig. 5. Effect of small R variations on T-junction coupler transmission.

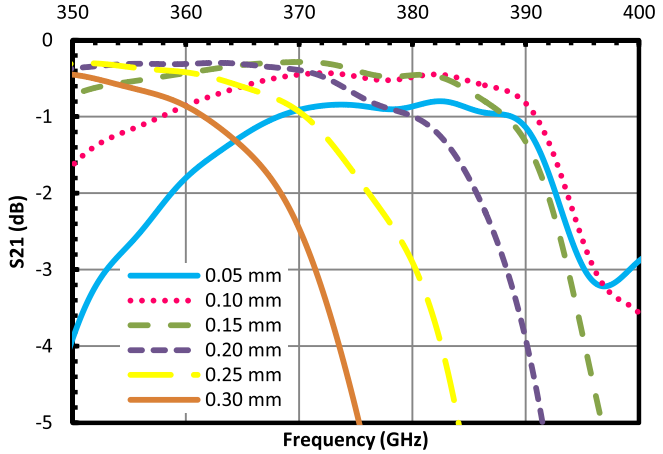

Fig. 4. L variation effect on T-junction coupler frequency response.

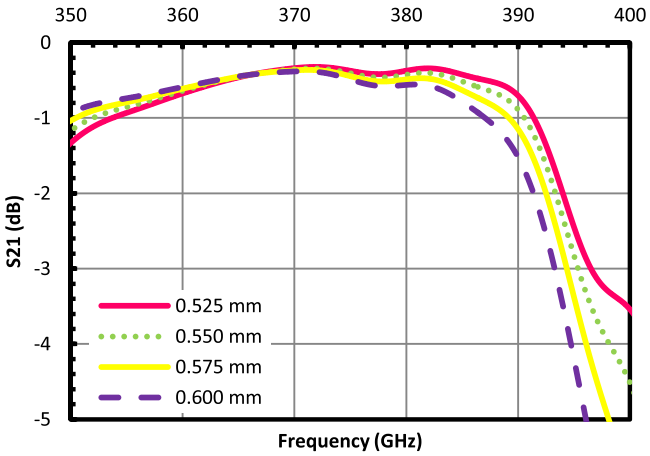

Fig. 6. Effect of a variation on T-junction coupler center frequency.

Transmission loss of larger than -1 dB was achieved over a ~10% bandwidth, which includes the operational frequency range of the low-terahertz gyro-TWA. A coupler of similar topology has been shown to achieve a bandwidth of 20% [15]; however, this design would only be applicable to a structure where a small diameter waveguide reflector, in comparison to the operating wavelength, is permissible. The Bragg reflector was effective in preventing the transmission of significant levels of radiation toward the electron gun with S_{31} of less than -15 dB achieved over the desired bandwidth.

The T-junction coupler topology displayed a degree of frequency tunability with a variation of the waveguide length between the Bragg reflector and the near edge of the input rectangular waveguide (L). The change in transmission frequencies is shown in Fig. 4 for variations in length L for the fixed values of a, b, and R. The frequency shifts exhibited are a result of reflected wave phase changes from the Bragg structure caused by changes in waveguide length. An increase in L is shown to lower the center frequency of the T-junction coupler alongside reducing the coupling bandwidth.

To test the feasibility of the input coupler, a tolerance study was undertaken. A review of the effect from 10 to 20 μm changes to R on the input coupler transmission for the fixed values of a and b is shown in Fig. 5. The resultant plot shows that small variations in the interaction waveguide radius will result in the degradation of the total coupling achieved by the waveguide structure. The spark erosion technique, which can be used to manufacture circular waveguides of submillimeter radius, can achieve a tolerance of ± 5 μm about the optimum value. Fig. 5 suggests that a variation of 5 μm to R would ensure that high coupling to the TE_{11} mode is still achieved despite the radius discrepancy. A similar process involving waveguide width and height variations for fixed R was undertaken. The study highlighted that up to ± 25-μm variations of a about the optimum value of 0.55 mm will result in a center frequency shift of ~2 GHz with a minimal effect on coupling strength (Fig. 6). Alternatively, Fig. 7 shows that ± 25-μm alterations to b will have no effect on the frequency response; however, the coupling strength is reduced by ~50% at the center frequency. The Computer Numerical Control (CNC) milling technique, used to manufacture waveguide channels, has a low limit positional accuracy of ± 1 μm. Therefore, if a modern milling machine is used in the coupler design, the frequency shift caused by a and b variations will not result in the input coupler being unfit for operation at 360–384 GHz.

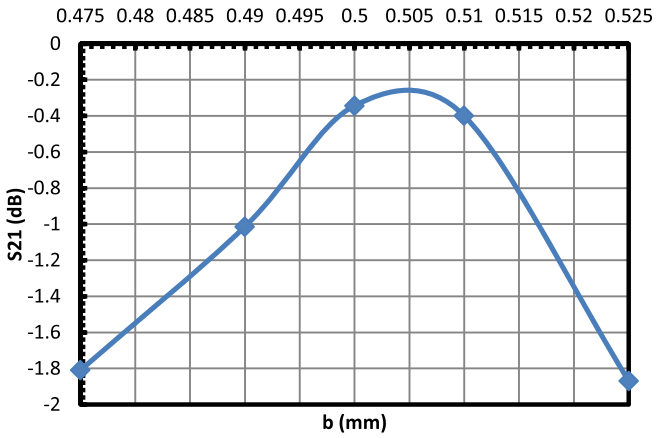

Fig. 7. Effect of b discrepancies on transmission at 372 GHz.

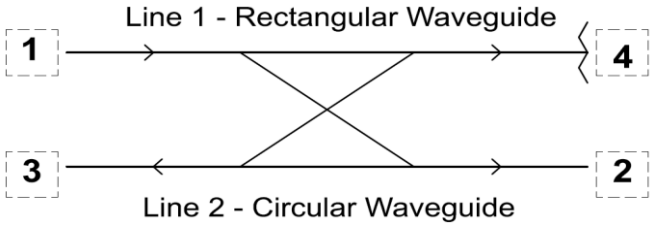

Fig. 8. Power flow of four-port directional coupler with Port 1—input, Port 2—coupled, Port 3—isolated, and Port 4—through.

III. Multiple-Hole Input Coupler

A low-terahertz, rectangular TE_{10} to circular TE_{11}, multiple-hole input coupler was also evaluated through numerical simulations. The multiple-aperture coupler is, unlike the three-port designs described in Section II, a four-port device consisting of two transmission lines electromagnetically coupled through a series of common wall apertures. A commonly used power flow schematic of a four-port network is shown in Fig. 8. Directional couplers can be designed for arbitrary power division with the common coupling factors of 3, 6, 10, and 20 dB commonly employed as a method of energy extraction from a millimeter-wave cavity. The theory of small aperture coupling between transmission lines [16] provides a description of the field profile through an individual coupling hole. A waveguide directional coupler consists of two waveguides coupled through a series of apertures on a common broad wall [17]; however, narrow wall coupling has also been demonstrated [18]. EM coupling between rectangular and circular waveguides is also feasible [19]. The design of a rectangular-to-circular multiple-hole coupler, centered at 372 GHz, is based on achieving a high coupling factor for the desired mode and a high directivity. The coupling between the rectangular and the circular transmission lines is defined as the ratio of the power at the input port to the power at the coupled port. The directivity is the ratio of the power at the coupled port to the power at the isolated port. For an ideal multiple-aperture coupler, the directivity would be infinite. Choung *et al.* [20] show that the coupling (C) for a small aperture with uniform displacement as

$$C = \frac{\sum_{i=1}^{i=N} a_i \cos\left(\frac{2i-1}{2N-1}\right)\pi\theta_C}{\sum_{i=1}^{i=N} a_i} \tag{1}$$

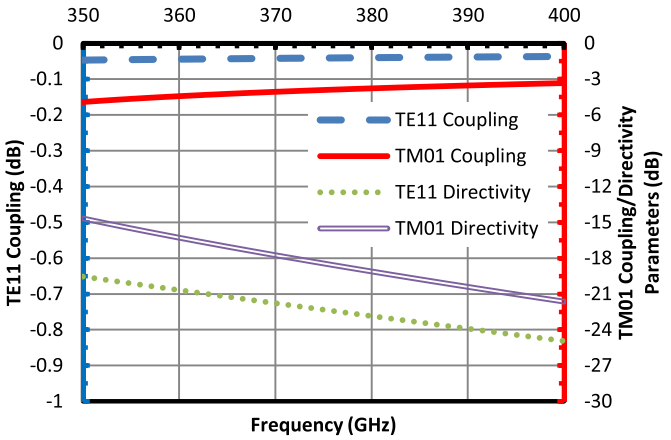

Fig. 9. Coupling and directivity parameters of wanted and unwanted modes.

and, similarly, the directivity (D) as

$$D = \frac{\sum_{i=1}^{i=N} a_i \cos\left(\frac{2i-1}{2N-1}\right)\pi\theta_D}{\sum_{i=1}^{i=N} a_i} \tag{2}$$

where θ_C and θ_D are the coupling and the directivity parameters, respectively, defined as

$$\theta_C = \frac{L}{2\pi}(\beta_1 - \beta_2) \tag{3}$$

$$\theta_D = \frac{L}{2\pi}(\beta_1 + \beta_2) \tag{4}$$

where L is the coupling section length. The coupling length, L, is defined by the product of the number of apertures and the separation between adjacent apertures ($2N * s$). For a 30-hole coupling section, $N = 15$. The phase constant, β, is unique to each of the rectangular and circular transmission lines. For a circular waveguide of $R = 0.35$ mm, the phase constants, β_{10}^R and β_{11}^C, are matched when $a \approx 0.60$ mm. The separation between neighboring holes is equated as half the radiation wavelength ($s = 0.50$ mm). The coupling (3) and directivity (4) parameters for TE_{10}^C and TM_{01}^C are plotted as a function of frequency in Fig. 9. For the analysis, β_1 is the phase constant in the rectangular waveguide and β_2 is the phase constant in the circular waveguide.

In order to achieve high coupling, the propagation of unwanted modes must also be considered. For the TE_{11} mode coupler, the three subsequent higher order modes (TM_{01}, TE_{21}, and TE_{01}) are also evaluated. The only unwanted mode that will propagate is TM_{01}^C. Therefore, the coupler design should ensure that the TM_{01} mode has a lower coupling parameter than the TE_{11} mode.

Fig. 9 shows that strong coupling to the TE_{11}^C mode is achieved, while coupling to the TM_{01}^C mode is weak compared with the desired mode. Maximum coupling is achieved for a coupling parameter equal to 0 dB. The directivity parameter of the TE_{11} mode is less than θ_D for the TM_{01} mode over the entire frequency range; hence, TM_{01} is isolated. Therefore, the TE_{11} mode would be dominant at the coupled port of the four-port network.

The coupling strength of the TE_{11} mode into Line 2 varies with the number of coupling apertures. In the analysis of (1),

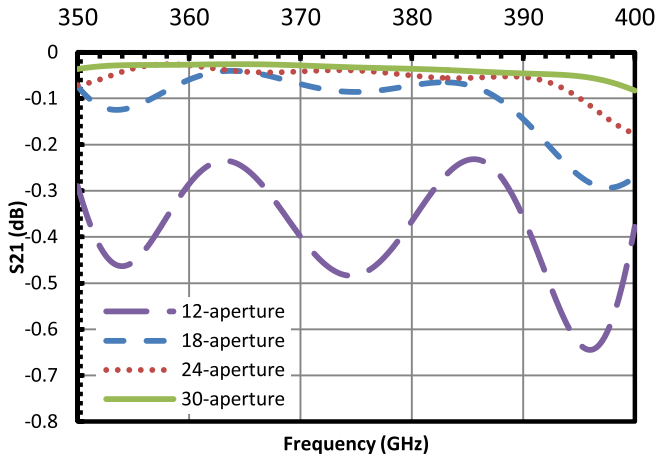

Fig. 10. Simulated transmission of 12-, 18-, 24-, and 30-aperture couplers.

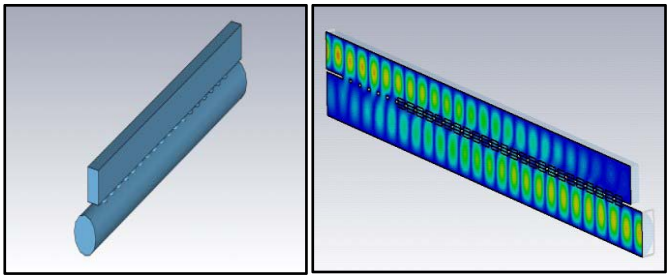

Fig. 11. 3-D multihole geometry (L) and microwave field progression (R).

the coupling parameter (θ_C) and the coupling strength (a_i) are constant. Equation (1) suggests strong coupling for $N = 12 - 30$. A coupling aperture radii array can improve the coupling and directivity [21]; however, a distributive array will enhance the manufacturing complexity, especially the aperture size is small at high operating frequencies. Therefore, a linear aperture distribution is employed. A numerical simulation is carried out in a bid to analyze the TE_{10}^{R}–TE_{11}^{C} transmission for 12-, 18-, 24-, and 30-hole couplers (see Fig. 10) for optimized hole radii.

Fig. 10 has indicated that the transmission from Fig. 9 for the multiple-aperture coupler is comparable with the theoretical prediction. However, a similar level of coupling can be achieved for 18-, 24-, and 30-aperture couplers provided the hole radius, R', is optimized. For 18 apertures, $R' = 0.17$ mm whereas 24- and 30-aperture couplers are optimized with $R' = 0.16$ and 0.15 mm, respectively. The coupling strength achieved with 12 apertures is less than the 18-, 24-, and 30-aperture couplers; however, the magnitude of the coupling strength is larger than -1 dB meaning it is within the target boundaries set for the input coupler design. For all four structures, the separation between Lines 1 and 2 is 0.05 mm. The desired coupling response over the required bandwidth can be achieved with 12 apertures. Therefore, subsequent designs will use 12 coupling holes (Fig. 11).

The dimensions of the theoretically calculated parameters are shown in Table III. The waveguide height (b) to waveguide width (a) ratio is initially set at 2:1. Optimization of the

TABLE III
THEORETICAL AND OPTIMIZED PARAMETER SET

Parameter	Theoretical	Optimised
N	12	12
a	0.60 mm	0.59 mm
b	0.30 mm	0.36 mm
R	0.35 mm	0.35 mm
s	0.50 mm	0.40 mm

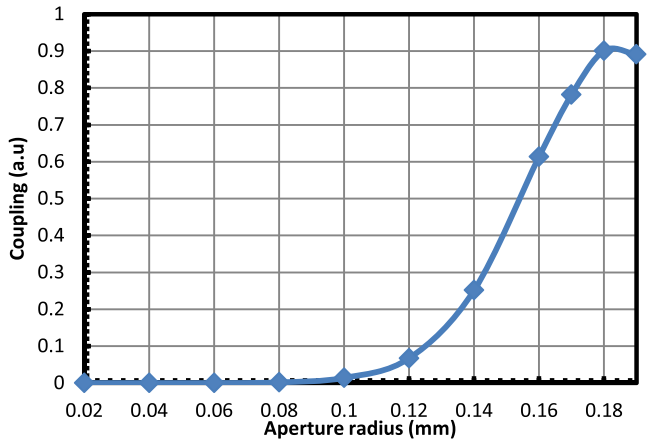

Fig. 12. Transmission variation as effected by aperture radius at 372 GHz.

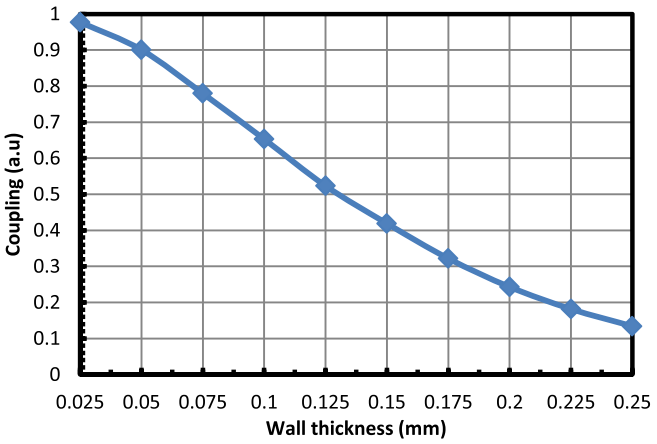

Fig. 13. Transmission variation with increase in aperture height at 372 GHz.

transmission and reflection within the coupling structure is carried out through parametric sweeps of the waveguide width and height (a and b), the radius of the coupling apertures (R'), and the spacing between Lines 1 and 2, i.e., the aperture height. It is known that the spacing between the center of adjacent coupling apertures (s) is ~0.4 mm; however, the R' value can be set for optimum performance within the upper limit of $s/2$. The effect of R' variation on the TE_{10}^{R}–TE_{11}^{C} coupling for a 12-aperture coupler is shown in Fig. 12. The aperture height is determined by considering the potential thickness of the metal sheet used to separate the rectangular and circular waveguides in a practical coupler. The effect of sheet metal thickness on the TE_{11} transmission to the coupled port for a 12-hole structure is shown in Fig. 13.

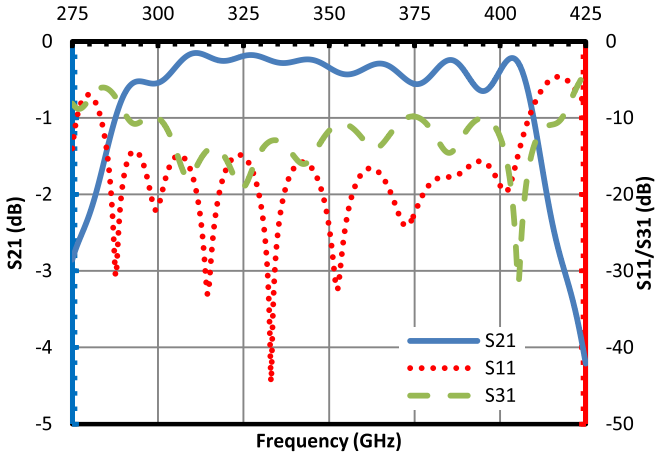

Fig. 14. Transmission and reflection of 372-GHz 12-hole input coupler.

Fig. 12 shows that coupling to the desired mode is enhanced with increasing R' up to 0.18 mm. The upper limit of 0.19 mm is dictated by the optimal pitch between the centers of adjacent apertures (0.4 mm), allowing space for machining of adjacent holes. The effect of increasing separation between Lines 1 and 2 is shown in Fig. 13, where a decrease in energy delivered to the coupled port is evident with increased separation. A metal thickness of 0.05 mm would be chosen for a manufactured multiple-hole coupler. A sheet thickness of this magnitude would allow for a high transmission to the TE_{11}^{C} mode, while ensuring that a high mechanical stability is achieved in the gap spacing. The CST-MS simulated scattering of the optimized 12-aperture coupler is shown in Fig. 14.

Fig. 14 shows that an operational frequency range of 121 GHz, equating to a bandwidth of over 35%, is achieved with the 12-aperture coupler. Fig. 10, however, shows that marginal increases in coupling strength can be achieved by increasing the aperture number but additional length will lead to higher losses in the waveguide structure. The frequency range of the proposed fundamental mode gyro-TWA (360–384 GHz) is enclosed within the operational bandwidth of the 12-aperture input coupler and, therefore, is suitable for the proposed application. The optimized parameter set is documented in Table III, showing that the theoretically calculated set provided a good basis upon which to explore the coupler design. The optimized structure has a waveguide height (b) of 0.36 mm, minimizing the reflections at the input port.

Due to the coupler operation at low-terahertz frequencies, the dimensional tolerances on certain structural parameters of the multiple-hole waveguide coupler are very sensitive. The input waveguide (Line 1) will be considered. The height of the input guide affects the coupling to the TE_{11}^{C} mode in Line 2; however, the effect of b variations between 0.30- and 0.50-mm inclusive is minimal to the overall coupling strength. Therefore, a larger tolerance can be applied to the b dimension in the manufacture of the waveguide coupler. However, the feasibility study highlighted a $\sim$20% reduction in the power coupled to Port 2 with a 40-μm deviation from the optimum value of a. A $\pm$10-μm variation to the waveguide width, the typical tolerance of a state-of-the-art CNC mill, would ensure that the coupling coefficient is acceptable for the gyro-TWA. Therefore, it is permissible to construct the 12-aperture coupler with modern numerically controlled manufacturing techniques.

The waveguide line sheet separation of 0.05-mm thickness will allow the microhole drilling technique to be used in the manufacture [22]. The drilling process can micro-machine apertures with a minimum diameter of 0.05 mm and an aspect ratio of 7:1 in reference to the length of aperture required to the diameter of the drill bit. Therefore, a hole of length 0.05 mm and $R' = 0.18$ mm, values used in the multiple-hole coupler simulation, is achievable.

IV. Conclusion and Discussion

The design of two fundamental mode rectangular-to-circular input couplers has been presented. The design of the T-junction coupler and the multiple-aperture coupler has focused on achieving a high coupling factor from the TE_{10}^{R} mode to the TE_{11}^{C} mode over a broad bandwidth. The use of a Bragg reflector has proved to be an effective method of providing frequency selective feedback of EM radiation at high frequency.

The operational frequency range of transmission for the T-junction input coupler is shown to be 352–390 GHz, equating to a bandwidth of $\sim$10%. The bandwidth of the T-junction design is limited because the required beam input port diameter is relatively large compared with the wavelength. The bandwidth of the multihole coupler is 35% (289–410 GHz). The coupler exceeds the bandwidth exhibited by the multiple-arm coupler of [19]. The use of a multiple-aperture directional coupler means that the requirement for a frequency selective wave reflector is eliminated. The 12-hole coupler design has $<$10% of the incident radiation propagated to Port 3.

Ohmic losses are not included in the simulations with a perfect electrical conductor background employed. However, at 372 GHz, the skin depth is $\sim$0.1 μm, which is comparable with, or smaller than, the surface roughness. This will result in increased ohmic loss. The effect of the surface roughness and skin depth can be analytically evaluated with a reduced electrical conductivity background material in CST-MS. While there is no comprehensive measured conductivity as a function of the surface roughness published at the operating frequency, an arbitrary reduction factor of 12 was used to monitor the potential losses within the designed couplers. The simulated waveguide losses for the T-junction coupler are 0.25 and 0.42 dB for the multiaperture coupler at 372 GHz with a respective corresponding bandwidth of 8% (357–387 GHz) and 28% (301–399 GHz). Coupling degradation of this magnitude would not pose a significant problem to either input coupler operation.

To achieve strong TE_{10}^{R}–TE_{11}^{C} coupling, strict manufacturing tolerances must be applied to the construction of the couplers to achieve optimum coupling strength. The sensitivity of the T-junction input coupler to variations in R means that strict tolerances must be applied to this parameter. Similarly, the 12-aperture coupler is very sensitive to variations in the aperture radius (R') and the input rectangular waveguide width (a). Therefore, manufacture of the low-terahertz passive

components will present a significant challenge. However, due to the large coupling bandwidth, which results in the coupler performance being less sensitive to operational frequency shifts, it is proposed a 0-dB 12-aperture directional coupler would be used for a fundamental mode input coupler on a 372-GHz gyro-TWA.

REFERENCES

[1] K. R. Chu, "The electron cyclotron maser," *Rev. Modern Phys.*, vol. 76, no. 2, pp. 489–540, May 2004.

[2] T. C. Luce, "Applications of high-power millimeter waves in fusion energy research," *IEEE Trans. Plasma Sci.*, vol. 30, no. 3, pp. 734–754, Jun. 2002.

[3] M. E. MacDonald, J. P. Anderson, R. K. Lee, D. A. Gordon, and G. N. McGrew, "The HUSIR W-band transmitter," *Lincoln Lab. J.*, vol. 21, no. 1, pp. 106–114, Jan. 2014.

[4] M. Y. Glyavin *et al.*, "Experimental tests of a 263 GHz gyrotron for spectroscopic applications and diagnostics of various media," *Rev. Sci. Instrum.*, vol. 86, no. 5, p. 054705, 2015.

[5] G. G. Denisov *et al.*, "Gyrotron traveling wave amplifier with a helical interaction waveguide," *Phys. Rev. Lett.*, vol. 81, no. 25, pp. 5680–5683, 1998.

[6] G. G. Denisov, V. L. Bratman, A. Phelps, and S. V. Samsonov, "Gyro-TWT with a helical operating waveguide: New possibilities to enhance efficiency and frequency bandwidth," *IEEE Trans. Plasma Sci.*, vol. 26, no. 3, pp. 508–518, Jun. 1998.

[7] W. He, C. R. Donaldson, L. Zhang, K. Ronald, P. McElhinney, and A. W. Cross, "High power wideband gyrotron backward wave oscillator operating towards the terahertz region," *Phys. Rev. Lett.*, vol. 110, p. 165101, Apr. 2013.

[8] G. G. Denisov, S. V. Samsonov, S. V. Mishakin, and A. A. Bogdashov, "Microwave system for feeding and extracting power to and from a gyrotron traveling-wave tube through one window," *IEEE Electron Device Lett.*, vol. 35, no. 7, pp. 789–791, Jul. 2014.

[9] K.-L. Wu, M. Yu, and A. Sivadas, "Novel modal analysis of a circular-to-rectangular waveguide T-junction and its application to design of circular waveguide dual-mode filters," *IEEE Trans. Microw. Theory Techn.*, vol. 50, no. 2, pp. 465–473, Feb. 2002.

[10] N. Yoneda, M. Miyazaki, H. Matsumura, and M. Yamato, "A design of novel grooved circular waveguide polarizers," *IEEE Trans. Microw. Theory Techn.*, vol. 48, no. 12, pp. 2446–2452, Dec. 2000.

[11] G. Chattopadhyay, B. Philhour, J. E. Carlstrom, S. Church, A. Lange, and J. Zmuidzinas, "A 96-GHz ortho-mode transducer for the Polatron," *IEEE Microw. Guided Wave Lett.*, vol. 8, no. 12, pp. 421–423, Dec. 1998.

[12] N. Yoneda, M. Miyasaki, T. Nishino, H. Asao, H. Nakaguro, and S.-I. Betsudan, "Analysis of circular-to-rectangular waveguide T-junction using mode-matching technique," *Electron. Commun. Jpn. II, Electron.*, vol. 80, no. 7, pp. 37–46, Jul. 1997.

[13] C. K. Chong *et al.*, "Bragg reflectors," *IEEE Trans. Plasma Sci.*, vol. 20, no. 3, pp. 393–402, Jun. 1992.

[14] L. Zhang, W. He, C. R. Donaldson, J. R. Garner, P. McElhinney, and A. W. Cross, "Design and measurement of a broadband sidewall coupler for a W-band gyro-TWA," *IEEE Trans. Microw. Theory Techn.*, vol. 63, no. 10, pp. 3183–3190, Oct. 2015.

[15] V. L. Bratman *et al.*, "High-gain wide-band gyrotron traveling wave amplifier with a helically corrugated waveguide," *Phys. Rev. Lett.*, vol. 84, no. 12, pp. 2746–2749, 2000.

[16] H. A. Bethe, "Theory of diffraction by small holes," *Phys. Rev. Lett.*, vol. 66, nos. 7–8, pp. 163–182, Oct. 1944.

[17] W. Shelton, "Compact multi-hole waveguide directional couplers," *Microw. J.*, vol. 4, no. 2, p. 89, Jul. 1961.

[18] H. Schmiedel and F. Arndt, "Field theory design of rectangular waveguide multiple-slot narrow-wall couplers," *IEEE Trans. Microw. Theory Techn.*, vol. 34, no. 7, pp. 791–798, Jul. 1986.

[19] W. X. Wang, W. Lawson, and V. L. Granatstein, "The design of a mode selective directional coupler for a high power gyroklystron," *Int. J. Electron.*, vol. 65, no. 3, pp. 705–716, Mar. 1988.

[20] Y. H. Choung, K. R. Goudey, and L. G. Bryans, "Theory and design of a *Ku*-band TE_{21}-mode coupler," *IEEE Trans. Microw. Theory Techn.*, vol. 30, no. 11, pp. 1862–1866, Nov. 1982.

[21] J. Ruiz, W. Kasparek, C. Lechte, B. Plaum, and H. Idei, "Numerical and experimental investigation of a 5-port mitre-bend directional coupler for mode analysis in corrugated waveguides," *J. Infr. Millim. Terahertz Waves*, vol. 33, no. 5, pp. 491–504, May 2012.

[22] (Apr. 30, 2015). *Microdrilling*. [Online]. Available: www.microdrilling.co.uk

Jason R. Garner received the B.Sc. (Hons.) degree in physics and the M.Sc. degree in high-power radio frequency science and engineering from the University of Strathclyde, Glasgow, U.K., in 2010 and 2012, respectively, where he is currently pursuing the Ph.D. degree with the Scottish University Physics Alliance.

His current research interests include the design of passive components for millimeter-wave gyro-amplifiers.

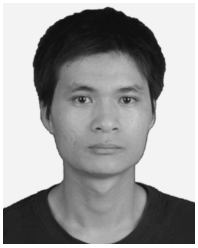

Liang Zhang received the B.Sc. degree in applied physics from the University of Science and Technology of China, Hefei, China, in 2004, the M.Sc. degree in application of nuclear techniques from the China Academy of Engineering Physics, Mianyang, China, in 2007, and the Ph.D. degree in physics from the University of Strathclyde, Glasgow, U.K., in 2012.

He is currently with the Scottish Universities Physics Alliance, University of Strathclyde.

Craig R. Donaldson received the B.Sc. (Hons.) degree in physics and the M.Sc. degree in high-power RF and the Ph.D. degree from the University of Strathclyde, Glasgow, U.K., in 2005, 2006, and 2009, respectively.

He has since continued as a Research Fellow with the Department of Physics, University of Strathclyde. His current research interests include high-frequency gyrotron traveling-wave amplifiers/backward-wave oscillators and electron beam generation.

Adrian W. Cross received the B.Sc. degree in physics and the Ph.D. degree from the University of Strathclyde, Glasgow, U.K., in 1989 and 1993, respectively.

He joined the Atoms, Beams, and Plasmas Group, University of Strathclyde, initially as a Research Fellow. He became a Professor with the Department of Physics, University of Strathclyde, in 2014. His current research interests include terahertz radiation sources.

Wenlong He received the B.Sc. degree in physics from Soochow University, Suzhou, China, in 1983, the M.Sc. degree in accelerator physics from the China Academy of Engineering Physics, Mianyang, China, in 1988, and the Ph.D. degree in physics from the University of Strathclyde, Glasgow, U.K., in 1995.

He is currently a Senior Research Fellow with the Scottish Universities Physics Alliance, University of Strathclyde.

Design Study of a 372-GHz Higher Order Mode Input Coupler

Jason R. Garner, Liang Zhang, Craig R. Donaldson, Adrian W. Cross, and Wenlong He

***Abstract*— The design of a higher order mode (HOM) input coupler for a low-terahertz gyrotron travelling wave amplifier is presented. A two-branch waveguide coupler based on the even distribution of incident power is designed to couple the rectangular TE_{10} mode to the circular TE_{61} mode. The optimised tapered waveguide input coupler achieved an operating frequency range of 359–385 GHz, equating to a bandwidth of 7%. A prototype waveguide coupler scaled to *W*-band (75–110 GHz) was manufactured. The vector network analyser measured return loss of the HOM coupler is shown to be <10 dB at 90–96 GHz. A transmission and phase measurement is presented to analyse TE_{61} mode conversion in the coupler.**

***Index Terms*— Gyrotron travelling wave amplifier (gyro-TWA), mode coupling, terahertz input coupler, waveguide coupler.**

I. Introduction

GYRO-DEVICES are the sources of coherent EM radiation based on the cyclotron resonance maser instability [1], capable of delivering high power microwave signals at terahertz frequencies. The applications of the gyro-devices include plasma heating [2], RADAR systems [3], and spectroscopes [4].

A *W*-band gyrotron travelling wave amplifier (gyro-TWA) has been developed at the University of Strathclyde for use on a cloud profiling RADAR system. The *W*-band device uses a threefold helically corrugated interaction region (HCIR) [5]. The HCIR couples the TE_{21} mode to the first spatial harmonic of the TE_{11} mode [6] to generate an operating eigenwave, improving the instantaneous bandwidth [7]. A *W*-band gyrotron backward wave oscillator with similar setup compared with the gyro-TWA achieved a maximum output power of 12 kW when driven by a 40 kV, 1.5 A, annular-shaped large-orbit electron beam [8]. The frequency tuning band of 88–102.5 GHz was achieved through cavity magnetic field adjustments.

A gyro-TWA operating at a center frequency of 372 GHz is being studied for the applications of electron paramagnetic resonance (EPR) and dynamic nuclear polarization (DNP) in a nuclear magnetic resonance (NMR) system. High power, wide bandwidth (>5%) gyro-amplifiers are ideal for pulsed EPR and DNP-NMR applications. If a threefold HCIR is used in the device, the mean radius is ∼0.4 mm. A higher order mode (HOM) operation is proposed to increase the cavity dimensions and, hence, enhance the power handling capability of the waveguide cavity.

The gyro-TWA will require the efficient coupling of the TE_{61} mode into the interaction cavity. Minimal power loss at the coupling interface will enable as much of the millimeter-wave drive power to be available to the high-efficiency interaction. The input coupler was designed focusing on the following three parameters.

1) The bandwidth of the input coupler should span the 360–384-GHz frequency range (∼7%).
2) Transmission loss from TE_{10}^{R}–TE_{61}^{C} should be <1 dB over the desired frequency range.
3) The mode purity of the TE_{61} mode should exceed 90%.

By adding the HOM coupling requirement, the design of the input coupler is more complex than designing a fundamental mode coupler, due to the possibility of lower order mode (LOM) competition in the cavity. A TE_{11} field pattern is readily excited and is the dominant mode within a cylindrical waveguide. Therefore, to ensure high TE_{61} field purity, a complex waveguide coupling geometry is required.

The design of a power dividing input coupler for a 372-GHz HOM gyro-TWA is presented. The numerical modeling of a waveguide splitter input coupler with a linear taper power divider is presented in Section II. The linear taper and *E*-plane waveguide bend were simulated individually before the full design of the waveguide channel was completed. A tolerance study of the optimized waveguide coupler is discussed in Section III. A prototype waveguide coupler, scaled to operate at 90–96 GHz, was manufactured. A discussion of the coupler manufacture is included in Section IV and the vector network analyzer (VNA) prototype testing is presented in Section V. Section VI discusses the design of the coupler at 93 and 372 GHz.

II. 372-GHz Tapered Waveguide Input Coupler

The design of a 372-GHz TE_{10}^{R}–TE_{61}^{C} waveguide coupler employs the principal of incident wave power distribution to couple to an HOM [9]. The waveguide splitter divides an incident TE_{10} mode into equal signal intensities, propagating with matched phase toward the cylindrical coupled cavity. The possible modes, which may be coupled into the interaction cavity, are dependent on the number of branches employed

Manuscript received June 2, 2016; accepted June 13, 2016. Date of publication July 7, 2016; date of current version July 21, 2016. This work was supported by the Engineering and Physical Sciences Research Council, U.K., under Grant EP/K029746/1. The review of this paper was arranged by Editor M. Thumm.

The authors are with Department of Physics, Scottish Universities Physics Alliance, University of Strathclyde, Glasgow, Glasgow G4 0NG, U.K. (e-mail: j.garner@strath.ac.uk; liang.zhang@strath.ac.uk; craig.donaldson@strath.ac.uk; a.w.cross@strath.ac.uk; w.he@strath.ac.uk).

Color versions of one or more of the figures in this paper are available online at http://ieeexplore.ieee.org.

Digital Object Identifier 10.1109/TED.2016.2581314

TABLE I
WAVEGUIDE SPLITTER BRANCH NUMBER AND POTENTIAL MODES

Branch No.	Converting Mode	Cavity TE_{mn} Modes
2	TE_{21}	TE_{21}, TE_{41}, TE_{61}, …
3	TE_{31}	TE_{31}, TE_{61}, TE_{91}, …
4	TE_{41}	TE_{41}, TE_{81}, $TE_{12,1}$ …
5	TE_{51}	TE_{51}, $TE_{10,1}$, …

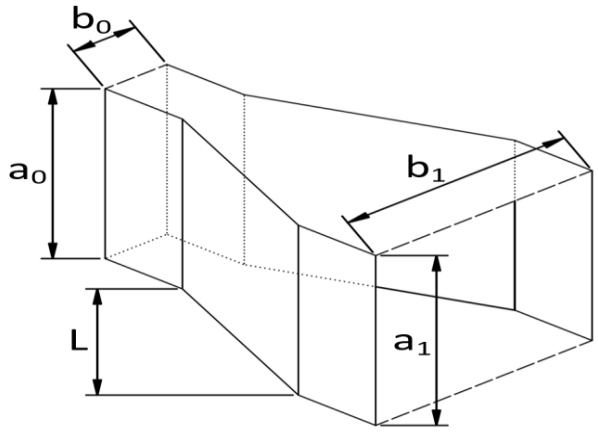

Fig. 1. Schematic of a rectangular-to-square linearly tapered waveguide.

within the designed waveguide splitter. A table of branch numbers and the relevant potential coupled modes, when equal length waveguide branches are used, is shown in Table I. By implementing the waveguide splitter, the generation of an HOM in the interaction cavity is simplified due to a reduction in mode competition.

The design of a waveguide TE_{61}^{C} input coupler can include a waveguide splitter with two or three branches (Table I). The three-branch splitter would result in less mode competition inside the cylindrical cavity with a single lower order TE_{m1} mode propagating within the cavity (TE_{31}); however, the phase matching of the three waveguide channels results in added complexity to the coupler design and manufacture. Therefore, a TE_{10}^{R}–TE_{61}^{C} input coupler with a two-branch waveguide splitter was designed for a 360–384 GHz gyro-TWA.

A tapered waveguide can be employed to provide an impedance match between the two waveguides of similar geometries without the complex manufacturing of step discontinuities. Tapered waveguides have been designed with linear or part-sinusoidal axial tapers with single E-plane variations [10], or double tapers, which vary in the E- and H-planes simultaneously [11]. A linearly or sinusoidally tapered waveguide can be analytically examined using infinite step discontinuities [12]. A 372-GHz waveguide taper with a linear wall profile was designed for a rectangular-to-square (impedance ratio, $Z = 2.00$) waveguide transition.

A rectangular-to-square waveguide taper is shown in Fig. 1. The reflection coefficient (Γ) of a rectangular waveguide taper supporting TE_{10} mode propagation can be defined as [11]

$$\Gamma = \frac{\lambda_g}{L}\left[\frac{K_0^2 + K_1^2}{64\pi^2} - \frac{K_0 K_1}{32\pi^2}\cos(4\pi l)\right]^{\frac{1}{2}} \tag{1}$$

where λ_g is the guide wavelength and L is the tapering section length. K_0, K_1, and l are given, respectively, by

$$K_0 = \frac{\frac{(b_1-b_0)}{b_0} - \left(\left[\frac{(a_1-a_0)}{a_0}\right] \Big/ \left[1-\left(\frac{\lambda_g}{2a_0}\right)^2\right]\right)}{\sqrt{1-\left(\frac{\lambda_g}{2a_0}\right)^2}} \tag{2}$$

$$K_1 = \frac{\frac{(b_1-b_0)}{b_1} - \left(\left[\frac{(a_1-a_0)}{a_1}\right] \Big/ \left[1-\left(\frac{\lambda_g}{2a_1}\right)^2\right]\right)}{\sqrt{1-\left(\frac{\lambda_g}{2a_1}\right)^2}} \tag{3}$$

$$l = \frac{1}{\lambda_g}\int_0^L \sqrt{1-\left(\frac{\lambda_g}{2a}\right)^2}\,dx \tag{4}$$

where a and b denote the waveguide width and height with the subscripts 0 and 1 representing the initial and final magnitudes, respectively. A variation of a is only witnessed for a taper with an H-plane projection. For an E-plane rectangular-to-square taper where $a_0 = a_1$ and $b_1 = 2 \cdot b_0$, (1) simplifies to

$$\Gamma = \frac{\lambda_g}{16\pi L}\left[5 - 4\cos\left(\frac{4\pi L}{\lambda_g}\right)\right]^{\frac{1}{2}}. \tag{5}$$

The analysis of (5) highlights a minimum reflection coefficient when $L \approx N \cdot \lambda_g$, where N is a whole integer number. The guide wavelength at 372 GHz is ~1.10 mm; therefore, the taper length is set at $N \cdot 1.10$ mm. To minimize wall losses, the taper length should be minimized. Therefore, $N = 1$.

A 372-GHz impedance matching tapered waveguide was designed using CST Microwave Studio (CST-MS). The waveguide width (a) was initially set at 0.60 mm with a waveguide width-to-height (a:b) ratio of 1:2. The taper length (L) was set at 1.10 mm. A parametric optimization of a was performed to minimize reflections at the rectangular input port (Port 1). The numerically simulated transmission and reflection of a $Z = 2.00$ rectangular-to-square E-plane waveguide taper is shown in Fig. 2. The topology of the simulated waveguide taper is included in Fig. 2 (inset). The waveguide width (a) was optimized at 0.570 mm, equating to $b_0 = 0.285$ mm and $b_1 = 0.570$ mm, with the reflection at Port 1 less than −27 dB over the desired operating bandwidth. Therefore, the low reflection component may be used at the incident port.

An E-plane waveguide bend is a fundamental component of waveguide engineering. A rotation of a waveguide about an angle, commonly between 15° and 90°, creates a smooth-walled waveguide junction. The smooth E-plane transition can be designed to be compact (small R_{IN}) or broad (large R_{IN}) with small return losses. A smooth-walled 90° E-plane waveguide bend with $a = 0.570$ mm and $b = 0.285$ mm was designed using CST-MS. The waveguide dimensions $a \times b$ coincide with the optimized tapered waveguide. The inner radius of the E-plane bend (R_{IN}) was

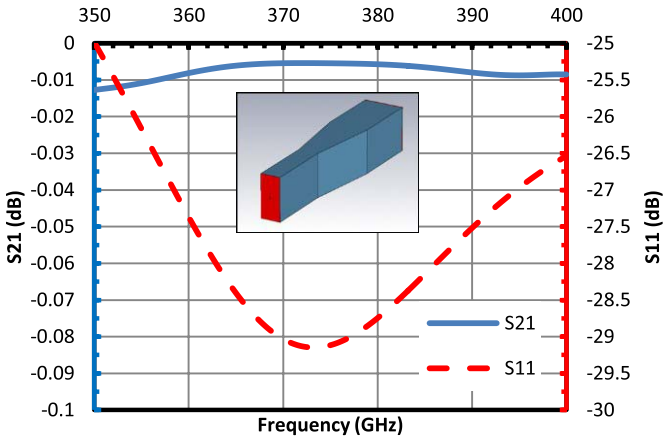

Fig. 2. Simulated scattering of a 372-GHz rectangular-to-square waveguide taper.

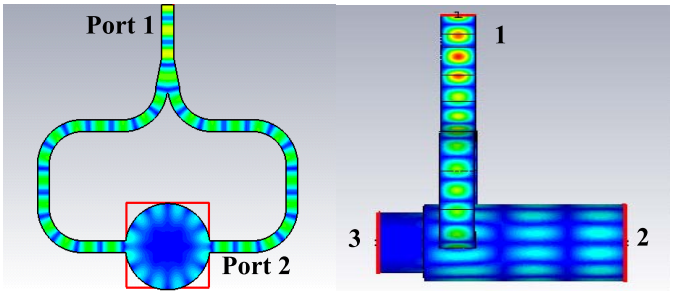

Fig. 3. Microwave field progression in xz plane (left) and yz plane (right) for tapered waveguide splitter input coupler.

optimized to minimize reflections at the incident waveguide port. All the values of $R_{\mathrm{IN}} > 0.05$ mm will result in $S_{11} \leq -20$ dB; however, a radius increase up to 0.25 mm is shown to improve transmission. The radii selection is then dependant on minimizing reflection at the center of the operating bandwidth. The return loss from the E-plane bend is <40 dB over the required 360–384-GHz operating bandwidth.

The 372–GHz-HOM tapered-waveguide input coupler is designed using CST-MS to couple the $\mathrm{TE}_{10}^{\mathrm{R}}$ mode to the $\mathrm{TE}_{61}^{\mathrm{C}}$ mode using the waveguide transition and E-plane waveguide bend adjoined to a circular cavity of radius (R). The average radius (R_0) of the interaction cavity for the 372-GHz gyro-TWA is 1.24 mm; however, due to the enhanced coupling complexity to the TE_{61} mode, a small taper may be employed between the input coupler and the cavity to permit maximum coupling into the interaction cavity. Therefore, R can be varied within 1.00 (cutoff radius of TE_{61} at 360 GHz) to 1.40 mm to support the desired TE_{61} mode and, hence, the optimization of R may be carried out on the HOM input coupler. The beam tunnel is coupled to the rectangular input port from two discrete waveguide branches, which consist of three E-plane bends adjoined to the tapered waveguide transition. The two waveguide branches evenly split the signal from the input port (Port 1), propagating the divided wave in the $\pm x$-direction before propagating the two synchronous signals into the beam cavity. The 2-D progression of the millimeter-wave propagation is shown in Fig. 3.

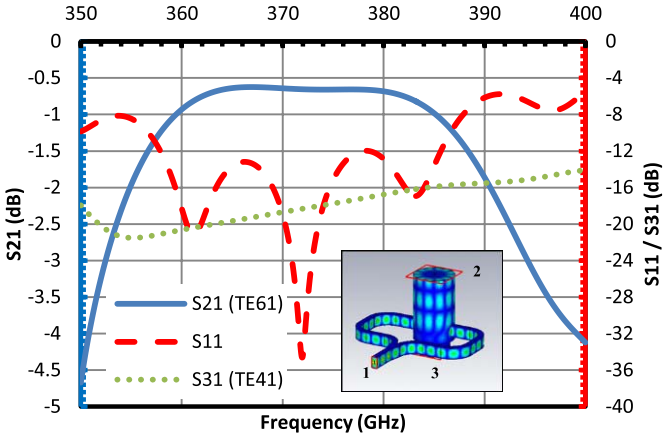

Fig. 4. Numerical scattering of a TE_{10}–TE_{61} tapered waveguide splitter input coupler.

Fig. 3 (left) highlights coupling to the $\mathrm{TE}_{61}^{\mathrm{C}}$ mode for an optimized cavity radius (R) of 1.03 mm. The generated HOM will be able to freely propagate toward the cavity and the diode region unless Port 3, the port defined as being adjacent to the electron gun, is terminated. The average electron beam radius (R_B) from the electron gun is 0.20 mm [13]; therefore, due to the HOM cavity a cutoff waveguide [Fig. 3 (right)] may be employed to prevent the propagation of incident radiation into the diode, without intercepting the electron beam. A parametric optimization of R_C is performed with a range of 0.70–0.85 mm to cut off all modes higher in frequency than the TE_{41} mode whilst ensuring a large beam tunnel diameter.

Fig. 4 shows the 372-GHz $\mathrm{TE}_{10}^{\mathrm{R}}$–$\mathrm{TE}_{61}^{\mathrm{C}}$ tapered waveguide splitter input coupler operating between 359 and 385 GHz. The 3-D E-field progression on the conductor walls is shown in the inset with port numbers defined. The bandwidth of the input coupler equates to ∼7%. The cutoff waveguide reflector ($R_C = 0.80$ mm) is effective at preventing significant wave power from propagating toward the electron gun with a signal level of less than −15 dB for the dominant TE_{41} mode. The distance between the near edge of the rectangular waveguide branches and the waveguide reflector (L_1) is 0.272 mm. The coupler shows a high TE_{61} mode selectivity performance with low magnitude coupling to subsequent LOMs and HOMs. A gyrating electron beam will occupy ∼25% of the cutoff reflector cross-sectional area; hence, the potential of electron bombardment on the cavity boundaries is minimal and an increased beam diameter may be employed. Return loss at the input port (Port 1) is <12 dB over the operating bandwidth of 360–384 GHz.

At 372 GHz, the skin depth of a millimeter-wave signal in a copper waveguide is ∼0.1 μm. Hence, the depth at which the signal propagates within the waveguide wall is comparable to, or smaller than, the surface roughness. Therefore, ohmic losses will increase with an uneven waveguide finish. With the consideration of the surface effects on electrical conductivity, a reduction factor was applied to the copper conductivity (0.5×10^7 Sm^{-1}). The coupling strength at 372 GHz, numerically simulated with CST-MS, was shown to decrease by 0.91 dB with a coupling strength of −0.77 dB for a perfect

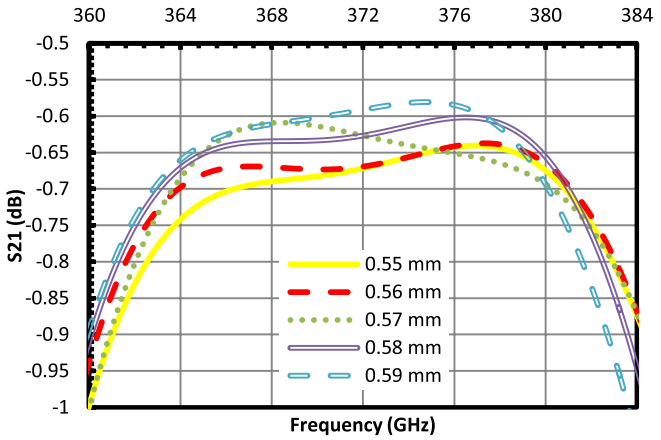

Fig. 5. Effect of a parametric variation on TE_{61} input coupler transmission response.

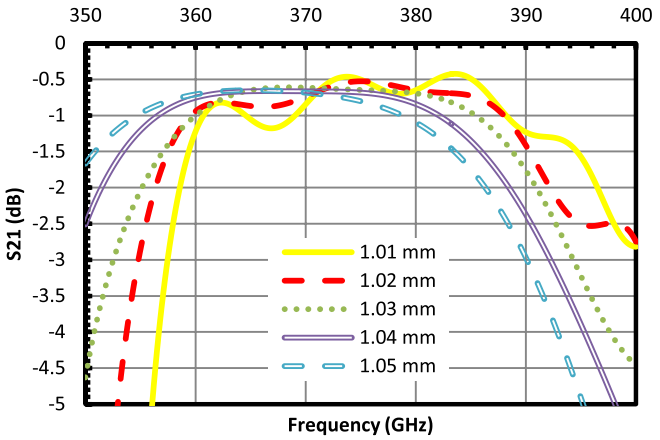

Fig. 6. TE_{61} input coupler transmission with R variations.

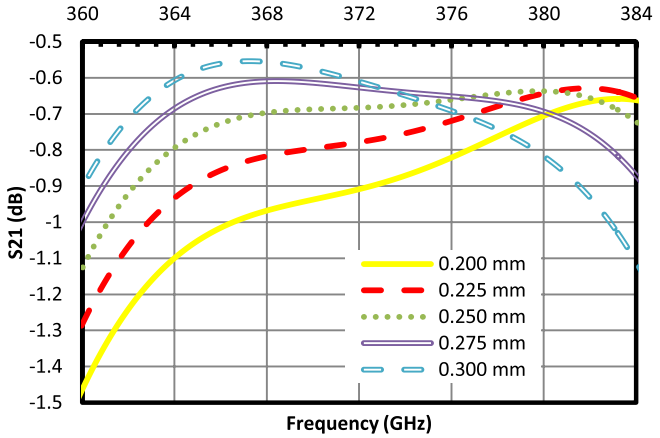

Fig. 7. Effect of L_1 variation on input coupler transmission response.

electrical conductor background material and -1.68 dB for a reduced conductivity copper background. A smooth surface finish (R_a = 2–3 μm) must be achieved in manufacture to ensure a high TE_{61} coupling factor.

III. Tolerance Study

A tolerance study was performed on the 372-GHz tapered waveguide input coupler to test the feasibility of the coupler performance with parametric discrepancies resulting from fabrication tolerances. Initially, the rectangular splitter waveguide is analyzed. The parameters, which govern the waveguide dimensions (a, b, L, and R_{IN}) were varied from the optimum value to test the tolerance range over which the coupler may operate. A plot of waveguide width variation (a) for fixed values of b and L is shown in Fig. 5.

The resultant change to the transmission coefficient for $a = \pm 20$ μm highlights an operational frequency shift of $\sim$0.5 GHz for a 10-μm variation. A frequency shift of 0.5-GHz magnitude would not affect the coupler operation at 360–384 GHz; however, larger magnitude, a, discrepancies would result in a frequency shift that was out with the desired bandwidth. The waveguide height (b) was varied for fixed a and L. The investigation highlighted minimal frequency or coupling strength response for $\Delta b = \pm 20$ μm; therefore, the waveguide height has no strict tolerance requirement. The taper length (L) is subsequently varied with no detrimental effects on coupling performance for $\Delta L \pm 25$ μm. The waveguide bend radius (R_{IN}) was investigated with the optimum values of a, b, and L. For ΔR_{IN} values of ± 100 μm, no effect on coupling strength or frequency response was observed. However, an R_{IN} increase will result in enhanced waveguide losses due to an increase in propagation length. The coupler performance, as a result of rectangular waveguide discrepancies, remains broadly unaffected.

An investigation into the coupled cavity is subsequently performed for R and L_1. The cavity radius (R) should be carefully manufactured to ensure a tight tolerance. Fig. 6 shows the effect of up to $\Delta R = \pm 20$ μm on the tapered input coupler performance. The effect of R variations is shown to have a significant effect on the coupler center frequency with a 10-μm discrepancy in R resulting in a 3-GHz shift. Hence, the machining of R must be very precise.

A review of the L_1 parameter was performed (Fig. 7). Alterations resulting in 25 μm increases to L_1 are shown to decrease the center frequency by $\sim$2 GHz. The discrepancies to L_1, which result in a phase mismatch between the incident and reflected wave at Port 3, is shown to affect the coupler bandwidth and coupling strength with deviation from the optimum.

IV. Input Coupler Manufacture

A W-band prototype TE_{61} tapered-waveguide input coupler was manufactured to confirm the simulated reflection results. The coupler was scaled to operate at 90–96 GHz due to limitations on achievable tolerances using in-house manufacture. The circular coupled waveguide was scaled directly with a 4$\times$ dimension increase on the 372-GHz design. The rectangular input waveguide was designed to maintain the aspect ratio used in the 372-GHz design between standard WR2.2 ($a' \times b'$) waveguide and $a_0 \times b_0$. A tapered section from standard W-band waveguide to the optimized coupler waveguide is included in the scaled design.

The aluminum block was split into two discrete sections. A waveguide channel was manufactured into each split block

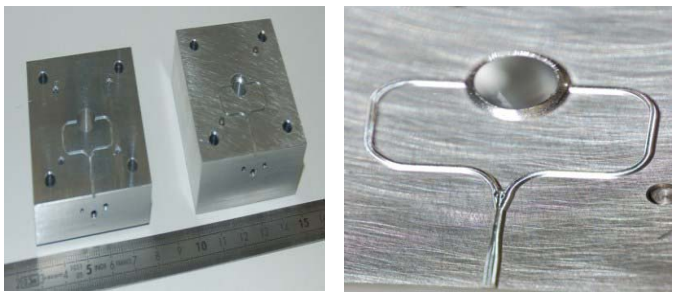

Fig. 8. Images of the manufactured split-block waveguide input coupler.

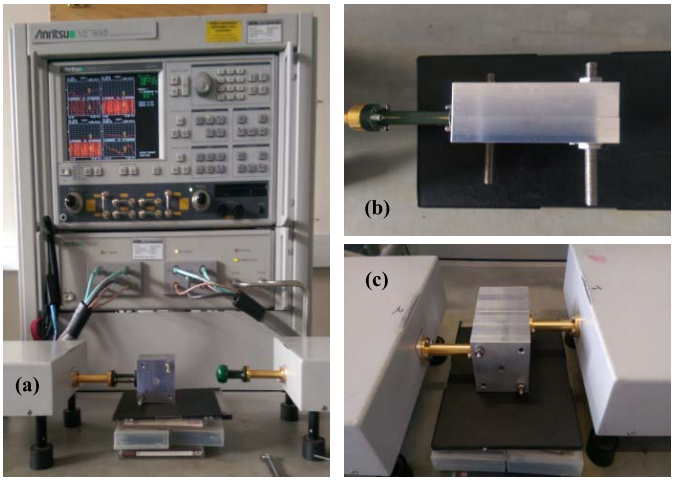

Fig. 9. VNA measurement setup with two- and four-block coupler.

using a three-axis computer numerically controlled (CNC) milling technique. The tool path was machined into each split block using a 0.60-mm end mill with half the waveguide channel width (1.27 mm depth) milled into each aluminum block. The length of the end mill cutter would prohibit the machining of the full waveguide width into a single block. The circular waveguide and waveguide reflector radii ($R = 4.10$ mm and $R_c = 3.20$ mm) were subsequently drilled. A flange connection was machined into the split-block coupler to allow for direct attachment to the VNA. A series of threaded rods were used to join the split-block structure to prevent any loss of signal between the block faces. The manufactured waveguide channel is shown in Fig. 8.

V. Vector Network Analyzer Testing

The experimental study was performed on an Anritsu 37000D Lightning series VNA with attached Oleson Microwave Labs heads to enable frequency measurements in the range of 75–110 GHz. The images of the split-block coupler attached to the VNA are shown in Fig. 9(a) and (b).

A comparison of the prototype 94- and 372-GHz waveguide coupler dimensions is shown in Table II. A discrepancy between the designed and manufactured parameter sets was highlighted with the precision measurement of the manufactured waveguide channel using a travelling microscope. The manufactured parameter set is included in Table II. A comparison of the 90–96-GHz waveguide coupler numerical

TABLE II
Waveguide Coupler Dimension Comparison

Parameter	372 GHz Design (mm)	93 GHz Design (mm)	93 GHz Actual (mm)
R	1.030	4.10	4.12
R_C	0.800	3.20	3.45
a_0	0.570	2.60	2.60
a'	0.560	2.54	2.60
b_0	0.235	0.95	0.90
b'	0.280	1.27	1.23
b_1	0.570	1.90	1.80
R_{IN}	0.800	2.72	2.75
R_{OUT}	1.085	3.67	3.65
L_1	0.272	1.10	1.17

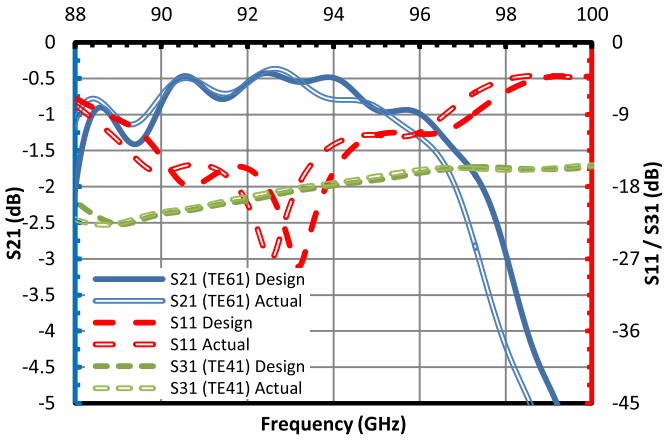

Fig. 10. Simulated transmission and reflection of W-band split-block coupler for design and manufactured parameter sets.

scattering with the designed and actual parameter set is shown in Fig. 10. The parametric discrepancies are shown to down shift the operating frequency range of the W-band tapered waveguide coupler.

The HOM coupler numerical reflection for the designed and actual parameter set and VNA reflection results are shown in Fig. 11. Fig. 11 shows that the measured VNA reflection from the rectangular input port (Port 1) is in good agreement with CST-MS simulation results when open boundaries replace waveguide ports at Port 2 and Port 3. The S_{11} reflection at the input port is less than -10 dB between 90 and 96 GHz; therefore, $>90\%$ of incident radiation is propagated into the coupled waveguide.

A reciprocal waveguide coupler was manufactured to allow for transmission and phase measurement. Therefore, the waveguide mode can be evaluated. The four-block experimental setup is shown in Fig. 9(c). The transmission of two identical waveguide couplers back-to-back is shown in Fig. 12. The average transmission loss is ~ 3 dB, equating to an individual coupler loss of -1.5 dB. The circuit loss in an individual aluminum coupler block was measured at -1 dB; therefore, high mode conversion is exhibited by the HOM waveguide coupler.

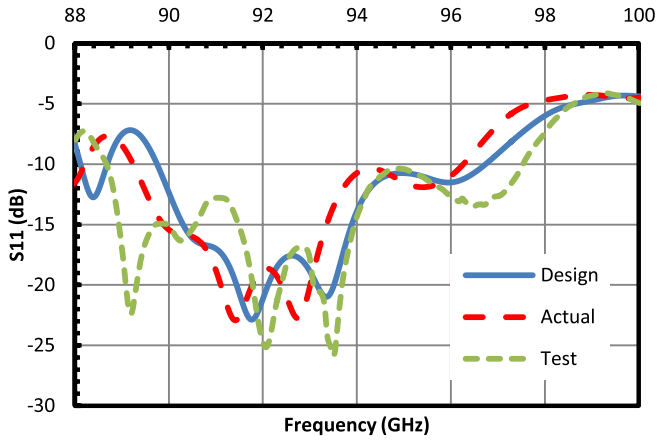

Fig. 11. Comparison of CST-MS and VNA coupler reflection results.

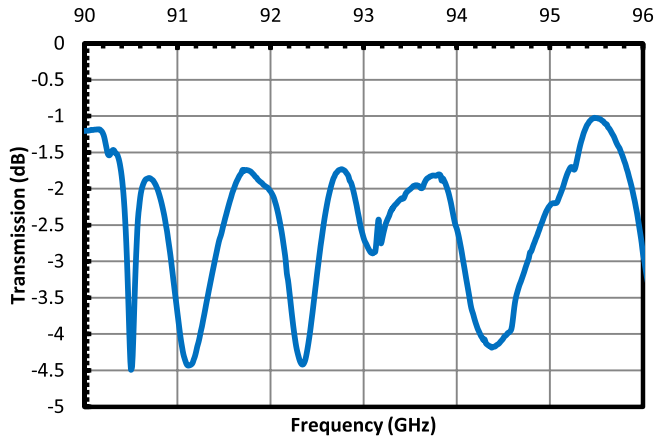

Fig. 12. Transmission of a W-band HOM input coupler.

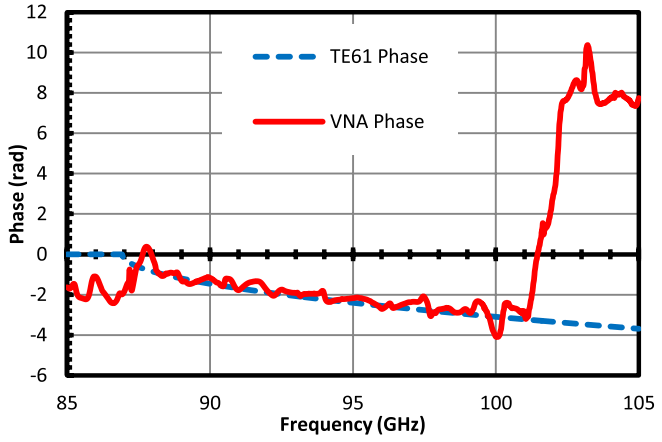

Fig. 13. Theoretical and numerical dispersion of TE_{61} mode in coupler.

To confirm the mode of conversion, an additional waveguide section of length 3.00 mm was manufactured and inserted between the two couplers to measure the phase response. The measured phase was then compared with the theoretical phase response of the TE_{61} mode in a waveguide of radius $R = 4.10$ mm. The theoretical and measured phase is shown in Fig. 13. The phase measurement has close correlation with the theoretical TE_{61} phase at 88–98 GHz; therefore, the waveguide coupler is shown to have a high TE_{61} mode conversion efficiency. The insertion loss (<10 dB) and phase measurements suggest >90% transmission to the TE_{61} mode.

VI. Discussion and Conclusion

The design of a 372-GHz TE_{10}^{R}–TE_{61}^{C} input coupler for a gyro-TWA has been presented. The design of the HOM input coupler focused upon achieving a broadband coupling with a high transmission coefficient, whilst ensuring the TE_{61} mode was dominant within the coupled cavity. The tapered waveguide input coupler was designed with low-loss rectangular waveguide components. The tapered waveguide was shown to have a return loss of <27 dB. The incident split signal was coupled into a circular waveguide through smooth walled E-plane waveguide bends. The waveguide bends had a reflection coefficient of less than −40 dB over the 360–384-GHz operating bandwidth. The tapered waveguide input coupler achieved an operating bandwidth of 7% (359–385 GHz). A copper background with reduced conductivity caused a decrease in coupling by ∼1 dB. The reduction factor of ∼12 was chosen as a representation of the wall losses at terahertz frequencies and uncertainty in surface finish. An investigation into the W-band aluminum prototype coupler showed good agreement was achieved between numerical and experimental data when a reduction factor of 10 was employed.

A tolerance study of the TE_{10}^{R}–TE_{61}^{C} tapered waveguide input coupler was performed to analyze the effect of manufacturing discrepancies on the coupler performance. The coupler was shown to be stable with manufacturing discrepancies associated to the rectangular splitter waveguide. A maximum coupling change of 0.1 dB was observed for 20-μm variations of $a$corresponding to a frequency shift of ∼0.5 GHz. An investigation into the coupled cylindrical beam tunnel, however, highlighted a frequency and coupling strength sensitivity with R and L_1 variations. For $\Delta R = \pm 10$ μm, a 3-GHz center frequency shift was observed and for $\Delta L_1 = \pm 25$ μm the center frequency was shifted by ∼2 GHz. A decrease in coupling strength was also associated with R and L_1 discrepancies (Figs. 6 and 7). Therefore, to ensure high coupling over the desired 360–384-GHz bandwidth, the beam tunnel must be accurately manufactured with strict tolerances applied.

A W-band TE_{61} prototype coupler was manufactured to allow for the VNA testing of the tapered waveguide input coupler. A CNC milling technique was used to machine a waveguide channel designed to operate at 90–96 GHz. The waveguide dimensions were scaled from the optimized 360–384 GHz TE_{10}^{R}–TE_{61}^{C} tapered waveguide input coupler. The two-piece aluminum split-block coupler design allowed for the VNA testing of the coupler reflection. The measured S_{11} reflection from the input rectangular port (Port 1) of the coupler structure was shown to be less than −10 dB between 90 and 96 GHz. The VNA measurement agreed well with simulated data, suggesting that ∼90% of incident radiation is transmitted into the circular coupled waveguide. A transmission and phase measurement with a reciprocal input coupler was presented. The phase difference

analysis permitted the determination of the TE_{61} conversion into the coupled waveguide with the measurement shown to be in good agreement with theoretical TE_{61} phase over the operating bandwidth.

The manufacturing technique outlined for the W-band HOM input coupler may be used in the manufacture of a 372-GHz waveguide coupler; however, the state-of-the-art micromilling technology must be employed. High precision laboratories [14] have the capability to machine waveguide channels of 0.1 mm width with a positional accuracy of $\pm$ 0.3 μm using five-axis micromilling machines and an appropriate end-mill tool piece. A surface finish with $R_a = \sim 2$ μm would ensure that ohmic losses would be minimized. Therefore, the design of an HOM power splitting waveguide coupler with waveguide sub-mm $a \times b$ cross section (0.57 mm $\times$ 0.24 mm) is realistic.

REFERENCES

[1] K. R. Chu, "The electron cyclotron maser," *Rev. Modern Phys.*, vol. 76, no. 2, pp. 489–540, May 2004.

[2] S. Coda *et al.*, "Electron cyclotron current drive and suprathermal electron dynamics in the TCV tokamak," *Nucl. Fusion*, vol. 43, no. 11, pp. 1361–1370, 2003.

[3] M. G. Czerwinski and J. M. Usoff, "Development of the haystack ultrawideband satellite imaging radar," *Lincoln Lab J.*, vol. 21, no. 1, pp. 28–44, 2014.

[4] E. A. Nanni, A. B. Barnes, R. G. Griffin, and R. J. Temkin, "THz dynamic nuclear polarization NMR," *IEEE Trans. Terahertz Sci. Technol.*, vol. 1, no. 1, pp. 145–163, Sep. 2011.

[5] L. Zhang *et al.*, "Multi-mode coupling wave theory for helically corrugated waveguide," *IEEE Trans. Microw. Theory Techn.*, vol. 60, no. 1, pp. 1–7, Jan. 2012.

[6] L. Zhang, W. He, C. R. Donaldson, J. R. Garner, P. McElhinney, and A. W. Cross, "Design and measurement of a broadband sidewall coupler for a W-band gyro-TWA," *IEEE Trans. Microw. Theory Techn.*, vol. 63, no. 10, pp. 3183–3190, Oct. 2015.

[7] V. L. Bratman *et al.*, "High-gain wide-band gyrotron traveling wave amplifier with a helically corrugated waveguide," *Phys. Rev. Lett.*, vol. 84, no. 12, pp. 2746–2749, 2000.

[8] W. He, C. R. Donaldson, L. Zhang, K. Ronald, P. McElhinney, and A. W. Cross, "High power wideband gyrotron backward wave oscillator operating towards the terahertz region," *Phys. Rev. Lett.*, vol. 110, p. 165101, Apr. 2013.

[9] C.-F. Yu and T.-H. Chang, "High-performance circular TE_{01}-mode converter," *IEEE Trans. Microw. Theory Techn.*, vol. 53, no. 12, pp. 3794–3798, Dec. 2005.

[10] K. Matsumaru, "Reflection coefficient of E-plane tapered waveguides," *IRE Trans. Microw. Theory Techn.*, vol. 6, no. 2, pp. 143–149, Apr. 1958.

[11] R. C. Johnson, "Design of linear double tapers in rectangular waveguides," *IRE Trans. Microw. Theory Techn.*, vol. 7, no. 3, pp. 374–378, 1959.

[12] R. A. Waldron, "Theory of reflections in a tapered waveguide," *Radio Electron. Eng.*, vol. 32, no. 4, pp. 245–254, 1966.

[13] J. R. Garner, L. Zhang, C. R. Donaldson, A. W. Cross, and W. He, "Design study of a fundamental mode input coupler for a 372-GHz gyro-TWA I: Rectangular-to-circular coupling methods," *IEEE Trans. Electron Devices*, vol. 63, no. 1, pp. 497–503, Jan. 2016.

[14] Science and Technologies Facilities Council. (2016). *CNC Nano-Machining*. [Online]. Available: http://www.ralspace.stfc.ac.uk

Jason R. Garner received the B.Sc. degree (Hons.) in physics and the M.Sc. degree in high-power radio frequency science and engineering from the University of Strathclyde, Glasgow, U.K., in 2010 and 2012, respectively. He is currently pursuing the Ph.D. degree with the Scottish University Physics Alliance, Glasgow.

His current research interests include the design of passive components for millimeter-wave gyro-amplifiers.

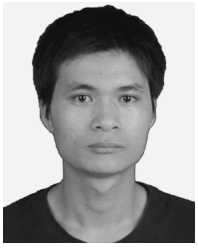

Liang Zhang received the B.Sc. degree in applied physics from the University of Science and Technology of China, Hefei, China, in 2004, the M.Sc. degree in application of nuclear techniques from the China Academy of Engineering Physics, Mianyang, China, in 2007, and the Ph.D. degree in physics from the University of Strathclyde, Glasgow, U.K., in 2012.

He is currently a Research Associate with the Scottish Universities Physics Alliance, Glasgow.

Craig R. Donaldson received the B.Sc. degree (Hons.) in physics, the M.Sc. degree in high-power RF, and the Ph.D. degree from the University of Strathclyde, Glasgow, U.K., in 2005, 2006, and 2009, respectively.

He has since continued as a Research Fellow with the Department of Physics, University of Strathclyde. His current research interests include high-frequency gyrotron traveling-wave amplifiers /backward-wave oscillators and electron beam generation.

Adrian W. Cross received the B.Sc. degree in physics and the Ph.D. degree from the University of Strathclyde, Glasgow, U.K., in 1989 and 1993, respectively.

He joined the Atoms, Beams, and Plasmas Group, University of Strathclyde, as a Research Fellow. He has been involved in various aspects of research on gyrotrons and cyclotron autoresonance masers. He is currently involved in research on terahertz radiation sources.

Wenlong He received the B.Sc. degree in physics from Soochow University, Suzhou, China, in 1983, the M.Sc. degree in accelerator physics from the China Academy of Engineering Physics, Mianyang, China, in 1988, and the Ph.D. degree in physics from the University of Strathclyde, Glasgow, U.K., in 1995.

He is currently a Senior Research Fellow with the Scottish Universities Physics Alliance, Glasgow.